THÈSE DE DOCTORAT

Université Paris IV - Pierre et Marie Curie

École Doctorale des Sciences de l' Environnement d'Ile de France

Spécialisation : **Météorologie**

présentée par

Maksimovich Elena

Sujet de la thèse

L'impact des Conditions Météorologiques sur la Variabilité de Démarrage de la Fonte sur la Glace de Mer en Arctique centrale

Timo VIHMA	Directeur de thèse
Jean Claude GASCARD	Directeur de thèse
Klaus DETHLOFF	Rapporteur
Gerhard KRINNER	Rapporteur
Sebastian GERLAND	Examinateur
Jean Louis DUFRESNE	Examinateur
Hervé LE TREUT	Président du jury

PhD THESIS

University Paris IV - Pierre and Marie Curie

Doctoral School of the Environmental Sciences
in the Region Ile de France

Speciality: **Meteorology**

by

Maksimovich Elena

Title

The effect of Meteorological Conditions on variability in the Spring Onset of Snow Melt in the central Arctic Ocean

Timo VIHMA	Supervisor
Jean Claude GASCARD	Supervisor
Klaus DETHLOFF	Opponent
Gerhard KRINNER	Opponent
Sebastian GERLAND	Examinator
Jean Louis DUFRESNE	Examinator
Hervé LE TREUT	President of jury

Resumé

Le moment de démarrage de la fonte sur la glace de mer (Snow Melt Onset, SMO) a un impact sur la fonte intégrale de la glace de mer au cours de l'été et sur le volume résiduel de la glace à la fin de l'été polaire. La variabilité interannuelle et régionale de la SMO est régulée par des flux de chaleur sur la glace. Une SMO précoce (retardé) est seulement et entièrement conditionnée par une accumulation de chaleur intense/hâtive (lente/tardive). Des observations satellitaires (SSM/I) démontrent que le démarrage de la fonte apparente (Melt Onset, MO) varie de 20-30 jours sur une distance de 25-50 km et d'une année à l'autre. Notre analyse des séries temporelles MO a révélé que ces données constituent une combinaison de la SMO (sur la glace) avec l'ouverture divergente dans les champs de glace (sans aucune fonte préalable). Pour extraire la SMO à partir de la MO il a fallu prendre en compte les concentrations de glace de mer. Les séries temporelles des flux de chaleur radiatifs et turbulents (ERA Interim) ont été appliqués pour examiner si elles peuvent expliquer les variations dans la SMO. Nous avons établis que les anomalies de bilan de flux (avant la fonte) expliquent une part importante de la variabilité interannuelle et régionale dans SMO en Arctique centrale. Le flux thermique radiatif a représenté/restitué les variations dans SMO mieux que d'autres termes de flux. Le rôle de la chaleur latente et sensible dans la fonte précoce (tardive) s'est manifesté par la perte réduite (renforcée) de la chaleur. Le rayonnement solaire n'a pas eu d'effet sur la variabilité de la SMO. Les anomalies des flux ont ensuite été examinées en relation avec les conditions météorologiques.

Abstract

Timing of spring Snow Melt Onset (SMO) on Arctic sea ice strongly affects the heat accumulation in snow and ice during the short melt season. This summertime heat uptake is quasi-linearly and inversely proportional to the remnant ice volume by the end of the melt season. On top of sea ice SMO timing, as well as its interannual and regional variations are controlled by surface heat fluxes. Anomalously early (delayed) SMO is due to large and early (weak and retarded) heat accumulation within the snowpack. Satellite passive microwave (SSM/I) observations show that the *apparent* Melt Onset (MO) varies by 20-30 days interannually and over 25-50 km distance. These apparent MO records appear to be a complex blend of SMO on sea ice and sea ice opening due to divergent ice drift. We extracted SMO out of the apparent MO record using sea ice concentration data. Applying 20-year ERA Interim reanalysis of radiative and turbulent surface heat fluxes we examined how well the heat fluxes reflect the variations in SMO. Anomalies of heat fluxes in the pre-melt period explained a significant portion of the interannual and spatial variations in SMO within the central Arctic. The main term was the downward longwave radiation locally accounting for up to 90% of the temporal SMO variations. The role of the latent and sensible heat fluxes in earlier/later SMO was not to bring more/less heat to the surface but to reduce/enhance the surface heat loss. Solar radiation alone was not an important factor for SMO timing. Anomalies in surface fluxes were examined also in relation to meteorological conditions. 20-year MO and SMO trends are towards earlier spring melt in the central Arctic Ocean.

Contents

Acknowledgments

Four years of my PhD work was a challenging and remarkable period of my life. Birth of my son, discovering the Arctic meteorology and learning French were big projects, together sometimes creating an explosive chemical composition. In the meantime I had a chance to travel a lot and meet many talented and wonderful personalities. During one of the meetings, approximately in the middle of my PhD, we had a very interesting conversation with Timo Vihma, and this became the tipping point in my work. Now I want to express my warm feelings, gratefulness and all my appreciation to Timo who guided this core study of my PhD work that I defend now. Timo, you learned and inspired me a lot! I am amazed how well and fast you could understand and find a exact answer to all my questions. Always by e-mail, wherever you were, even during Antarctic expeditions, during vacations, in the night you were very efficient to maintain and boost this study, making it light and fun.

I wish to express my gratitude to Martin Vancoppenolle and Dirk Notz who gave very helpful suggestions in the revision of this final manuscript. My appreciation to Michael Tjernstrom for his kind attitude and fast reaction whatever the scientific question was. I am grateful to Julienne Stroeve, Thorsten Markus and Walter Meier for providing MO time series and the timely interaction during the study. I acknowledge the two very attentive and meticulous Opponents Prof. Gerhard Krinner and Prof. Klaus Dethloff, the two Examinators Prof. Sebastian Gerland and Prof. Jean Louis Dufresne, and the President of Jury and my favourite Professor of Climatology Hervé Le Treut who devoted their time and energy to comment my work.

My thankfulness to the IPLS data-treatment and data-storage group, and in particular to Mme Sophie Bouffiès-Cloché, who helped me to obtain the required ERA Interim and ERA-40 data sets for this study.

Many thanks to Mme Laurence Eymard, M. Gilles Reverdin, Prof. Hervé Le Treut, Mme Laurence Touchon and Mme Nelly Lecquyer for guiding me in all my administrative questions. I also would like to express my gratitude to the technical and informatics support group at LOCEAN and now my friends Julien Vincent, Paule Zakharov and Pierre Brochard.

This PhD study was part of the EU-founded DAMOCLES and SEARCH for DAMOCLES projects, and carried out at the Laboratory LOCEAN (Paris, France). Those two EU-projects were also IPY projects.

At the end, I wish to say a few words to the people who surrounded me every day. Particularly, I thank Philippe Lattes who learned me how to implement in life all my ideas in Matlab. In this big job he was a great teacher! All my best wishes to my friends who brought many smiles and wonderful small moments in these days - Laetitia, Hervé LeGoff, Dany, Pascaline, Luigi, Anastase, Hugo, Manu, Marion, Gaelle, Pierre C., Yannis, Adrien, Carlos, Simon, Jean Festy, Agathe, Alexis B., Julien B., Soukeye and many others, whom I did not mention here.

There is no word to express my gratefulness to my family for all the support I had while working on this PhD, and first of all to my husband Simon and my son Roman. They demonstrated a lot of patience and comprehension, and a great organization. I could dedicate all my thoughts and energy to my work because there were sincerity, joy and smiles at home.

Now, with the accomplished manuscript in my hands, I feel that it is just a beginning of something.

Preface

Complete 30-year satellite record made a good deal in documenting the seasonal and interannual evolution in the Arctic sea ice cover. These illustrative and credible images demonstrate a spectacular reduction in summer ice extent, accelerating during the course of recent 5 years [*Comiso*, 2006; *Stroeve et al.*, 2007; *Deser and Teng*, 2008; *Parkinson and Cavalieri*, 2008; *Liu et al.*, 2009]. Since 1979 both September minimum and March maximum ice extents were reducing (at about -9% and -3% per decade respectively), with the annual average trend around 4% per decade [*Stroeve et al.,* 2007; *Comiso et al.,* 2008]. Thus the summer ice extents in 2005-2011 were the lowest since 1979, characterized by a pronounced ice retreat within the East-Siberian, Chukchi and Beaufort Seas [*Lindsay and Zhang*, 2005; *Comiso*, 2006; *Cuzzone and Vavrus*, 2011].

Arctic sea ice thinning was less well documented. However there is a good agreement between different data sources that ice is shrinking throughout the Arctic Ocean [*Comiso et al.,* 2008; *Kwok et al.*, 2009]. These changes occur primarily at the expense of the perennial sea ice and thinning of ridged ice, while the thickness changes within the seasonal ice zone are negligible [*Bitz and Roe*, 2004; *Rothrock and Zhang*, 2005; *Comiso*, 2006; *Nghiem et. al.*, 2007; *Kwok et al.*, 2009]. In the period between 2004 and 2008 the perennial ice area reduced by more than 1.5 million km^2, which means that at least 42% of the perennial ice area has been replaced by the seasonal ice. In terms of ice thickness, in 2003-2004 the mean ice thickness of the perennial ice zone was about 3-3.4 m during fall-winter season, and approximately 2.3-2.8 m during 2007-2008 [*Kwok et al.*, 2009b].

Uncertainties in forcing mechanisms and the complexity of interactions between the sea ice, ocean and the atmosphere have received much attention. If the ice is thinning and the ice extent reduces: what is the relative contribution of the summer ice melt, wintertime ice accumulation, and the ice export - to the ice volume changes? How sensitive the ice is to different perturbations [*Holland et al.*, 1993; *Makshtas et al.*, 2003]? What could have caused this rapid loss of Arctic summer sea ice cover [*Francis and Hunter*, 2006; *Overland*, 2006]? And whether there exist a "tipping point" for Arctic sea ice when changes in sea ice cover become irreversible [*Lindsay and Zhang*, 2005; *Winton*, 2006; *Notz*, 2009; *Eisenman and Wettlaufer*, 2009; *Armour et al.*, 2011; *Tietsche et al.*, 2011]?

Satellite retrievals on sea ice thickness and velocity showed that in the period 1999-2008 the overall melt during summer played a more significant role, rather than the ice export [*Kwok et al.*, 2009]. This result was supported by several numerical experiments [*Lindsay and Zhang*, 2005; *Rothrock and Zhang*, 2005]. However, some alternative estimates with the satellite data in higher spatial resolution doubt this conclusion

[*Smedsrud et al.*, 2011].

Numerous studies addressed the question on the relative role of the summer ice melt versus winter ice growth. These agree that the amount of the remnant summer sea ice cover is controlled primarily by the summer surface heating and the duration of the melt season, rather than winter ice accumulation and freezing conditions [*Deser et al.*, 2000; *Makshtas et al.*, 2003; *Rothrock and Zhang*, 2005; *Drobot et al.,* 2006; *Perovich et al.*, 2007a,b; *Perovich et al.*, 2008; *Vihma et al.*, 2008; *Notz*, 2009; *Kwok et al.*, 2009; *Graversen et al.*, 2011]. This finding has been explained by the fact that the ice floe in winter is always covered by snow, damping the cooling effect of the atmosphere and slowing down the basal sea ice growth. Thus with the snow cover the wintertime ice growth is quite inertial despite the intensity of the atmospheric cooling and is pretty slow, less than 15 cm per month for the ice thickness above 1 meter [*Maykut*, 1986]. This hypothesis is consistent with the observations showing that the snow cover builds-up rapidly already in September-October [*Warren et al.*, 1999; *Strum et al.*, 2002b; *Richter-Menge et al.*, 2006; *Kwok et al.*, 2009]. In contrast, during the melt season the surface radiative heating of snow and sea ice is a cumulative process: where all the supplementary heat works to warm and melt the snowpack and sea ice without any retarding and damping obstacles. To note, over the ice covered areas this heating process cannot be seen in the near-surface air temperatures since all the extra heat at the surface is rapidly used for melting [*Vihma et al.*, 2008]. Thus the near-surface air temperatures in both seasons are not an appropriate indicator for the changes occurring in sea ice.

Regarding the sources of summer heating, several parallel hypotheses could be suggested. The most classic one is called "the ice-albedo feedback" [*Kellogg*, 1973; *Lindsay and Zhang*, 2005; *Serreze and Francis*, 2006]. This feedback turns on with the reduction in sea ice concentration, and due to additional absorption of solar radiation the ice melt amplifies and the ice concentrations reduce further. However, it is obvious: to initiate this positive feedback cycle (less ice − more solar heat absorption − additional ice melt − enhancing solar heat absorption − less ice) there should exist some primary (dynamic/thermodynamic) perturbation in sea ice fraction. On one hand, the recent acceleration of transpolar ice drift [*Hakkinen et al.*, 2008] could have caused some changes in the dynamic stress on sea ice and provoke these *initial/first* perturbations in spring. According to our knowledge, there was no study yet investigating the relationship between the accelerating ice drift and the timing of summer ice break-up. On the other hand, a very interesting, brief and logic result was performed by *Francis et al.* [2005]. Based on satellite retrievals of the downwelling longwave (LWd) radiation *Francis et al.* [2005] demonstrated that the anomalies in LWd during spring-summer period (10-80 days prior to the maximum ice retreat) account for approximately 40-60% of the interannual variability in the following summer ice extent anomalies. However this finding has not received much attention yet. Curiously simultaneous studies *e.g.* by *Schweiger* [2004], *Francis et al.* [2007] and *Wang and Key* [2003, 2005b] have detected significant positive 20-year trends in springtime (March-May) cloudiness, total-column precipitable water and LWd, the strongest within the central Arctic. At this stage one may pose an eligible question: how these LWd anomalies, the sea ice melt rates and summer ice edge are related one with other? What is the physical mechanism? It seems that this subject has not been documented yet neither.

Introduction

In this study we continue the reasoning by *Francis et al.* [2005, 2007], *Perovich et al.* [2007a] and *Notz* [2009] who evidenced that summer heating and ice melt rates strongly depend on the atmospheric heat supply during spring-summer season.

We hypothesize that *the downward longwave (LWd) radiation anomaly controls the spring snow melt onset on sea ice*. In turn, *the snow melt serves as the initial (first) perturbation for sea ice melt and sea ice fraction changes*. Thus the entire mechanism likely looks as followed. *A positive (negative) LWd anomaly in spring triggers a larger (weaker) heat accumulation within the dry snowpack, earlier (later) snow melt, and then - in combination with the ice-albedo feedback - a reduced (increased) summer ice extent*. Terms *initial* and *first* refer here only to the chain of spring-summertime processes/interactions, without any pretension on being the *primary* cause of the overall sea ice changes. It is of evidence that LWd anomalies itself are triggered by some specific weather conditions.

The first part of this chain: *LWd anomaly versus heat accumulation within the dry snowpack* is quite obvious, but has not been evidenced yet. Prior to snowmelt (typically occurring in May-June) the daily mean LWd and SWd fluxes are of the same magnitude, but only 10-20% of the downward solar radiation (SWd) is absorbed in the snowpack [*Frolov et al.*, 2005; *Perovich et al.*, 2007b]. Thus in the pre-melt period (April-May) LWd is a dominant source of heat for the snow and ice surface [*Zhang et al.*, 1996]. And a larger/faster heat accumulation means faster/earlier warming of the snowpack from the typical wintertime temperatures up to the melting point, and as a result − earlier snow melt onset (MO) on top of sea ice.

The second part of the chain: *relationship between snow MO and the intensity of summer melt* has been quantified with the radiation measurements. About 55-80 cm of surface ice melt (reaching locally 90 cm) have been observed during summer 1994, 1998 (SHEBA camp) and 2007 within the Beaufort Sea [*Richter-Menge et al.*, 2006; *Perovich et al.* 1999 and 2008], where the surface melt was either the only or the dominant mechanism to thin the ice before the ice started to break-up, typically in early July. Parallel study by *Perovich et al.* [2007b] with the same SHEBA observational data conducted a numerical experiment and quantified that one day earlier snow MO on top of the sea ice increases the melt season cumulative absorbed solar energy at the sea ice - ocean surface by approximately 8.7 MJ/m^2, corresponding to the additional 3 cm of summer ice melt [*Perovich et al.*, 2007b]. For comparison, a 1-day delay in fall freeze-up resulted in an increase by only 1.5 MJ/m^2, or less than 0.5 cm of additional cumulative ice melt. One of the pioneer observations of summer ice ablation by *Langleben* [1972] established about 110 cm of top ice melt already during the first four week period after the snow was gone (around 20 May - 18 June). This experiment was carried out within the Canadian Archipelago in 1965 and started with the initial spring ice thickness of 2.5 m. Thus already in early July the ice floe was less than 1.5 m thick.

Based on energy balance thermodynamic sea ice model more recent studies by *Ebert et al.* [1995] and *Notz* [2009] came-up to an interesting conclusion. Both suggested that all the sea ice that has thinned to about 1.2-1.5 m thickness by July − early August may completely melt in the same season.

Thus the spring weather conditions and the snow MO timing on sea ice strongly affect the initial snow and ice top thinning in early melt season, and contribute the total summer ice ablation. To add, with earlier ice thinning there should be more solar heat storage in the upper ocean, and with a larger ocean heat content, naturally it takes more time in autumn to cool warmer water masses down to the freezing point [*Perovich et al.*, 2007a,b]. As a result, the freeze-up can be retarded [*Armstrong et al.*, 2003; *Gerdes*, 2006; Steele et al., 2010], which may contribute to sea ice thinning in the following year [*Laxon et al.*, 2003; *Serreze and Francis*, 2006; *Lindsay et al.*, 2009; *Wang et al.*, 2010].

In fact, over the past three decades, in line with the extinction of the summer sea ice cover and sea ice thinning [*Giles et al.*, 2008; *Kwok and Rothrock*, 2009], a tendency towards earlier MO has been revealed in the Arctic as well [*Anderson and Drobot.*, 2001; *Belchansky et al.*, 2004; *Stroeve et al.*, 2006; *Markus et al.*, 2009]. These changes are the essential elements in the recent Arctic warming but, according to our knowledge, reasons for the statistically significant 30-year trends in MO have not been explained yet.

Before attributing trends in MO, some effort is needed to understand existing MO data sets. First step in this direction and **the primary objective of this work** was the **evaluation on whether the spatial and interannual variations in apparent MO are physical, meaningful and reasonable?**

To argue and judge how physical and reasonable are these remote sensed MO retrievals one should either go and measure the surface and internal snowpack temperature within the same 25 km area (comparable to MO pixel) every day two times daily during April-June period. Otherwise one should search for some alternative solution. As we will discuss later the near-surface air temperatures are not really applicable for the validation of the remote sensed snow MO retrievals.

If addressing the physical mechanisms, on top of the snow covered compact sea ice, the timing of *SMO, its interannual and regional variations, and trends are controlled by the surface heat fluxes. An early (late) snow MO on top of sea ice is only due to an early and fast (late and retarded) net heat flux accumulation.* In turn surface heat fluxes themselves are affected by the air temperature and humidity, wind speed, clouds, ice thickness, and presence or absence of the snow cover on top of the sea ice [*Yackel et al.*, 2007].

In this study we argue: if both data (1) meteorological reanalysis and (2) the remote sensed MO are realistic and credible, than the year-to-year (temporal) and regional (spatial) differences in the MO on top of compact sea ice (= SMO) should be explained/justified by the year-to-year and regional differences in the surface heat fluxes (on top of compact sea ice) and corresponding meteorological conditions.

Specifically, **we addressed the following questions**:

1. *what is regarded for apparent MO* in SSM/I-based record?
2. what is the *relative importance of the individual surface fluxes in SMO timing*? SWd and LWd radiation, as well as the turbulent fluxes of sensible and latent heat, and various combinations of these fluxes were considered.
3. *which surface heat fluxes in ERA Interim* best reflect/reproduce the spatial and temporal variations in SSM/I-based SMO?
4. what is the *length of the relevant pre-melt period* when surface heat flux anomalies are crucial for further timing of SMO?
5. *which meteorological state variables* (ERA Interim) best reflect/explain the spatial and temporal variations in surface heat fluxes (ERA Interim) and SSM/I-based SMO?
6. whether ERA Interim surface heat fluxes may explain the *long-term trends in apparent MO and SMO*?

Our independent data sets are (a) the Snow Melt Onset on top of compact Arctic sea ice and (b) the surface heat fluxes and weather conditions from meteorological reanalysis. Vast Arctic Ocean and a 20-year period (1989-2008) were our initial frame.

Previous studies on the factors controlling the spring snow MO on sea ice have addressed either the role of a large-scale atmospheric circulation on the regional annual average apparent MO timing [*Drobot and Anderson*, 2001; *Belchansky et al.*, 2004], or the local effect of surface heat fluxes on local snow melt processes during field campaigns [*Andreas and Akley*, 1982 ; *Granskog et al.*, 2006; *Yackel et al.*, 2007; *Cheng et al.*, 2008; *Vihma et al.*, 2009]. It seems that in former (regional) studies there was no specific distinction between two totally different processes blended within the same apparent MO time series: (1) MO on top of sea ice (Snow Melt Onset) and (2) dynamically driven sea ice opening without any melt. And without this distinction the understanding/attribution/interpretation of MO changes is impossible and non-physical. In turn, studies that dealt with the measured fluxes were often limited to a very small domain (less than hundred of meters) and addressed only temporal changes in fluxes and snow melt, without any simultaneous quantification of snow melt process on top of distant ice floes with different ice thickness and different snow properties.

To summarize, little attention has been paid to small-scale spatial differences and interannual variations in the snow MO and surface heat fluxes, both on top of sea ice. And, as we just said: understanding and validation of these spatial and interannual variations is the basis for any argumentation (justification) for the long-term MO trends. None of the existing papers considered modern reanalysis data for a snow melt onset study. And very few papers questioned the reliability of reanalysis surface fluxes in the Arctic Ocean, and even lees - during spring seasonal transition and within the central Arctic.

We did not pretend to fill in all these gaps, moreover - our study would not see life without all these existing results and ideas. We acknowledge all the huge effort that has been done to produce meteorological reanalysis and the apparent MO time series - both of high complexity. And also all our appreciation to the field scientists who managed to carry out interesting and unique measurements in hard polar conditions, creating the basis of our nowadays knowledge.

Chapter 1

Arctic Environment: Meteorology, Sea Ice, Snow Cover and Surface Heat Fluxes

This Chapter introduces the general overview on meteorological, cloud cover, sea ice and snow conditions and their seasonal cycle in the Arctic Ocean. These components are tightly related one with the other, controlling together and all affected by the radiative and turbulent heat exchange at the air-sea interface. In Section 1.1 we discuss the seasonal cycle in the classic meteorological variables: sea level pressure, cyclonic activity, near surface temperatures and humidity, and near-surface winds. In Section 1.2 we pay attention to some specifics of Arctic clouds. In Section 1.3 we outline a short summary on Arctic sea ice properties and some feedbacks between the sea ice and meteorological conditions. Section 1.4 is dedicated to the snow properties on top of Arctic sea ice, which is of special interest for understanding the spring Snow Melt Onset study developed during this work. In Section 1.5 we describe the seasonal cycle and particularities of the surface radiative and turbulent heat fluxes in the maritime Arctic based on (a) previous studies and (b) our calculations with three meteorological reanalysis products (ERA Interim, ERA-40 and NCEP/NCAR). At this stage we short-cut the typical features and highlight some differences between these three widely used meteorological data sets in terms of surface heat fluxes. A particularity of this Section is that the comparison of surface heat fluxes between three reanalysis is done for the common 13-year period (1989-2001). The rest of this manuscript is built on the data for the period 1989-2008.

To be specific, **Arctic Ocean domain is defined** here as the area bounded by the Bering Strait, the Canadian Archipelago, Greenland, Fram Strait, northern Barents Sea and the Siberian coast. Within these boundaries, the Arctic Ocean covers the area of approximately 7.2 million km^2. Polar night and polar day are divided here schematically into four seasons: winter (DJF), spring (MAM), summer (JJA) and fall (SON). Under the term "surface" we further consider either the interface between the open sea and the atmosphere (when the study area is ice free), or the interface between the snow covered sea ice and the atmosphere (when sea ice is present).

1.1 General meteorological conditions

Atmospheric energy budget of the polar cap (70-90^{o}N)

Atmospheric thermal advection is the major source of heat for the total Arctic energy budget year-round, injecting about 80-110 W/m^2 of heat (vertically integrated at 70^{o}N) throughout the year [Nakamura and Oort, 1988; Overland and Guest, 1991; Semmler et al., 2005; Serreze and Barry, 2005; Serreze et al., 2007]. For comparison, the atmospheric advection of moisture is an equivalent of 10-25 W/m^2 [Serreze et al., 2007], and the annual mean horizontal ocean heat convergence via Atlantic and Pacific inflows is about 15 and 40 TW [Rudels et al., 2008], corresponding to the under-ice (upward, wintertime) ocean heat flux of 1-4 W/m^2 [Perovich and Elder, 2002].

Atmospheric thermal and moisture transports are both strongest within the lower troposphere around 850-990 mb pressure level in all seasons [Nakamura and Oort, 1988; Serreze et al., 1995b; Jakobson and Vihma, 2010]. And both atmospheric thermal and moisture transports are governed by the cyclonic activity in all seasons [Oort, 1973; Overland and Guest, 1991; Zhang et al., 2004; Jakobson and Vihma, 2010]. Thermal advection northward is intensified during winter [Serreze and Barry, 2005]. This is because of the large horizontal surface thermal gradients during polar night, primarily localized in the North Atlantic and North Pacific. In contrast the moisture transport across 70^{o}N is the largest in summer [Groves and Francis, 2002; Serreze et al., 2007; Jakobson and Vihma, 2010; Cullather and Bosilovich, 2011]. Accordingly, summer moisture convergence accounts for about 35% of the annual moisture transport across 70^{o}N, and, as in winter, occurs mostly within the maritime areas, in particular in the Norwegian and Chukchi Seas [Sorteberg and Walsh, 2008; Jakobson and Vihma, 2010]. However, the estimates of the total moisture transport into the Arctic are challenging and strongly diverge between different data sets, ranging within 50-205 mm per year [Sellers, 1965; Sorteberg and Walsh, 2008].

Thermal and moisture convergence in the Arctic atmosphere increases the air temperature and atmospheric moisture content, and these largely affect the surface energy budget via the longwave (thermal) radiative emission of the atmosphere and clouds, and via the turbulent heat exchange between the air masses and the sea ice - open sea surface [Gerding et al., 2004]. Yet, a large portion of the advected atmospheric heat never reaches the surface and is emitted as longwave radiation in space.

Seasonal features: atmospheric circulation (SLP), near-surface air temperatures and winds

The atmospheric heat convergence, depth of cyclones and the frontal activity are the most intense during **Arctic winter** [Zhang et al., 2004; Sorteberg and Walsh, 2008; Simmonds et al., 2008; Sepp and Jaagus, 2010]. In this period the stratospheric circulation (polar vortex) is well developed, and due to sea ice formation large surface thermal gradients build-up on the Atlantic side (within Greenland, Norwegian and Barents Seas) and on the Pacific side (across Chukchi and Bering Seas) of the Arctic. Thus, during December-February (**Fig 1.1a**) the typical **near-surface air temperatures (SAT)** are within -20-40^{o}C over the sea ice and near the freezing point (about -2^{o}C) over the open sea (Greenland, Norwegian, Barents and Bering Seas), with a huge thermal difference across the narrow boundary between the sea ice and open sea. 20-year mean (1989-2008) **sea level pressure (SLP)** averaged for December-February months (**Fig 1.1a**) reflects the typical circulation structure: with a low-pressure trough over the Greenland-Norwegian-Barents Seas (Icelandic Low) and the broad high-pressure core extending over the Arctic Ocean, centred on the East-Siberian - Beaufort Seas (Beaufort High). On the Atlantic side within the zone of the sharp thermal gradients the extra-tropical cyclones shape and advance along [Tsukernik et al., 2007], tracing this low pressure trough on the time-average SLP maps. In contrast, very homogeneous thermal conditions (with intense surface cooling) within a vast sea ice domain of several millions of square kilometres build-up and maintain the Beaufort High. Winter cyclones are also common in the Bering Sea (Aleutian Low), but relatively few of them migrate into the Arctic [Serreze and Barret, 2008]. The day-to-day fluctuations in SAT can be large during the polar night, with the warmest near-surface temperatures of -20^{o}C occurring under the overcast skies and strong winds, and the coldest air temperatures of -40-45^{o}C observed under the clear skies and weak winds [Overland and Guest, 1991; Lindsay and Rothrock, 1994; Lindsay 1998; Walsh and Chapman, 1998].

In **spring** (March-May) in presence of the extensive sea ice cover with a highly insulating snowpack on top, the surface radiative cooling continues to dominate the increasing downward solar heating. Spatially uniform cold surface temperatures continue to maintain the Beaufort High (**Fig 1.1b**). With higher solar elevation and increasing moisture advection (increasing atmospheric thermal emission) the snow and air temperatures gradually rise to 10-20^{o}C in April, and already in May the snow melt starts [Serreze and Barry, 2005].

Throughout the **melt season**, typically lasting 2-4 months (June - August) the snow-ice surface temperatures are tightly kept near the melting point -2-0^{o}C (**Fig 1.1c**), where all the heat received at the surface is spent on snow and sea ice melt, and evaporation. In contrast to Antarctic melt season, the surface (snow and ice) melt largely dominates evaporation in the Arctic [Andreas and Akley, 1982; Nicolaus et al., 2009]. The departure of SAT is within $\pm 2^o$C during summer, both over the sea ice and open water areas [Persson et al., 2002; Serreze and Barry, 2005]. During this period the horizontal thermal gradients develop across the Eurasian and North-American coast. Thus in summer the major frontal zone is located over the land areas, roughly between 65-70^{o}N and 140-270^{o}E [Serreze and Barret 2008]. Roughly a half of the total number of summer cyclones observed in the Arctic Ocean develop over the Eurasian continent, with the North Pacific, North Atlantic and North American continent accounting together for another half [Serreze and Barret, 2008]. Cyclone tracks shift northward during summer following the retreat in sea ice edge. Number of cyclones within 70^{o}N appears to be larger in summer compared to winter [Serreze and Barret, 2008]. However, the number of cyclones entering the Arctic was found to be largest in winter [Sorteberg and Walsh, 2008; Simmonds et al., 2008].

Already in **August**, one month before the solar heat source vanishes, the freeze-up starts. First, the melt ponds freeze in the central Arctic and then freezing conditions advance southward. By October-November sea ice establishes all around the Arctic Ocean. In consequence, the horizontal thermal gradients in the Greenland, Barents and Chukchi Seas sharpen and the cyclonic activity intensifies in these areas. SAT stay around -5-10^{o}C within the open sea areas and drop fast to -25-30^{o}C over the sea ice domain. By **November** the wintertime atmospheric circulation structure settles down with two low pressure cores in the North Atlantic and North Pacific and the Beaufort High stretching from the Canadian Archipelago across the central Arctic into the eastern Siberia.

North of 70^{o}N **precipitation** peaks its maximum of 95-105 mm (3 month average) during summer and autumn, and is about 30-60 mm during winter and spring seasons [Frolov et al., 2005; Serreze and Barry, 2005; Serreze and Barret, 2008; Jakobson and Vihma, 2010]. The relative contribution of the moisture advection into the Arctic (70-90N) and the evaporation within the region were found to be of equal importance in the seasonal amounts of precipitation during summer, with a relatively larger role of the horizontal moisture advection during winter [Walsh et al., 1994; Jakobson and Vihma, 2010]. A recent study by Sorteberg and Walsh [2008] with NCEP/NCAR reanalysis [1] evaluated that the moisture transport across 70N accounts for about 79% of summer precipitation and 72% of the annual precipitation within 70-90^{o}N. Alternative study

1. NCEP/NCAR reanalyses [Kalnay et al., 1996] is discussed in Chapter 2

with ERA-40 reanalysis [1] by Jakobson and Vihma [2010] evaluated that the moisture flux across 70^{o}N accounts for about 59% of the annual Arctic precipitation. Although these estimates diverge, there is however a general agreement on the relative importance of processes controlling precipitation amounts and its seasonal cycle. To note that precipitation is a very challenging quantity, both for direct measurements and for numerical modelling.

Winds have the major effect on the ice drift velocities, turbulent water mixing in leads and the turbulent heat exchange (condensation, evaporation) between the snow-ice-open sea surface and the atmosphere. Monthly means of the near-surface winds within the sea ice covered Arctic are about 5-7 m/sec [Andreas and Akley, 1982; Nilsson et al., 2001; Curry et al., 2002; Persson et al., 2002; Frolov et al., 2005; Vihma et al., 2008]. The strongest winds were observed in winter when the largest spatial surface thermal gradients emerge and the atmospheric fronts are the most violent [Frolov et al., 2005].

Vertical thermal stratification in the lowermost 2-3 km: seasonal features

During winter the snow-sea ice radiative cooling is intense and larger than the atmospheric radiative cooling. In such conditions the sharp surface-based inversion prevails, reaching heights of 500-2000 m above the sea surface, with the occurrence (mostly on the Atlantic side) of strong elevated (capping) inversions above the shallow (30-180 m) mixed boundary layer [Overland and Guest, 1991; Tjernstrom and Graversen, 2009]. Vertical temperature difference within the inversion depth is of the order of 10-15^{o}C during winter [Chiacchio et al., 2002; Overland, 2009; Pavelsky et al., 2011]. Formation of these wintertime elevated inversions have been explained by the presence (passage) of stratus and stratocumulus cloud-types and the related radiative and dynamic processes [Tjernstrom and Graversen, 2009].

In spring, as the sun rises the surface heating rate starts to compete with the surface radiative heat loss. As a result, snow temperatures gradually increase. Observations show that near-surface inversions are still present in April [Pinto et al., 1997]. Further on, the horizontal thermal gradients loosen on the Atlantic and Pacific sides of the Arctic, and the atmospheric thermal advection into the Arctic slightly weakens [Serreze and Barry, 2005]. By the month of May and during the rest of summer infirm near-surface inversions alternate with the unstable stratification capped by the thermal and moisture inversions [Persson et al., 2002; Vihma et al., 2008; Tjernstrom and Graversen,

1. ERA-40 reanalysis [Uppala et al., 2005] is discussed in Chapter 2

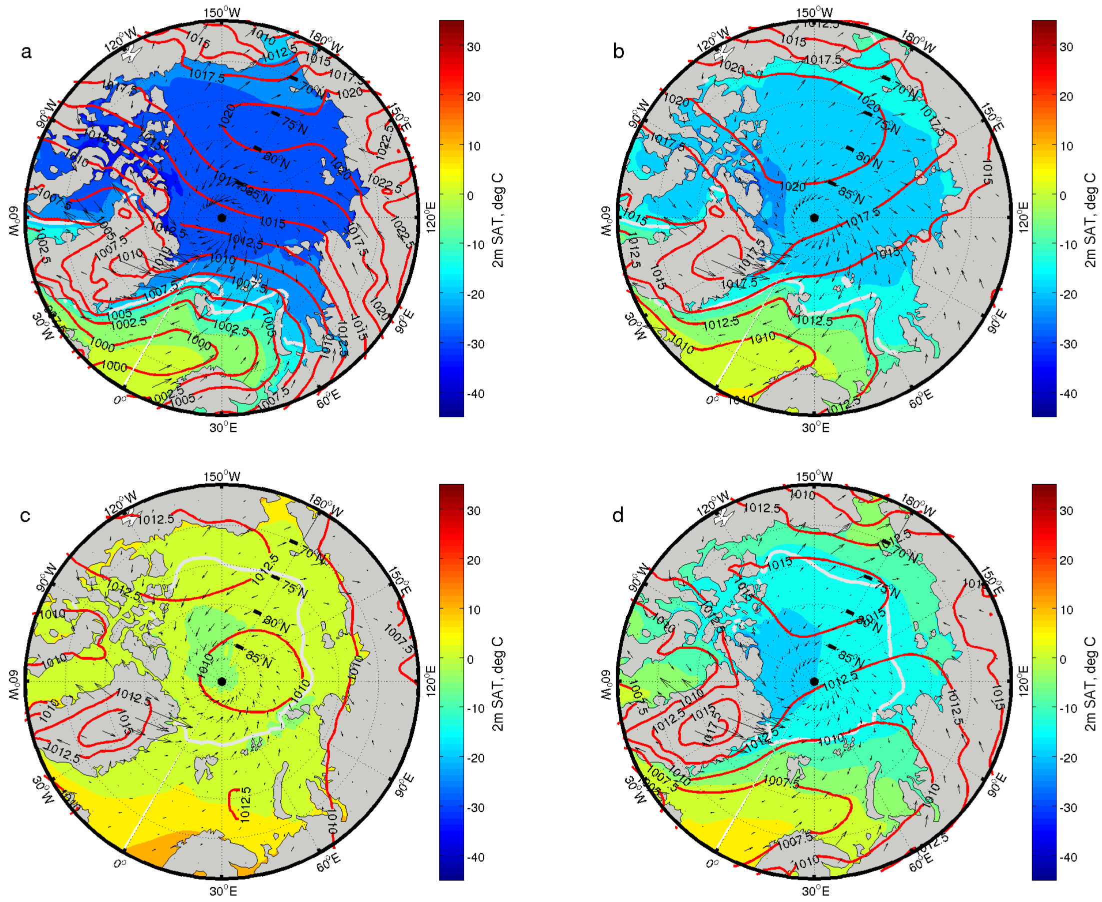

Figure 1.1: Mean Sea Level Pressure, 10m wind field, 2m air temperature and 80% SIC edge averaged during (a) DecJanFeb, (b) MarAprMay, (c) JunJulAug, (d) SepOctNov. White contour localizes the sea ice covered area with the seasonal ice concentration of 80-100%. Data: ERA Interim reanalysis (see Chapter 2, Section 2.2), mean for the period 1989-2008.

2009; Overland, 2009; Graversen et al., 2011].

By August the surface radiative cooling again starts to prevail the surface heat sink. During some period, even under the intense cooling, the open sea surface stays relatively warm compared to the air aloft, and the unstable vertical stratification builds-up over the open sea (below 850 hPa level) during August-September. These conditions favour intense atmospheric convection and cloud formation during early freezing season, until the growing sea ice thickness and snow deposition on top of sea ice do not cancel the huge ocean heat loss to the atmosphere [Schweiger et al., 2008]. By November-December the sea ice thickens and spreads over the marginal seas. Under the intense surface radiative cooling and increased horizontal thermal advection, stable vertical stratification (near surface inversion) develops again over the vast ice covered domain for the rest of the freezing season. Episodically, the intrusion of atmospheric fronts and sea ice cracks perturb these stable conditions.

Near-surface air temperature: diurnal cycle

Over the Arctic sea ice the diurnal cycle in SAT is the largest in spring [Richter-Menge et al., 2006] and early fall, with the greatest amplitudes (of about 3-5^{o}C) observed in April [Goddard, 1973; Persson et al., 2002], both field campaigns in the Beaufort Sea. Mast measurements show that this largest diurnal cycle in SAT occurs within the lowermost well mixed 10-20 m layer capped by temperature inversion. In April SAT is around -10-30^{o}C over the sea ice covered Arctic, the daily mean surface energy budget is still negative, and the diurnal amplitude in solar radiation can be already about 200-250 W/m^2 [Rigor et al., 2000; Martin and Munoz 1997; Persson et al., 2002]. Capped by stable stratification (best with some clouds and no wind), solar radiation and the atmospheric thermal emission both tend to increase the snow and near-surface air temperatures. In the meantime the stable near-surface stratification prohibits the immediate turbulent mixing between the shallow near-surface layer and the air above. In the nigh-time the solar elevation is low and the radiative heat loss again dominates the solar heating at the surface. And since the heat content of snow and the atmospheric moisture content are low, snow and near-surface air cool fast in the night.

During the melt season the diurnal fluctuations in SAT stay tightly within -2-0^{o}C imposed by snow and sea ice melting [Rigor et al., 2000; Nilsson et al., 2001; Persson et al., 2002; Tjernstrom, 2005; Inoue et al., 2005; Vihma et al., 2008]. Thus, on midday, all the additional solar heat is pumped for the snow and ice melt, preventing the surface and near-surface air temperatures from rising above the melting point (0^{o}C). And on the midnight, when the solar heating reduces, the latent heat releases due to freeze-up, maintaining SAT and snow surface temperatures at the freezing point about -1.5-2^{o}C.

Near-surface air humidity

Atmospheric moisture exists in a form of water vapour, liquid droplets, and ice crystals. In polar regions, on average, the water vapour accounts for approximately 99% of the total moisture content in the atmosphere [Tietvinen and Vihma, 2008]. The specific humidity of the polar air masses is very low, with the near-surface specific humidity generally below 3 g/kg. However the relative humidity with respect to ice is almost always at the saturation level both in winter and summer [Persson et al., 2002; Vihma et al., 2008]. Detailed analysis of field observations suggests that the extremely high near-surface relative humidity values are primarily due to leads that moist the near-surface air [Andreas et al., 2002], enclosed at the surface by thermal inversions. This relatively moist air from leads is further cooled by radiative and turbulent exchange at the air-snow interface, however, this surface heat exchange is not fast enough to equilibrate the supersaturated near-surface air with the snow moisture content [Andreas et al., 2002].

1.2 Cloud cover

Seasonal cycle

Cloudiness over the Arctic Ocean is ample, on average, about 60% in winter and 80-90% in summer [Curry and Ebert, 1992; Intrieri et al., 2002; Wang and Key, 2005a]. Wintertime clouds are represented by middle and high-level clouds, associated with the large-scale atmospheric circulation, cyclonic activity, convection and evaporation over the open sea [Xin Lin, 2008]. Around April low-level mixed phase stratus clouds build-up very near the surface. Summertime field observations documented the continuous multi-layer stratus clouds with the cloud base within the lowest 100 m above the ice surface, frequently overlapping (co-existing) with fog and the high-level clouds [Tjernstrom, 2005; Xin Lin, 2008].

Evaporation versus horizontal Moisture Advection

Interestingly, while the evaporation and horizontal moisture advection largely contribute to the Arctic atmospheric moisture and heat budget year-round, they do not control the seasonality of stratiform clouds in the Arctic Ocean. As demonstrated by Beesley and Moritz [1999] in spring the low-level cloud cover develops already one month before the horizontal moisture advection and evaporation intensify. The formation and persistent nature of these stratiform clouds during spring and summer was explained by the particularities of the dissipative mechanisms (such as precipitation), solar heating and the convective mixing, which are relatively weak over the Arctic Ocean compared to mid-latitudes [Beesley and Moritz, 1999; Intrieri et al., 2002; Dong and Mace, 2003]. Water phase transitions (liquid water ice) and the water droplet / ice crystal size were found to be crucial for initialization and life-cycle of Arctic stratiform clouds [Beesley and Moritz, 1999].

Cloud radiative forcing

The impact of clouds on radiative fluxes (cloud radiative forcing, CRF) largely depends on cloud fraction, cloud height and depth, the phase of cloud particles (liquid or ice), the amount of liquid water, and the size and shape of the cloud particles [Curry and Ebert, 1992; Intrieri et al., 2002; Gorodetskaya et al., 2008]. Yet, conventionally

CRF is mostly attributed to the total cloud fraction and is often defined as the difference in the radiative flux under the overcast and the clear skies [Walsh and Chapman, 1998; Intrieri et al., 2002]. In the Arctic over the course of the year clouds have a net warming effect on the surface, except for a few weeks in mid-summer (around July) when the incident solar radiation and its absorption at the surface are at their maximum. During this relatively short period the attenuation of solar rays by clouds generates smaller solar heating of the surface, compared to the green-house effect of clouds [Curry and Ebert, 1992; Schweiger and Key, 1994; Intrieri et al, 2002].

Clouds and, in particular low-level clouds, backscatter at the cloud bottom in solar spectrum. This effect becomes particularly important over a highly reflective snow-ice surface, producing multiple reflections between the clouds and the snow-ice, in turn increasing the resulting downward solar radiation at the surface on cloudy days [Curry and Ebert, 1992; Shine, 1984; Wendler et al., 2004]. This effect of clouds is particularly pronounced in the Arctic where a vast "white" surface persists until late June July. The accuracy of existing cloud products and the related CRF estimates remains uncertain. Recent comparison of several high resolution cloud products in the period 2006-2008 was done by Liu et al. [2010]. Accordingly, errors in the surface net CRF of about 9% were detected, which corresponds to approximately $\pm$2-6 W/m^2 uncertainty in the surface net flux. Alternative study by Sedlar et al. [2010] suggested $\pm$10-15 W/m^2 uncertainty in the observed net CRF.

Atmospheric aerosols, clouds and radiative fluxes

Atmospheric aerosols affect the **shortwave (SW)** and **longwave (LW)** radiative transfer trough the atmospheric column. They act as the cloud condensation nuclei (CCN), affecting the cloud microphysical and radiative properties as well as the persistence (life-time) of clouds in time [Boucher and Lohmann, 1995; Curry, 1995; Garrett et al., 2002]. The higher concentration of CCN, increases the cloud droplet concentration, reduces the droplet size, thus weakening the precipitation process and, as a result, increasing the total liquid water content within the atmospheric column [Garrett et al., 2009]. In turn, larger atmospheric moisture content (larger optical depth) modifies the radiative fluxes at the surface: decreases the direct SW rays, enhances the diffused (scattered) SW radiation, and strengthens the atmospheric thermal (LW) emission [Garrett et al., 2002]. To mention, the anthropogenic pollution advected to the Arctic from lower latitudes was found to be the greatest during winter and spring [Barrie, 1986; Sirois and Barrie, 1999; Garrett et al., 2002]. This indicates that atmospheric aerosols might have an indirect effect on spring Snow Melt Onset timing on top of sea ice by means of surface fluxes.

1.3 Sea ice

Extended Arctic winters generate an intense surface radiative cooling and sea ice formation during most of the year. Only during 2-4 months (May-August) the incoming radiation (solar and atmospheric thermal radiation together) dominates the surface heat loss, allowing the snow and sea ice melt. While the melt season is short, the ice melt rates are typically much higher than the sea ice growth rates in winter. Thus the characteristic surface ice melt rate (for unponded ice) is of the order of 1-2 cm/day [Langleben, 1972; Eicken et al., 2001a; Luthje et al., 2006; Perovich et al., 2008], 23 times larger in presence of the melt ponds [Fetterer and Untersteiner, 1998], and the basal ice melt is about 0.2-0.3 cm/day [Perovich et al., 1999]. In terms of the total (surface and bottom) ice melt this is an equivalent of 50-120 cm melt during the melt season [Persson et al., 2002], reaching 270 cm of the total ice melt, or 4-11 cm/day melt rates within the marginal seas [Perovich et al., 2008]. For comparison the typical (total = basal) wintertime ice accretion rate is less than 1 cm/day for the ice floe thicker than 60-100 cm or just a snow covered ice floe [Maykut, 1986; Wadhams, 2000]. In consequence, even during short polar summer a large sea ice volume melts every year, and first of all, the young and thin sea ice within the marginal Arctic seas. Satellite images nicely illustrate the seasonal retreat of the sea ice edge northwards each summer.

Sea ice extent, area and concentrations

Conventionally in the remote sensing the sea ice extent accounts for all ice covered pixels with at least 15% ice concentration. Thus the size of any grid cell covered by more ice than the defined threshold contributes fully to total sea ice extent. For sea ice area only the truly ice-covered fraction of each pixel is considered. Estimates of total sea ice extent are generally more reliable than the estimates of sea ice area [Meier and Notz, 2010].

Annual cycle of the sea ice extent in the Arctic Ocean (within the limits determined at the beginning of this Chapter) varies between 4 and 7.2 mln km^2 [Kwok et al., 2009], with the maximum ice edge advance in February-March and the strongest ice retreat during August-September. Yet, some areas stay ice-free even during the winter season. The inflow of the warm Atlantic current prevents the sea ice formation within the vast areas in the Barents, Norwegian and Greenland Seas. Divergent ice drift under the effect of ocean currents, waves, tides and the wind stress generate and maintain the areas of open water (leads and polynyas) in the middle of the continuous ice field, occurring all over the Arctic Ocean. In these ice-free areas the intense water cooling generates a rapid sea ice production.

Sea ice thickness and ice age

Arctic sea ice is composed schematically of the multi-year (perennial) and the first-year (seasonal) ice types. Sea ice thickness depends on the age and the degree of deformation. The largest undeformed ice floe thickness estimates attain 1.5-2 m for the first-year ice, 3-3.4 m for 7-9 year old ice-types, and the pressure ridges can be as high as 20 m [Bourke and Garrett, 1987; Ebert et al., 1995; Maslanik et al., 2007]. Regional average sea ice thickness throughout the year is approximately 2-3 m [Kwok and Cunningham, 2008; McLaren et al., 1994; Kwok et al., 2009].

Evaluation of the sea ice thickness is a challenging task. Satellite-based altimeters estimate the free-board that is the height of the ice floe above the sea level [Kwok et al., 2009b; Laxon et al., 2003; Giles et al., 2008]. This free-board estimate and empirical equations are then used to evaluate the total sea ice thickness. However, there is a large uncertainty in satellite retrievals of sea ice thickness, reaching 40-70 cm [Laxon, 2003; Kwok and Cunningham, 2008]. Arctic sea ice thickness was also measured locally with a help of drifting buoys deployed into the ice floes [Perovich and Richter-Menge, 2006], submarine sonars [Bourke and Garrett, 1987; McLaren et al., 1992; Wadhams and Davis, 2000; Tucker et al., 2001; Yu et al., 2004; Rothrock et al., 1999 and 2008; Melling et al. 2005], upward looking sonars deployed on moorings fixed at the sea-floor [Proshutinsky et al., 2004], aerial laser measurements of the freeboard [Bourke and Garrett, 1987], and aerial electromagnetic induction soundings [Haas et al., 2009; Rabenstein et al., 2010].

Sea ice drift

Arctic sea ice cover is constantly in motion under the effect of winds, tides and the other ocean currents. Under the stress sea ice floes crush, diverge and build-up to the pressure ridges. Ice divergence and upwelling of ocean heat create the open sea areas specifically called: leads and polynyas [Wadhams, 2000]. Arctic sea ice motion mirrors closely the major atmospheric circulation patterns [Inoue and Kikouchi, 2007].

In winter a well developed Beaufort High in the western Arctic, and frequent and intense cyclonic motion in the eastern Arctic remove sea ice from the Siberian coast (Laptev, Kara and East-Siberian Seas) towards Greenland and the Fram Strait [Pfirman, 2004]. **Fig 1.2** illustrates the averaged ice velocities and trajectories for December-March period during 1988-2003. In summer these transpolar winds and related ice drift speeds weaken (not shown).

From year-to-year and day-to-day the atmospheric circulation evolves in strength, modulating the ice drift trajectories and velocities. Ice drift velocities range within 0-25 km per day [Thorndike, 1986; Zhao and Liu, 2007].

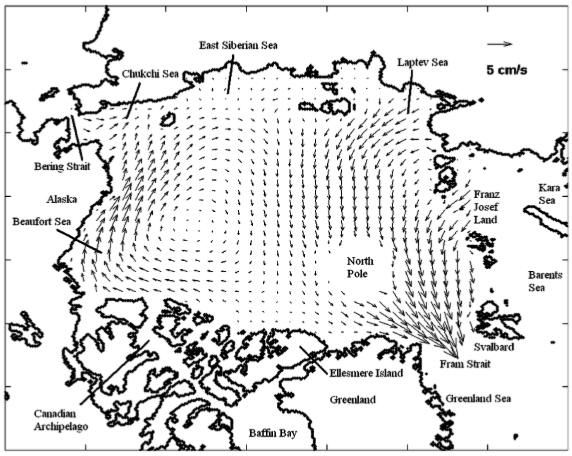

Figure 1.2: Mean sea ice motion for 15 winter seasons (Dec-March), 1988-2003. Reprint from Zhao and Liu [2007].

1.4 Snow cover on top of sea ice

Snow depth

The snow depth varies around 0-100 cm on the distances of 10-100 meters, with no relationship to the ice type and ice thickness [Walsh and Chapman, 1998; Perovich et al., 2002; Perovich and Richter-Menge, 2006; Gerland and Haas, 2011].

Heat fluxes and temperature within the snowpack Two important thermodynamic properties of the snow are the thermal conductivity (λ) and the specific heat capacity (c_p). The thermal conductivity is the intensity of the heat flux through the snowpack in response to temperature gradients. Thermal conductivity in pure snow is about 0.1-0.4 [W m^{-1} K^{-1}], increasing with denser and decreasing for saltier snow [Strum et al., 2002a; Steffen and DeMaria, 1996]. A specific heat capacity (c_p) represents the amount of energy required to rise the snow temperature by 1^{o}K, is about 2 kJ kg^{-1} K^{-1}.

$$\lambda = kc_p\rho \tag{1.1}$$

Here ρ is the snow density, ranging within 100-500 kg/m^3 and k is thermal diffusivity of snow is about 10^{-6} m^2 s^{-1}. Low thermal conductivity and high heat capacity of the snow explain the fact that snowpack acts as a good insulator for the sea ice. In presence of snow the response of the sea ice temperature to atmospheric perturbations in temperature is largely weakened, and with a 20 cm snowpack the temperature contrasts within the ice are practically absent [Kondratyev, 1996].

Snow temperatures

From November to March snow temperatures on Arctic sea ice vary within 10^{o}C and 40^{o}C at the snow surface and within 16^{o}C and 6^{o}C at the snow-ice interface [Overland and Guest, 1991; Persson et al., 2002]. In winter period the snow temperatures tend to be warmer during cloudy days, compared to clear sky days. Observations show that the largest variations in temperature occur in the uppermost snow layer, attenuating in deeper layers. In winter at about 5-15 cm depth the temperature amplitude within a few consecutive days may reach 20^{o}C, but less than 5^{o}C below 35 cm depth [Jordan et al., 1999]. The largest diurnal cycle within the snowpack was found in spring (April) before the snow melt starts [Yackel, 1999]. In this period the snow and near-surface air temperatures are still below zero (-10-20^{o}C), but with a large diurnal cycle in solar radiation the punctual heating of snow and the near-surface air may take place in the afternoon (the strongest under stable vertical stratification without vertical mixing).

In nature, the near-surface air temperature (SAT at 2 m) does not depart from the upper snowpack temperature by more than 2^{o}C, except for vary calm clear sky days with no wind [Overland and Guest, 1991; Lindsay, 1998; Persson et al., 2002]. During the melt season, although there is a large SW diurnal cycle and episodic stable stratification, a diurnal cycle in the snow temperature cannot occur. In this period snow temperatures and SAT both and tightly constrained at about -2-0^{o}C by the melting of snow and re-freezing of the melt water.

Aerosols within the snowpack

Atmospheric aerosols (dust and soot) deposited on the highly reflective snow and bare ice surface reduce snow albedo. In presence of soot the absorption of solar radiation is more efficient and the internal heat storage is bigger, favouring the earlier and faster snow melt [Clarke et al., 1985; Grenfell et al., 2002; Hansen and Nazarenko, 2004].

1.5 Surface radiative and turbulent heat fluxes

Downward Shortwave Radiation

Seasonal cycle in the downward solar shortwave radiative flux (SWd) over the maritime Arctic northward from 70^{o}N (plain curve) and along 85^{o}N (dashed curve) are illustrated in **Fig 1.3a**. SWd is the most intense during May-July months, with the daily mean flux about 250-300 W/m^2 and the midday values reaching 450-500 W/m^2 under clear skies [Walsh and Chapman, 1998; Jordan et al., 1999; Persson et al., 2002; Wang et al., 2007; Sorteberg, 2007a; Vihma et al., 2008; Overland, 2009].

Regionally, on average (13-year mean during 1989-2001, ERA-40 and ERA Interim [1]), the smallest SWd during summer solstice is found on the Atlantic side of the Arctic Ocean (220±60 W/m^2), and the strongest SWd (270±50 W/m^2) takes place in the East-Siberian - Chukchi Beaufort Sea sector (not shown).

In reality SWd cloud radiative forcing is the most pronounced in June-July when the solar radiation is the most intense and the optically thick liquid multi-layer stratiform clouds attenuate efficiently this strong SWd flux [Intrieri et al., 2002; Wang and Key, 2005a; Sedlar et al., 2010]. Field and numerical experiments suggest that, on average SWd cloud radiative forcing is about 20-60 W/m^2 in early and late summer (April and August months) and 100-160 W/m^2 in July, with non-linear relationship between the cloud fraction and SWd reduction [Intrieri et al., 2002; Shupe and Intrieri et al., 2004; Gorodetskaya et al., 2008].

We found a huge difference in SWd values between NCEP/NCAR reanalysis and two ECMWF reanalysis products (ERA-40 and ERA Interim), see **Fig 1.3a**. This inconsistency has been noted already by Serreze et al. [1998], Serreze and Hurst [2002], Semmler et al. [2005], Liu et al. [2005] and Sorteberg [2007a,b]. Thus, the comparison of different reanalyses with the SWd observations at SHEBA [2] field camp [Curry et al., 2002; Liu et al., 2005] and at the North Pole drifting camps [Serreze et al., 1998] evidenced that both NCEP/NCAR overestimated SWd, whereas ERA-40 reproduced SWd better. Our comparison suggested the bias between NCEP/NCAR and both ECMWF reanalyses by up to 70-100 W/m^2 in the daily mean SWd flux (May-July), the largest during the summer solstice. So far the difference in SWd between NCEP/NCAR and ERA products is not localised (much stronger) within some particular area of the Arctic Ocean, but it is found within the entire polar cap within 70-90^{o}N. Although, there was no study published yet on the accuracy of surface fluxes in the most recent ERA Interim reanalysis, apparently, it is closer in respect to SWd to its predecessor ERA-40, rather than NCEP/NCAR SWd product (**Fig 1.3a**).

This difference in SWd between NCEP/NCAR and ERA-40 reanalysis had been linked to a large underestimation in the cloud cover in NCEP/NCAR [Walsh and Chapman, 1998; Liu et al., 2005; Bromwich et al., 2007]. Comparison of NCEP/NCAR with ERA-40 reanalysis and observations at Point Barrow by Bromwich et al. [2007] established that ERA-40 captures the day-to-day variability in the total cloud cover (and seasonality) much better than NCEP/NCAR, although itself producing too optically thin clouds for SWd. In the other words, ERA-40 better represents SWd (the diurnal amplitude and values) on the clear sky days, whereas SWd diurnal maximum is much

1. ERA Interim reanalysis [Uppala et al., 2008] is discussed in Chapter 2
2. Surface Heat Budget of the Arctic Ocean (SHEBA) field campaign in 1998-1999 [Uttal et al., 2002]

too high in ERA-40 on cloudy days during summer (with the error in the diurnal amplitude reaching 150-300 W/m^2 on cloudy days in June). NCEP/NCAR total cloud fractions were very small compared to observations in June at Point Barrow, with the corresponding diurnal minimum in SWd about 50 W/m^2 to high and the diurnal maximum in SWd about 100-400 W/m^2 too intense in NCEP/NCAR [Bromwich et al., 2007].

We just made a quick test for the total cloud cover easily available for three reanalysis. We compared the mean total cloud fraction during 3 summer months (May-July), average during the common 13-year period (1989-2001). There is in fact a striking difference between NCEP/NCAR and both ECMWF reanalysis (ERA Interim and ERA-40) within the entire Arctic Ocean. Summertime Arctic cloud cover in NCEP/NCAR is about 40-50% with a large year-to-year variability, whereas in both ECMWF reanalysis there is 80-90% cloud cover (overcast) with very few year-to-year variability.

The observational error for SWd term depends on the absolute magnitude of the observed flux, is approximately ±5-10 W/m^2 [Serreze et al., 1998; Intrieri et al., 2002].

Absorbed Shortwave Radiation

The amount of solar energy absorbed by the snow-ice-open sea (SWnet) increases with the solar incident angle and reduces with larger surface albedo and atmospheric optical depth. In early spring (April) solar elevation is low and with a dry snow albedo of 0.8-0.9 [Walsh and Chapman, 1998; Vihma et al., 2008] only about 40-50 W/m^2 of SWd is absorbed in the snowpack [Ebert et al., 1995; Walsh and Chapman, 1998]. With the onset of snow melt in May-June surface albedo starts to weaken and SWnet increases to 80-150 W/m^2 in May-July (daily means) following the diurnal cycle and the day-to-day changes in SWd [Walsh and Chapman, 1998; Intrieri et al., 2002]. Further as melt season progresses, the highly reflective snow-ice surface transforms into a patchy mixture of blue melting ice floes and the dark highly absorptive melt ponds and leads. This pronounced albedo evolution explains the largest SWnet occurring not in June, but in July (**Fig 1.3b**), when the concurrent roles of the surface albedo and solar inclination produce the best surface heating with smaller albedo and still high solar elevation. On average, the monthly mean in July SWnet is within 70±30 W/m^2 in the central ice covered Arctic and 120±50 W/m^2 within the marginal seas.

All three reanalysis agree that SWnet is smaller within the sea ice covered central Arctic (85^{o}N), compared to the regional average SWnet (**Fig 1.3b**). Where the regional average takes into account the vast open sea area with much smaller albedo. Yet, the absolute SWnet values are much larger in NCEP/NCAR, compared to ERA-40 and ERA Interim: with the difference (in daily mean values) reaching 60 W/m^2 at 85^{o}N,

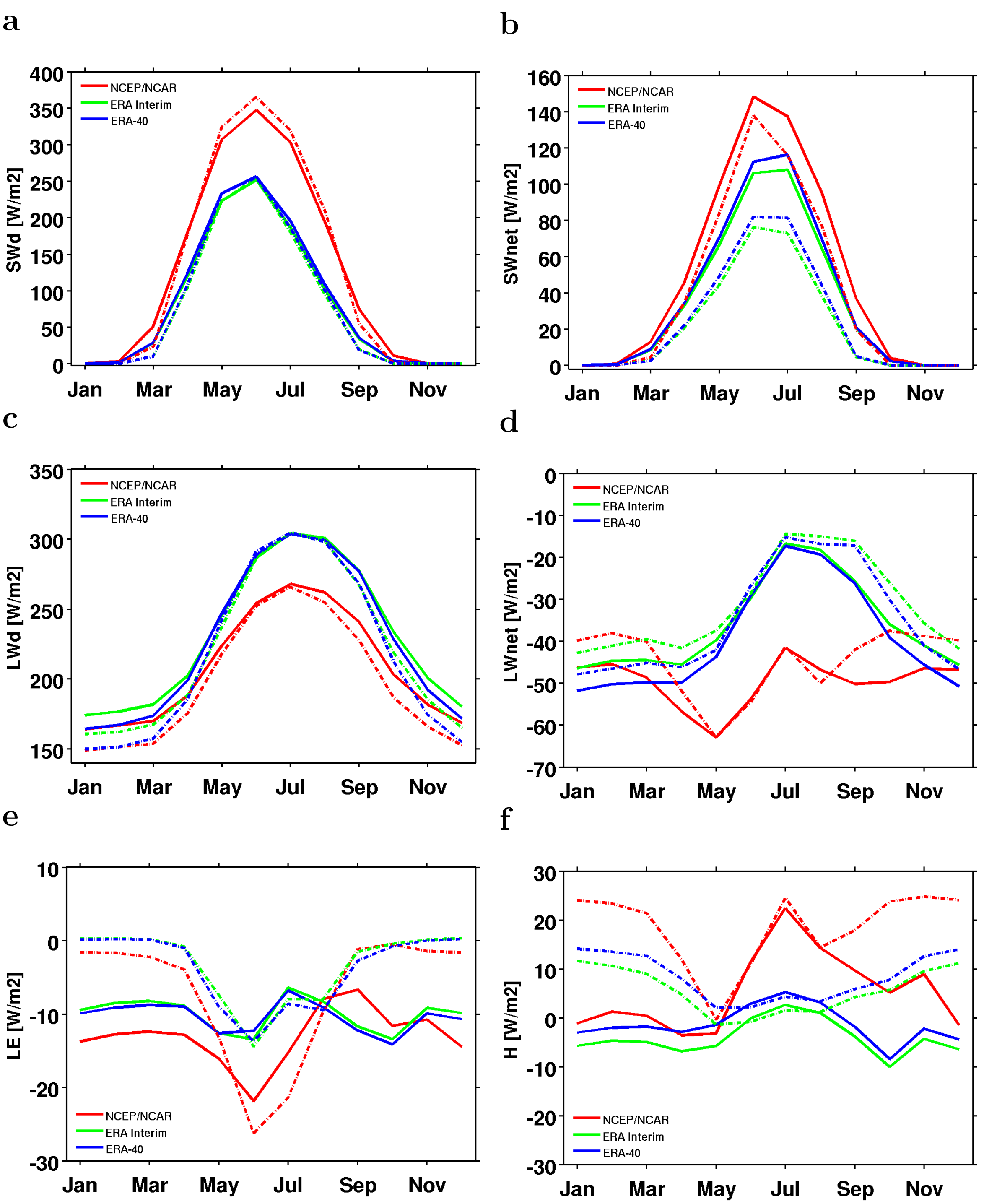

Figure 1.3: Seasonal cycle in (a) downward shortwave (SWd) radiative flux, (b) absorbed shortwave (SWnet) radiative flux, (c) downward longwave (LWd) radiative flux, (d) net longwave (LWnet) radiative flux, (e) latent heat flux, (f) sensible heat flux. Fluxes are the regional average over the maritime Arctic northward from 72.5^{o}N (plain curves) and over the 85^{o}N (dashed curves).Three reanalysis: ERA Interim, ERA-40 and NCEP/NCAR are compared in the same period 1989-2001.

and with the regional mean difference about 30-50 W/m^2. Earlier Walsh and Chapman [1998] compared NCEP/NCAR against measured SWnet at the North Pole drifting stations. They also found that NCEP values were larger than the observations: by approximately 25 W/m^2 in May, June and August under clear skies, and 30-50 W/m^2 in May-June under cloudy skies.

The larger SWnet in NCEP might be due to (a) a greater SWd, (b) smaller albedo, (c) either both: greater SWd and smaller albedo in NCEP compared to both ERA reanalysis. Our comparison of Sea Ice Concentrations (SIC) between NCEP/NCAR, ERA Interim and ERA-40 (not shown here) did not evoke the negative bias in the seasonal mean (May-July) climatology (1989-2001) in NCEP, compared to both ERA products. In contrast, we find even larger SIC in NCEP/NCAR, compared to both ERA reanalysis: in particular within the Kara, Laptev, East-Siberian Seas and Baffin Bay. It seems that the positive bias in SWnet found in NCEP/NCAR (compared to ERA products) is primarily due to the huge overestimation of SWd in NCEP/NCAR.

Regarding the error-bars, the observational error for SWnet term depends on the absolute magnitude of the flux, being is approximately 5-7 W/m^2 in summer months [Intrieri et al., 2002].

Downward Longwave Radiation

Downward longwave radiative flux (LWd) is a major source of energy for the Arctic surface all year round. Seasonal cycle of LWd in the Arctic Ocean (**Fig 1.3c**) is shifted towards later seasonal maximum compared to SWd and SWnet, with the seasonal amplitude in LWd being much smaller as well. The daily mean values are about 250-300 W/m^2 in May-September and 100-220 W/m^2 during November-April [Overland and Guest, 1991; Bjrk and Sderkvist, 2002; Curry et al., 2002; Francis et al., 2003; Sorteberg, 2007a; Vihma et al., 2008].

The 30-40 W/m^2 difference in the seasonal cycle between both ECMWF reanalysis and NCEP/NCAR is apparent in **Fig 1.3c** and has been documented earlier by Curry et al. [2002], Liu et al. [2005] and Sorteberg [2007b]. Compared to the observations it seems that ERA-40 reproduces LWd very well, while NCEP/NCAR has a large negative bias, for example in June of the order 50-75 W/m^2 [Serreze et al., 1998; Liu et al., 2005; Bromwich et al., 2007]. This bias in LWd in NCEP/NCAR is most likely due to errors in cloud representation [Liu et al., 2005; Bromwich et al., 2007; NCEP/NCAR problem list].

Meridional gradients in LWd flux are the most prominent during the cold season (from August to May): few LWd radiation further to the North and large LWd sink in the North Atlantic Barents Sea region. In summer, on average, LWd flux is very uniform regionally (not shown). Strange (patchy) spatial structure in the monthly mean LWd is apparent in winter (March) LWd in NCEP/NCAR (not shown). This might be related to the spectral noise problems in NCEP/NCAR reanalysis mentioned by Rogers et al. [2001]. Yet, this is an open issue.

Day-to-day and year-to-year variations and the seasonal cycle in LWd are tightly related to the atmospheric moisture content and cloud radiative properties. In contrast to SWd, the larger atmospheric moisture and thicker cloud cover intensify LWd [Overland and Guest, 1991; Wang and Key, 2005a; Pinto et al., 1997]. The atmospheric moisture content has the strongest (exponential) effect when varying within the low values, within 0-30 kg/m^2 for the total water vapour content [Zhang et al., 1997]. To mention, the typical total water vapor content values during Arctic summer are those within 10-20 kg/m^2. Cloud LWd radiative forcing is mainly a function of the cloud base temperature (cloud base height) and the cloud thickness, rather than the cloud fraction [Chiacchio et al., 2002; Shupe and Intrieri, 2004; Tjernstrom et al., 2008]. Cloud LWd radiative forcing is of the order of 10-40 W/m^2 during November-April and 40-80 W/m^2 during the melt season from May to October [Beesley, 2000a; Intrieri et al., 2001; Wang and Key, 2005a; Sedlar et al., 2010]. The explanation for this seasonal cycle in LW radiative forcing is the following. In winter the Arctic clouds are fewer, ice-phase, higher and generally thinner, and the atmospheric total water vapour content is very small. In these conditions the atmospheric column and clouds emit relatively few LWd towards the surface and in the meantime - are nearly transparent for the LW radiation emitted upward by the surface. In contrast, during summer the persistent low-level liquid thick multi-layer stratiform clouds constitute a large thermal heat storage, which increases LWd efficiently.

For the surface-based measurements the inaccuracy in LWd flux estimate is of the order of 5 W/m^2 [Chiacchio et al., 2002; Intrieri et al., 2001; Vihma et al., 2008; Sedlar et al., 2010].

Net Longwave Radiation

Net longwave radiative flux (LWnet) at the snow-ice-open sea surface is the difference between the incoming atmospheric LWd (downward flux) and the surface LW emission (upward) that depends on the surface temperature. Naturally, LWup is larger for a warmer open sea surface, compared to the snow covered sea ice. During the polar winter there is no SWd term and the LWup heat loss at the snow-ice-open sea surface largely dominates LWd heat sink, producing large negative LWnet. On clear-sky winter days with weaker LWd the radiative deficit in LWnet is the most pronounced. During summer, starting already in April-May, the increasing surface heating (SWd plus

LWd) competes with the increasing surface cooling (by LWup). Radiative heating first increases the surface (snow) temperature to the melting point and then the additional heat is stored in a form of latent heat of fusion. Thus within the ice-covered areas LWup stays still during the melt period (because the temperature cannot increase above 0C) and LWnet deficit reduces. However, even during the melt season LWnet stays upward (negative) in the Arctic Ocean, both over sea ice and open sea areas.

Field observations over the thick ice floes far away from leads indicate that LWnet varies within 0-80 W/m^2 along the year [Walsh and Chapman , 1998; Persson et al., 2002, Jordan et al., 1999]. The smallest (near zero) LWnet loss have been measured under low-level clouds and large LWd emission - in all seasons.

If comparing different meteorological reanalysis and remote-sensing estimates in terms of the seasonal cycle in LWnet, the results diverge [Sorteberg, 2007a] showing the largest LWnet deficit (regional mean) either in July-September (POLAR ISCCP-based estimates [1]), either in November-May (ERA-40 and ERA Interim), either in April-May (NCEP/NCAR and AVHRR-based APP-X estimates [2]), with quite different seasonal cycle between data sets [Sorteberg, 2007a]. Our comparison of the regionally average seasonal cycle in LWnet between NCEP/NCAR, ERA-40 and ERA Interim reanalysis products, during the common period 1989-2001 (**Fig 1.3d**) shows a good agreement with the earlier results by Walsh and Chapman [1998], Sorteberg [2007a] and Serreze et al. [2007], thought being evaluated for different years.

Interestingly, Walsh and Chapman [1998] noted that LWnet seasonal cycle in NCEP agrees well with the LWnet estimations at the North Pole drifting camps, although they indicate that negative peak occurs too early in NCEP (in April). If following their illustrations, the seasonal cycles fit well between LWnet in NCEP/NCAR and the observed LWnet, however LWnet in NCEP is 10-20 W/m^2 stronger (larger heat loss) compared to the North Pole field observations.

We speculate that the negative peak in NCEP LWnet in May (**Fig 1.3d**) could be related to that fact that LWd is not large enough and, in the meantime, SWd, SWnet and the resulting surface heating are already too large in May in NCEP. In this situation, it is logic that the surface warms by means of SW absorption and the LWup enhances. And with the relatively weak LWd, the net LW radiative balance drops in May to larger negative values.

LWnet in March, May and July in three reanalysis were compared. Similar to LWd flux we found a physically inconsistent patchy structure in the monthly mean LWnet

1. Surface radiation budget estimate based on the International Satellite Cloud Climatology Project (ISCCP POLAR), Rossow and Schiffer [1999], and Key et al. [1999]

2. AVHRR-based APP-X is the Version 1 of the Extended Advanced Very High Resolution Radiometer (AVHRR) Polar Pathfinder dataset (APP-X), spanning the period 1985-1993

in NCEP/NCAR during March, May and July (not shown). This doesnt seem to be related to the sea ice cover changes in NCEP/NCAR. The only possible explanation that we dispose is the spectral noise of the model used for NCEP/NCAR reanalysis [Rogers et al., 2001].

However, even with this unphysical patchy structure in LWnet in NCEP, the resulting "monthly mean regional average" in March is within -45-50 W/m^2, which is very close to both ERA products (!), see **Fig 1.3d**. This example shows that with the same regional climatology, the local values are totally different in these three reanalysis data! Another issue appears: in May LWnet is surprisingly uniform within 70-90N in NCEP (not shown), with almost no distinction between the open sea and the sea ice domain (!), although it is not yet the melting season and there should be some difference in surface (skin) temperatures and LWnet across the ice margin!?

In July-August the difference in the monthly mean LWnet between NCEP and both ERA reanalysis is the largest of all months: about 20-30 W/m^2 all around the Arctic Ocean (**Fig 1.3d**). Although LWd continues to increase as summer progresses, the excessive SWnet in July foresters large LWup throughout the melt season and with the insufficient LWd, the resulting LWnet (heat loss) is much larger in NCEP, compared to both ERA products. Yet, it is of a question, whether ERA-40 and ERA Interim produce better LWnet, than NCEP/NCAR? If following the LWnet cycle deduced from the Russian North Pole drifting stations by Walsh and Chapman [1998, their Figure 12], the shape of the observed seasonal cycle in LWnet is compares well with the NCEP, rather than both ECMWF reanalyses. Yet the magnitudes of the heat fluxes in NCEP/NCAR are questionable.

Latent heat flux

Turbulent latent heat flux (LE) is the energy spent on evaporation, sublimation of the snow into the water vapor, or the energy released with the near-surface condensation. In the Arctic, on average, the net LE heat flux at the air/snow or air/ice interface is upward year round, complementing the radiative LW heat loss, and together - inducing the cooling of the sea water, ice and snowpack [Nilsson et al., 2001; Serreze et al., 2007]. Thus the evaporation and sublimation dominate the near-surface condensation. Monthly mean LE over the sea ice field is of the order of -5-0 W/m^2 during winter and -10-20 W/m^2 during April-September. The largest day-to-day and seasonal variations in LE occur within the marginal Arctic seas, Greenland and Barents Seas. In these areas the large horizontal and vertical near surface thermal gradients build-up over the vast open sea domain in early winter (September-November), generating stronger winds, convection, turbulent mixing and evaporation, with LE reaching on certain years/areas/days 100 W/m^2 within the Chukchi, Laptev, northern Kara and Barents Seas. Measurements of the latent heat flux over Arctic leads documented the daily LE values reaching 130 W/m^2 [Shaw et al., 1991; Hartman et al., 1994]. Episodically when condensation occurs within the near-surface layer over sea ice, the daily latent heat flux can be downward, up to 10-15 W/m^2.

Regional-mean 13-year average monthly climatology of LE northward from 70^{o}N (**Fig 1.3e**) illustrates that over the sea ice the strongest evaporation occurs in summer. Regional mean climatology evokes two peaks in the seasonal LE heat loss one in May-July, another in October, having different origin. The first peak is due to the large sea ice and snow heating rate (under the combined effect of increasing SWd and LWd) favouring the stronger evaporation and surface melt on top of the vast sea ice field. The second peak in fall is due to the intense turbulent near-surface mixing over the open sea before the fall freeze-up.

We find a large difference in LE between NCEP/NCAR and both ECMWF reanalyses in all months (**Fig 1.3e**). Interestingly, the climatology in the monthly mean regional average LE is exactly the same in ERAI and ERA-40. Our results for NCEP/NCAR are consistent with the excessive evaporation in NCEP/NCAR reported by Cullather et al. [2000] and Jakobson and Vihma [2010]. According to Cullather et al., [2000] north of 70^{o}N the evaporation is at least 40% too large in NCEP/NCAR compared to the Russian North Pole drifting stations. Naturally the model suggesting the excess in SWd and SWnet should be warmer with larger evaporation [Serreze et al., 1998]. And this is the case of NCEP/NCAR that has a warm bias in SAT (within 5^{o}C) on cloudy days during at least September-April period [Walsh and Chapman, 1998]. However, ERAI and ERA-40 turbulent fluxes are likely neither free of errors. As shown by [Cuxart et al. 2006] the atmospheric model used for ERAI tends to overestimate turbulent fluxes under stable stratification conditions.

Sensible heat flux

Turbulent sensible heat flux (H) over the snow-sea ice covered surface has an overall warming effect during October-April period, with the monthly mean (positive) values of 10-15 W/m^2, and weak cooling effect (negative H values) of about 0-5 W/m^2 during the melt season from May to September [Lindsay and Rothrock, 1994; Lindsay, 1998; Nilsson et al., 2001; Persson et al., 2002; Makshtas et al., 2003] and **Fig 1.3f** (dashed curves for ERA-40 and ERA Interim). Field measurements during fall-winter period showed that the presence of clouds, and in particular the low-level stratiform clouds, was often associated with a slight snow warming (by a few degrees), disturbing the near-surface stable stratification and promoting sensible heat loss at the snow surface, with the instantaneous H flux values reaching 25 W/m^2 over the thick (2-3 m) compacted ice floe [Overland and Guest, 1991; Beesley, 2000a].

Over open water areas: leads, coastal polynyas and the warm Greenland, Barents and Chukchi Seas, huge sensible heat loss takes place during the cold season, where H may reach 600 W/m^2 [Alam and Curry, 1997, 1998; Serreze and Barry, 2005]. Over these open sea areas the strong unstable vertical stratification builds-up, with the sea surface temperatures being at the freezing point and the cold (-40^{o}C) polar air sliding from the surrounding ice floes and generating the efficient atmospheric turbulent mixing, intense sensible heat loss, evaporation and convective cloud formation.

Seasonal cycle in sensible heat flux averaged within the entire maritime Arctic northward from 70^{o}N (**Fig 1.3f**, plain curves) shows slightly negative H (heat loss) in winter and positive in summer. This indicates that the regional average H is largely affected by the open sea areas, where large wintertime H loss within the Greenland, Barents and Chukchi Seas is accounted in the regional averaging.

As for LE flux component, ERAI tends to overestimate H turbulent flux under stable stratification conditions [Cuxart et al., 2006; Graversen et al., 2011].

Conductive heat flux

Heat conduction (Q_c) within the snow and ice is proportional to the thermal gradient (dT/dz) within the snow or ice, and the thermal conductivity of the material (λ, W m^{-1} K^{-1}). In the most simple formulation the thermal gradient (dT/dz) is the difference between the upper and lower boundaries (negative dT/dz in winter), and the thermal conductivity is a function of the snow and ice density, salinity, age and temperature. Thus first-year ice containing more brine (dissolved salt) has a smaller conductivity than relatively fresh multi-year ice [Maykut, 1986]. Minus in the equation indicates that the positive conductive flux is directed upwards within the ice floe and the snowpack (ocean heat loss and atmospheric heat gain).

$$Q_c = -\lambda \frac{dT}{dz} \tag{1.2}$$

During polar winter the underside of sea ice is warmer than the snow and the air aloft, which maintains the upward conductive flux at the snow-ice interface. In this situation the amount of heat conducted upward to the ice-snow interface is the sum of the sensible heat input from the ocean and the latent heat released by bottom accretion and brine freezing within the ice floe [Maykut, 1986].

In spring and summer when snowpack becomes isothermal, the conductive (upward) heat flux within the sea ice weakens. To notice, the ocean heat loss does not have a direct effect on the snow and ice surface temperatures. If the ocean-ice heat flux at the ice bottom exceeds the conductive heat flux through the ice, the bottom ice melt takes place. If the conductive heat flux through the ice exceeds the ocean-ice heat flux, there is bottom growth of ice.

During the course of the year the *conductive heat flux in sea ice* can be as large as 130-200 W/m^2 in 20-40 cm ice [Steffen and DeMaria, 1996] and +15-(-2) W/m^2 for a snow covered 1.5-3 meter thick sea ice [Nilsson et al., 2001; Maykut, 1986; Untersteiner, 1961; Perovich and Elder, 2001]. Thus the snowpack reduces ice surface cooling, and, in consequence, reduces the bottom sea-ice growth rates [Maykut, 1986; Yackel et al., 2007]. The average ocean heat flux at the ice bottom is of the order of 2-5 W/m^2 [Maykut, 1986; Barry, 1986; Maykut and McPhee, 1995; Krishfield and Perovich, 2005], the largest in late melt season when SWnet accumulation is large in the ice free areas.

Conductive heat within the snowpack is of the order of 5-20 W/m^2 during winter (November-March), 2-5 W/m^2 during April-May and naturally near zero during the melt season on top of 1-3 m sea ice [Persson et al., 2002].

Net heat flux

Surface net flux (NF) is defined here as the sum of the net radiation and the turbulent heat fluxes, similar to Beesley [2000a], Adams et al. [2000] and Serreze et al. [2007].

$$NF = LWnet + SWnet + H + LE \tag{1.3}$$

NF is largely dominated by the radiative terms, following closely the seasonal cycle in absorbed SW radiation. In sea ice covered Arctic, on average, NF is positive during May - early August and negative during the rest of the year, **Fig 1.4**. Episodic upward and downward NF fluctuations occur in all seasons depending on the sea ice concentrations, heat advection and the cloud cover. The annual regional (70-90^{o}N) average NF is negative (heat loss) of about 11 W/m^2 according to ERA-40 [Serreze et al., 2007].

During the freezing season (roughly September-April) NF is the energy eliminated from the snowpack and sea ice. Regarding the entire ice depth, this snow/ice surface cooling (negative NF flux on top) is balanced by the conductive flux through the ice and the latent heat released due to ice growth at the bottom of the ice floe. Consistent with Serreze et al. (2007) and Persson et al. (2002), the regional average monthly mean NF heat loss is the largest during October-February: within -50 W/m^2 and +10 W/m^2, **Fig 1.4**. On top of the snow covered thick ice slab positive NF in winter occurs during overcast days when LWnet is near zero and the sensible heat flux is downward in a shallow mixing layer [Persson et al., 2002]. Thus during winter the net cloud radiative forcing is positive of 60 W/m^2 over the sea ice [Schweiger and Key, 1994]. Over the open sea areas in winter NF is negative reaching -400 W/m^2 within the Greenland Norwegian - Barents Seas and over leads and polynyas.

In spring when the heat absorption starts to dominate the heat loss at the snow and sea ice surface, NF becomes positive (around May), **Fig 1.4**. During this period the net cloud radiative forcing is positive of the order of 25 W/m^2: where the cloud cover increases NF heat gain [Schweiger and Key, 1994]. By definition, positive NF induces warming of the snowpack from the initial winter temperatures, and the vertical thermal profile within the snowpack gradually smooth. With a large enough accumulated NF the melting point is reached, typically first within the sub-surface (2-5 cm) snow layer [Cheng et al., 2008].

When the snow and sea ice melt start, roughly a half of received heat is released for melting, another half is transmitted to the neighbouring snow and sea ice layers and the minor part (a particularity of the Arctic region) is lost with evaporation and sensible heat loss [Ebert et al., 1995; Lindsay, 1998].

The energy available for melting experiences a strong diurnal cycle, following the diurnal cycle in SWd and SWnet, though there is almost no diurnal cycle in snow and near-surface air temperature during the melt season [Lindsay, 1998; Tjernstrom, 2005]. The regional average monthly mean NF heat gain is the largest in July, about 80 W/m^2, with the daily means of 35-130 W/m^2. During several weeks in July the net cloud radiative forcing shifts from positive to negative values, of the order of 25 W/m^2 [Schweiger and Key, 1994]. In this short period the shading effect of clouds for the incident solar radiation dominates the green-house effect.

Already in early August NF becomes negative and shortly the freeze-up starts. During September-October NF is about -25-50 W/m^2 over the sea ice areas and 50-150 W/m^2 in the seasonal ice zone. The strongest NF heat loss occurs within the open sea areas of the Chukchi, Barents and Greenland Seas, reaching 200-400 W/m^2. Net cloud radiative forcing is positive of the order of 40-70 W/m^2 in fall [Schweiger and Key, 1994; Sedlar et al., 2010].

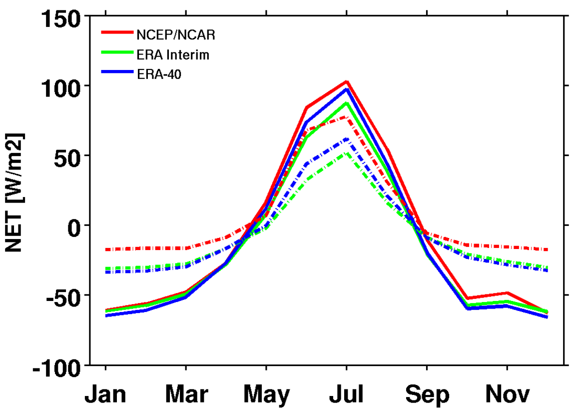

Figure 1.4: Seasonal cycle in net flux (NF). The regional average over the maritime Arctic northward from 72.5^{o}N (plain curves) and over the 85^{o}N (dashed curves).Three reanalysis: ERA Interim, ERA-40 and NCEP/NCAR are compared in the same period 1989-2001.

Chapter 2

Data

This Chapter describes five data sets used in our study. The original SMMR-SSM/I Melt Onset data set is described in Section 2.1. Sea ice concentration data are outlined in Section 2.2. Three meteorological reanalysis products (ERA Interim, ERA-40 and NCEP/NCAR) are summarized in Sections 2.3-2.5.

2.1 SMMR-SSM/I Melt Onset time series

Recently updated Arctic-wide Melt Onset (MO) record by *Markus et al.* [2009] is derived from the Scanning Multichannel Microwave radiometer and Special Sensor Microwave Imager (SMMR-SSM/I) passive microwave measurements of the brightness temperature. The spatial resolution (pixel size) is approximately 25 km with the northward limit around 87^oN.

MO is defined as the first day of the *continuous melt*, *e.i.* when the liquid water stays continuously present within the snowpack and/or on top of bare sea ice. If no clear snow melt can be detected on top of sea ice, then the day when the sea ice concentration drops below 80% for the last time before the area becomes ice-free is "seen" as MO [*Markus et al.*, 2009]. This means that formation of open water areas (leads and polynyas) is considered for MO.

MO distinction varied between *two ice types*: the **multi-year ice (MYI)** and the **first-year ice (FYI)**. The spectral gradient ratio (GR) and a quantity P=V19+0.8*V37 were used to determine the MYI versus FYI. Here V denotes the vertical polarization. If both GR and P overcome the pre-defined thresholds on April 1st the ice pixel is marked as either MYI or FYI.

The defined thresholds are:
for MYI: P increases at the onset of melt, no matter GR values;
for FYI: GR > -0.03 , P drops at the onset of melt.

Fig 2.1 illustrates the emissivity signature as a function of the wave frequency, which is the basis for ice type distinction.

This MO retrieval has been compared by *Markus et al.*, [2009] with the *near-surface air temperature* (SAT) from buoy observations and the reanalysis of the National Center for Environmental Prediction / National Center for Atmospheric Research (NCEP/NCAR). At two locations (one with MYI and another with FYI) SSM/I-based

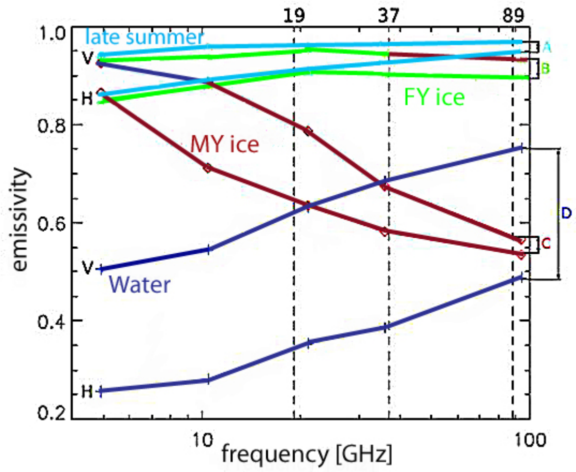

Figure 2.1: Dependence of the microwave emissivity on surface properties: sea ice or open water. Two sea ice types are the multi-year (MY) and first-year (FY) sea ice type. Late summer emissivity of the FY ice represents the effect of desalination on sea ice emissivity. H and V denote the horizontal and vertical polarization. A, B,C and are the emissivity differences Reprint from *Spreen et al.*, 2008.

and SAT-based snow MO agree within less than 8 days (better over FYI). Over the entire Arctic Ocean three MO estimates (SSM/I, buoy SAT and reanalysis SAT) were compared during one particular year in terms of their spatial distribution statistics. While spatial distribution curves do not perfectly mirror one another, they are in very good agreement. This comparison, however, does not provide the conclusive quantitative validation for the SSM/I-based MO retrievals. First, because SAT data themselves have unknown errors. Second, because melt within the snowpack does not necessarily coincide with 0^{o}C, -1^{o}C or positive air temperatures at 2 m height [*Andreas and Ackley*, 1982; *Richter-Menge et al.*, 2006; *Hanesiak et al.*, 1999]. Third, because when varying the threshold applied to SAT data by $\pm 2^o$C, the resulting SAT-based MO ranges by as much as $\pm$50 days [*Markus et al.*, 2009].

Compared to the other SMMR-SSM/I MO time series, the major advantage of this record is that until recently it was the only one to cover the complete 30-year period of 1979-2008, and both MYI and FYI areas. We say "until recently" because in early 2011 the MO data by *Drobot and Anderson* [2001] was updated for the recent years, now also spanning the same period 1979-2008. According to our knowledge, there is no complete 20-year region-wide time series of MO based on the active microwave remote sensing, though it has great potential performing a better spatial resolution.

2.2 SMMR-SSM/I sea ice concentration

We applied a daily Arctic sea ice concentration (SIC) data set produced by *Cavalieri et al.* [1996], which is based on the same SMMR-SSM/I brightness temperature measurements with the same spatial resolution as MO data of approximately 25 km. This SIC data were produced with NASA Team Algorithm and obtained from the National Snow Ice Data Center website http://nsidc.org/data/nsidc-0051.html. To notice, in the algorithm for MO detection developed by *Markus et al.* [2009] the same NASA Team Algorithm was applied for SIC estimation. These SIC time series have been widely used in Arctic climate research, *e.g. Drobot et al.* [2007].

Meteorological reanalysis

Meteorological reanalysis produces a global data set that is as close as possible to reality [*Tjernstrom and Graversen*, 2009]. Based on the initial weather analysis the numerical weather model produces a short forecast (first-guess), typically for a 6-hour time step. Thereafter the first-guess is adjusted according to the observations available for the valid time of the forecast. Thus the reanalysis is a result of an optimum combination of the model-generated meteorological fields and sparse observations. It is considered that current global reanalysis data are most reliable in quantities that are constrained by the observations (e.g., atmospheric pressure, air temperature and winds), and least reliable for the sub-grid processes such as evaporation, precipitation, refreeze-thaw, water phase transitions and cloud-related quantities [*Arkin and Kalnay*, 2008].

Advantages of the modern meteorological reanalysis are:

1. reanalysis incorporates all available observational data received too late for inclusion in the operational weather forecast [*Walsh and Chapman*, 1998];
2. the use of the same ("frozen") model with the same physical parametrizations prevents from the discontinuities associated with any model changes [*Walsh and Chapman*, 1998];
3. data are dynamically consistent, three dimensional (global coverage) and continuous in time [*Tjernstrom and Graversen*, 2009].

Although an extensive validation of different reanalysis in polar regions has not been done yet, the individual focused studies progressed in this direction quite well. One of the most comprehensive summaries on the reanalysis performance in high latitudes (both Arctic and Antarctic) appeared after the workshop organized by the British Antarctic Survey in 2006. This workshop report is available online at
http://ipo.npolar.no/reports/archive/reanalWS_apr2006.pdf.

2.3 NCEP/NCAR reanalysis

NCEP/NCAR reanalysis [*Kalnay et al.*, 1996; *Kistler et al.*, 2001] is a cooperative project of the National Center for Environmental Prediction and the National Center for Atmospheric Research (NCEP/NCAR). It covers the period from January 1948 with a horizontal resolution of 2.5^o latitude by 2.5^o longitude and 28 vertical sigma levels. NCEP/NCAR assimilates an extensive observation data on the atmospheric pressure, temperature, humidity and winds from radiosondes, aircraft, buoys, ship reports. It does not assimilate 2m SAT and precipitation observations at the land meteorological stations [*Simmons et al.*, 2004].

Sea ice has a constant *thickness* of 3 m. *Sea ice concentrations* in each grid cell are either 1 or 0. Thus if satellite microwave data suggest the ice concentrations exceeding 0.55, the model ice concentration is set to 1 [*Cheng et al.*, 2008]. *Snow* accumulation is allowed. Snow depth is determined prognostically from a budget equation that accounts for accumulation and melting. The water equivalent of snow thickness is a model variable, generating variations in the conductive heat flux through the snow. Precipitation falls as snow if the air temperature at 0.85 sigma level is below 0^oC. Sublimation of snow contributes to surface evaporation. *Kwok and Cunningham*, [2008] have examined the net precipitation (precipitation minus evaporation), indicating the snow depth, and found "unphysical spatial patterns" likely associated with numerical discontinuities near the North Pole. Surface albedo is 0.85 for snow and 0.75 for ice [*Cheng et al.* 2008].

Skin (surface) temperature responds to the heat flux balance at the surface. 2m near-surface air temperature (SAT) is then interpolated between the skin temperature and the lowest model sigma-layer. Following *Walsh and Chapman* [1998] the seasonal cycle of 2m SAT was very well captured, compared against the Russian North Pole drifting stations. Yet NCEP/NCAR SAT was warmer on cloudy days during September-April period, generally by less than 5^oC [*Walsh and Chapman*, 1998]. *Curry et al.* [2002] and *Cheng et al.* [2008] found that NCEP/NCAR 2m SAT over the sea ice was more accurate than ECMWF products (within Beaufort-Chukchi Seas). This was attributed to the fact that NCEP/NCAR assimilates ship observation, unlike ECMWF. However, the skin temperatures and 2m SAT were announced to be significantly warmer at some polar locations in the period 1998-2004 [NCEP/NCAR problem list].

Cloud cover is entirely computed with a cloud parameterization scheme [*Kanamitsu et al.*, 1991; *Walsh and Chapman*, 1998]. Compared to the North Pole drifting station reports [1], NCEP/NCAR has too few clouds, with the cloud fractions unrealistically nearly identical in summer and winter [*Walsh and Chapman*, 1998]. Low, middle and high level clouds appeared to be erroneous in NCEP/NCAR [NCEP/NCAR problem list].

NCEP/NCAR showed larger *SWnet* values compared to those measured at the Rus-

1. Russian North Pole drifting stations (1950-1991)

sian North Pole stations, on both cloudy and clear sky days, with the largest error in July under clear skies [*Walsh and Chapman*, 1998]. This is partly due to excessive *SWd* [*Serreze et al.*, 1998], errors in clouds, and also due to errors in albedo [NCEP/NCAR problem list]. *Sensible heat flux* (H) strongly depends on winds in NCEP/NCAR. Thus under weak near surface winds of less than 0.75 m/s H cancels, which produces unrealistic H, LWup, LWd and wrong skin temperatures [NCEP/NCAR problem list]

Daily error in *LWd* was up to 20 W/m^2 compared to the North Pole drifting stations reports [*Walsh and Chapman*, 1998]. *Latent and sensible heat fluxes* over sea ice were shown to be too small over the Arctic sea ice [*Adams et al.*, 2000].

NCEP/NCAR overestimates annual total *precipitation* over the central Arctic Ocean and underestimates the precipitation on the Atlantic side of the Arctic Ocean, performing better during winter and the worst during summer [*Serreze and Hurst*, 2000]. At SHEBA [1] site it did not capture the day-to-day variations in precipitation [*Curry et al.*, 2002]. Compared to the observations at the Russian North Pole drifting stations and the land observations north of 60^{o}N over the period 1986-1993, NCEP/NCAR shows the annual maximum in precipitation in July, which is one month too early [*Serreze and Maslanik*, 1997]. Moreover during August-December NCEP/NCAR has too few precipitation [*Serreze and Maslanik*, 1997]. NCEP/NCAR evaporation is two time larger compared to the North Pole drifting stations [*Cullather et al.*, 2000]. However, NCEP/NCAR agrees well with the radiosonde observations of the moisture flux convergence at 70^{o}N [*Cullather et al.*, 2000].

Seasonal cycle in *SLP* was shown to be reasonable compared to the Russian North Pole drifting stations [*Walsh and Chapman*, 1998].

2.4 ERA-40 reanalysis

ERA-40 reanalysis is a predecessor of ERAI, both produced by ECMWF [*Uppala et al.*, 2005]. It covers the period from September 1957 to August 2002 with the global resolution of about 1.125^o latitude by 1.125^o longitude. ERA-40 is based on the spectral T-159 model with 60 coordinate (model) levels extending from about 10 m height - up to 0.1 hPa. The lowest 10 layers are located below 850 hPa. ERA-40 is an improved reanalysis with better vertical and horizontal resolution, relative to NCEP/NCAR (described in the following Section 2.4). It assimilates the land station measurements of 2m SAT, snow depth and air humidity [*Simmons et al.*, 2004; *Wang et al.*, 2006]. Unlike NCEP/NCAR, ERA-40 includes increasing greenhouse gases in the atmosphere [*Uppala et al.*, 2005].

1. Surface Heat Budget of the Arctic Ocean (SHEBA)

Sea ice concentrations and the sea surface temperatures come from the weekly NCEP analysis in the period 1981-2002, based on in situ observations from ships, buoys and satellite data [*Fiorino*, 2004]. Sea ice thickness is prescribed as 1.5 m and there are four model levels within the ice slab at the depth of 0.07, 0.21, 0.7 and 1.2 m [*Cheng et al.*, 2008]. Sea ice scheme allows a fractional ice cover for each grid cell. The ice fraction is kept constant during the forecast. Ice bottom temperature is a seawater freezing temperature of 271.2^{o}K. Thus the ice heat conduction is primarily a function of the net heat flux at the ice top. There is no snow on top of the sea ice, and the albedo is prescribed as 0.85 in winter and 0.5 in summer.

Simmons et al. [2004] compared SAT from NCEP/NCAR, ERA-40 reanalysis with observations and concluded that ERA-40 performed better. Another study by *Bromwich et al.* [2007] found that ERA-40 captures the day-to-day variability in the total cloud cover much better than NCEP/NCAR (in June at Point Barrow).

Seasonal cycle in the LWd and SWd is more realistic in ERA-40 than NCEP/NCAR [*Sorteberg*, 2007]. Thus *Liu et al.* [2005] demonstrated that ERA-40 SWd is in a very good agreement with SHEBA observations. However ERA-40 clouds were too optically thin for SWd, except when the cloud fraction is very large, of 95-100% [*Bromwich et al.*, 2007].

ERA-40 appeared to have a reasonably adequate description of the lower tropospheric thermal structure, where the assimilation of SHEBA soundings had a notable, but not drastic effect on ERA-40 thermal profiles [*Tjernstrom and Graversen*, 2009]. However, the vertical thermal structure in ERA-40 showed a random error in the boundary layer compared to SHEBA [1] soundings, reaching 2.5^{o}C at the lowest levels, with a systematic warm bias reaching 1^{o}C [*Tjernstrom and Graversen*, 2009]. SHEBA profiles revealed the presence of multiple inversion layers at the same time. ERA-40 typically had fewer inversions in each profile: capturing the main inversion, but rarely the secondary and third inversion. Compared to SHEBA, the winter period when surface-based inversions dominate is too short in ERA-40, and the inversion bases are too high in late summer and fall. Bromwich et al. [2002 and 2007] noted the cold bias in the low and middle troposphere over the central Arctic Ocean (until 1996). Compared to the radiosonde vertical thermal profiles over the land north of 65^{o}N during 1979-1996, the vertical profiles produced by ERA-40 showed a smaller error compared to NCEP/NCAR [*Graversen et al.*, 2008].

One of the most recent studies by *Screen and Simmonds* [2011b] focused on the regional mean (70-90^{o}N) seasonal and annual averages in NCEP/NCAR, JRA and ERA-40. They manifested that all reanalysis products are "poorly suited for the study

1. several hundred of soundings during Oct 1997-Oct 1998

of thermal trends, particularly below 600 hPa". Thus in ERA-40 there is a clear shift in the temperature bias from negative to slightly positive in 1997 due to data assimilation changes.

Comparison with the rawinsonde archives done by *Bromwich and Wang* [2005] demonstrated that ERA-40 and NCEP/NCAR performed reliably the geopotential height, wind speed and direction and the tropospheric temperatures. In turn it was suggested that ERA-40 had a more realistic representation of winds than NCEP/NCAR. *Crochet* [2007] established the realistic Islandic precipitation in ERA-40 in all seasons along the entire reanalysis period 1958-2002.

Wang et al. [2006] investigated the cyclones in NCEP/NCAR and ERA-40, and found that ERA-40 has more strong cyclones and fewer weak cyclones over the Arctic (44-year mean), in particular over the western Arctic during October-March season. Similarly, a larger number of intense cyclones and fewer weak cyclones were found in ERA-40 within the North Atlantic during Jan-September months [*Wang et al.*, 2006]. Alternative comparison by *Bromwich et al.*, [2007] evoked a very good agreement between NCEP/NCAR and ERA-40 in terms of cyclonic activity in the Northern Hemisphere during 1979-2002: with a discrepancy only in some weak cyclones in the Northern Hemisphere.

2.5 ERA Interim reanalysis

ERA Interim reanalysis [*Uppala et al.*, 2008], called here further ERAI, is an improved product upon the previous ERA-40 and ERA-15 reanalysis created by the European Centre for Medium-Range Weather Forecast (ECMWF). ERAI has a global coverage with a spatial resolution of 0.72^o latitude by 0.72^o longitude, 60 vertical model levels, and since recently covering the period from 1979 onwards. ERAI benefits from the previous reanalysis experience, with major improvements: higher spatial resolution, assimilation of more extensive and diverse observational data with a more sophisticated technique (four-dimensional variational data assimilation), revised model physics, better radiative transfer model, a more detailed hydrological cycle and a variational bias correction of satellite radiance data [*Dee and Uppala*, 2009; *Cuzzone and Vavrus*, 2011]. Compared to ERA-40, ERAI demonstrated a better vertical consistence of the air temperature in Arctic [*Uppala et al.*, 2008; *Dee and Uppala*, 2009]. Thus with the implementation of the variational bias correction in ERAI, the vertical structure is now more efficiently constrained by radiosonde observations.

Sea-ice fraction and *sea-surface temperatures* are prescribed in ERAI in the same way as for ERA-40 prior to Jan 2002 [*Fiorino*, 2004; ECMWF IFS Part II, 2008; *Dee* *et al.*, 2011]. From 1 Jan 2002 − to 31 Jan 2009 ERAI follows ECMWF operational forecasting system using the National Center for Environmental Prediction real-time global SST analysis, called NCEP RTG SST [*Thibaux et al.*, 2003; *Stark et al.*, 2007]. SIC north of 82.5^{o}N are set to 100% [ECMWF IFS Part II, 2008]. South of 82.5^{o}N the sea ice concentrations are based on SMMR-SSM/I passive microwave measurements. Sea ice concentrations below 20% are set to 0% . *Sea ice thickness* is 1.5 m without snow accumulation or melt. No data on snow or ice surface temperature were assimilated in ERAI. Sea ice temperature and conductive heat flux are resolved at 4 model levels, with the bottom ice temperature at the freezing point. In this formulation, the variability (both in space and in time) of the conductive heat flux through the ice depends primarily on the atmospheric fluxes and near surface air temperature and humidity.

Sea surface (skin) temperatures from individual ships and buoys are assimilated in ERAI. The monthly *albedo* of sea ice and open water are prescribed in ERAI in a way as determined by *Ebert and Curry* [1993], **Fig 2.2** . The bare sea ice albedo value in *Ebert and Curry* [1993] is taken as a representative value for summer from July to August, and the dry snow albedo value is used for the winter months from September to May [ECMWF IFS Part IV, 2008]. In ERAI, the sea ice albedo does not vary along the day with the solar zenith angle. Dry snow albedo is about 0.98 in the visible spectrum (0.25-0.69 m) and decreasing to 0.03-0.05 in 2.38-4.00 m (near and short-wave infrared spectrum), with the spectral integrated albedo of approximately 0.77. Bare ice albedo is about 0.77 in the visible spectrum, about 0.04 in the near and short-wave infrared spectrum, with the spectral integrated albedo of 0.51 [Screen and Simmonds, 2011a]. The open water albedo is approximately 0.06 [*Ebert and Curry*, 1993; ECMWF IFS Part IV, 2008].

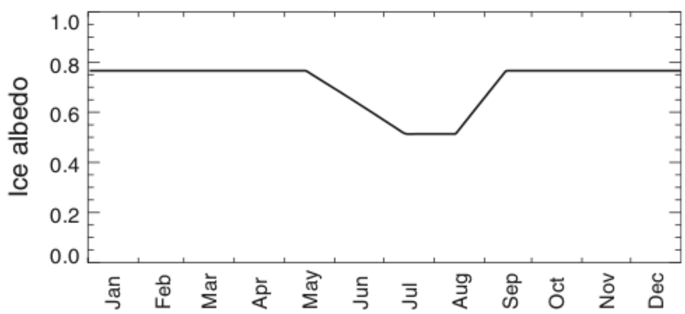

Figure 2.2: Seasonal evolution of the spectral integrated albedo on Arctic sea ice in ERA Interim. Reprint from *Screen and Simmonds.*, [2011b].

Liquid/ice water content, cloud fraction, precipitation and evaporation are computed by the model at all levels (6-h forecast). Clouds types are defined as followed: low-level clouds occur in the lowest troposphere, roughly within 1000-800 hPa, medium-level clouds are comprised within about 800-450 hPa, and the high-level clouds occur above 450 hPa. Cloud scheme is described in detail by *Tiedtke* [1993]. Water vapour data are assimilated: humidity profiles from radiosondes and raw radiances from a number of satellite instruments.

Annual monthly mean cycle of the aerosol distribution in space with various aerosol types (maritime, continental, urban and desert) developed by *Tegen et al.* [1997] has been implemented in ERAI. Carbon dioxide, methane, nitrous oxide, CFC-11 and CFC-12 are prescribed with the constant volume concentrations [ECMWF IFS Part IV, 2008].

The shortwave radiation (SWd) scheme originates from *Fouquart and Bonnel* [1980], and the longwave radiation (LWd) rapid radiation transfer model (RRTM) is described by *Morcrette* [1991] and *Mlawer et al.* [1997]. Description of the schemes for calculating the radiative and turbulent fluxes are given in ECMWF IFS Part IV, 2008. Cloud SW radiative properties in ERAI are a function of solar zenith angle, cloud liquid water amount and the effective radius of the cloud water droplets and ice crystals [ECMWF IFS Part IV, 2008]. ERAI LW radiative fluxes depend primarily upon surface and air temperature, water vapour profile and the cloud cover [ECMWF IFS Part IV, 2008].

The greenhouse gases: carbon dioxide, methane, nitrous oxide, CFC-11 and CFC-12 are assumed to be globally well-mixed. The concentrations for these gases are set to observed 1990 values plus a linear trend as specified in the IPCC 2nd Assessment Report 1996 [*Dee et al.*, 2011].

Previous studies with ERAI data for the Arctic Basin

Over Arctic sea ice, ERAI vertical profiles of air temperature, humidity and wind have been compared against observations from three ship campaigns by *Lupkes et al.* [2010]. It was found that ERAI overestimates the near-surface humidity and air temperature during summer, whereas the near-surface winds in ERAI are represented more accurately, with the differences increasing at higher altitudes but remaining less than 1 m s^{-1}. According to our knowledge, the accuracy of ERAI surface fluxes on top of Arctic sea ice is yet to be validated.

ERAI total cloud cover is generally larger over the areas with higher sea ice concentrations, the most pronounced during fall-winter-spring period [*Cuzzone and Vavrus*, 2011]. This relationship is explained that over higher SIC the air temperature and specific humidity are lower throughout the column, resulting in higher relative humidity, and in consequence more clouds and in particular − low-level clouds [*Cuzzone and Vavrus*, 2011].

4 years (2006-2009) of cloud data (north of 65°N) have been evaluated by *Marta Zigmuntowska et al.* (*in press*). Accordingly, (1) ERAI monthly mean total cloud frac-

tions are within 80-95% year trough (with a very weak seasonal cycle). (2) ERAI total cloud fractions are much larger (year round) compared to the total cloud fractions estimates from CALIPSO/CloudSat, (3) The seasonal cycle in the total cloud fraction perfectly mirrors the seasonal cycle in the low level cloud fractions in ERAI in this 4 year period. (4) Monthly mean wintertime low-level cloud fractions are of 0.7-0.9 in ERAI, which does not really agree with the observed climatology of the low-level clouds [Marta Zigmuntowska; *Beesley and Moritz*, 1999].

Annual average estimates of precipitation (P), evaporation (E) and net precipitation (P-E) in the Arctic Ocean agree very well between MERRA [1] and ERAI reanalysis, with the absolute values ranging within 28-30 cm/yr, 12-15 cm/yr and 13-18 cm/yr respectively [*Cullather and Bosilovich*, 2011]. Compared to the observations of precipitation at the Russian North Pole drifting ice stations, a positive bias was found in MERRA during the year (about 2% for the monthly means), reaching 60% in the monthly mean in April-June values [*Cullather and Bosilovich*, 2011]. This indicates that ERAI precipitation and evaporation are also biased.

Compared to National Climatic Data Center (NCDC) observations in the central Arctic and over the land north of 60^oN, ERAI had near-zero bias in 2m dewpoint in July 2007 [*Wilson et al.*, 2011].

1. Modern Era Retrospective Analysis and Applications (MERRA)

Chapter 3

Snow Melt Onset on sea ice: climatology, interannual and spatial variability, remote sensing

3.1 What is the Snow Melt Onset?

Field observations of the snow recrystallization, snowpack thermal profiles and surface radiative and turbulent heat fluxes are the major source of knowledge about the Snow Melt Onset (SMO) on top of sea ice. Accordingly, before SMO the lowest temperatures are found at the snow-air interface, increasing in the upper 5-10 cm snow layer and decreasing again in the deeper snow layers and at the snow-ice interface [Nicolaus et al., 2003 and 2009]. Here within this sub-surface snow layer the ratio between the heat accumulation and the heat loss is the largest. In comparison at the snow-air interface the evaporation (latent heat loss) and turbulent sensible heat loss retard the heating and snow melt. And deeper, at the snow-ice interface the snow is either cooled by the colder (thick) sea ice, or is cooler just due to thermal damping effect of the snowpack itself. In consequence, the snow melt often starts a few centimeters below the snow surface [Colbeck, 1982; Jordan et al., 1999; Frolov et al., 2005; Cheng et al., 2006; 2008; Nicolaus et al., 2009].

Definition of SMO

Studies on the snow metamorphism [Colbeck, 1982] determined the SMO as a transition phase starting with the wet snow metamorphism (early melt) and going on until the snowpack is saturated throughout (advanced melt). In this transition period due to more and more intense internal melt, liquid water occupies the pore space between snow grains and percolates downwards. Similarly, the airborne and satellite-based monitoring of the surface state, distinguish the early episodic snow melt and continuous snow melt [Livingstone et al., 1987; Winebrenner et al., 1994; Markus et al., 2009]. Where the continuous SMO means that the water in liquid phase (free-standing water) is present on top of the sea ice throughout the diurnal cycle and for the rest of the melt season [Yackel et al., 2007]. Model experiment carried out by Nicolaus et al. [2003] has determined SMO as the instance when the first meltwater reaches the snow-ice interface. In this formulation SMO is precisely determined as an exact instance [Julian day], yet this snow melt might be a temporary event and doesn't require snow saturation throughout the snow depth. So far the snow melt is quite a subtle and reversible process, which complicates the comparison of different SMO estimates.

In our study we adopt the terminology utilized in the remote sensing, considering the SMO as the moment when permanent snow melt establishes within the snowpack [Livingstone et al., 1987 and Markus et al., 2009]. Our choice is determined and restricted by the analysis that we develop. We expect that if comparing the remote sensed data on the continuous SMO (described in Section 2.1) with the meteorological data (described in Sections 2.2-2.4), the continuous SMO should be represented in both data sets more accurately, rather than any episodic and short (of the order of few hours) snow melt event.

Direct factors controlling SMO: surface heat fluxes

Absorption of the incident solar shortwave radiation (SWnet) and the balance of the longwave radiation (LWnet) within the snowpack in combination with the atmospheric turbulent fluxes and the heat conduction through the snow-sea ice, control together the heat budget (net flux, hereafter NF) and the temperature of each snow layer. Positive NF within some snow layer signifies the heat gain and snow heating, and the negative NF - the heat loss and snow cooling. Large enough accumulated NF increases the snow temperature from the initial winter values up to the melting point. Then after an additional amount of heat is needed for the phase change from frozen to liquid state.

Radiative measurements established that radiative fluxes at the air-snow interface have a dominant influence on snowpack properties including snow temperature, snow grain metamorphism and water phase transitions [*Barber et al.*, 1994]. During the premelt April-May months both SWd and LWd (daily mean) are both about 180-250 W/m^2 on top of the snow covered sea ice at 70-90N [Beesley, 2000a; Francis et al., 2003; Perovich et al., 2007b; Schweiger and Key, 1994], see also **Fig 1.3a,c**). Prior to SMO the snowpack is dry with the surface shortwave albedo of 0.8-0.9 [Maykut and Church, 1973), reflecting most part of SWd. With a higher solar elevation SW absorption within the dry snow increases to about 50 W/m^2 in April and 110 W/m^2 in May, which are the daily mean estimates for all sky weather conditions north of 62^{o}N [Schweiger and Key, 1994; Intrieri et al., 2002]. A model study with and without SWd diurnal cycle by Hanesiak et al. [1999] suggested that SWd diurnal cycle strongly influences the snowmelt initiation, where the time resolution of the model runs (hourly or daily SWd forcing) appeared to be an essential element in the relationship between SWd and snow melt. Similarly *Cheng et al.* [2008] also showed that success in modelling of the diurnal thaw-refreeze cycles strongly depends on the vertical resolution applied: with a 15-20 layer snow model resolving the snow melt better than a 3 layer model.

Turbulent latent (LE) and sensible (H) heat fluxes are relatively weak compared to the surface radiative fluxes. Both LE and H are within ± 20 W/m^2 during spring months on top of compact sea ice [Ebert and Curry, 1993]. LE heat loss usually takes place during the pre-melt April-May period [Persson et al., 2002], **Fig 1.3e**. Surface warming during May and early June results in a slightly unstable stratification near the surface [Persson et al., 2002]. As a result, in May-June the turbulent heat fluxes tend to cool the snow surface (**Fig 1.3f**). Thus during the pre-melt period LWd is the primary source of heat for the dry snow cover on top of the Arctic sea ice [Ambach, 1974, Beesley, 2000a, Wendler, 1986].

Indirect factors controlling SMO

At the snow surface with high shortwave albedo LWd, LWnet and NF are greater under cloudy conditions compared to clear skies [Ambach, 1974; Barber and Thomas, 1998b; Graversen et al., 2011; Wendler, 1986]. In the other words clouds contribute to the earlier spring SMO [Shine and Crane, 1984; Zhang et al. 1996]. Starting in April-May the Arctic cloud cover is dominated by the liquid low-level multi-layer clouds, which results from the increasing atmospheric vapor and liquid water content, more intense surface evaporation and the warm air advection towards the cold snow covered sea ice field. These relatively warm clouds have the indirect effect on snow temperatures and SMO by shaping surface heat fluxes. Intuitively, a larger and early northward heat advection with stronger wind speed should foster the surface heating and the early snow melt [Graversen et al., 2011; Serreze et al., 1993; Stone et al., 2005]. This has been observed on the Pacific side of the Arctic Ocean (East Siberian Chukchi - Beaufort Seas) where the snow melt tends to begin earlier when the Beaufort Sea anticyclone is weaker or shifted towards Canadian Archipelago during spring. Such an atmospheric circulation allows the injection of warm oceanic air masses from the north Pacific and/or the warm continental (Siberian or Canadian) air into the marginal Arctic seas [Serreze et al., 1993; Stone et al., 2005].

The time needed to warm the snowpack up to the melting point depends on the seasonal evolution of NF, the initial snow temperatures, snow density and thickness, and the aerosol contamination of the snowpack. It is of evidence that with the same meteorological forcing, the cold, light, thick and pure snowpack will take more time to warm-up, compared to the relatively warm, dense, thin and highly contaminated snowpack. Field observations in April-May demonstrated that thinner sea ice is 5-10^{o}C warmer at the snow-ice interface compared to thick ice [Perovich and Elder, 2001; Nicolaus et al., 2009]. This is due to a larger conductive heat flux through thinner ice. Thus, with the same meteorological forcing and a uniform snow depth, on top of thin ice it takes less time to heat the snowpack to the melting point. In consequence, SMO starts earlier on top of thinner (initially warmer) ice floe, compared to thick multi-year ice.

To summarize, there exist a multitude of factors modulating the heat fluxes on top of sea ice. These are the indirect factors controlling SMO timing. These include various cloud properties, atmospheric heat advection, near surface winds, snow temperatures, snow density and contamination, snow salinity, sea ice thickness and many more.

What happens after Snow Melt Onset?

Detailed analysis during the initial stages of spring snow melt and further melt progression has been done based on field observations [e.g. Barber et al., 1995; Perovich et al., 1994, 2002; Richter-Menge et al., 2006; Nicolaus et al., 2006 and 2009; Granskog et al., 2006; Vihma et al., 2009]. With SMO liquid water appears within the snowpack and snow crystals coarsen. This decreases the shortwave albedo and triggers a better absorption of SWd [Ehn et al., 2006; Yackel et al., 2007]. In consequence, with a larger heat gain both the snow melt and surface evaporation intensify.

As the melt season progresses, the snowpack melts out, bare ice reveals and shortwave albedo reduces again to about 0.6 [Perovich et al., 2002]. The duration of the snowmelt (the period between SMO and the beginning of the melt pond formation on the sea ice) was found to be related to the snow depth prior to SMO [Yackel et al., 2007]. Surface melt of the bare ice maintains the further melt pond formation. Depending on the melt pond depth, the surface albedo drops to 0.2-0.5. Reduced albedo of the melt ponds amplifies SW absorption within the melt ponds and accelerates sea ice melt. Field observations and numerical experiments indicate that the timing and change in surface albedo due to SMO has a strong effect on the further summer sea ice ablation, ice break-up timing, summer open water duration and the minimum sea ice extent by the end of the melt season [Eicken and Lemke, 2001; Hanesiak et al., 1999; Perovich et al., 2007b].

3.2 Snow Melt Onset detection with the remote sensing

Remote sensing of the snow cover

Already in 1966 the National Oceanographic and Atmospheric Administration (NOAA) began an operational program to map the snow extent in the Northern Hemisphere land areas, at the beginning using only visible-band satellite data [Matson et al., 1986]. Since then numerous studies focused on the snow extent and snow depth measurements inland, and only relatively few progress have been done in snow mapping on top of the sea ice and uniquely over the seasonal sea ice field [Comiso et al., 2003; Barber et al., 2003; Sturm et al., 2006; Langlois and Barber, 2007; Yakel and Barber, 2007; Kwok and Cunningham, 2008].

Snow cover mapping using optical data enables the observations of the snow-covered area with a relatively high spatial resolution, although impossible during the overcast days and polar night. Microwave-based observations identify both snow extent and snow water equivalent (SWE) regardless clouds and polar night. Empirical studies demonstrated that the decrease in brightness temperature [increase in the backscatter) is correlated with the thickness and density of the snow cover. The measured SWE and prescribed snow density allow the snow depth estimate. Yet the microwave-based snow depth detection has large limitations. (1) Active microwave snow monitoring measures only the upper 50 cm snow layer. (2) Snow depth evaluation is applicable only for dry snow. (3) Snowpack is visible only on top of the seasonal sea ice [Comiso et al., 2003].

Remote sensing of Snow Melt Onset

The appearance of liquid water within the snowpack makes the grains to cluster, resulting in bigger grains with a more rounded shape. As a result, the snow emissivity increases in the near-infrared and microwave wavelengths and the reflectivity decreases in the visible spectrum. The initial surface melt is often followed by repeating re-freezing and thaw episodes, each time affecting the emissivity and reflectivity of the surface [Barber et al., 1994; Yackel et al., 2007].

If comparing different observable wave bands, the cloud cover and precipitation have a strong effect on the electromagnetic signal in the visual and near-infrared spectrum [Forster et al., 2001; Lubin and Massom, 2006; Yackel et al., 2007]. In the permanent presence of multi-layer low-level clouds during May-October period, the microwave observations have become the most compatible for SMO detection in the Arctic Ocean.

However, the visible and near-infrared MO detection has been carried out as well, for example, by Robinson et al. [1986], Willmes et al. [2009a] and Anderson et al. [2011].

The advantage of the remote sensing SMO detection is that the same algorithm can be applied to a huge amount of rough satellite-based observations, with the entire Arctic Ocean resolved several times daily with a high spatial resolution. SMO detection done in the same way everywhere each year allows rather objective comparison of different areas and years.

There exist several important constraints for the remote detection of SMO. The one is that is that different algorithms should be developed and applied to different sea ice types (roughly: multi-year and first-year ice types), where pixels with a mixture of ice types are treated as a unique ice type. Another difficulty is that two totally different physical processes: SMO on top of compact sea ice and divergent ice drift are blended within one data set. Though both processes are essential for the sea ice and ocean surface heat budget, they have totally different origin. SMO on top of the compact sea ice is due to heat accumulation within the snowpack, while the divergent ice drift is caused by ocean waves, winds, ocean currents or bottom ice melt.

The potential of the remote-sensed blended Melt Onset data is obvious. The MO retrievals suggest an alternative point of view on the surface state in the Arctic Ocean. Thus, snow melt on sea ice could be used to constrain the albedo and surface heat fluxes in the weather forecast, for example. Moreover, the timing of spring seasonal transition and the weather conditions during summer were found to be the essential factors controlling the further summer sea ice conditions in the Arctic [Notz, 2009]. This means that the blended MO data may and should be adopted in seasonal sea ice forecasting.

For clarity, **we further apply the abbreviation SMO for the Snow Melt Onset on top of the compact sea ice and reserve the abbreviation MO for the apparent (blended) remote sensed data set**. This idea to isolate the thermal signature (SMO) from sea ice dynamics appeared briefly in the study by Nghiem et al. [2003], yet the concrete technique and results of this work have not been described.

Microwave detection of Snow Melt Onset

In the microwave (MW) part of electromagnetic spectrum the brightness temperature (measured with radiometer) and backscattered signal (measured with the synthetic aperture radar and scatterometer) are the function of the real surface (skin) temperature and emissivity/permittivity of the material (snow, sea ice and sea water). The later depend on the dielectric properties of the material: salinity, temperature, surface roughness and snow-ice granular structure. Lower temperature reduces MW emissivity and MW absorption at the sea ice surface. Higher brine content of sea ice increases the MW emissivity and absorption. Dry snow has a small MW emissivity and weak MW absorption, being almost transparent to the MW emission of the sea ice and the radar pulses sent out to the sea ice surface. With SMO the MW absorption and emissivity by the snowpack strengthen, which manifests by a sharp increase in the measured brightness temperature and a drop or increase (depending on the ice type: MYI or FYI) in the backscattered signal [Belchansky et al., 2004a; Yackel et al., 2007].

Passive microwave detection of Snow Melt Onset

Scanning Multichannel Microwave Radiometer (SMMR) and Special Sensor Microwave Imager (SSM/I) measure the brightness temperature at approximately 19, 22, 37 and 85 GHz frequencies (both in horizontal and vertical polarizations). The emissivity differs the most between dry and melting snow in 37 GHz channel, whereas the spatial resolution (pixel size) is the best at 85 GHz (about 6 km pixels). SMMR-SSM/I records of the brightness temperature are available since October 1978 until 2008, covering the Arctic Ocean up to 84^{o}N before 1987 (SMMR) and up to 87^{o}N after 1987 (SSM/I). The successor of SSM/I instrument was launched in 2002. This Advanced Microwave Scanning Radiometer for the Earth Observing System (AMSR-E) passive microwave radiometer measures the brightness temperature at approximately 7, 11, 18, 23, 36 and 89 GHz channels. The spatial resolution varies from 5 km at 89 GHz to 56 km at 7 GHz. For MO detection the most appropriate frequencies are 19 and 37 GHz, corresponding to spatial resolution of 12-25 km. SMMR-SSMI/I based MO detection has been performed by Anderson [1987], Livingstone et al. [1987], Crane and Anderson [1989], Serreze et al. [1993] and with the large-scale long-term data - by Smith [1998], Drobot and Anderson [2001], Belchansky et al. [2004], Stroeve et al. [2006] and Markus et al. [2009].

Active microwave detection of Snow Melt Onset

Scatterometer and synthetic aperture radar operate by transmitting high-frequency microwave pulses to the Earths surface and measuring the echoed radar pulses bounced back to the satellite. Compared to the passive microwave observations, there is no hole around the Poles. MO detection is possible with the daily observations by C-band and Ku-band scatterometers.

C-band scatterometers (5.3 GHz) were deployed on the European Remote Sensing satellites (ERS-1 and ERS-2) during 1991-2001. C-band pixel resolution extends from a few hundreds of meters to about 25 km. MO detection using C-band observations was demonstrated, for example, in the studies by Frey et al. [2003], Kwok et al. [2003] and Yackel et al. [2007].

Ku-band scatterometers (13.4 GHz) were deployed on the satellites launched by the National Aeronautics and Space Administration (NASA) since 1996, resolving the Arctic region with the pixel size also about 25 km. This sort of data with the specific modifications is also called NSCAT, SeaWinds and QSCAT. MO detection with Ku-band observations has been applied for example, in the studies by Yueh and Kwok [1998], Foster et al., [2001] and Perovich et al., [2007b].

In present the longest MO records for the Arctic Ocean are those based on SMMR-SSM/I brightness temperature measurements. Moreover, it seems that there are only two MO data sets spanning the complete 30-year period from 1979 up to 2008: those by Drobot and Anderson [2001] and Markus et al. [2009]. The former data set has not been completed yet (for the recent 2002-2008) at the beginning of our study. This is the reason why we focused on the data set by Markus et al. [2009].

Validation and inter-comparison of different Melt Onset and Snow Melt Onset retrievals

Observations show that the near-surface air temperatures (within the lowest 2 m height) are uniform over the areas of 10-30 km on top of the compacted sea ice field, with the spatial differences limited to 1-2^{o}C [Haggerty et al., 2003; Perovich and Elder, 2001; Perovich and Richter-Menge, 2006]. This feature enables the comparison between SAT and the satellite-derived SMO (characterizing the pixel area of about 25 x 25 km in case of SMMR-SSM/I resolution). Based on the daily SAT time series, SMO can be determined as the day when the daily mean air temperature remains above the melting point. However, the choice of the melting threshold appears to be quite subjective. Different have been applied when comparing SAT and the satellite-derived SMO, for example, 0^{o}C [e.g. Serreze et al., 1993; Martin and Munoz, 1997; Smith, 1998b], -0.5^{o}C [Lindsay, 1998], -1^{o}C [e.g. Rigor et al., 2000, Markus et al., 2009], -1.9^{o}C [Andreas and Ackley, 1982], -5^{o}C [Belchansky et al., 2004], and -5^{o}C for air temperature at 925 mb [Anderson et al., 2011].

Comparison of MO remote sensing retrievals against SAT has been done in most of the cited studies, e.g. by Winebrenner et al. [1994]; Yueh and Kwok [1998], Drobot and Anderson [2001a], and Yackel et al. [2007]. Thus MO retrievals by Winebrenner et al. [1994] and Smith [1998b] during spring 1992 agree within 2-4 days at 22 validation sites within the perennial ice zone, while being 10-20 days later than 0^{o}C SAT from

NCEP/NCAR reanalysis. Alternative and similar inter-comparison of MO records produced by Winebrenner et al. [1994], Drobot and Anderson [2001a] and Smith [1998b] at about 20 locations in the Western Arctic over perennial ice on the same year 1992, demonstrated the general agreement within 4 days as well. MO retrievals by Belchansky et al. [2004a] were compared against SAT from IABP/POLES , which showed that MO detected from SMMR-SSM/I was much earlier than the SAT-based MO, in particular over the seasonal ice. Forster et al. [2001] compared NSCAT Ku-band and SSM/I-based MO with the SAT from IABP/POLES during the spring 1997, with both MO data sets in 25 km resolution. Accordingly, the active microwave detection indicated 1-10 days earlier MO, compared to the passive microwave retrievals, and the daily mean SAT was fluctuating within -5-0^{o}C during this transition period Forster et al. [2001]. In the northern Canadian Archipelago the timing of the observed daily mean SAT reaching 0^{o}C and the remote-sensed MO on top of the FYI (synthetic aperture radar) differed by approximately 5-25 days [Yackel et al., 2007] in the period 1992-2002.

These comparisons of the remote sensed retrievals of the SMO do not mean the conclusive quantitative validation. First, because SAT time series themselves have uncertain errors. Second, because melt within the snowpack does not necessarily coincide with 0^{o}C, -1^{o}C, -5^{o}C or positive air temperatures at 2 m height, which is the particularity of the Arctic SMO [Andreas and Akley, 1982]. Field observations showed that in the Arctic the inner snow melt on top of sea ice is possible with the air temperatures below freezing, of -2-4^{o}C [Zubov, 1943; Frolov et al., 2005; Yackel et al., 2007], with SMO mostly depending on the net LW, absorbed SW radiation and the air relative humidity and related LE heat loss [Andreas and Ackley, 1982; Colbeck, 1982; Richter-Menge et al., 2006; Hanesiak et al., 1999]. Third, because when varying the threshold applied to SAT data by $\pm 2^o$C, the resulting SAT-based SMO timing ranges by as much as ± 50 days [Markus et al., 2009].

3.3 Melt Onset climatology

Snow Melt Onset and the stage of the surface melt vary considerably among the subregions, ice types and even within 10-100 meter scale over the same ice type [Walsh and Chapman, 1998]. Under the "stage of the surface melt" we mean, for example, the early and episodic melt or the advanced continuous snow melt. On average melt conditions establish in late May-early June within the peripheral Arctic seas and then advance rapidly northward reaching the North Pole about one month later [Robinson et al., 1992; Martin and Munoz 1997; Rigor, 2000; Eicken et al., 2001a; Belchansky et al., 2004a; Serreze and Barry, 2005; Richter-Menge et al., 2006; Perovich et al., 2007b]. The shape of melting isotherm reflects geographical position of heat sources for the Arctic region (**Fig 3.1a**). The earliest MO occurs typically on the Atlantic and Pacific sides, where warm ocean currents and warm and humid air masses inject a large amount of heat into the Arctic Basin (**Fig 3.1c**). The latest MO (on average) is located surprisingly in the eastern central Arctic at 60-120^{o}E 80-87^{o}N (**Fig 3.1d**).

The difference in the surface state is very different within the northern-western Greenland Sea and the northern Barents Sea. Here where within relatively small distances (500 km) the warm open sea surface borders the sea ice which starts to melt only in late June (on average). Typical year-to-year variability (one standard deviation about the 20-year average MO date) highlights the regions with a relatively stable MO timing (within $\pm$10 days about the mean MO date), and the areas that have ever experienced much earlier and much later MO (**Fig 3.1b**). Here we easily distinguish the major polynyas: Laptev Sea polynya, Cape Bathurst polynya in the Beaufort Sea, North Water polynya in the northern Baffin Bay and the NorthEast Water polynya situated in the north-western Greenland Sea. In the central Arctic we remark a few elongated shapes with the highly variable MO, which are suspected for the presence of leads in these areas, rather than extremely early or late snow melt onset.

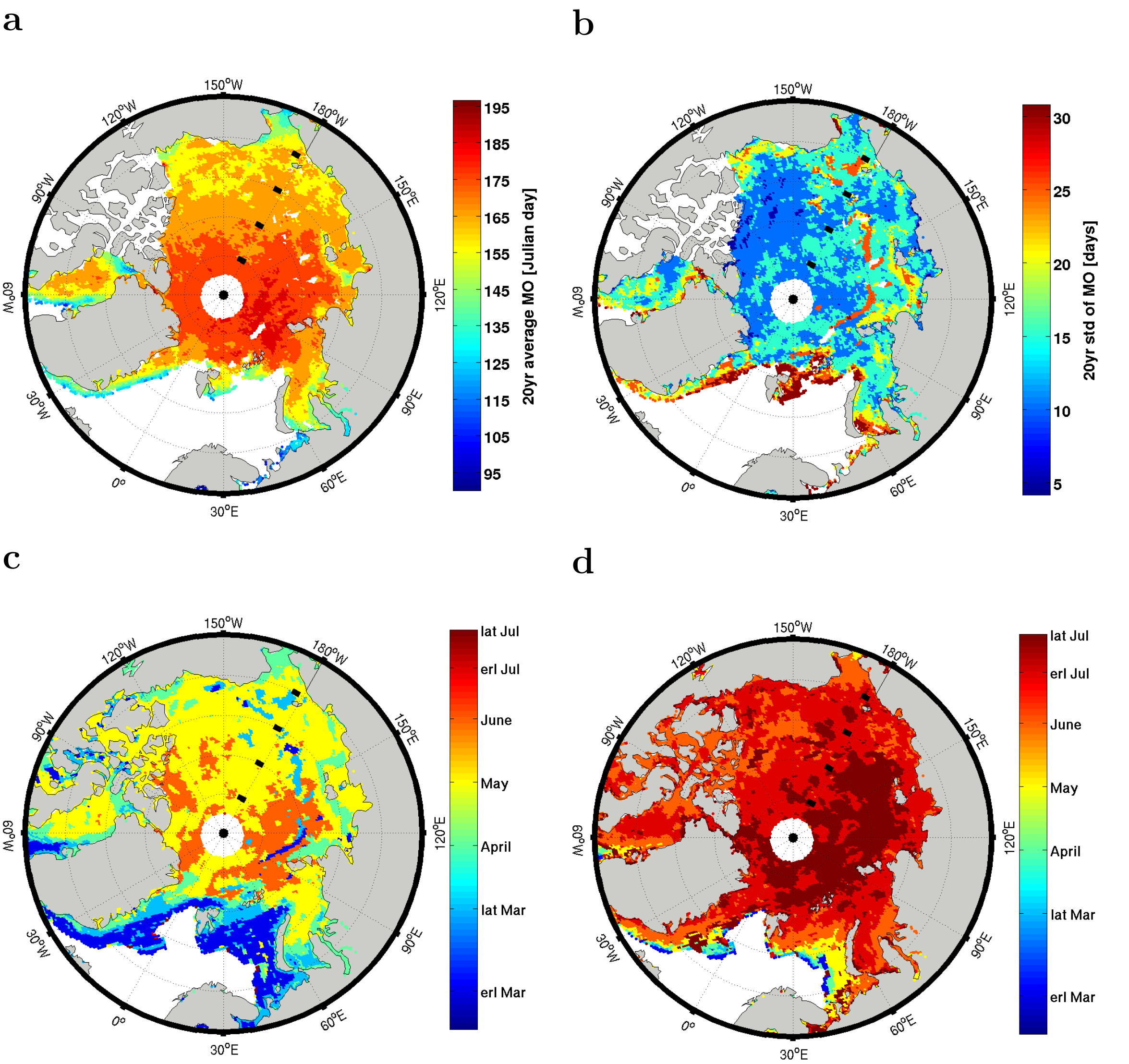

Figure 3.1: 20-year statistics of the 'apparent' Melt Onset (rough SSM/I-based time series) in the period 1989-2008. (a) 20-year average MO. (b) one standard deviation of the local MO (typical year-to-year variability). (c) the earliest local MO. (d) the latest local MO.

Chapter 4

Methodology

4.1 Discussion

Snow Melt Onset on sea ice occurs when a sufficient amount of heat (net energy budget) is accumulated within the snowpack. Thus, in nature, the year-to-year and regional variability, and tendencies in Snow Melt Onset timing [day of the year] are controlled by the year-to-year and regional differences and tendencies in heat accumulation in spring. The *objective of our study* was to compare independent data sets of the surface heat fluxes on top of sea ice (ERAI) and Snow Melt Onset on sea ice (SSM/I) in order to detect this relationship. In this Chapter we describe the methodology we have applied.

To remind: the heat accumulation within the snow depends on the intensity of the individual heat fluxes: incoming solar radiation (shortwave, SW), absorbed solar radiation (SWnet), atmospheric thermal emission (downward longwave radiation, LWd), proper thermal emission of the surface (upward longwave radiation, LWup), turbulent exchange of heat between the atmosphere and the surface (sensible H and latent LE fluxes) and the heat supply from underneath (conductive heat flux of snow and ice). The heat flux components taken into account in this study are demonstrated in **Fig 4.1**.

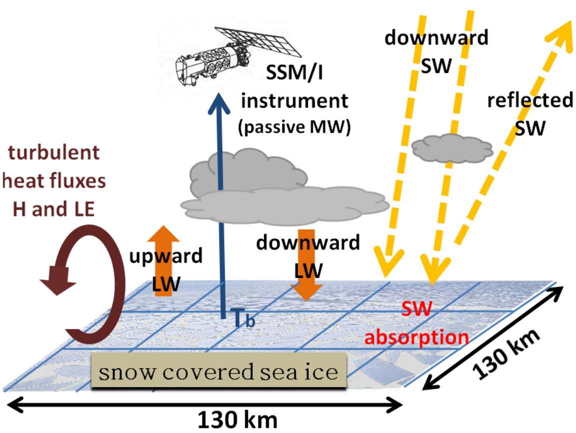

Figure 4.1: Variables taken into account in our study: surface fluxes (ERAI in 0.75^{o} resolution) and SSM/I-based Melt Onset (25 km resolution). H and LE are the sensible and latent heat fluxes at the snow surface. Tb is the brightness temperature measured by SSM/I twice daily. Day-to-day behaviour (variations) in emissivity of the surface (Tb) at several frequencies (wave lengths) were utilized to determine the day when continuous melt establishes (Melt Onset) by *Markus et al.* [2009].

In nature surface fluxes have specific local features, depending on the cloud cover, surface properties, and can/should be attributed to (compared with) the Snow Melt Onset ("seen" by SSM/I) within a relevant and common area and during the appropriate time period. Here further we discuss this issue in detail.

Choice of the Melt Onset time series: continuous or episodic Melt Onset

In Section 2.1 we briefly described the Melt Onset (MO) algorithm by *Markus et al.* [2009] applied to the daily brightness temperature measurements to evaluate, as we call, the "apparent" MO [Julian day] at each 25 km pixel and each year (1979-2008). "Continuous Melt Onset" is considered here. There is, however, usually some transition period characterized by alternating melting and re-freezing events. During this period the daily variance in brightness temperature increases until it reaches a maximum in the beginning of the continuous melt [*Markus et al.*, 2009]. Time-space resolution of both data sets (SSM/I-based MO and ERAI fluxes) is limited. So it is evident that many of the localized (of a few hundreds meters) episodic (of a few hours) snow melt events are not captured in either data set. From this point of view, it seems to us, that the onset of continuous snow melt is a more distinct event than any episodic melt, and we expect that it should be better represented in both: the remote sensing and meteorological reanalysis records.

Apparent Melt Onset: Snow Melt Onset and divergent ice drift

If following the definition of continuous MO by *Markus et al.* [2009], **Section 3.2**, one can imagine the following situation. During some period of spring the ice field diverges, creating a more or less persistent (from a few days to several weeks) vast open sea area (lead) comparable to SSM/I pixel size (about 25 km). Then the wind stress reverses and with to the sea ice convergence the pixel fills in with sea ice and sea ice concentration (SIC) increases to 80-100%. A few day-weeks after this event either a snow melt, either a divergent ice drift occur in the same pixel. From this instance the snow melt establishes (continuous melt) and/or sea ice continue to reduce. In this situation the MO algorithm determines the continuous MO at this "last event": either as the last drop in SIC (below 80% threshold) before the area becomes ice free, either as the definitive snow melt onset on sea ice. Yet, prior to this final (continuous) "regime change" the sea ice concentrations were free to vary in time!

This is a difficult issue for the MO detection and an essential one to discuss in our study. Variable sea ice concentrations (SIC) prior to continuous MO increases the absorption of solar radiation (SWnet) by the open sea, enhances the radiative thermal emission from the surface (upward LW), that strongly affects the net flux (NF) gain at the surface. Suppose that meteorological reanalysis successfully prescribe sea ice concentrations. Then the variations of ice concentrations should affect the reanalysis surface fluxes. This example illustrates that already prior to continuous MO, the surface fluxes might have been affected by variable sea ice concentrations. And if there is no "guaranty" that fluxes were not modulated by ice concentrations, then all following statements about the effect of surface fluxes on Snow Melt Onset can not hold. To guarantee the independence of surface fluxes of sea ice reduction already prior to MO (in the "pre-melt period"), the sea ice concentrations should be taken into account.

To verify our hypothesis on the possible effect of SIC on surface fluxes already before MO we focused on the daily SIC values prior to MO. MO is a day of the year (Julian day). Since we know the MO date at each location (pixel) and each year (1989-2008), we can evaluate the smallest daily SIC values in the "pre-melt period" in different years within a 20-year period (1989-2008). **Fig 4.2a** illustrates that already during the 40-day pre-melt period (before the exact MO date each year) the 40-day mean SIC (SSM/I), has ever dropped to 50-80% (at least once within the 20-year record). This map does not say anything about the frequency of such events. Similarly **Fig 4.2b** reflects the lowest one day SIC ever found during a 40-day pre-melt period. In both results (**Fig 4.2 a-b**) the MO day itself was not included in the pre-melt period.

Fig 4.3 a-b reflects the same result, but for the SIC taken from ERAI reanalysis. To evaluate SIC we considered the "reference MO date" to be the average of all "rough" MO pixels within a 130 km radius around each ERAI grid location. At this stage, a **130 km radius** is quite a subjective choice, related to the "typical" drift distances within a "40-day pre-melt period". For reference, ERAI spatial resolution is about 83 x 20 km at 70^{o}N. So that with a 130 km radius we tend to smoothen regional MO differences. 130-km radius is discussed further here. Now if comparing **Fig 4.3 a-b** with **Fig 4.2 a-b**, we get the following. ERAI cannot represent "extreme low" SIC during the pre-melt period in the Arctic Ocean (southward of 83^{o}N) and does not "feel" any SIC changes in the 40-day pre-melt period northward of 83^{o}N. The first conclusion: there is a strong indication that ERAI surface fluxes southward from 83^{o}N have ever (at least once during the 40-day pre-melt period) been affected by the reduced SIC already before MO.

These results manifest that the data set on the continuous MO should be treated and interpreted deliberately, keeping in mind that the continuous MO does not represent a definite transition from 100% sea ice covered surface (with a dry snow on top) to the melting and progressively reducing sea ice concentrations.

4.2 Snow Melt Onset sampling

To guarantee a (one-way) effect of surface fluxes and meteorological conditions on snow MO, the SIC during the pre-melt period should be high (100%), otherwise the a

b

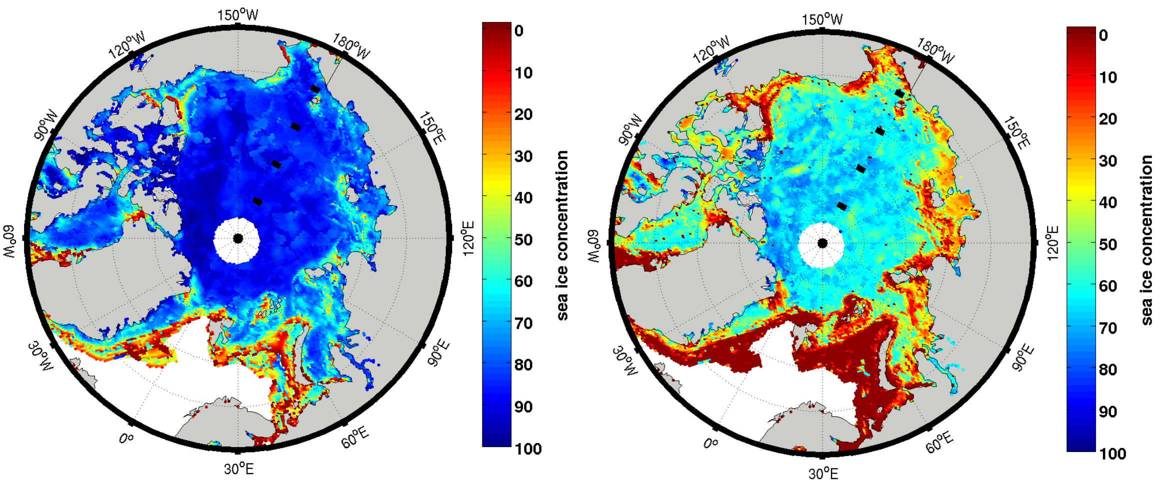

Figure 4.2: **Sea Ice Concentrations (SSM/I, 25 km resolution)** before the **apparent MO** (**SSM/I-based** data set, 25 km resolution), 20-year period 1989-2008. MO [Julian day] varies spatially and from one year to another.

(**a**) The smallest 40-day average SIC ever found during the 40-day pre-melt period and 20 years.

(**b**) The smallest 1-day SIC ever found during the 40-day pre-melt period and 20 years. MO day itself is not included in the pre-melt period. Since MO varies from year-to-year at the same location, the pre-melt period refers to a slightly different period of the year each year. Moreover the MO date is different at neighbouring pixels. So far the pre-melt period is very individual for each location (pixel) and each particular year. Only those pixels-years where MO has ever been detected are considered here.

reduced SIC affects the surface fluxes itself. So, first we tried to distinguish those MO cases (pixels-years) least affected by the SIC changes in the pre-melt period. Several "**SIC filters**" have been tested, so that the MO pixel was considered to be a snow MO pixel, if the daily (or time averaged) SIC values (SSM/I SIC data) prior to the MO did not fall below some threshold (40-day average SIC of 80, 85 or 95%).

Naturally, the stronger SIC filter we apply, the smaller will be the final SMO sample, and the study area reduces as well. Thus, for example, if we impose that a 1-day SIC (SSM/I) prior to MO should never fall below 90-95% (see **Fig 4.2b**), then we work with a very reduced MO data sample (with totally no appropriate MO data in certain years within vast areas). In contrast, if we impose too weak SIC filter, for example, admitting that time average (40-day mean) SIC during the 40-day pre-melt period can reduce to 70-80% (see **Fig 4.2a**), then we certainly include the areas where fluxes (in nature) have been largely affected by SIC.

In the study on the inter-annual variability the goal is to keep the time series as long

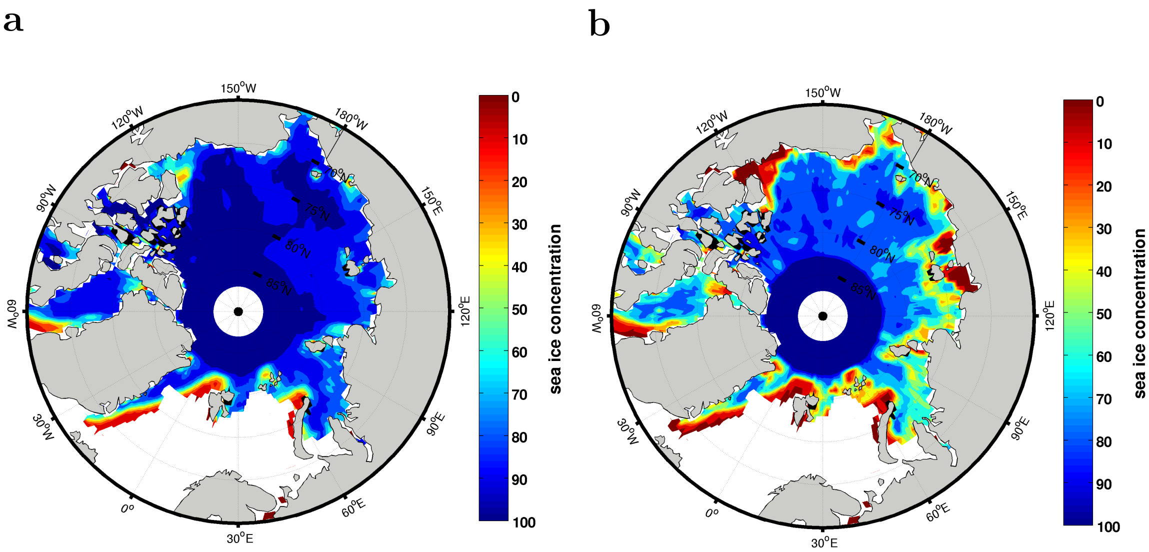

Figure 4.3: **Sea Ice Concentrations (ERAI)** before the **apparent Melt Onset (MO)** in the 20-year period (1989-2008). MO [Julian day] varies regionally and from one year to another. The reference MO date (individual for each year and each ERAI grid location) is the average of all (**rough MO**) pixels within 130 km radius around each ERAI grid location (**0.75 deg lat x 0.75 deg lon resolution**).

(**a**) The smallest 40-day average SIC ever found during the 40-day pre-melt period and 20 years.
(**b**) The smallest 1-day SIC ever found during the 40-day pre-melt period and 20 years. MO day itself is not included in the pre-melt period. Since MO varies from year-to-year at the same location, the pre-melt period refers to a slightly different period of the year each year. Moreover the MO date can be different at neighbouring grid locations. So far the pre-melt period is very individual for each ERAI grid location and each particular year. Those grid locations and years are considered here, where at least one "rough MO" observation (pixel) exists.

as possible (20 years), to exclude MO pixels largely affected by SIC changes already in the pre-melt period, and to keep MO pixels least affected by SIC variations.

SIC reductions in the pre-melt period were not as dramatic in ERAI (**Fig 4.3 a-b**) compared to SSM/I-based SIC (**Fig 4.2 a-b**). It means that ERAI fluxes in the pre-melt period were weakly affected by SIC changes.

Now, before determining definitively the "SIC filter", another aspect should be considered and taken into account. After removing the MO pixels largely affected by the SIC changes already prior to MO, the resulting MO time series and surface fluxes have to be converted to a *comparable spatial resolution.* A question appears: what is the sea ice area that is affected by the surface fluxes at a fixed grid location? In fact, a drifting sea ice floe is under the effect of the heat fluxes at a fixed grid cell only during some limited period of time. Before and after that the ice slab is affected by the surface fluxes at the neighbouring grid cells.

Naturally, if focusing on the short pre-melt period (of a few days) and the spatial scales of data of 25-80 km, than the ice drift might be roughly neglected. But if considering the monthly and seasonal history of the surface fluxes, meteorological conditions and heat accumulation within the snowpack, then the ice drift of about 25 km per day (typical value) is non-negligible.

A comparison of different solutions (not shown here) led to the formulation of the following assumptions. Those "rough" MO pixels with a 40-day average SSM/I-based SIC = 85% during 40 pre-melt days were considered to be snow MO pixels. Several tests with other thresholds (not shown here) suggested that 85% threshold of "SIC filter" works well to remove those rough MO pixels with very low SIC already in the pre-melt period.

Snow MO timing in ERAI grid coordinates was then determined as the average MO value of all snow MO pixels within roughly a 130 km radius around each ERAI grid location (schema in **Fig 4.4**). Those rough SSM/I MO pixels that had a persistent open water area already in the pre-melt period are not accounted in this spatial averaging (white area in **Fig 4.4**). Within a radius of 130 km around each ERAI grid location (dashed red square), about 140 SSM/I MO pixels (25 km each) can be included in the resulting SMO sample.

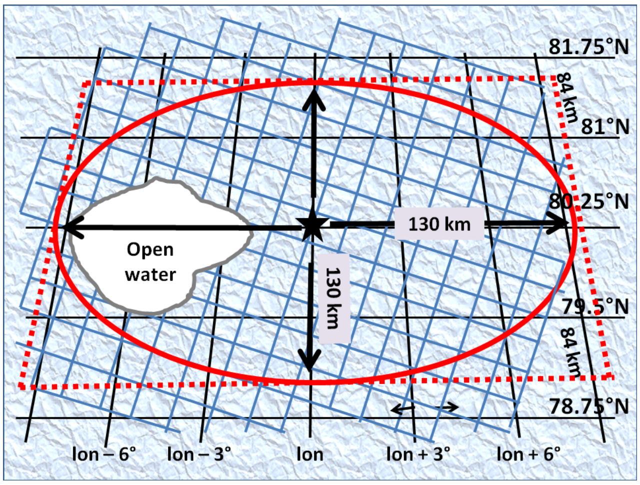

Figure 4.4: Scheme for calculating SMO in ERAI grid coordinates: which is the average of all MO pixels the least affected by SIC in the 40-day pre-melt period. Black grid is ERAI grid, blue grid are SSM/I based MO pixels. White zone is the area where the 40-day average SIC has dropped below 85% during the 40-day pre-melt period in some year. Each year this "white zone" is located differently and has different size, which affects the SMO sampling. More or less MO pixels end up in the final SMO sample each year.

The radius of 130 km is based on the following assumptions: with a typical wind speed of 5 m/s in spring [Curry et al., 2002; Vihma et al., 2008], assuming that sea ice drift speed is 1% of the wind speed [Thorndike and Colony, 1982; Serreze and Barry, 2005], the monthly ice displacement is approximately 130 km. Naturally, ice velocities vary a lot in space and time, but we rather need an order of magnitude estimate for a relevant scale for spatial averaging. For reference, buoy and satellite data on sea ice displacements reported 7±4 km/day ice drift velocities in the central Arctic [Frolov et al., 2005; Nghiem et. al., 2007]. In continuation of this study, the tracking of the ice floes with the backward trajectories is expected to give a better result.

For clarity, we introduce a new abbreviation **SMO** for the *snow melt onset on top of consolidated sea ice* and reserve the abbreviation **MO** for the *apparent melt onset* according to *Markus et al.* [2009] data set.

Fig 4.5 a-b illustrates the most extreme reduction of *sea ice concentrations* (ERAI data) in a 40-day pre-melt period prior to exact SMO each year. SMO day itself is not considered in the pre-melt period. The dark blue circle, is caller here further **circum-polar central Arctic** (83.25-87^{o}N) has a prescribed SIC of 100% in ERAI throughout the entire pre-melt period every year. South of 83^{o}N the daily mean SIC has ever fell below 85% (even down to 0%) in at least one day within a 40-day pre-melt period, see **Fig 4.5b**. Major polynya areas strongly manifest in **Fig 4.5 a-b**. We distinguish the Laptev Sea polynya, Cape Bathurst polynya in the Beaufort Sea, North Water polynya in the northern Baffin Bay and the NorthEast Water polynya situated in the north-western Greenland Sea. This result was expected, since we were searching for (extracting) those 25 km SSM/I pixels (25 km ice floes) weakly affected by local (same pixel) SIC reductions, and we have not imposed that within a vicinity (0.75^{o}lat x 0.75^{o}lon radius for example) there should be no reduction in SIC. Thus, **Fig 4.5 a-b** shows where the snow melt on sea ice (SSM/I SMO sample) has ever occurred in a close proximity to an open sea area (lead or polynya). In this situations the open water area should have affected: (1) in nature the local evaporation, cloud and fog properties, surface fluxes on sea ice and SMO timing, and (2) ERAI grid-box average surface fluxes within a mixed ice free and ice covered surface.

Depending on the sea ice conditions, different amount of *rough* MO pixels (in different years and different locations) ends-up in the resulting SMO sample. **Fig 4.6** reflects the areas where the amount of included rough MO pixels varied a a lot/few between different years. Several preliminary conclusions can be deduced already at this stage. Vast areas in the central Arctic indicate a more or less constant amount of rough MO data taken into account with the difference in "good MO pixels" about 5-20 (dark blue). It means that in these areas: (1) the MO detected by SSM/I was primarily the snow melt onset on top of sea ice (within the entire 20-year record); (2) SIC variations during the pre-melt period were rare/few, with the surface heat fluxes least affected by SIC in the pre-melt period (surface fluxes in nature, we are not talking about the reanalysis quality); (3) in consequence of (1) and (2), within the areas where snow melt onset was a predominate process further analysis on the effect of surface fluxes on snow melt onset becomes more robust. In contrast the red colour in **Fig 4.6** highlights the

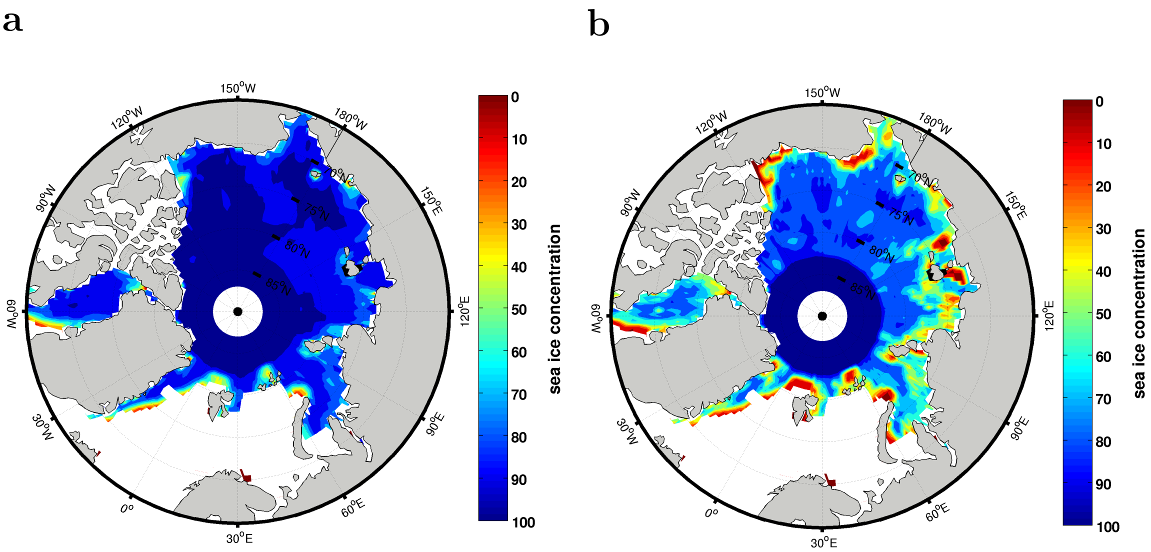

Figure 4.5: **Sea Ice Concentrations (ERAI)** before **Snow Melt Onset (SMO)**, 20-year period 1989-2008. Reference SMO date (at each ERAI grid location) is the average of those MO pixels within 130 km radius (around given ERAI grid location), that were more than 80% sea ice covered throughout the 40-day pre-melt period (prior to MO). MO and SMO [Julian day] vary regionally and from one year to another.

(**a**) The smallest 40-day average SIC (ERAI) ever found during the 40-day pre-melt period (prior to SMO) and 20 years.
(**b**) The smallest 1-day SIC ever found during the 40-day pre-melt period (prior to SMO) and 20 years. SMO day itself is not included in the pre-melt period. Since SMO varies from year-to-year at the same location, the pre-melt period refers to a slightly different period of the year each year. Moreover the SMO date can be different at neighbouring grid locations. So far the pre-melt period is very individual for each ERAI grid location and each particular year. Those grid locations and years are considered here, where at least one SMO observation (pixel) exists.

areas where very few MO pixels were "snow melt onset pixels" (in any/some year), which was certainly due to SIC reductions already in the pre-melt period.

Another issue we should notice is that SMO sampling determined in such a manner might include also the initialization in formation of the open sea areas: leads and polynyas. The possible solution to exclude the formation of the open water areas from the Snow Melt Onset sample could/should be the use of a high resolution remote sensed ice drift (divergence) data in the same period 1989-2008. Yet, this work is still to be done in future.

Bilateral and multi-linear regression analyses were applied to those ERAI grid locations (1) where there is a complete 20-year SMO time series and (2) where a 1-day SIC (ERAI data) during the 40-day pre-melt period (prior to SMO) has never fell below 85%, that is a circumpolar central Arctic (83.25-87^{o}N) only.

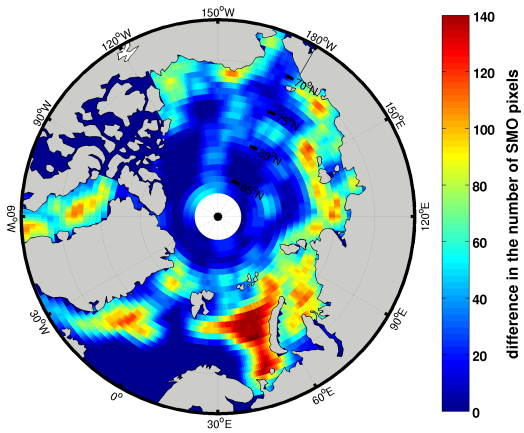

Figure 4.6: Variability in the number of rough MO pixels that end-up in the final SMO sample. Depending on SSM/I SIC some rough MO pixels were not included in our SMO sampling. Thus in some years have about 150 of "good MO pixels" and some years less. Here "difference" = maximum minus minimum number of "good MO pixels" out of 20 values at each grid location.

4.3 Comparison: Snow Melt Onset on top of compact sea ice versus surface heat fluxes

We compared the data on SMO against daily flux anomalies relative to the 20-year climatology. Meteorological data output used in this study are the daily means. Climatology of the seasonal cycle for each variable was computed for each ERAI grid location individually, based on the 20-year daily record for each variable.

The flux anomalies were averaged over 1-40 days before a reference SMO date, and then compared with the SMO anomaly at the same location and year. Here 1 .. 40 day time lag is a first guess for the duration of the pre-melt period. Time averaging up to 40 days was used in the final study since it appeared that longer periods prior to SMO did not improve the capability of surface fluxes to explain the SMO timing.

Three calculation methods: M1, M2 and M3

The definition of the reference SMO date and the further flux averaging were done using three different methods, schematically illustrated in **Fig 4.7**.

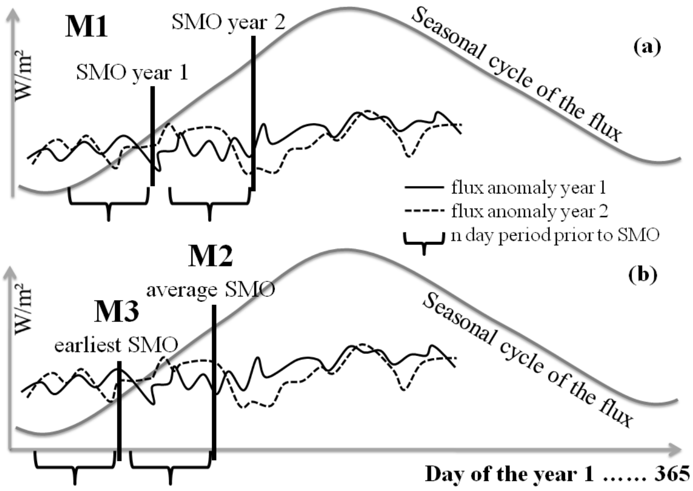

Figure 4.7: Scheme of three methods for flux anomaly calculations. **Method M1** focuses on the pre-melt period just before the exact SMO date. **Method M2** focuses on the period before the local 20-year average SMO date. **Method M3** focuses on the pre-melt period before the earliest SMO. n-days = 1 to 40 days before the reference SMO date, not including SMO date itself.

With method M1, the flux anomalies were calculated right before the exact SMO date (different date at different locations, varying from year-to-year). Since SMO date is different each year and varies from one location to another, the variations in the reference date may hamper the year-to-year comparison of the flux anomalies. To *fix* the reference SMO date, we chose the 20-year average SMO date (method M2), and the 20-year earliest SMO date (method M3). Thus with M2 and M3 the timing of the pre-melt period is always the same at each particular location, but depends on the location. This makes the comparison of flux anomalies between different years more eligible, but the drawback is that the period just a few days before SMO is usually (M3) or approximately in half of the cases (M2) not included in the calculations.

Description of the bilateral and multi-linear regression analyses

Bilateral linear regression analysis was used to compare (correlate) two 20-year time series: the time average (between 1 and 40 days) anomaly of the predictor and the SMO anomaly, both in the same ERAI grid. Two MATLAB functions *regress*(Y,X) and *corrcoef*(Y,X) were used to calculate the correlation coefficient and appeared to give the same result. For calculations Y should be a vector (time series) for Snow Melt Onset anomalies and X is a vector for one predictor (time average anomaly of some flux or of some meteorological variable). Over a consolidated sea ice cover, a ***causal effect*** of the surface flux anomaly on SMO requires a negative correlation coefficient (r): a positive flux anomaly (a larger heat gain) precedes an early SMO (negative SMO anomaly) and vice versa. Thus in all other conditions unchanged, anomalously large heat gain at the snow surface warms it up better (compared to the typical situation), which, naturally, should produce anomalously early SMO (compared to an average). Interpretation of the bilateral regressions (correlations) for the meteorological variables (wind direction, heat advection, cloud cover) requires more attention to a "zero" state, that is a climatology for each variable.

Stepwise multiple linear regression analysis [*Draper and Smith*, 1998] was applied to find out how well various combinations of possible predictors explain the inter-annual variance of SMO and which combination of predictors best explains inter-annual variance of SMO. MATLAB function stepwisefit(X,Y) was applied to distinguish the best combination of predictors and also to estimate the statistics of the resulting multi-linear regression "model" (equation). Here Y is a vector (time series) of Snow Melt Onset anomalies and X is matrix (group) of predictors (flux anomalies or meteorological variables). Stepwise regression starts with no predictors included and then adds one predictor that is most correlated to SMO timing (bilateral linear regression). The original SMO time series is then replaced by the residual from this linear fit, and another predictor most correlated to the residual is added to the linear regression equation. This is repeated until best predictors have been added. The significance (quality, applicability) of the multi-linear regression equation is evaluated by the value of the explained variance (squared correlation coefficient, r^2) and the root mean square error (RMSE) in [days] units. For reference, the same stepwise technique has been adopted by *Lindsay et al.* [2008] for the seasonal sea ice prediction.

Statistically significant relationship with a 99% confidence level is established when the explained variance (r^2) of the bilateral / multi-linear regression "model" exceeds 0.31.

Chapter 5

Results: Factors controlling the interannual and spatial variability in Snow Melt Onset

Our major results were divided here in three Sections. First Section addresses the direct factors controlling the Snow Melt Onset timing on top of compact sea ice, which are the surface heat fluxes. Second Section considers the indirect and only meteorological factors affecting Snow Melt Onset timing (by means of surface heat fluxes). Third Section illustrates some ideas regarding the trends in the chosen Melt Onset record, and also trends in ERA Interim surface heat fluxes, and our Snow Melt Onset sample. Only results for the central circumpolar Arctic within 83-87^{o}N were demonstrated in this Chapter and Manuscript. Our choice of this region was motivated by the fact that within this area there is a uniform 100% sea ice cover in ERA Interim. Thus within 83-87^{o}N ERAI surface heat fluxes were not affected by sea ice changes (reductions) in the pre-melt period. This interesting and essential issue is discussed here further.

5.1 The effect of surface heat fluxes on Snow Melt Onset

A brief framework

The question that we address in this Section and in this manuscript in general is *whether the surface heat fluxes (as represented in meteorological reanalysis, for example ERAI) were anomalously weak/strong on those years and in those locations where the Snow Melt Onset (detected by SSM/I) was anomalously late/early?* In the other words we investigate if two independent data sets (ERAI surface fluxes and SSM/I-based Snow Melt Onset) agree in terms of the spring seasonal transition.

To successfully quantify the effect of surface fluxes on the interannual and spatial variability of Snow Melt Onset a number of assumptions have been adopted (discussed in Chapter 4). First we extracted those rough Melt Onset pixels-years (SSM/I data) least affected by the sea ice reduction already in the pre-melt period. This resulting data sample is called here further Snow Melt Onset (SMO), with a few limitations that are mentioned below. Three alternative and complementary methods (M1, M2 and M3) were proposed then to determine the duration and timing of the relevant pre-melt period (explained Chapter 4). At the end, at each ERAI grid location the linear regression analysis was applied to evaluate the strength of the relationship between two 20-year records: (1) the surface heat flux anomalies (averaged during the pre-melt period), and (2) SMO anomaly, both in common period 1989-2008. The results from bilateral and stepwise multi-linear regression analysis are presented and discussed in this Section.

5.1.1 Snow Melt Onset climatology

Same as in **Fig 3.1** for the apparent MO time series, the basic statistics of the SMO sample are illustrated in **Fig 5.1** SMO is determined as described in Chapter 4. Visual comparison suggests that the regional features of SMO climatology (20-year average) in ERAI grid resolution (**Fig 5.1a**) has not changed drastically compared to the 20-year pattern in the original MO time series (**Fig 3.1a**). To notice, this 20-year average SMO date is chosen as a reference moment when determining the pre-melt period with our method M2. Thus with M2 the time-average (1-40 days) flux anomalies are calculated prior to this local 20-year average SMO date.

Local interannual variability in SMO is illustrated in **Fig 5.1b**. Compared to the interannual variability in MO (**Fig 3.1b**), the year-to-year variability in SMO has

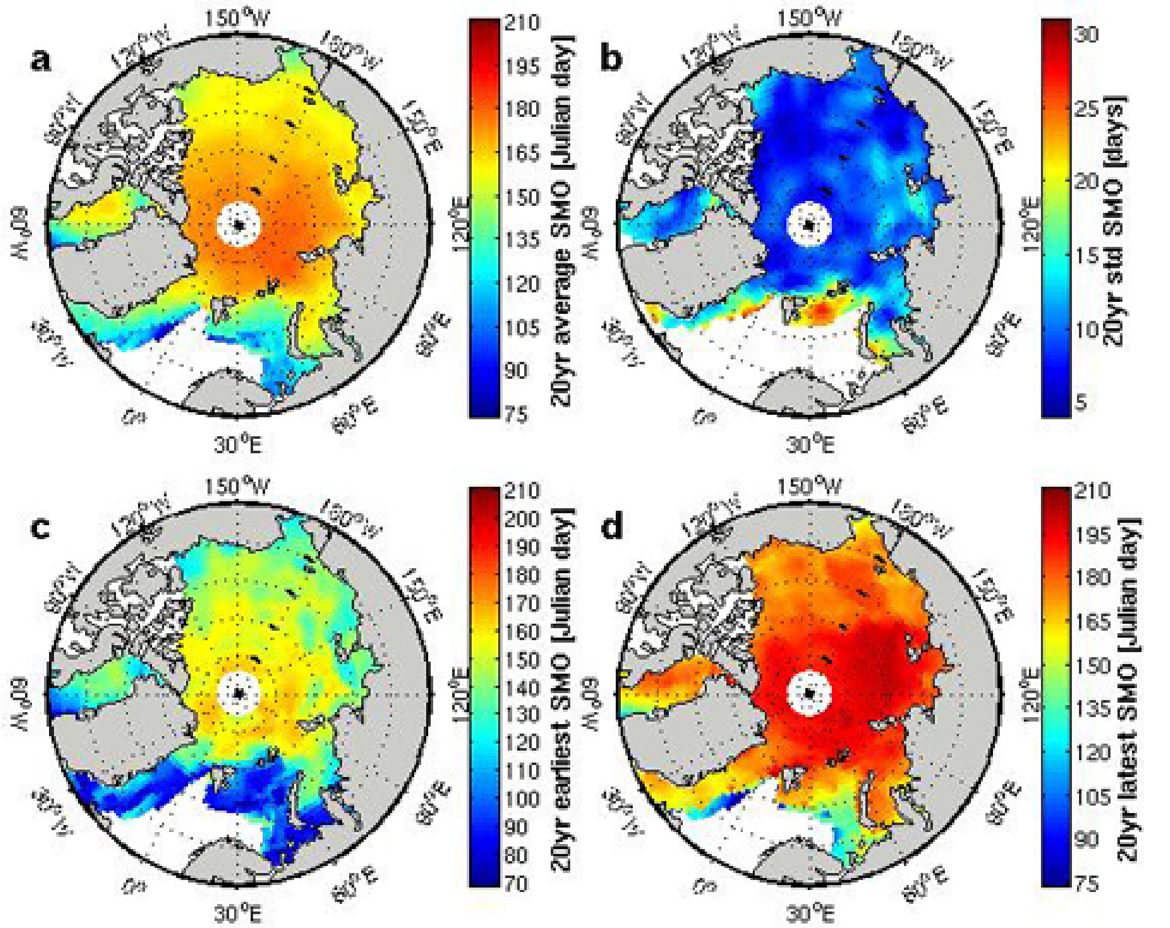

Figure 5.1: 20-year statistics of Snow Melt Onset (SMO) in the period 1989-2008: (a) 20-year average SMO; (b) one standard deviation of the local SMO (typical year-to-year variability); (c) the earliest local SMO; (d) the latest local SMO.

reduced to 5-10 days over most of the Arctic (**Fig 5.1b**). The typical interannual variability in SMO is within 15 days in the major polynya areas and up to 20-25 days along the ice margin in the Greenland-Barents Seas (**Fig 5.1b**). This large interannual variability in SMO within polynya areas may be caused by the local anomalies in surface heat fluxes. These large values also indicates that probably we have not totally escaped the initialization of the open water areas and polynyas when creating our SMO sample. As discussed earlier in Chapters 2 and 4, both: snow melt initiation and divergent ice drift are classified as apparent MO in the SSM/I-based record by *Markus et al.* [2009]. And possibly, SSM/I-based sea ice concentrations (SIC) on the MO day and even a few days after MO date - both should be accounted to strengthen the filter for SMO sampling in order to avoid the initialization of open water areas seen for MO.

The earliest and the latest ever observed SMO in 1989-2008 (**Fig 5.1 c-d**) also give an idea about the reference SMO date and the timing of the pre-melt period.

To remind, our method M3 takes for the reference moment the earliest ever observed SMO date at each location (**Fig 5.1c**). And similar to M2, in M3 the pre-melt period varies spatially but not interannually. **Fig 5.1c** says that with M3 the 30-40-day pre-melt period coincides with the month of May - early June at 83-87^{o}N and occurs approximately in April - early May within the marginal Arctic seas. In contrast, method M1 is defined to start 1 - 40 days prior to the exact local SMO date, which varies both interannually and spatially. **Fig 5.1 c-d** indicate that in the central Arctic (83-87^{o}N) the exact 30-40-day pre-melt period occurs the earliest - in May, and the latest in June - early July.

Additional assumption was adopted to better distinguish those areas where ERAI heat fluxes were least effected by SIC changes in the pre-melt period. Only the **central circumpolar Arctic within 83-87^{o}N** is considered here, where SIC is set to 100% in ERAI throughout the year.

5.1.2 Bilateral regression results: Snow Melt Onset versus surface heat fluxes

Bilateral (first order) linear regression analysis was applied at each ERAI grid location with two 20-year time series (a) of SMO anomalies, which is an explainable variable, and (b) the corresponding surface heat flux anomaly averaged during 1-40 day pre-melt period (predictor). The reference date for the pre-melt period was determined with methods M1, M2 and M3. The results for each time averaging period were then compared based on the squared correlation coefficient (r^2): one r^2 value for each time lag. Over a compact sea ice cover, a causal effect of the surface flux anomaly on SMO requires a negative r: a positive flux anomaly precedes an early SMO, and vice versa. Considering the physical interpretation, r^2 represents the percentage of the interannual variance in SMO timing explained by the interannual changes in the flux anomaly. Statistically significant relationship with a 99% confidence level was established when r^2 exceeded 0.31.

To illustrate how we interpret the results obtained with the bilateral linear regression we chose one grid location where NF manifests a significant correlation with SMO. For example, we found that at 57.75^{o}W 85.5^{o}N a 3-day average NF anomaly (method M1) explains 65% (r^2 = 0.65) of the interannual variance in SMO (**Fig 5.2**). At this location SMO varied within about 10 June - 14 July during 20 years. For reference, Julian day 150 is around 30 of May. At this location the seasonal cycle in NF increases from 10 to 55 W/m^2 during June - mid July (black curve, right axis). The grey scatter (left axis) and tells us what was the 3-day average NF anomaly prior to SMO date on each particular year. Each grey dot corresponds to some particular year. This example demonstrates that over a compact sea ice field in those years when SMO occurred **early (before the average SMO date)** the time-average NF anomaly was positive (about 0-20 W/m^2). In contrast, in those years when SMO was late (later than average SMO), NF anomaly in the preceding 3 days was primarily negative (up to -25 W/m^2). The linear regression of these two 20-year time series (SMO and NF anomaly) suggests that a 3-day average NF anomaly prior to SMO explains 65% of the interannual variance in SMO, with RMSE of 6.2 days. This linear fit between NF anomaly and corresponding SMO date is represented by the grey line (refers to the left axis).

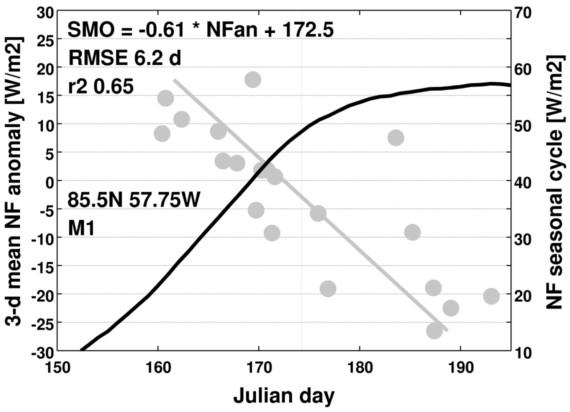

Figure 5.2: Causal relationship between a 3-day average NF anomaly and the corresponding SMO timing at one location (85.5^{o}N 57.75^{o}W). Black curve (right y-axis) shows the 20-year mean seasonal cycle of NF at this location. Gray circles and their linear fit show the relationship between SMO (day of the year, x-axis) and the preceding NF anomaly (left y-axis) averaged during a 3-day pre-melt period prior to SMO (method M1). The linear regression equation suggests that at given location a 3-day average NF anomaly prior to SMO explains 65% of the interannual variance in SMO, with RMSE of 6.2 days.

Large scatter and the explained variance (r^2) much below the unit indicate us that: (1) there are errors and limitations in our ERAI and SMO samples, and (2) that the preferential time averaging period of 3-days is likely not the only perfect solution for the duration of the pre-melt period. Thus, NF accumulation can be more or less fast and more or less efficient in different years, depending on meteorological, snow and sea ice conditions.

The year-round climatologies of surface fluxes have been revised in Chapter 1. Here below we pay attention to the pre-melt period: the averages and the anomalies in surface fluxes. 40-day time averaging period is utilized here for heat flux climatologies. Longer time averaging periods did not improve the capability (r^2) of surface fluxes to explain the interannual variations in SMO.

Downward shortwave radiation and net shortwave radiation

Within the circumpolar central Arctic the 40-day average downward shortwave radiation (SWd) prior to SMO is around 220-300 W/m^2 if determining the pre-melt period with M1 and M2 (early (**Fig 5.3 a-b**). By definition the pre-melt period starts earlier in the year when considering method M3, compared to M1 and M2. This explains why SWd values are relatively lower in the pre-melt period defined with M3, of about 150-250 W/m^2 (**Fig 5.3c**).

According to ERAI, the average net or absorbed solar radiation (SWnet) in the 40-day pre-melt period is about 60-70 W/m^2 with M1 and M2, and 35-55 with M3 (**Fig 5.3 d-f**). The absorption of SWd radiation depends on the intensity of SWd. Thus in late April-May (with M3) both SWd and SWnet are weaker compared to late May-June period (pre-melt phase with M1 and M2).

These climatologies, or more precisely, the seasonal cycle in SWd and SWnet were removed from the initial daily time series of surface fluxes in order to calculate the heat flux anomalies at each ERAI grid location, each year and each day of the year.

Linear regression of SWd and SWnet anomalies against SMO time series did not reveal the effect of solar radiation on the interannual variability in SMO. True for the entire circumpolar central Arctic within 83-87^{o}N. This result is quite reasonable because there is no snowmelt and no ice melt in ERAI. So far the representation of diurnal and day-to-day variations in surface albedo and SWnet on top of the compact sea ice cannot be captured in ERAI, both before, during and after SMO. However in reality already before the continuous snow melt establishes, the surface albedo and SWnet oscillate with the diurnal cycle within totally snow- and ice-covered areas [*Cheng et al.*, 2008; *Vihma et al.*, 2009]. And these diurnal and day-to-day variations in SWd may and should contribute to the net flux accumulation within the snowpack, and thus have an effect on SMO timing. According to our knowledge the representation of SWd and SWnet has not been validated yet for ERAI. Three ship campaigns during summer indicated that ERAI overestimates near-surface humidity in the Arctic [*Lupkes et al.*, 2010]. We speculate that this bias and/or error in atmospheric moisture content could have an impact on SWd and SWnet in ERAI. Another source of uncertainty may arise if multiple reflections between the clouds and a highly reflective snow-ice surface [*Curry and Ebert*, 1992; *Shine*, 1984] are mislead in the reanalysis model. These complex interactions between clouds and the snow surface are likely not reproduced in ERAI, which also reduces the reliability of SWd and SWnet fluxes, and the capability of solar flux anomalies to explain the interannual anomalies in SMO.

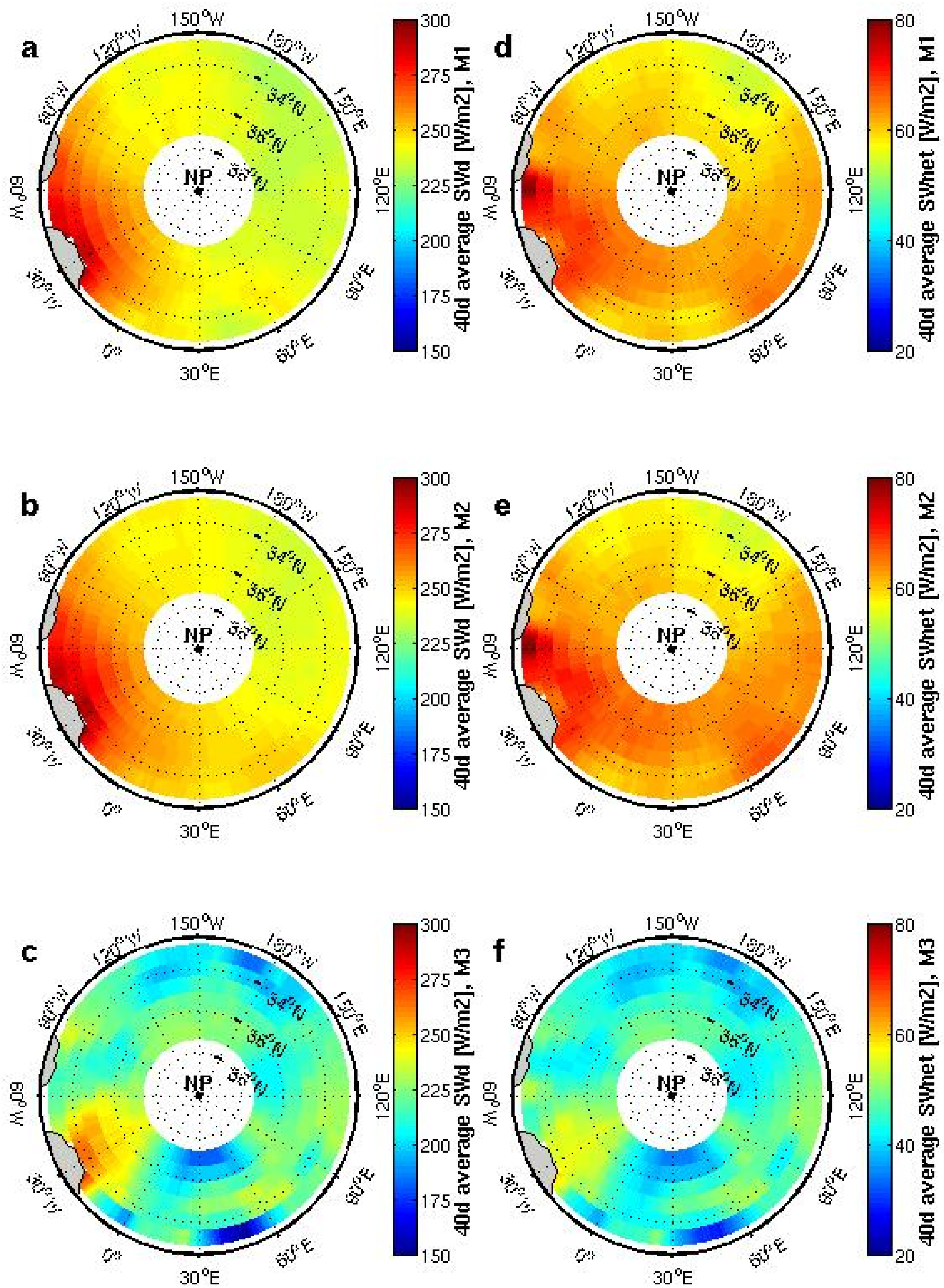

Figure 5.3: 20-year average SWd (left-hand maps) and SWnet (right hand maps) in the 40-day pre-melt period (prior to SMO) as defined with method M1 (upper two maps), method M2 (two maps in the middle), and method M3 (lower two maps).

Downward longwave radiation

Within the circumpolar central Arctic the 40-day average LWd prior to SMO is 250-280 W/m^2 if defining the pre-melt period with M1 or M2 (**Fig 5.4 a-b**), and 220-250 W/m^2 with M3 (**Fig 5.4c**).

LWd alone explained up to 90% (M1, **Fig 5.5a**), 82% (M2, **Fig 5.5c**) and 57% (M3, **Fig 5.5e**) of the local year-to-year SMO variance. Among different (1, 2 40-day) time averaging periods and methods (M1, M2 and M3), an anomalous LWd during 1-7 days (synoptic scale) before SMO (M1) best explained the local interannual SMO variance (**Fig 5.6a**). In terms of the flux anomaly magnitude, a 1-7-day average anomaly of +28±9 W/m^2 (-11±12 W/m^2) in LWd was followed by 15-20 days earlier (later) SMO. Where 28 W/m^2 is the average of different LWd anomalies (at different locations and in different years) corresponding to 15-20-day SMO anomalies (at the same location, same year), and 9 W/m^2 is the standard deviation of these LWd anomaly values. The effect of 1-7 day average LWd anomaly on SMO appeared within 577 x 10^3 km^2 with M1 (34% of the circumpolar central Arctic), geographically located within the shaded area in **Fig 5.5 a-b**. For comparison, the effect of 1-7 day average LWd anomaly on SMO was found within the area of 270 x 10^3 with M2 (somewhere within the shaded area in **Fig 5.5 c-d**) and 190 x 10^3 km^2 with M3 (within the limits of the shaded area in **Fig 5.5 e-f**).

With M2 the effect of 10-40 day LWd anomalies on SMO was most pertinent, revealing significant r^2 over the area of 723 x 10^3 km^2 (43% of the circumpolar Arctic) located within the shaded area in **Fig 5.5 c-d**. In terms of the flux anomaly magnitude, for example, a 17-19-day average LWd anomaly of +11±6 W/m^2 (-5±15 W/m^2) in LWd (M2) was followed by 15-20 days earlier (later) SMO, all occurring within the shaded area in **Fig 5.5 c-d**. The 17-19-day time averaging period is chosen for the example, showing the best capacity to explain interannual variance in SMO (**Fig 5.6b**).

With M3 the time averaging period of 1-20 days revealed few and relatively weak r^2 (below 0.55), with the best time averaging period of 10-17 days, **Fig 5.6c**. Here a 10-17-day averaging period was a common solution among different locations where at least some significant r^2 has been found. To precise, the grey curve on subplots in **Fig 5.6** refers to the right axis and indicates how many locations revealed r^2 > 0.31 for each time averaging period. If following M3, in those years when SMO occurred 15-20 days early (late) the 10-17-day average LWd anomalies were about +16±20 W/m^2 (-12±14 W/m^2).

Bilateral regression analysis was also applied to a composite of all maritime grid locations within the shaded area in **Fig 5.5 a-b** (M1). Local 1,2,40-day average LWd anomalies were regrouped and then compared with the corresponding SMO anomalies regrouped in the same way. Time averaging periods for the local LWd anomalies were always the same for the whole group of locations. In this manner we test whether there is some common/best solution for the pre-melt period length, *i.e.* when the effect of LWd on SMO timing is the most pertinent. To precise, if some location revealed significant bilateral r^2 with only one time lag (for example, only a 5-day lag), this location was also included into the group when calculating the correlation between the composite 40-day LWd anomalies versus SMO. It means that the group (composite) of locations has always the same length, no matter the time averaging period. This quite simple technique allowed to compare (correlate) longer time series, and many local data as a whole. At the end the results for different time averaging periods were compared in terms of r^2. Accordingly LWd anomalies during 6-day pre-melt period explained 27% of spatial and interannual variance in SMO (**Table 1**, page 98), significant at 99% confidence level.

And the other time lags also explained significant, but a smaller portion of SMO variance. The remaining (unexplained) SMO variance (lets say 70%) results partly from errors in ERAI heat fluxes, partly from the original MO and our SMO sample as well. This large unexplained variance also manifests that the preferential time averaging period of 6-days is not the only perfect solution for the duration of the pre-melt period.

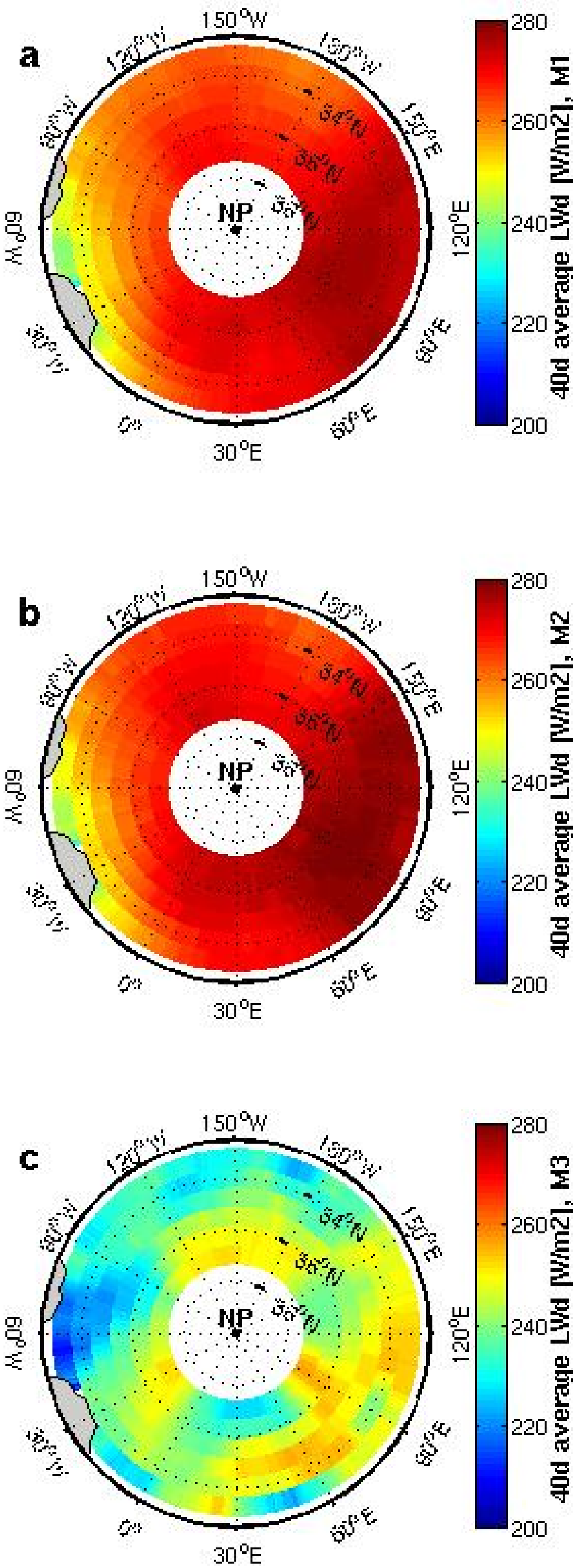

Figure 5.4: 20-year average LWd in the 40-day pre-melt period (prior to SMO) as defined with: (a) method M1, (b) method M2, and (c) method M3.

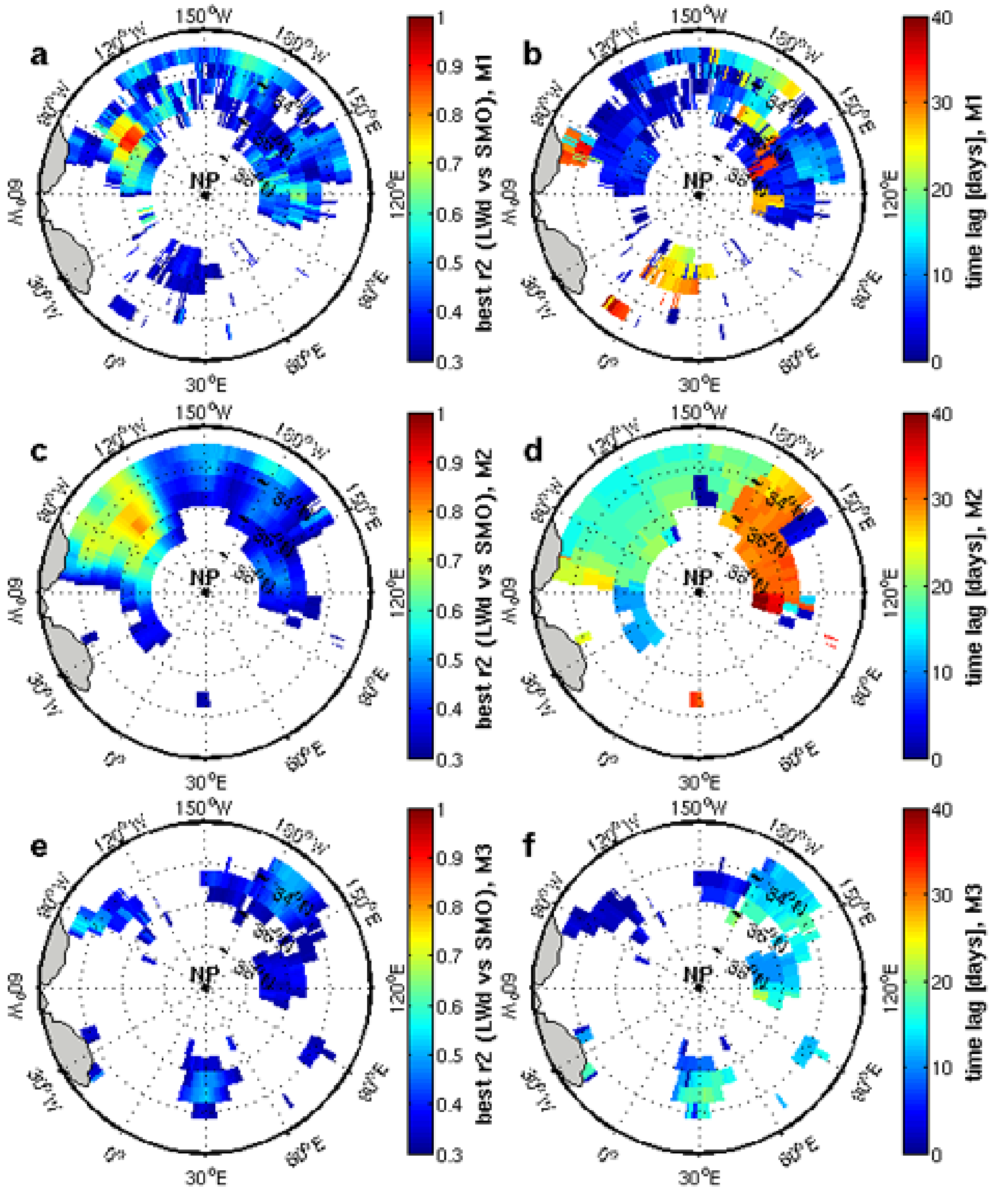

Figure 5.5: Results for downward longwave radiative flux. Bilateral regression results on the relationship between the LWd anomaly and the corresponding SMO anomaly (same location, same year). The flux anomaly is averaged over various pre-melt periods (1-40 days). Three methods M1, M2 and M3 are compared. Left-hand plots illustrate the best r^2 with thee methods. Only results with $r^2 > 0.31$ ($p < 0.01$) are shown. Right-hand plots reflect the corresponding time-averaging period.

For comparison, the composites of local LWd anomalies were regressed against SMO, where LWd anomalies were calculated with M2 and M3. Considering method M2, all maritime grid locations within the shaded area in **Fig 5.5 c-d** were regrouped. With M3 all maritime grid locations within the shaded area in **Fig 5.5 e-f** were considered. Accordingly, LWd anomalies explained 36% and 23% of the interannual and spatial variance in SMO with M2 and M3 respectively (**Table 1**, page 98). Consistent with the local bilateral regression results, the best time averaging periods are 21 days with M2 and 13 days with M3 (**Table 1**).

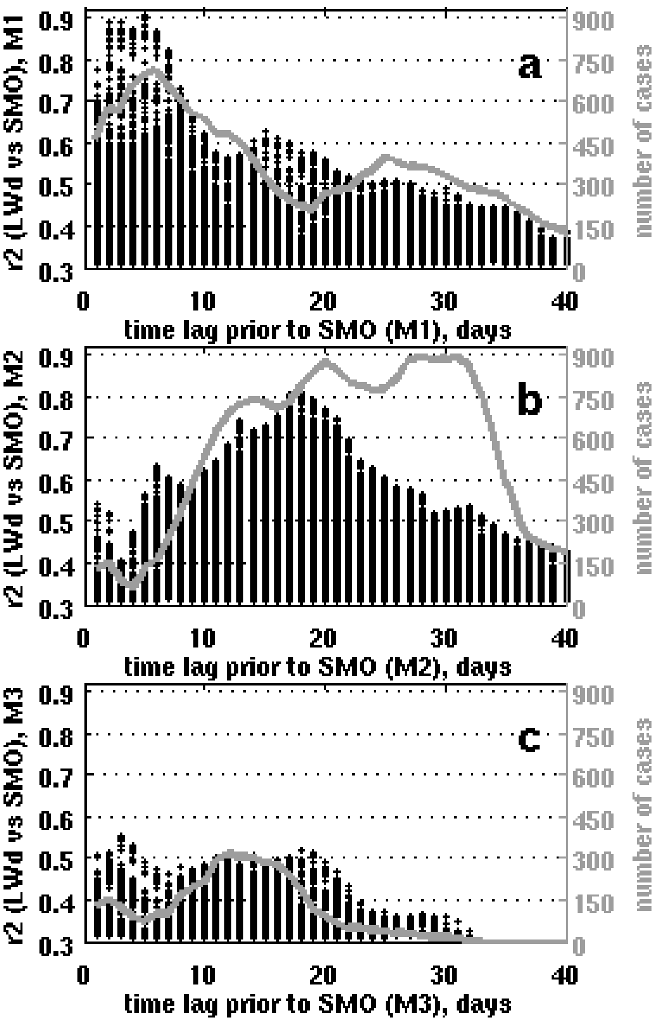

Figure 5.6: Downward longwave radiation: dependence of the squared correlation (r^2) on the length of the pre-melt period. The black dots show all significant r^2 values ($p < 0.01$) for each flux-averaging period. This indicates the largest r^2 at each time lag (independent of the location). The grey curve shows the number of ERAI grid locations where a significant r^2 was found with the given flux-averaging period. It indicates which time averaging period is the most successful in explaining interannual SMO variance (within the study region). Three methods M1 (a), M2 (b) and M3 (c) are compared.

Net longwave radiation

Net longwave radiation (LWnet) is the balance between the surface thermal emission (upward longwave radiation, LWup) and atmospheric thermal emission downwards (downward longwave radiation, LWd). Within the circumpolar central Arctic the 40-day average LWnet prior to SMO is negative, within -30-60 W/m^2 (**Fig 5.7**). The seasonal cycle of LWnet within the central Arctic was discussed in **Chapter I**.

In general, results for LWnet are very similar to those obtained for LWd. Linear regression of local LWnet anomalies against corresponding SMO anomalies revealed the causal effect of LWnet on SMO timing: with positive LWnet anomaly in those years when SMO occurred earlier than average, and vice versa. There positive LWne anomaly means weaker LWnet deficit during the pre-melt period. High r^2 was found with all tree methods (**Fig 5.8**). In respect to LWnet method M2 is likely the most appropriate of three (M1, M2 and M3), suggesting very high and significant r^2 (up to 0.7-0.8, black scatter in **Fig 5.9b**) within a vast area (**Fig 5.8 c-d**, and grey curve in **Fig 5.9b**). Thus with M2 significant results were found within the area of 798 x 10^3 km^2 (47% of the circumpolar central Arctic, shaded grid boxes in **Fig 5.8 c-d**). In terms of the flux anomaly magnitude, a 13-21-day LWnet anomaly of +10±4 W/m^2 (-6±10 W/m^2) was followed by 15-20 days early (late) SMO, all occurring within the shaded area in **Fig 5.8 c-d** (M2).

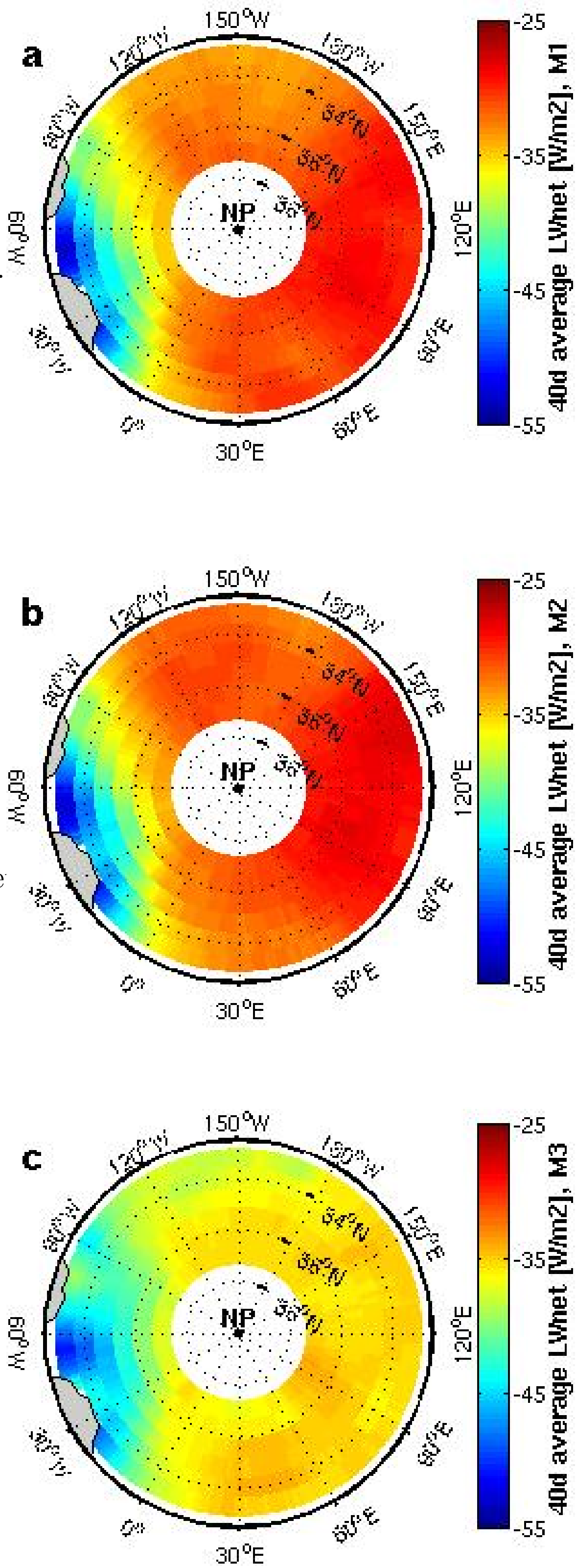

Figure 5.7: 20-year average LWnet in the 40-day pre-melt period (prior to SMO) as defined with: (a) method M1, (b) method M2, and (c) method M3.

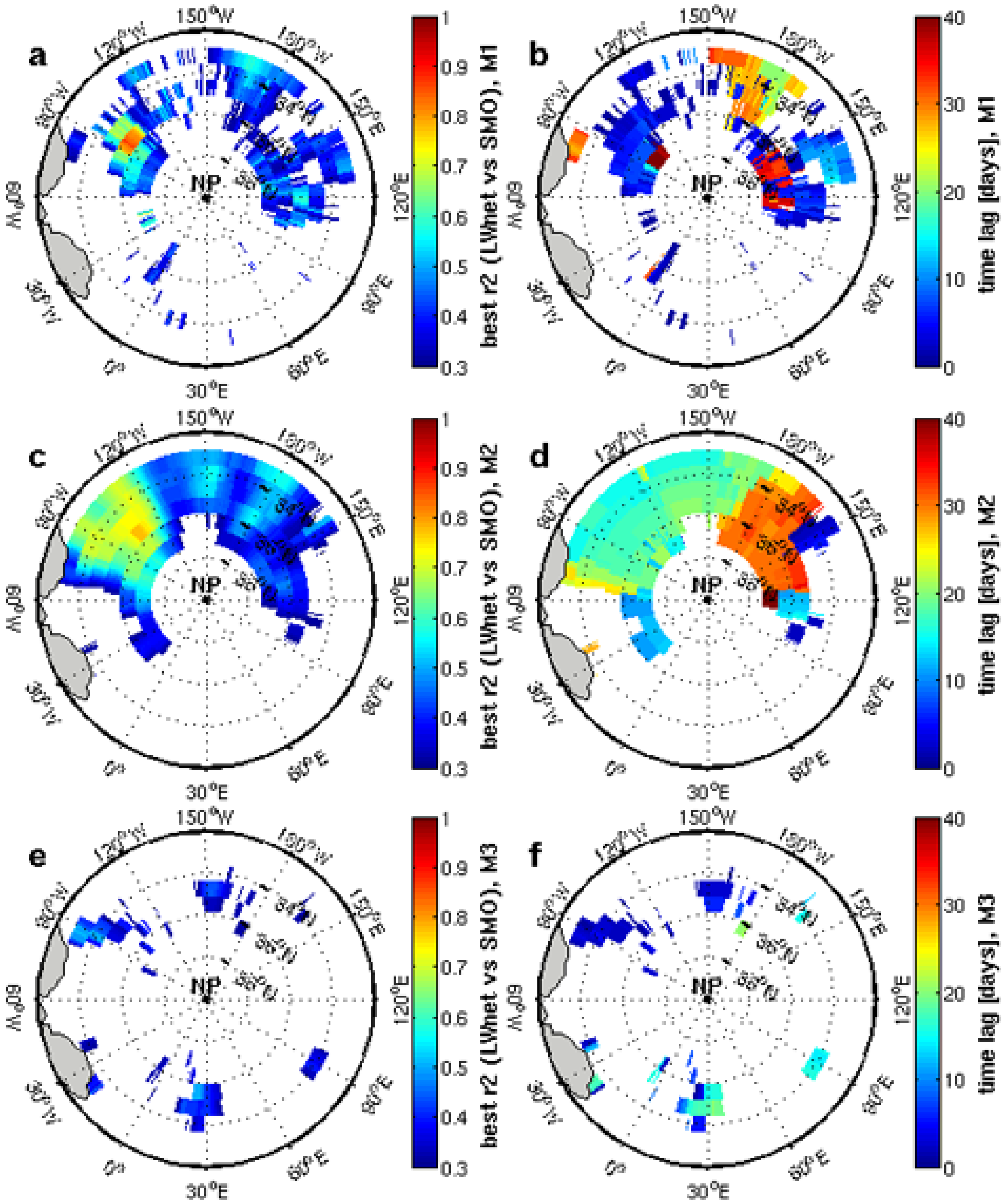

Figure 5.8: Results for the net longwave radiative flux. Bilateral regression results on the relationship between the LWnet anomaly and the corresponding SMO anomaly (same location, same year). The flux anomaly is averaged over various pre-melt periods (1-40 days). Three methods M1, M2 and M3 are compared. Left-hand plots illustrate the best r^2 with thee methods. Only results with $r^2 > 0.31$ ($p < 0.01$) are shown. Right-hand plots reflect the corresponding time-averaging period.

As for LWd a 1-7 day time averaging periods were the most illustrative for the seasonal transition (r^2 up to 0.9) when applying M1, with a secondary peak in r^2 up to 0.6 at about 30-day lag (**Fig 5.9a**).

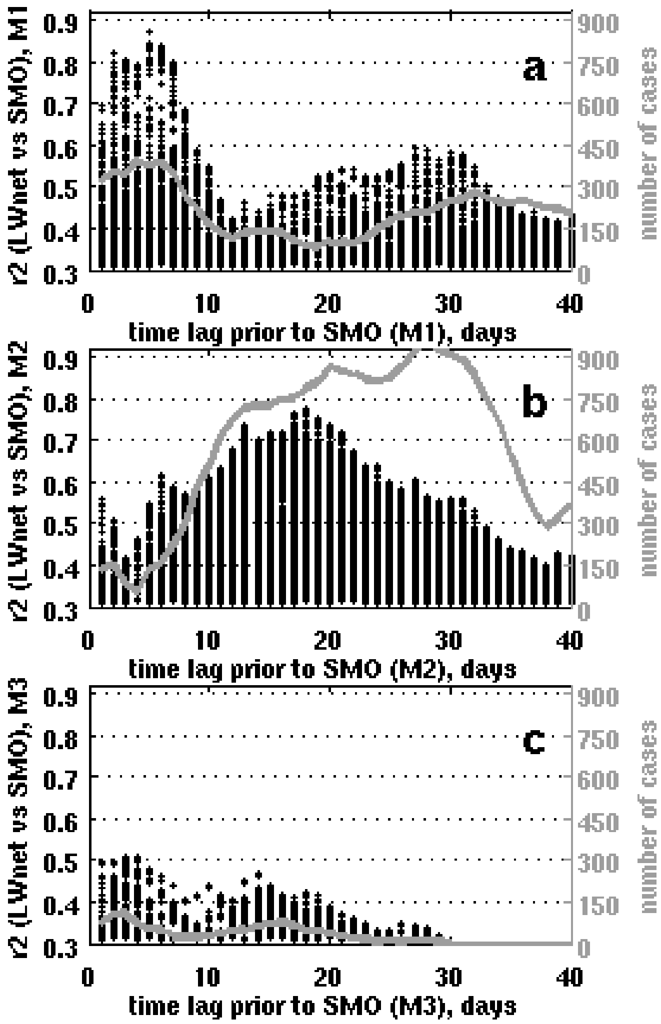

Figure 5.9: Net longwave radiation: dependence of the squared correlation (r^2) on the length of the pre-melt period. The black dots show all significant r^2 values ($p < 0.01$) for each flux-averaging period. This indicates the largest r^2 at each time lag (independent of the location). The grey curve shows the number of ERAI grid locations where a significant r^2 was found with the given flux-averaging period. It indicates which time averaging period is the most successful in explaining interannual SMO variance (within the study region). Three methods M1 (a), M2 (b) and M3 (c) are compared.

Similar to LWd, few and relatively weak r^2 (below 0.5) were detected for LWnet when presuming the pre-melt period with method M3 (**Fig 5.9c**). For comparison, with M1 and M3 significant r^2 was found within the area of 520 x 10^3 km^2 (**Fig 5.8 a-b**) and 162 x 10^3 km^2 (**Fig 5.8 e-f**), or 31% and 10% of the circumpolar central Arctic, respectively.

This established relationship between LWnet anomalies and SMO explicitly shows that there is a good correspondence between the surface (ice) thermal state in ERAI and SMO timing detected by SSM/I.

Turbulent heat fluxes

Local anomalies in LE and H were positive (negative) in early (late) SMO years. It means that either turbulent heat loss was weaker, or turbulent heat gain occurred in those years and at those locations where SMO was earlier than average. In contrast, the surface turbulent heat loss was stronger than average in the pre-melt period where/when SMO was anomalously late.

Latent heat flux

Within the circumpolar central Arctic the 40-day average latent heat flux (LE) prior to SMO is negative (upwards) about -10 - (-15) W/m^2 if defining the pre-melt period with M1 or M2, and -5 - (-10) W/m^2 with M3 (**Fig 5.10**). The day-to-day variability in LE is regionally uniform over the ice covered domain, below 5 W/m^2 during April-June [Persson et al., 2002].

Significant r^2 was found within the area of 370 x 10^3 km^2 with both M1 and M2 (shaded area in **Fig 5.11 a-b**), and 153 x 10^3 km^2 with M3 (shaded area in **Fig 5.11c**), or 22% (M1 and M2) and 9% (M3) of the circumpolar central Arctic area.

Seasonal 20-40 day average LE flux anomalies explained up to 61% of the local interannual SMO variance (**Fig 5.12**). On average a 2-7 W/m^2 weaker (stronger) LE loss (evaporation) during May - June contributed to the advance (delay) in SMO by approximately 6 days.

As for LWd, the bilateral regression analysis was applied to a composite of all maritime grid locations where at least one significant r^2 (with any time averaging period) had been established for LE. The local LE anomalies prior to the exact SMO (M1) explained 31% of the spatial and interannual variance in SMO within the shaded area in **Fig 5.11 a-b** (**Table 1**, page 98). For comparison local LE anomalies prior to the average (M2) and the earliest (M3) SMO explained 29% and 22% of the spatial and interannual variance in SMO, respectively (**Table 1**, page 98).

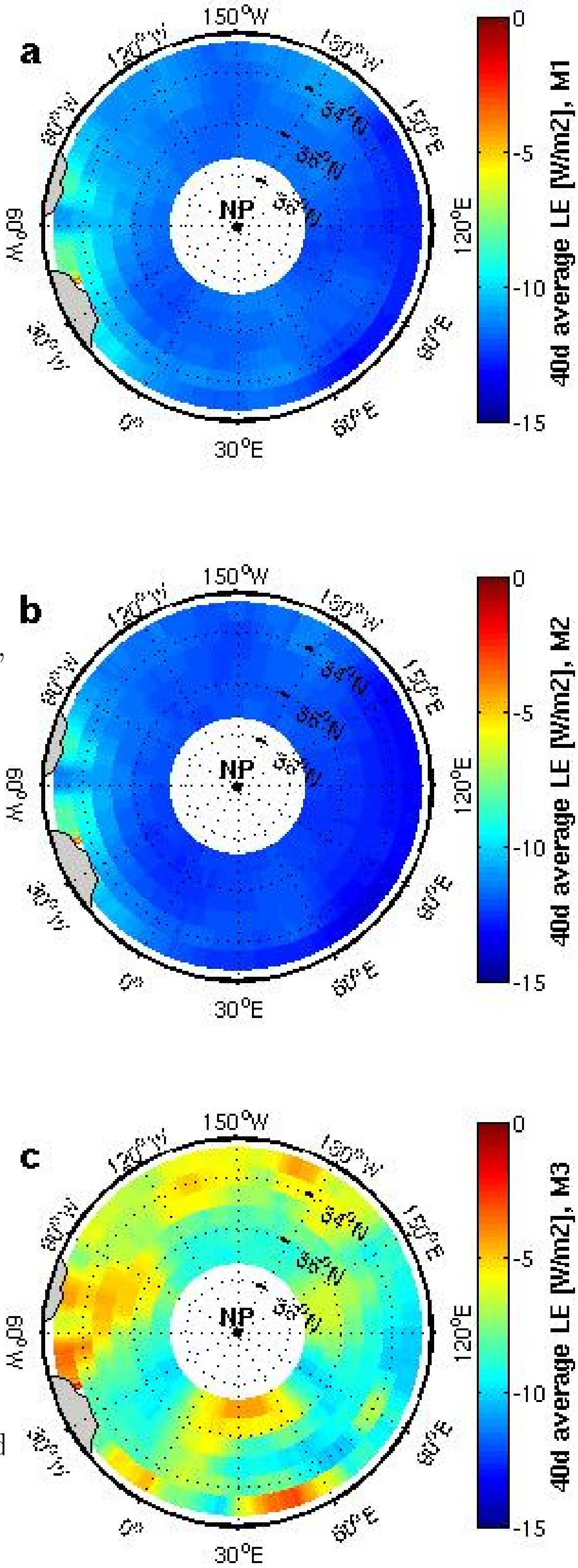

Figure 5.10: 20-year average LE in the 40-day pre-melt period (prior to SMO) as defined with: (a) method M1, (b) method M2, and (c) method M3.

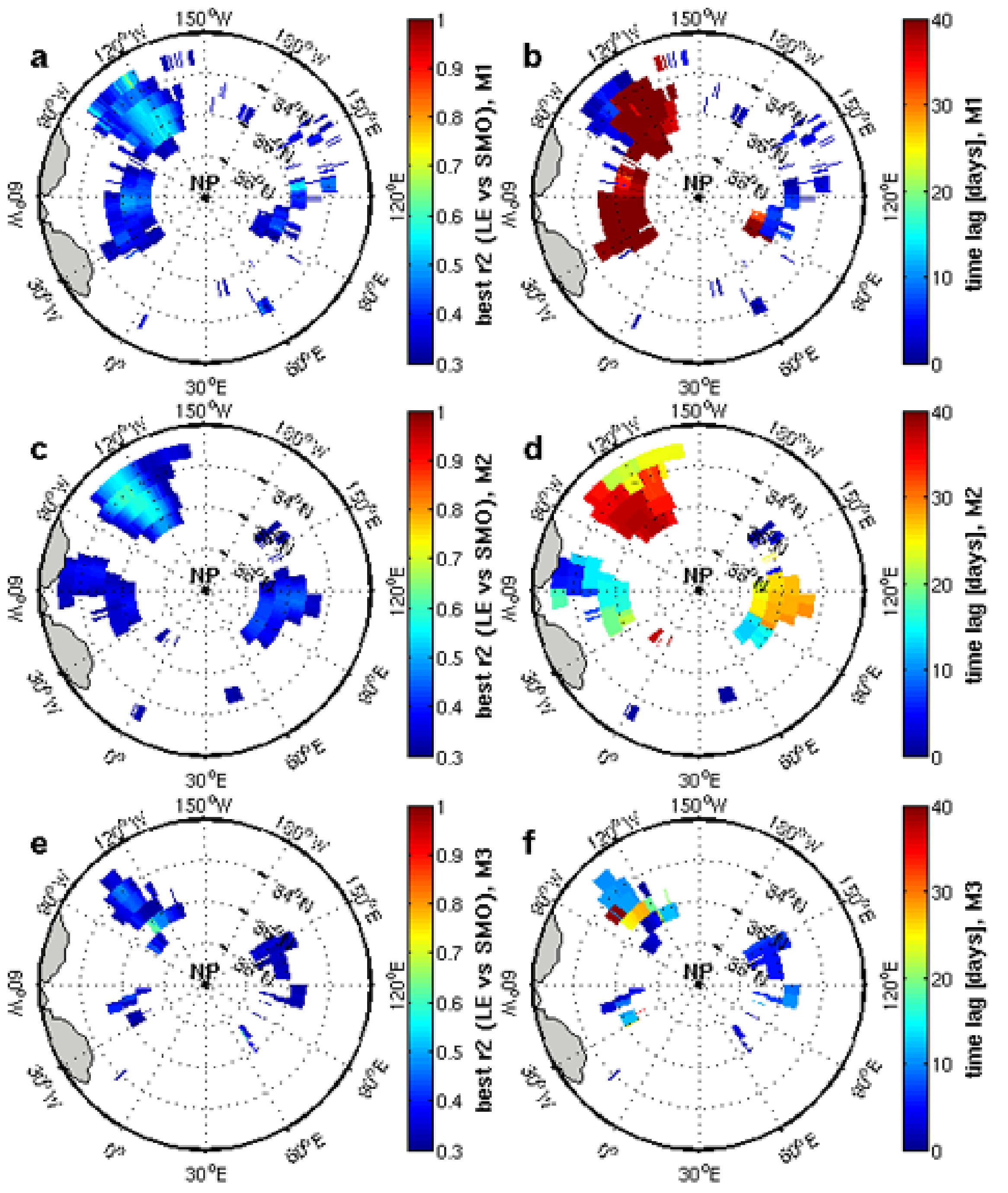

Figure 5.11: Results for the latent heat flux. Bilateral regression results on the relationship between the LE anomaly and the corresponding SMO anomaly (same location, same year). The flux anomaly is averaged over various pre-melt periods (1-40 days). Three methods M1, M2 and M3 are compared. Left-hand plots illustrate the best r^2 with thee methods. Only results with $r^2 > 0.31$ ($p < 0.01$) are shown. Right-hand plots reflect the corresponding time-averaging period.

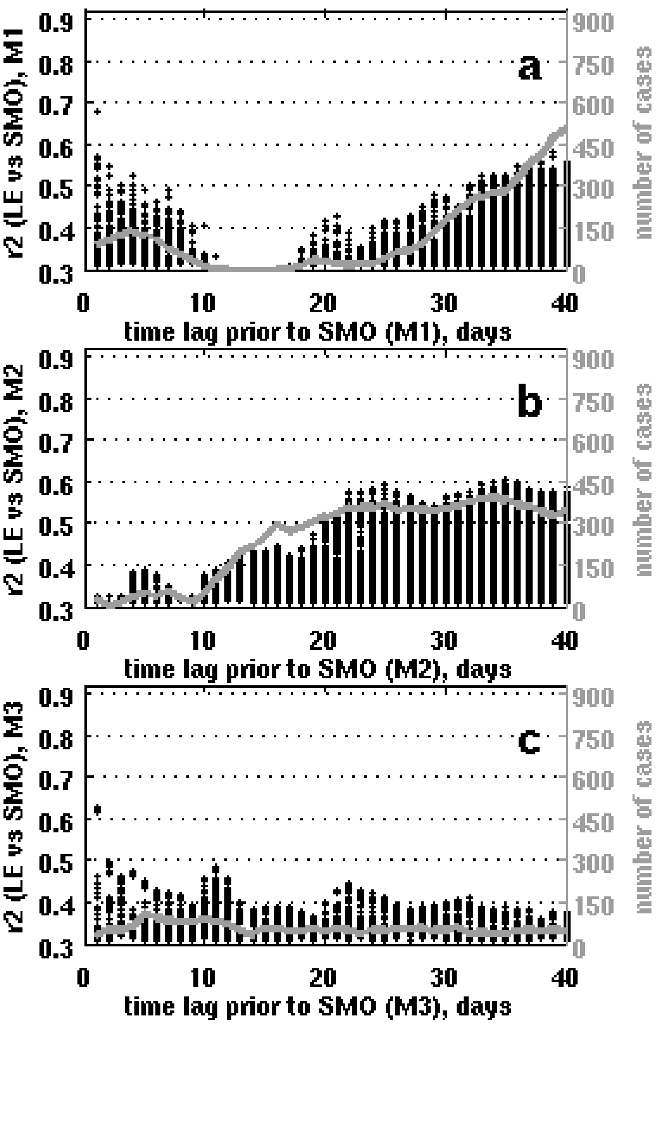

Figure 5.12: Latent heat flux: dependence of the squared correlation (r^2) on the length of the pre-melt period. The black dots show all significant r^2 values ($p < 0.01$) for each flux-averaging period. This indicates the largest r^2 at each time lag (independent of the location). The grey curve shows the number of ERAI grid locations where a significant r^2 was found with the given flux-averaging period. It indicates which time averaging period is the most successful in explaining interannual SMO variance (within the study region). Three methods M1 (a), M2 (b) and M3 (c) are compared.

Sensible heat flux

Within the circumpolar central Arctic a 40-day average sensible heat flux (H) was weak and negative (surface heat loss) in the pre-melt period, on average only about -2-0 W/m^2 with M1 and M2 (**Fig 5.13 a-b**). These values are consistent with the field observations [Persson et al., 2002]. By definition, with method M3 the pre-melt period typically occurs earlier in the year (compared to M1 and M2), and this explains positive H values (surface heat gain) during the pre-melt period: within ±4 W/m^2 (**Fig 5.13c**). Thus M3 captures the end of winter when H flux is directed downwards, with the near-surface atmospheric boundary layer heating the snow surface.

Significant r^2 was found within the area of 444 x 10^3 km^2 with M1 (shaded area in **Fig 5.14 a-b**), 319 x 10^3 km^2 with M2 (shaded area in **Fig 5.14 c-d**), and 200 x 10^3 km^2 with M3 (shaded area in **Fig 5.14 e-f**), or 26% (M1), 19% (M2) and 12% (M3) of the circumpolar central Arctic area.

H flux anomalies explained up to 73% of the local interannual SMO variance (**Fig 5.14 and 5.15**), suggesting relatively better results (higher r^2) when defining the pre-melt period with M1.

Considering different time scales, similar to LE results, the best r^2 were detected with 20-40 days time averaging period. Thus a 2-4 W/m^2 weaker (stronger) H loss during May - June contributed to the advance (delay) in SMO by approximately 13 days.

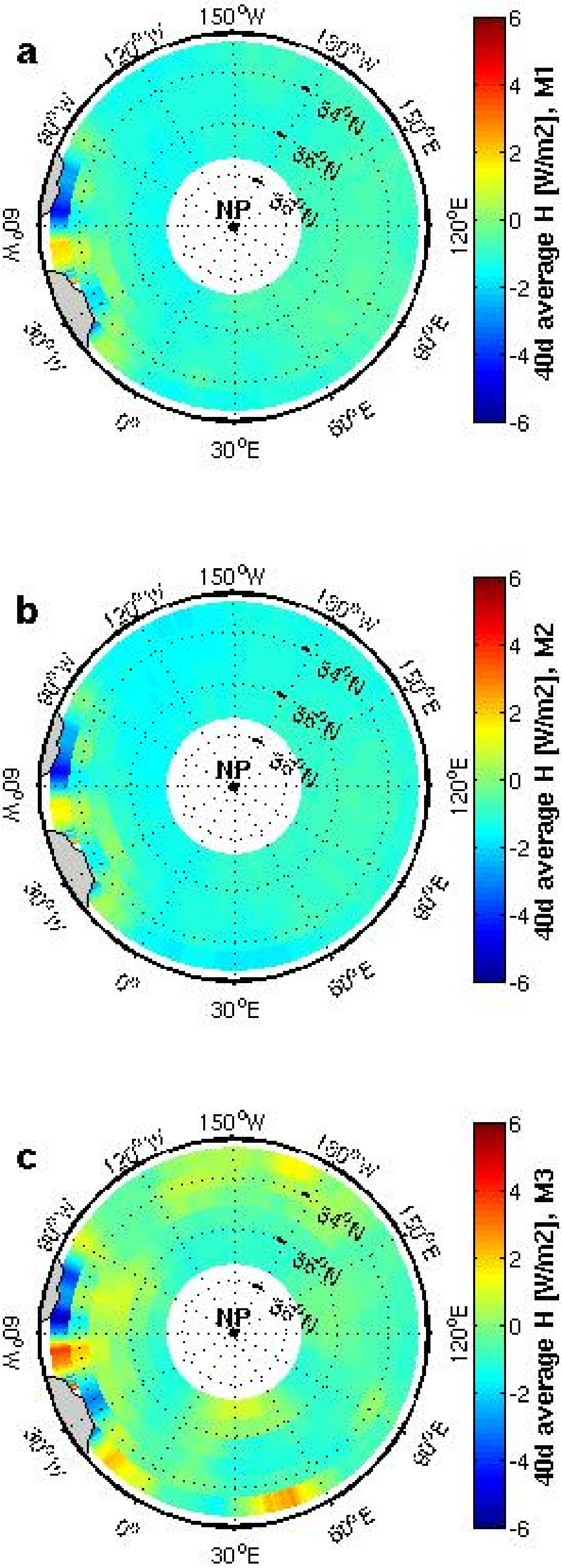

Figure 5.13: 20-year average H in the 40-day pre-melt period (prior to SMO) as defined with: (a) method M1, (b) method M2, and (c) method M3.

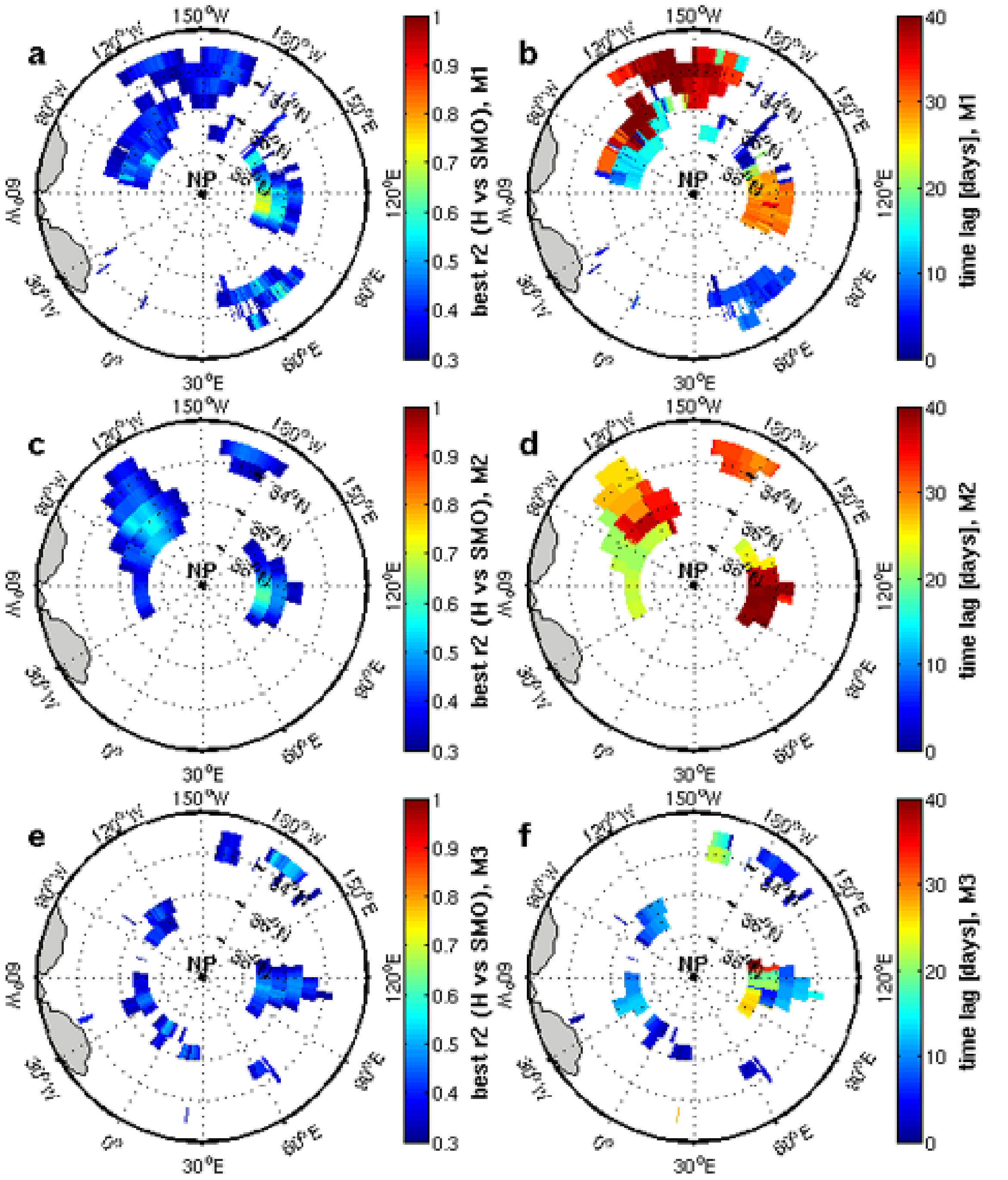

Figure 5.14: Results for the sensible heat flux. Bilateral regression results on the relationship between the H anomaly and the corresponding SMO anomaly (same location, same year). The flux anomaly is averaged over various pre-melt periods (1-40 days). Three methods M1, M2 and M3 are compared. Left-hand plots illustrate the best r^2 with thee methods. Only results with $r^2 > 0.31$ ($p < 0.01$) are shown. Right-hand plots reflect the corresponding time-averaging period.

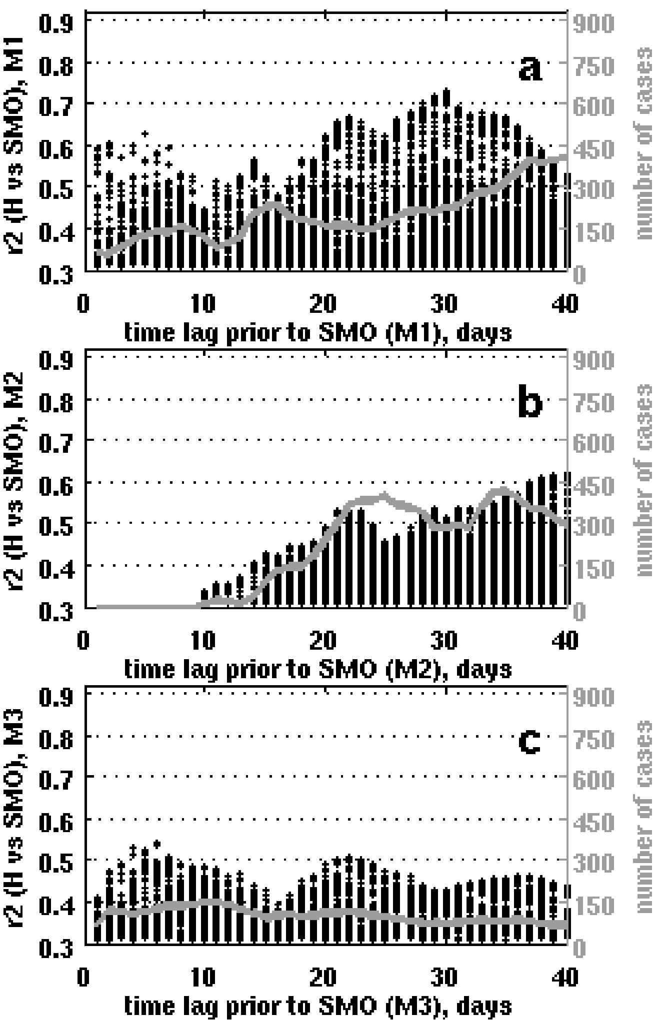

Figure 5.15: Sensible heat flux: dependence of the squared correlation (r^2) on the length of the premelt period. The black dots show all significant r^2 values ($p < 0.01$) for each flux-averaging period. This indicates the largest r^2 at each time lag (independent of the location). The grey curve shows the number of ERAI grid locations where a significant r^2 was found with the given flux-averaging period. It indicates which time averaging period is the most successful in explaining interannual SMO variance (within the study region). Three methods M1 (a), M2 (b) and M3 (c) are compared.

Bilateral regression analysis was also applied to a composite of all maritime grid locations where at least one significant r^2 (with any time averaging period) had been established for H. Accordingly, the local H anomalies prior to the exact SMO (M1) regrouped within the shaded area in **Fig 5.14 a-b** explained 25% of the spatial and interannual variance in SMO (**Table 1**, page 98). For comparison, the local H anomalies prior to the 20-year average SMO (M2) and the 20-year earliest SMO (M3) explained 32% and 21% of the spatial and interannual variance in SMO, respectively (**Table 1**).

Downward Flux and Downward Radiation

In this study the downward radiation (DR) is defined as a sum of the downward radiative fluxes LWd and SWd. Both LWd and SWd affect the local surface heat balance, but are not directly influenced by local feedbacks, such as changes in albedo and surface temperature. The downward flux (DF) is the sum of DR, H and LE. Compared to DR, DF is more sensitive to surface properties (SIC and albedo) and small-scale processes (wind and near-surface thermal stratification). Nevertheless, over the sea ice the climatology of DR and DF is very similar (**Fig 5.16**).

Within the circumpolar central Arctic the DR and DF are very large in the pre-melt period, with the daily means ranging within 300-600 W/m^2, and the 40-day average climatology of 400-550 W/m^2 (**Fig 5.16**).

The effect of DF and DR anomalies on the interannual variability in SMO was weak, see **Fig 5.17 - 5.19**. Although the anomalies locally explained up to 50% of the interannual variance in SMO (**Fig 5.20**), a significant r^2 was found only for less than 2% of the circumpolar Arctic.

Few results with relatively weak causal effect of DR and DF on SMO might be interpreted as followed. In the pre-melt period (April - June) SWd and LWd radiative fluxes are the dominant heat sources for the snow surface, both with the daily values of 100-300 W/m^2 depending on the cloud cover. In this period, during overcast days the additional LWd flux (positive LWd anomaly) overlaps the simultaneous reduction in SWd (negative anomaly in SWd). In contrast, during the clear-sky events the increasing SWd heat input (positive anomaly in SWd) coincides with the smaller LWd flux (negative LWd anomaly). Thus in both cases, under overcast and clear skies, the resulting sum of SWd and LWd anomalies is roughly suppressed, suggesting relatively weak day-to-day changes in DR and DF, of about $\pm$50 W/m^2 (one standard deviation of the daily flux values during 20 years and a 40-day pre-melt period). However, the magnitude of the anomalies does not impact the correlation strength, but the sign does. As a matter of fact the additional (and/or reduced) DR has different origin on different days/years. One day (year) the anomalously large DR is due to strong LWd, and another day (year) it is due to anomalously intense SWd flux. Indeed anomalously large LWd and SWd by 50 W/m^2 have unequal contribution to the net flux accumulation within the dry snowpack. And with the surface albedo of 0.77, as prescribed in ERAI [*Screen and Simmonds*, 2011a], the anomalous large DR (DF) by 25-50 W/m^2 due to SWd has a much smaller effect on surface heating, rather than if positive DR (DF) anomaly was due to intense LWd. To summarize, DF and DR are probably not appropriate fluxes for explaining the regional and interannual differences in SMO timing.

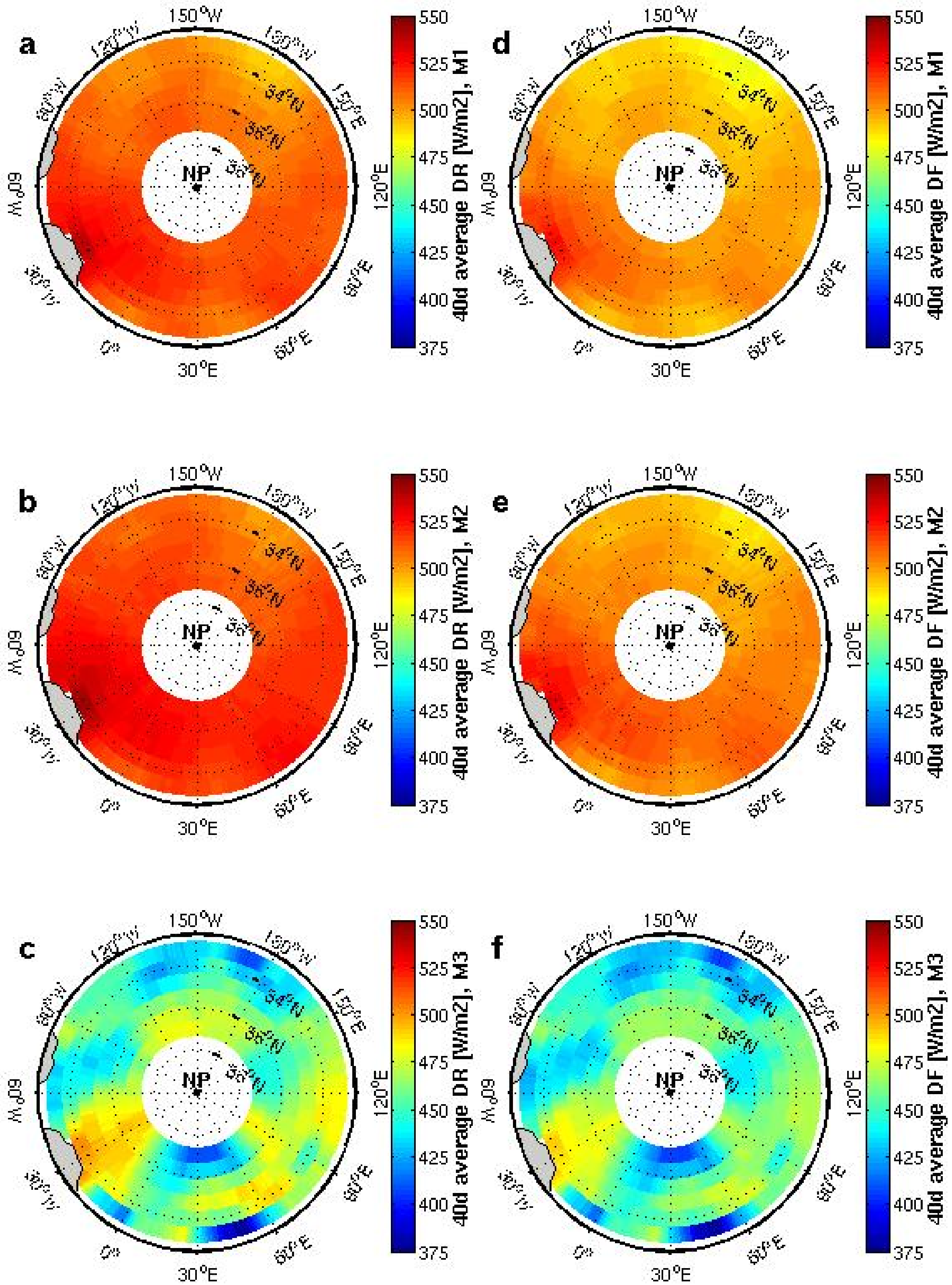

Figure 5.16: 20-year average DR (left-hand maps) and DF (right-hand maps) in the 40-day pre-melt period (prior to SMO) as defined with: method M1 (upper two maps), method M2 (two maps in the middle), and method M3 (lower two maps).

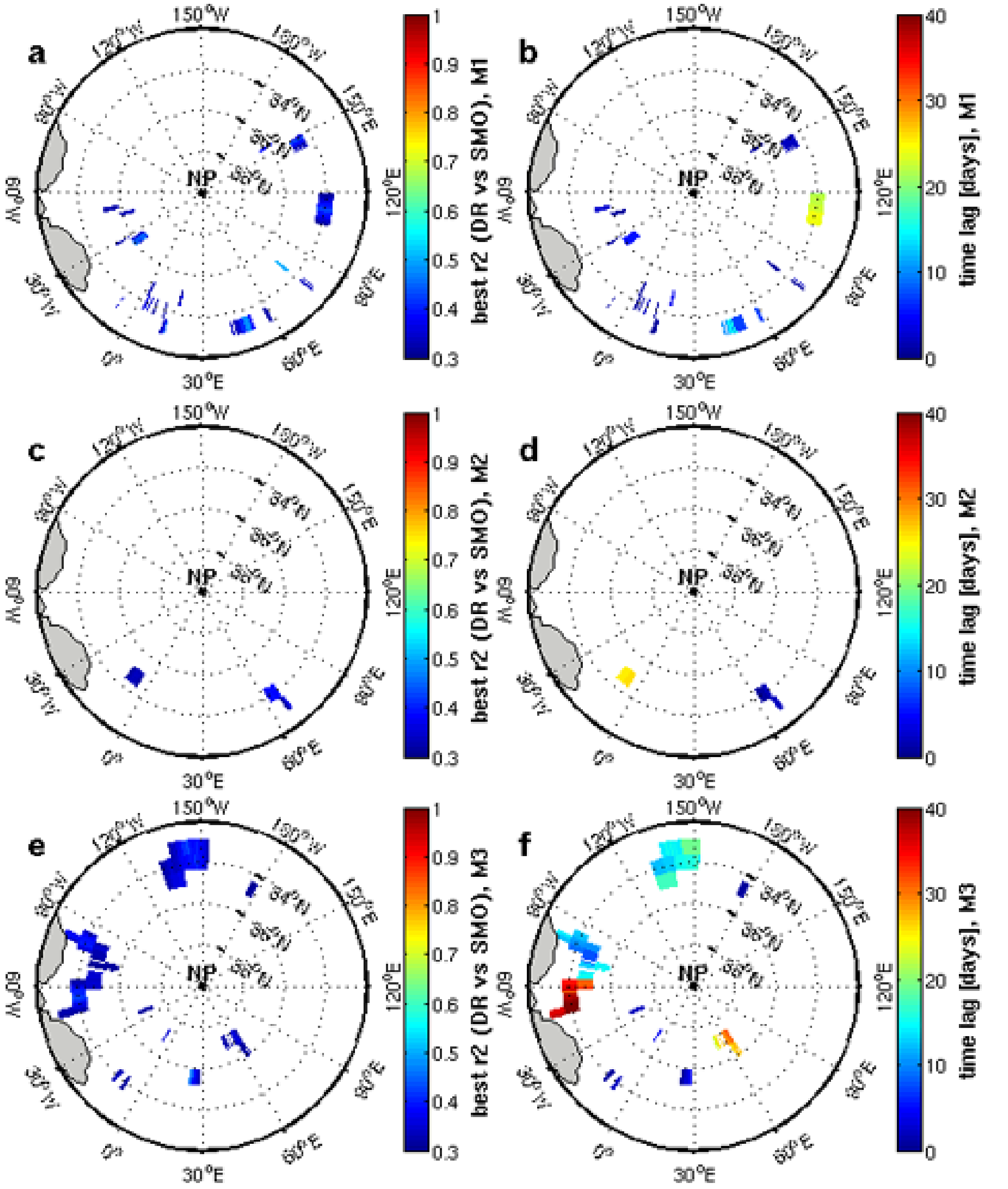

Figure 5.17: Results for the Downawrd Radiation. Bilateral regression results on the relationship between the DR anomaly and the corresponding SMO anomaly (same location, same year). The flux anomaly is averaged over various pre-melt periods (1-40 days). Three methods M1, M2 and M3 are compared. Left-hand plots illustrate the best r^2 with thee methods. Only results with $r^2 > 0.31$ ($p < 0.01$) are shown. Right-hand plots reflect the corresponding time-averaging period.

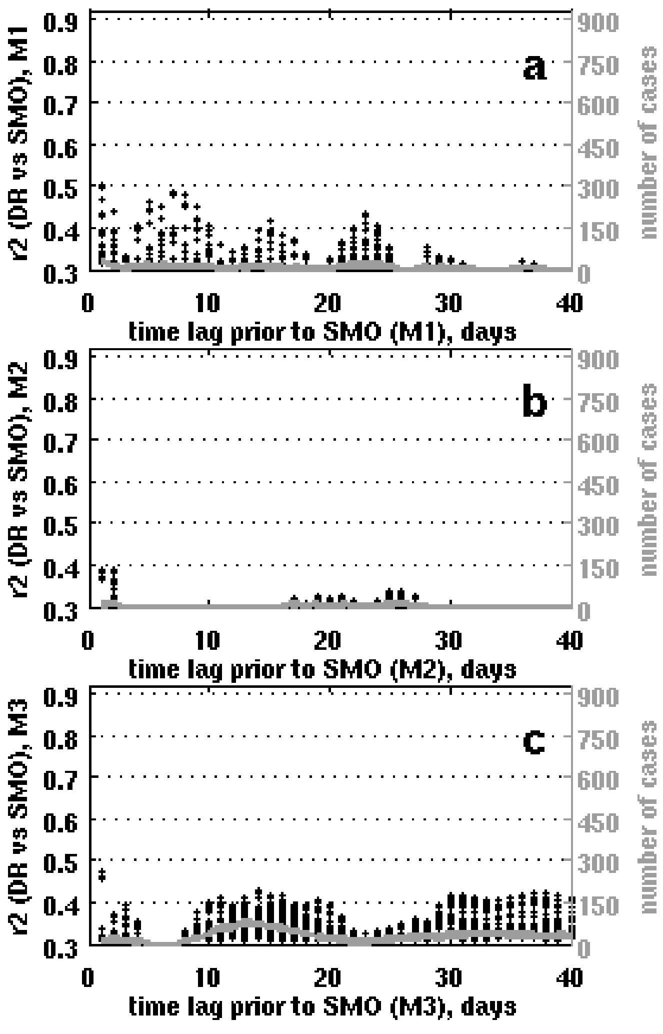

Figure 5.18: Downward Radiation: dependence of the squared correlation (r^2) on the length of the pre-melt period. The black dots show all significant r^2 values ($p < 0.01$) for each flux-averaging period. This indicates the largest r^2 at each time lag (independent of the location). The grey curve shows the number of ERAI grid locations where a significant r^2 was found with the given flux-averaging period. It indicates which time averaging period is the most successful in explaining interannual SMO variance (within the study region). Three methods M1 (a), M2 (b)and M3 (c) are compared.

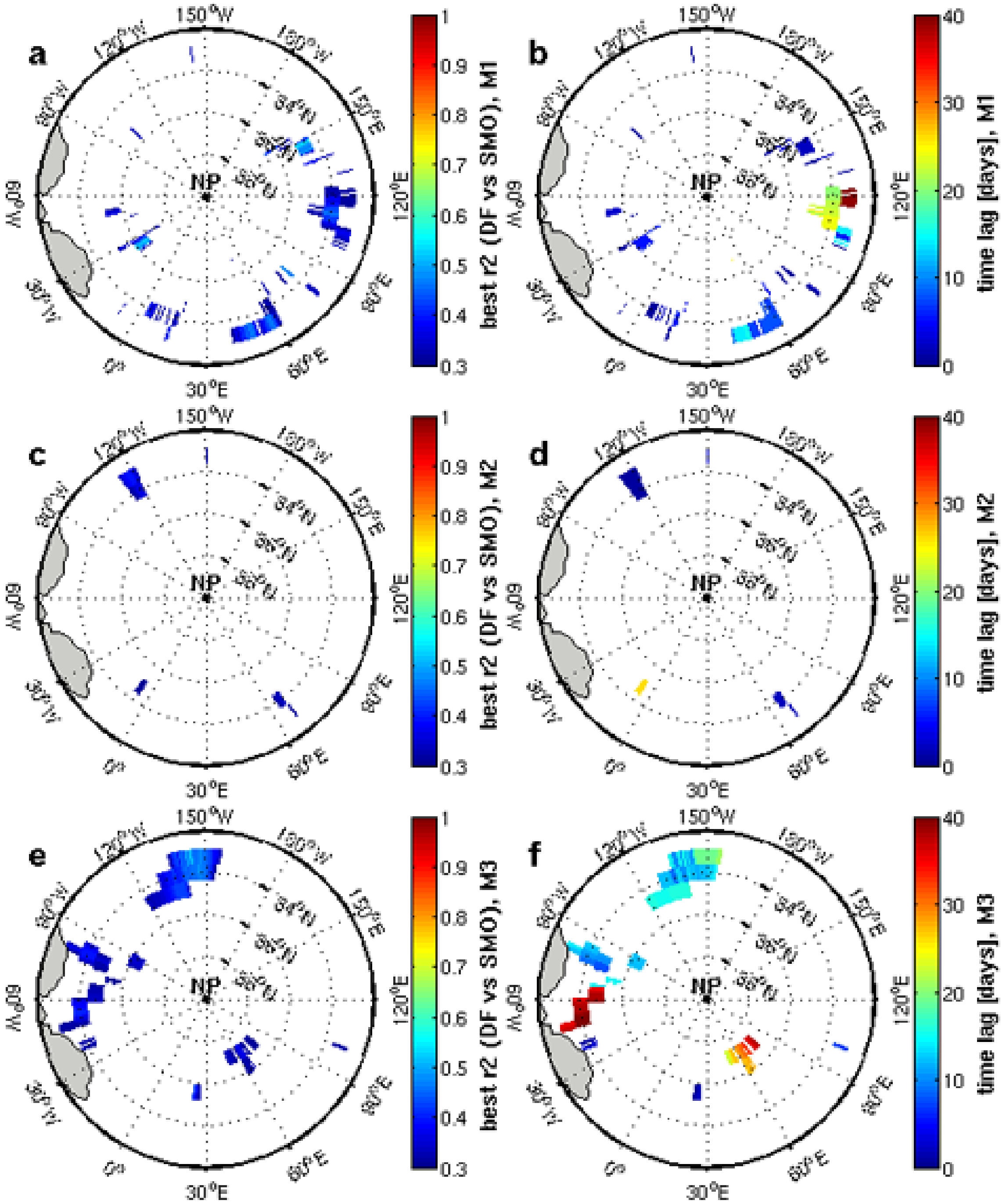

Figure 5.19: Results for the Downward Flux. Bilateral regression results on the relationship between the DF anomaly and the corresponding SMO anomaly (same location, same year). The flux anomaly is averaged over various pre-melt periods (1-40 days). Three methods M1, M2 and M3 are compared. Left-hand plots illustrate the best r^2 with thee methods. Only results with $r^2 > 0.31$ ($p < 0.01$) are shown. Right-hand plots reflect the corresponding time-averaging period.

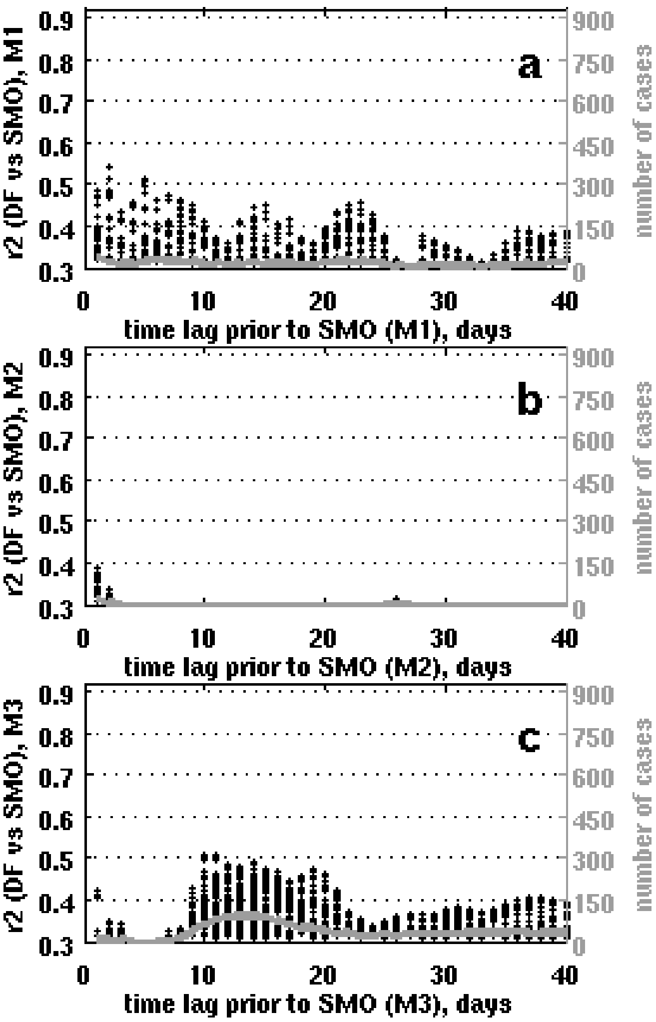

Figure 5.20: Downward Flux: dependence of the squared correlation (r^2) on the length of the premelt period. The black dots show all significant r^2 values ($p < 0.01$) for each flux-averaging period. This indicates the largest r^2 at each time lag (independent of the location). The grey curve shows the number of ERAI grid locations where a significant r^2 was found with the given flux-averaging period. It indicates which time averaging period is the most successful in explaining interannual SMO variance (within the study region). Three methods M1 (a), M2 (b) and M3 (c) are compared.

Net flux

To remind, the net surface flux (NF) is defined as the sum of the net radiative fluxes (SWnet and LWnet) and turbulent heat fluxes (LE and H). Positive NF holds for the heat accumulation and warming within the snowpack and/or sea ice. Since the initial springtime snow-ice temperatures are about -10-30^{o}C (in April) there is always some lag between the instance (day) when NF accumulation starts and the snow melt onset.

Within the circumpolar central Arctic the 20-year average NF is positive in the 40-day pre-melt period: about 10-20 W/m^2 if defining the pre-melt phase with methods M1 and M2 (**Fig 5.21 a-b**). Since the pre-melt period is shifted earlier in the year with method M3 (compared to M1 and M2), the corresponding NF climatology is closer to the wintertime NF values. 20-year average NF is within $\pm$5 W/m^2 in late April-May period (**Fig 5.21 c**), with the typical daily NF values within -30 - (+10) W/m^2.

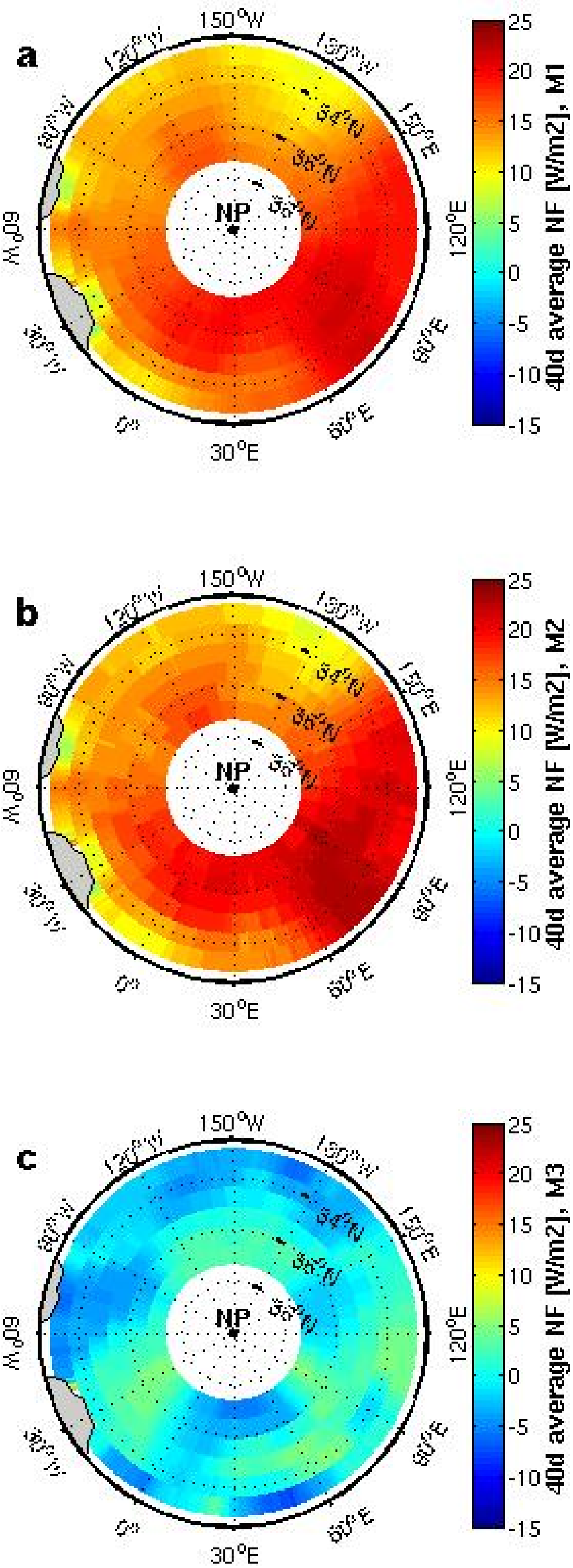

Figure 5.21: 20-year average NF in the 40-day pre-melt period (prior to SMO) as defined with: (a) method M1, (b) method M2, and (c) method M3.

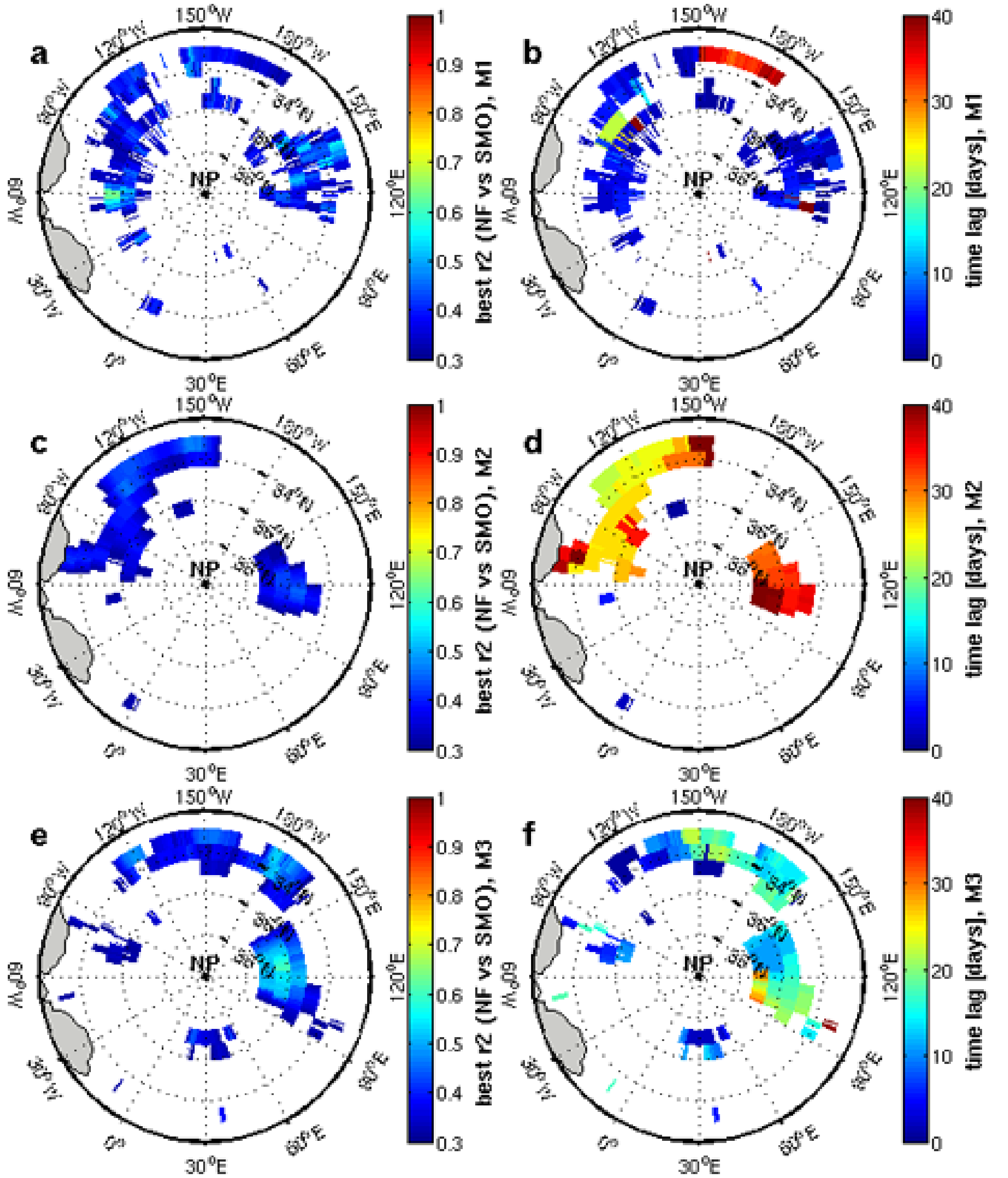

Figure 5.22: Bilateral regression results on the relationship between the NF anomaly and the corresponding SMO anomaly (same location, same year). The flux anomaly is averaged over various pre-melt periods (1-40 days). Three methods M1, M2 and M3 are compared. Left-hand plots illustrate the best r^2 with thee methods. Only results with $r^2 > 0.31$ ($p < 0.01$) are shown. Right-hand plots reflect the corresponding time-averaging period.

Fig 5.22 reflects the performance of three alternative methods M1, M2 and M3 within the circumpolar central Arctic. All three methods evoke a causal effect of the time average NF anomaly on SMO timing (**Fig 5.22** left-hand maps): with a positive NF anomaly corresponding to early SMO, and vice versa. Significant r^2 was found within the area of 413 x 10^3 km^2 with M1 (shaded area in **Fig 5.22 a-b**), 344 x 10^3 km^2 with M2 (shaded area in **Fig 5.22 c-d**), and 387 x 10^3 km^2 with M3 (shaded area in **Fig 5.22 e-f**), or 25% (M1), 20% (M2) and 23% (M3) of the circumpolar central Arctic area.

With M1 the synoptic scale (1-7 days) NF anomalies explained up to 65% of the local interannual SMO variance (**Fig 5.23a**), whereas with M2 and M3 a 10-40 day NF anomalies explained interannual SMO variance best, up to 60% (**Fig 5.23 b-c**).

Accordingly, a 1-7 day average negative (positive) NF anomaly of -19±8 W/m^2 (+19±9 W/m^2) contributed to the anomalously late (early) SMO by 15-20 days (grid locations within the shaded area in **Fig 5.22 a-b**). With M2 a 20-40 day average negative/positive NF anomaly of -3±9 W/m^2 (+6±5 W/m^2) contributed to the anomalously late (early) SMO by 15-20 days (grid locations within the shaded area in **Fig 5.22 c-d**). With M3 a 10-20 day average negative (positive) NF anomaly of -7±3 W/m^2 (+12±12 W/m^2) contributed to the anomalously late (early) SMO by 15-20 days (grid locations within the shaded area in **Fig 5.22 e-f**).

To summarize, over most of the circumpolar central Arctic methods M2 and M3 failed to detect the effect of brief 1-7 day average NF anomalies on interannual SMO variability, whereas M1 found a significant correlation between SMO and NF over the area of 355 x 10^3 km^2 (21% of the circumpolar central Arctic). Instead M2 and M3 were better in detecting the areas where SMO correlated with the seasonal NF anomaly (over the preceding 20-40 days): 330 x 10^3 km^2 for M2, 210 x 10^3 km^2 for M3, and only 100 x 10^3 km^2 for M1.

Bilateral linear regression analysis was applied to the composite of all maritime grid locations within the shaded area in **Fig 5.22a**, with the flux anomalies calculated according to the method M1. Comparison of different time averaging period (1-40 days) suggests that the best time averaging period is about 4 days, explaining 28% of the total (spatial and interannual) variance in SMO (**Table 1**, page 98). Same exercise with M2 and M3 resulted in 33% and 26% of explained SMO variance, with the best time averaging period of 32 and 18 days respectively (**Table 1**, page 98). Considering this result, the remaining 70% of unexplained variance was partly explained by the other time averaging periods. Thus, each of the time averaging periods between 15-40 days suggests that NF anomalies account for about 20-24% of SMO variance. And NF anomalies averaged over time lags between 1 and 15 days explain about 5-20% of SMO variance (p>0.01). Depending on the time lag, RMSE varies between 7.4 and 8.3 days. Indeed a large portion of SMO variance is not explained by NF. This is related to (a) our simplified methodology with a "fixed" duration of the pre-melt period each year and all locations, and (b) to inaccuracies in MO, SMO sample and NF. The latter are originating from errors in the individual fluxes and the neglect of the conductive heat flux.

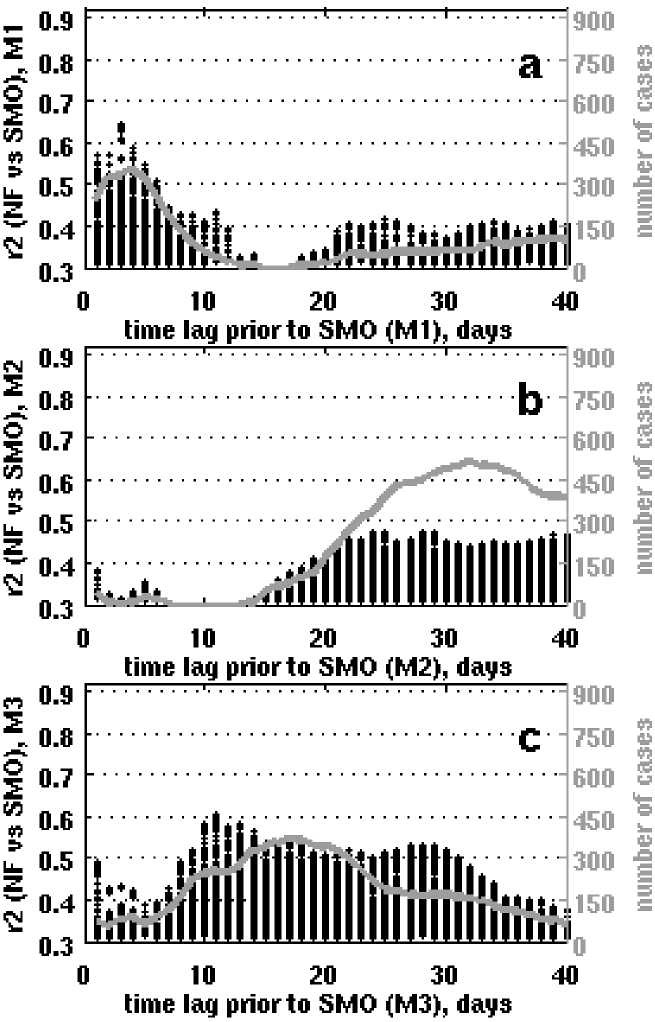

Figure 5.23: Net flux: dependence of the squared correlation (r^2) on the length of the pre-melt period. The black dots show all significant r^2 values ($p < 0.01$) for each flux-averaging period. This indicates the largest r^2 at each time lag (independent of the location). The grey curve shows the number of ERAI grid locations where a significant r^2 was found with the given flux-averaging period. It indicates which time averaging period is the most successful in explaining interannual SMO variance (within the study region). Three methods M1 (a), M2 (b) and M3 (c) are compared.

5.1.3 Stepwise multi-linear regression results: Snow Melt Onset versus surface heat fluxes

Stepwise forward multiple linear regression analysis was applied to find those combinations of surface fluxes that best explain interannual variance in SMO. Four individual fluxes (predictors) were taken into account: LWd, SWd, LE and H. These 4 fluxes and various combinations of them are the direct factors controlling SMO. Only those multi-linear regression results were accepted, where the following conditions met: (1) there were complete 20-year records of fluxes and SMO, and (2) the resulting regression was significant at 99% ($p < 0.01$).

Results obtained with method M1 are illustrated in **Fig 5.24**. Accordingly, a combination of 2-4 fluxes explained locally from 31 to 92% of the local interannual SMO variance within roughly a half (46% of the circumpolar central Arctic area (**Fig 5.24a**), with a root mean square error (RMSE) about 6-7 days (not shown). In the western central Arctic, within the area where 3-7 day average flux anomalies (**Fig 5.24b**) explained up to 80-90% of SMO variance (**Fig 5.24a**), at least 3 fluxes (**Fig 5.24 c-f**) appeared in the multi-linear regression equation, with LWd the dominating term (**Fig 5.24c**). Within another sector also in the western Arctic, were a 40-day time averaging period appeared to be the most relevant for local interannual SMO "prediction" (**Fig 5.24b**): LE and H were either the only or most important terms included in the best multi-linear regression equation (**Fig 5.24 e-f**). Although SWd by itself did not correlate with SMO, the inclusion of SWd term into the multi-linear regression equation improved the explained variance of SMO over most of the central circumpolar Arctic (**Fig 5.24d**).

Stepwise multi-linear regression analysis was also applied to the composite of all maritime grid locations (2862 in total) within the circumpolar central Arctic. The time average anomalies of 4 fluxes (all with the same time averaging period) were regrouped in 4 time series of 2862 values each. At the end, these 4 large time series of LWd, SWd, LE and H fluxes were regressed against the corresponding SMO anomalies (on the same year, at the same location). The aim of this exercise was to test whether there is some best length of the time averaging period when NF anomalies best explain (reflect) spatial and interannual SMO features. Calculated with method M1, the combination of 5-day average LWd, SWd, LE and H anomalies best explained (18% the total SMO variance, with the standard error of about one week (**Table 1**, page 98).

Fig 5.25 demonstrates how well the best multi-linear regression equation with the 5-day average heat flux anomalies (**Table 1**, method **M1**, page 98) reconstructs the local SMO features in three years: 1990, 2003 and 2007. Year 2003 is illustrated as a typical year with SMO close to the 20-year average (**Fig 5.25 c-d**). Year 2007 is taken for comparison as the most famous for its unique sea ice conditions (**Fig 5.25 e-f**). SMO in 1990 is shown in contrast to SMO pattern observed in 2007, with essentially opposite regional pattern of SMO anomalies (**Fig 5.25 a-b**). General comparison of 20 years suggested that this best combination of 2-4 fluxes (multi-linear regression equation in **Table 1**, page 98) well captured the general behaviour of SMO, but cannot explain SMO anomalies larger than 15 days.

Similar results for the local stepwise multi-linear regression analysis were found with methods M2 and M3 (**Fig 5.27** and **Fig 5.29**, **Table 1**, page 98). Significant r^2 were found within the area of 502 x 10^3 km^2 with M2 (**Fig 5.27 a-b**) and 400 x 10^3 km^2 with M3 (**Fig 5.29 a-b**), that represent respectively 30% and 24% of the circumpolar central Arctic area. As for method M1, the LWd term was the dominant the combination of several individual fluxes with M2 (**Fig 5.27c**). Analogously, in the area where the combination of fluxes explained 80% of interannual SMO variance (marked with orange in **Fig 5.27a**), LWd term was the first included in the multi-linear regression equation (**Fig 5.27c**), with the best time averaging period of 15-20 days. In line with M1, in those areas where 30-40 days averaging period suggested the best results with M2 (marked in red in **Fig 5.27b**), LE and H were either the only or most important terms included in the best multi-linear regression equation (**Fig 5.27 e-f**).

5.1.4 Comparison of the bilateral versus multi-linear regression results

Fig 5.26 compares the best results obtained with the bilateral and multi-linear regression analysis, method M1. Over most of the central Arctic, a combination of fluxes explained SMO better than any of the individual fluxes (**Fig 5.26c**) or their sum. LWd largely dominated over the other fluxes within the Pacific and Atlantic sectors of the central Arctic (**Fig 5.26c**). Surprisingly the best time averaging period within the Atlantic sector was rather constant, approximately 25 days (not shown). On the Pacific side the best time averaging period was more variable: with two peaks at 4-7 days and 20-27 days. These interesting features are a subject of our planned continuation study.

Comparison between the bilateral and multi-linear regression analysis results for methods **M2** and **M3** is illustrated in **Fig 5.28** and **5.30** respectively. Same conclusions as for M1 hold for M2 and M3.

Fig 5.31 demonstrates the **overall comparison of three methods (M1, M2 and M3), all time averaging periods, all heat fluxes** (SWd, SWnet, LWd, LWnet, LE, H, DR, DF and NF) and different combinations of 4 fluxes (multi-linear regression with SWd, LWd, LE and H terms). This figure illustrates the main result of the study. Causal effect of surface heat flux anomalies on the interannual local variance in SMO (significant r^2) was found within the area of 1.41 x 10^6 km^2, representing 83.5% of the circumpolar central Arctic. We found that combination of 2-4 fluxes (multi-linear regression of LWd, SWd, LE and H) explains local SMO variance better than any individual flux or their sum (NF, DR and DF), **Fig 5.31c**. This must be due to a different accuracy of the individual fluxes. However, if all fluxes were equally accurate in ERAI, NF should correlate with SMO better than any of its components or any combination of some of its components. Abbreviation "F" in **Fig 5.31c** refers to SWnet, LWnet, DF, DR or NF. All three methods (M1, M2 and M3) revealed significant r^2, with none of the methods being explicitly better than the others, but complementing one another (**Fig 5.31e**). Duration and timing of the pre-melt period depended on the heat flux considered (**Fig 5.31b**). NF, LWd and LWnet correlated best when averaged over the synoptic scales (1-7 days), and the other fluxes explained SMO better when considered over longer 20-40 day pre-melt period. The standard error (RMSE) of the linear bilateral and multi-linear regression approximation was found to be quite uniform with the study region: ±4-8 day error in the "predicted" SMO timing (**Fig 5.31d**).

In those grid locations where no significant r^2 was detected with neither method, heat flux component and time averaging period the additional examination is yet to be done. The possible solution could be the calculation of bilateral and multi-linear regressions with variable time averaging periods for different years, different locations and different fluxes. Such an adoptive/mild methodology likely will increase the explained variance in SMO, however the interpretation of the results at 2862 grid locations within the area of 1.7 mln km^2 will require a more advanced technique. More close examination of SSM/I sea ice concentrations (SIC) within 83-87^{o}N could be another possible solution. Thus, for example, there certainly exist some errors in ERAI heat fluxes due to sea ice errors. To note that ERAI SIC is set to 100% within 83-90^{o}N [ECMWF IFS Part II, 2008]. Localization of errors in ERAI SIC values (both in time and in space), and extermination of obviously erroneous heat fluxes from the analysis (as we demonstrated in this Section) might also increase the explained variance in SMO.

For curiosity we calculated the smallest in SSM/I SIC (25 km pixels) in the vicinity of each ERAI grid location during the pre-melt period. In this manner we can localize the areas where SIC was changing a lot (already in the pre-melt period) in reality, but not in ERAI. Obviously in the areas of large SIC reduction there should be some difference in surface heat fluxes between the reality and ERAI. To determine the pre-melt period we took SMO date for each year and at each grid location. Then in the vicinity of each grid location we found the daily SIC values (SSM/I) during a 41-day pre-melt period (including the SMO day itself). SSM/I SIC values were considered within a 50 km radius (first guess). 50 km distance is comparable to the half distance between two latitude circles (84/2 = 42 km). As a result, at grid location we get at least 16 SSM/I pixels for each day, and we examine 41 days in total. 16 x 41 = 656 SIC values for each year at each ERAI grid location. The smallest of these 656 SIC values gives an idea about SIC reduction in the vicinity of each ERAI grid location. **Fig 5.32** demonstrates the smallest 25 km SSM/I SIC in the vicinity of each ERAI grid location during the pre-melt period and in any year. To note, these SIC reductions occurred in different years at different locations. This is just an example, but more extensive additional analysis is needed to evaluate how/where/when errors in ERAI SIC affected the surface heat fluxes.

Table 1. Linear relationships between the surface heat flux anomaly (prior to SMO, **methods M1, M2, M3**) and SMO anomaly within the circumpolar Arctic (significant with $p < 0.01$). The stepwise multi-linear regression equation for the entire circumpolar central Arctic (83.25-87°N) ranks the contribution of fluxes in the equation.

Linear regression equation	**Time averaging period [days]**	r^2	**RMSE [days]**	**Area where the equation is valid**	**Method**
SMO = - 0.38 × NF + 0.03	4	0.28	7.5	Shaded area in **Fig. 5.22 a-b**	M1
SMO = - 0.85 × NF – 0.3	32	0.33	7.2	Shaded area in **Fig. 5.22 c-d**	M2
SMO = - 1.15 × NF – 0.86	18	0.26	7.5	Shaded area in **Fig. 5.22 e-f**	M3
SMO = - 0.35 × LWd + 0.96	6	0.27	7.3	Shaded area in **Fig. 5.5 a-b**	M1
SMO = - 0.57 × LWd + 0.43	21	0.36	6.8	Shaded area in **Fig. 5.5 c-d**	M2
SMO = - 0.31 × LWd + 0.3	13	0.23	7.5	Shaded area in **Fig. 5.5 e-f**	M3
SMO = - 2.58 × LE – 1.38	40	0.31	7.3	Shaded area in **Fig 5.11 a-b**	M1
SMO = - 1.65 × LE – 1.02	27	0.29	7.4	Shaded area in **Fig 5.11 c-d**	M2
SMO = - 0.87 × LE – 0.96	5	0.22	7.6	Shaded area in **Fig 5.11 e-f**	M3
SMO = - 4 × H – 0.68	37	0.25	7.5	Shaded area in **Fig. 5.14 a-b**	M1
SMO = - 4.96 × H – 0.58	35	0.32	7.2	Shaded area in **Fig. 5.14 c-d**	M2
SMO = - 2.23 × H – 0.58	9	0.21	7.3	Shaded area in **Fig. 5.14 e-f**	M3
SMO = - 0.31 × LWd – 0.08 × SWd – 0.67 × H – 0.03 × LE + 0.45	5	0.18	7.7	Entire circumpolar area within 83.25-87°N	M1
SMO = - 0.35 × LWd – 0.46 × LE – 0.46 × H + 0.01 × SWd - 0.05	31	0.23	7.5		M2
SMO = - 0.29 × LWd – 0.09 × SWd – 0.43 × LE – 0.17 × H – 0.1	15	0.15	7.9		M3

5.1.5 Discussion

The first general comment refers to the distinction between two sea ice types in the MO algorithm (SSM/I). Our results demonstrated that the combination of LWd, SWd, LE and H anomalies (with the stepwise multi-linear regression) well captured the spatial and interannual differences in SMO. Large SMO anomalies (of 15-35 days) were, however poorly explained by surface heat fluxes. This is certainly related to errors in fluxes (ERAI) and possibly also to the distinction of two sea ice types in the MO algorithm (SSM/I). The algorithm for MO detection applied by *Markus et al.* [2009] is different for the multi-year and first-year ice. We suspect that differences between ice types, most likely contributed to the interannual and spatial variations in SMO. Recently a similar guess but in another formulation was suggested in the study by *Anderson et al.* [2011]. Its authors suspect that the snowpack differences between the FYI and MYI contribute to SMO timing difference between FYI and MYI: with thicker snow on MYI retarding SMO and albedo changes. However observations show that this last argument can be merely justified (discussed in Section 1.4). Further studies (with another methodology) are needed to find out how well surface fluxes (reproduced by meteorological reanalysis) explain SMO timing on top of different ice types.

Another essential comment concerns the uncertainty in ERAI reanalysis heat fluxes. ERAI is constrained by the satellite-derived data on vertical thermal and moisture profiles, and also by the direct field and buoy observations (SAT, winds) generally deployed on the thick first-year and multi-year ice floes. Naturally, one would expect that meteorological reanalysis are likely better in representing the spatial differences in the downward radiative fluxes, air temperatures and cover fraction, compared to the upward LW, absorbed SW, LE and H fluxes over the mixed ice types and open sea areas [*Walsh and Chapman*, 1998]. Due to lack of reliable data on sea ice and snow thickness and under-ice water temperatures, the effect of the conductive flux through sea ice and snow on SMO could not be investigated. Yet, it should be noted that ERAI calculates the conductive heat flux of sea ice, resolved at four model levels. Thus in ERAI the under-ice temperature is set to the freezing point depending on (climatological) salinity and the thickness of the sea ice slab is always set to 1.5 m. In this formulation the under-ice temperature and salinity do not vary in time, and the conductive heat flux of ice in ERAI is primarily controlled by the meteorological conditions, which is not realistic. It should be noted that this conductive flux has affected the surface fluxes that we utilized in our study: LWup, LWnet, NF, and the turbulent sensible heat flux (H).

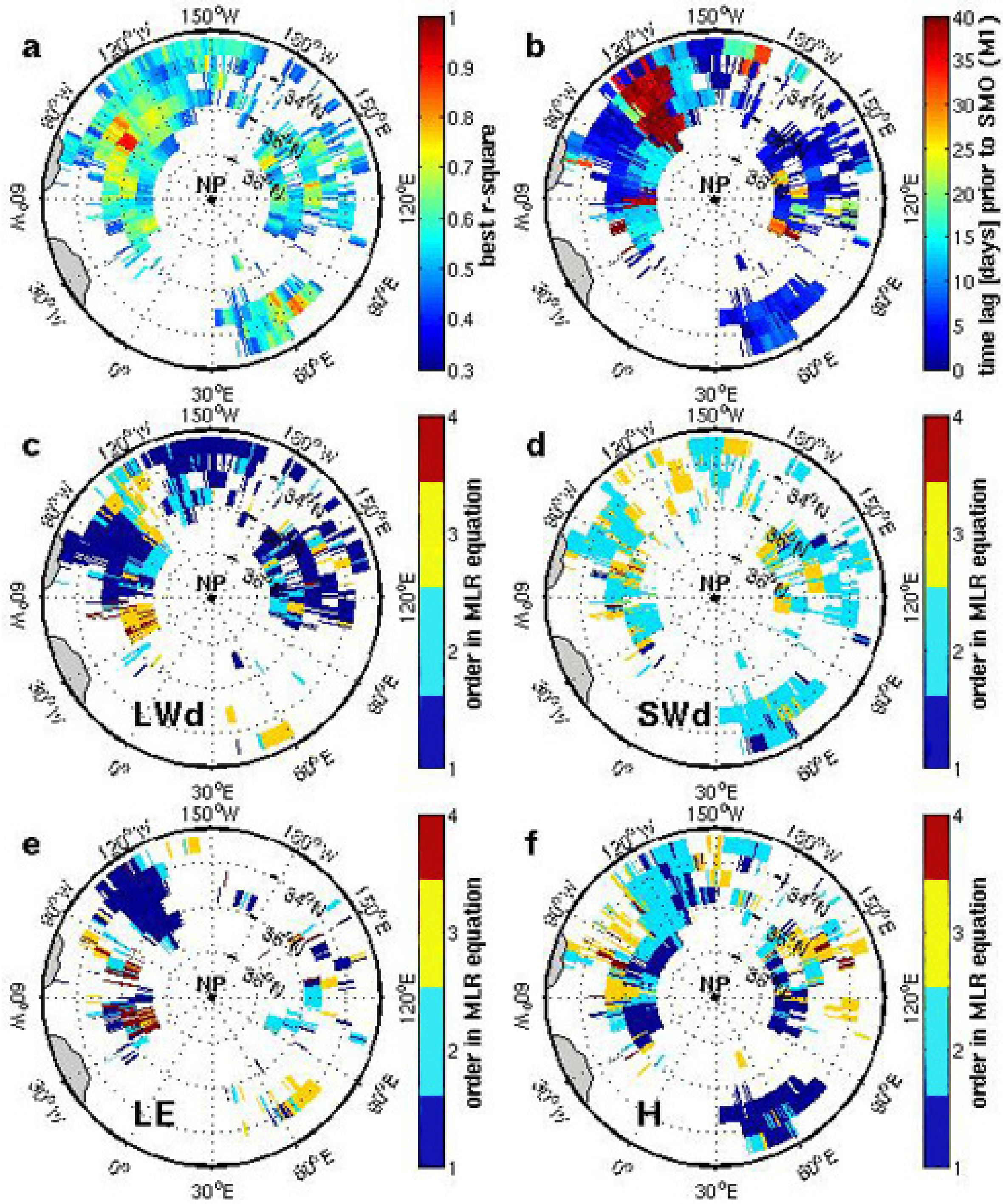

Figure 5.24: Best results for the stepwise multi-linear regression (MLR) analysis at each individual grid location (**method M1**.)

(a) Fraction of the local interannual SMO variance (r^2) explained by the best combination of four fluxes: LWd, SWd, LE and H. At each particular location r^2 value is the highest among all combinations of these four fluxes and 40 different flux-averaging periods.

(b) Flux-averaging period suggesting the best r^2 that results from any combination of individual fluxes at each grid location.

(c-f) Rank of the flux components in the best multi-linear regression equation (at each individual grid location). For example, in (c) at those locations where the color code refers to 1, LWd is the most significant flux component (with the smallest p-value) and the first included in the multi-linear regression equation.

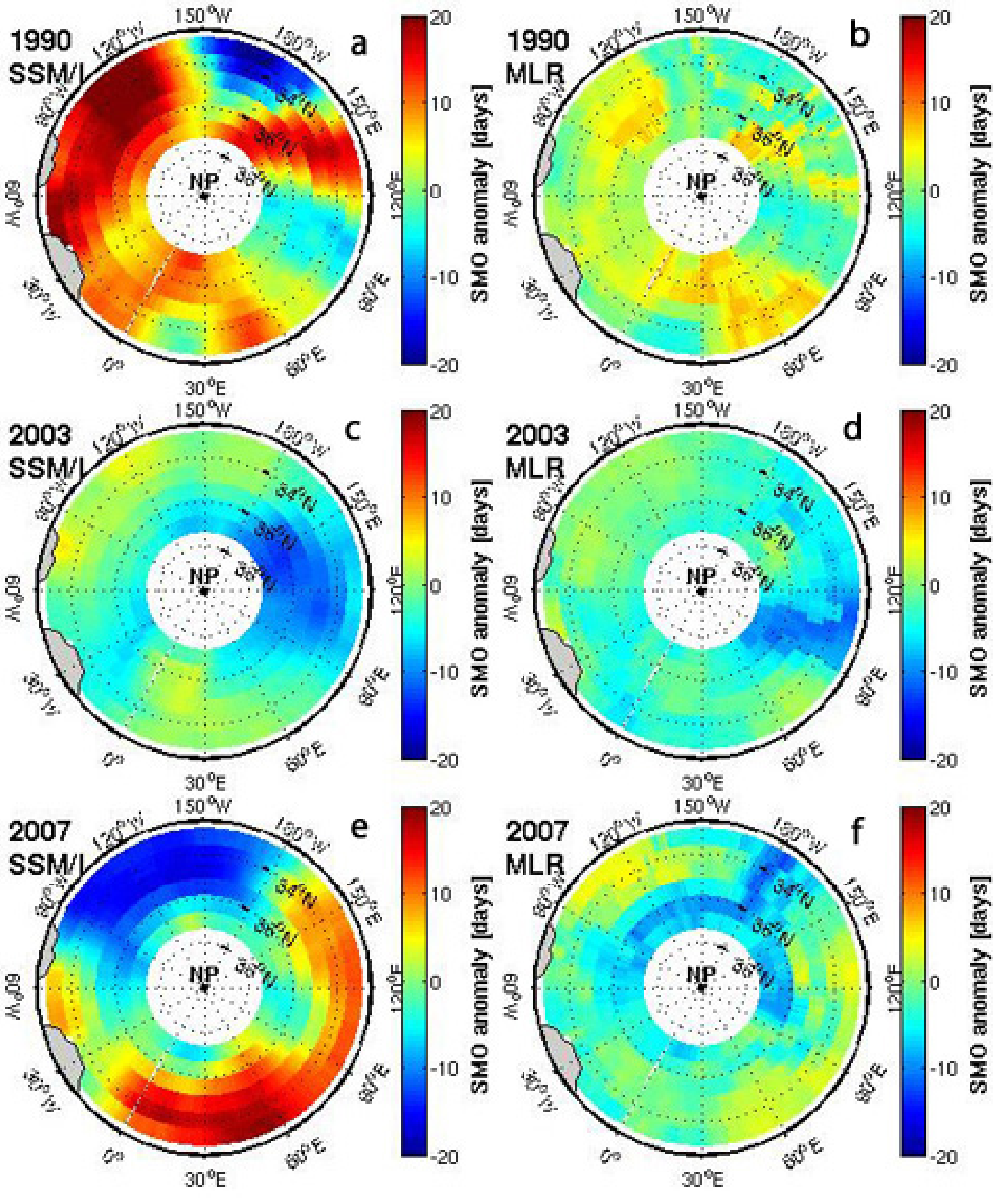

Figure 5.25: Comparison of the original SMO time series (left-hand maps) versus the reconstructed SMO time series (right-hand maps) in 1990 (a-b), 2003 (c-d) and 2007 (e-f). The multi-linear regression (MLR) equation from **Table 1** (**method M1**, page 98) and the local heat flux anomalies (5-day average) were applied to reconstruct SMO timing at each ERAI grid location.

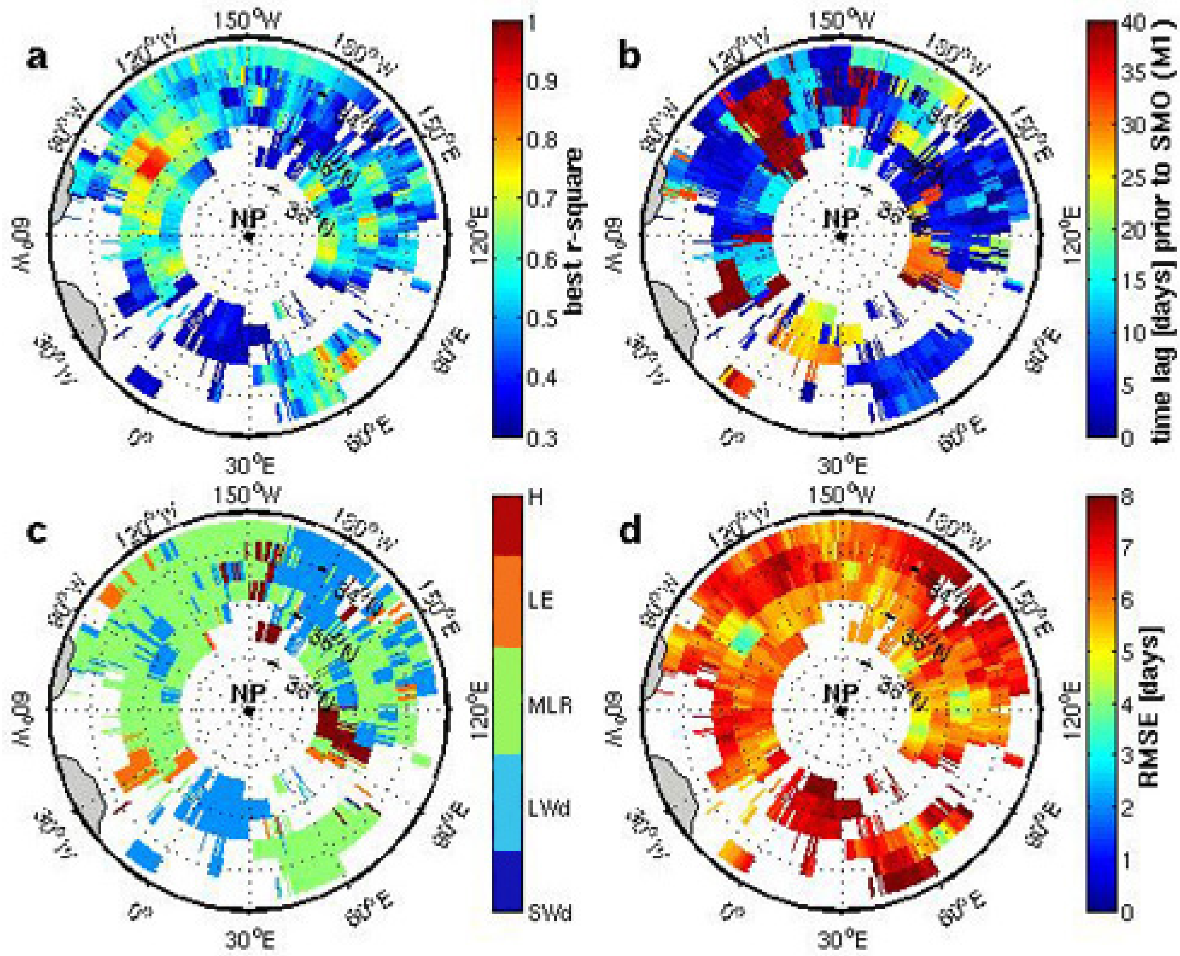

Figure 5.26: Comparison of the bilateral versus multi-linear regression results (**method M1**).

(a) Fraction of the local interannual SMO variance explained by the surface fluxes (r^2): LWd, SWd, LE, H and/or any combination of these 4 fluxes. At each particular location, this r^2 value is the highest among four individual fluxes, all combinations of these four fluxes and all flux-averaging periods.
(b) Flux-averaging period suggesting the best r^2 that results from any individual flux or combination of individual fluxes at each grid location.
(c) The factor best explaining SMO variance: individual fluxes or some combination of them, ranked by r^2. Multi-linear regression (MLR) refers to some combination of LWd, SWd, LE and H flux anomalies, suggesting the best r^2.
(d) RMSE corresponding to the best explaining factor shown in (c).

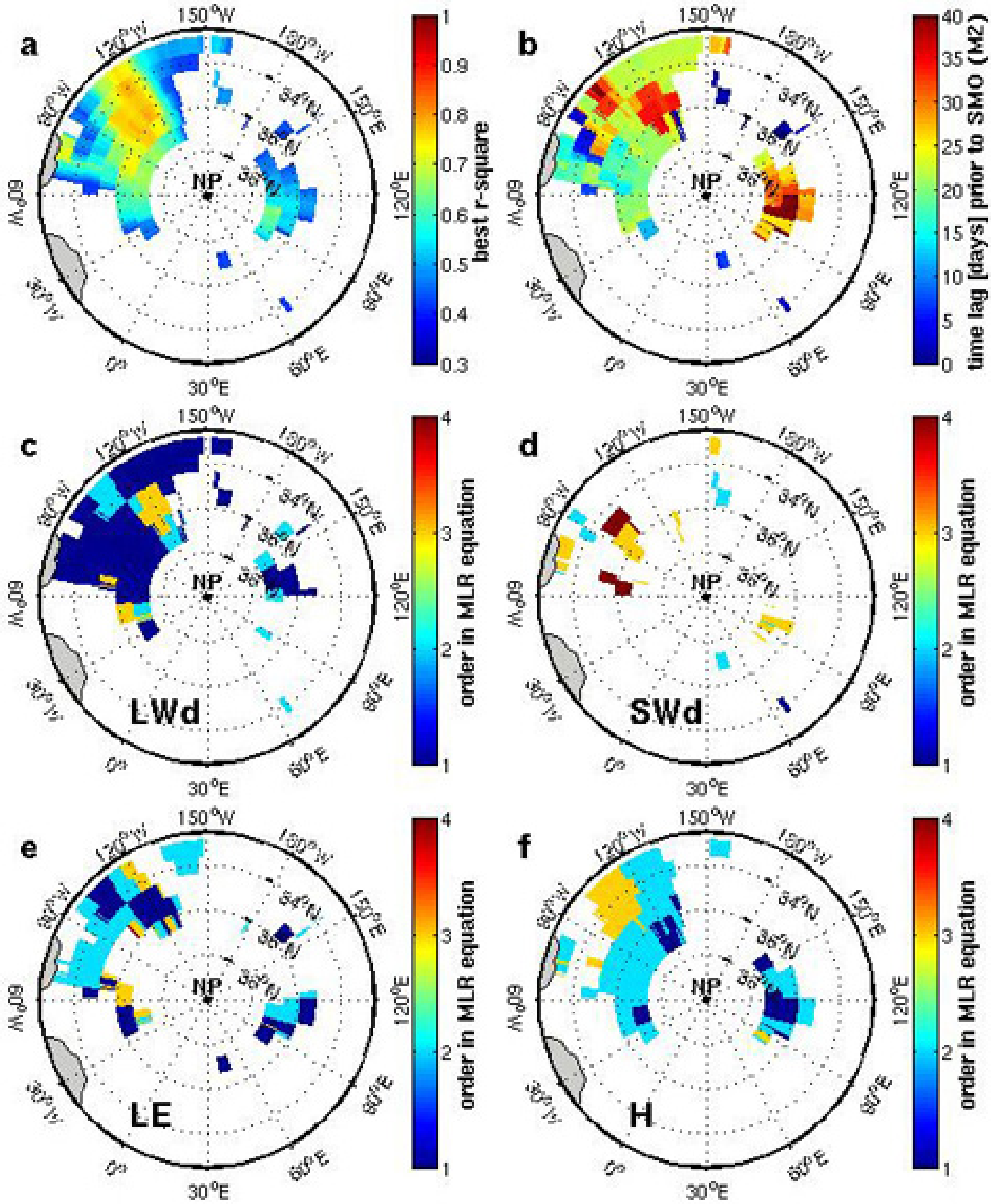

Figure 5.27: Best results for the stepwise multi-linear regression (MLR) analysis at each individual grid location (**method M2**).

(a) Fraction of the local interannual SMO variance (r^2) explained by the best combination of four fluxes: LWd, SWd, LE and H. At each particular location r^2 value is the highest among all combinations of these four fluxes and 40 different flux-averaging periods.

(b) Flux-averaging period suggesting the best r^2 that results from any combination of individual fluxes at each grid location.

(c-f) Rank of the flux components in the best multi-linear regression equation (at each individual grid location). For example, in (c) at those locations where the color code refers to 1, LWd is the most significant flux component (with the smallest p-value) and the first included in the multi-linear regression equation.

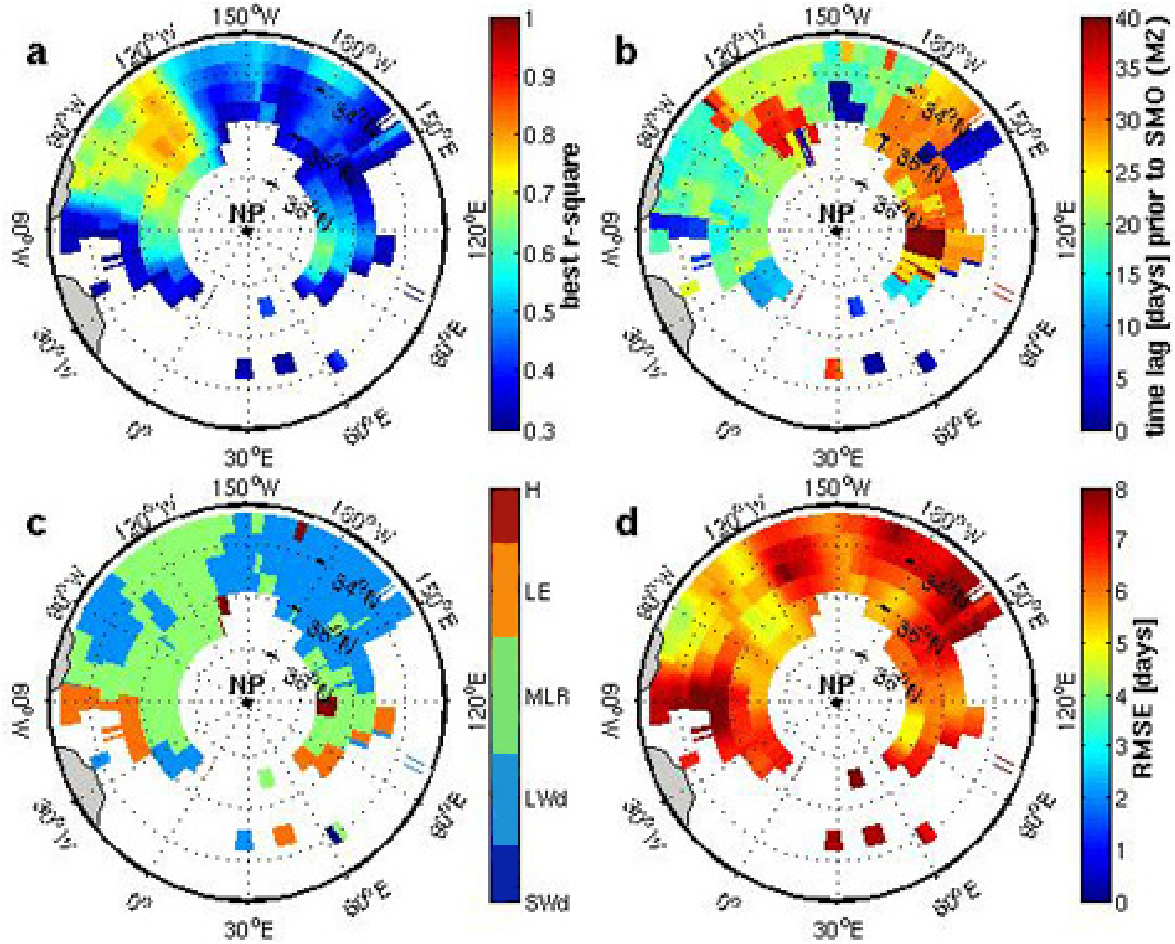

Figure 5.28: Comparison of the bilateral versus multi-linear regression results (**method M2**).

(a) Fraction of the local interannual SMO variance explained by the surface fluxes (r^2): LWd, SWd, LE, H and/or any combination of these 4 fluxes. At each particular location, this r^2 value is the highest among four individual fluxes, all combinations of these four fluxes and all flux-averaging periods.
(b) Flux-averaging period suggesting the best r^2 that results from any individual flux or combination of individual fluxes at each grid location.
(c) The factor best explaining SMO variance: individual fluxes or some combination of them, ranked by r^2. Multi-linear regression (MLR) refers to some combination of LWd, SWd, LE and H flux anomalies, suggesting the best r^2.
(d) RMSE corresponding to the best explaining factor shown in (c).

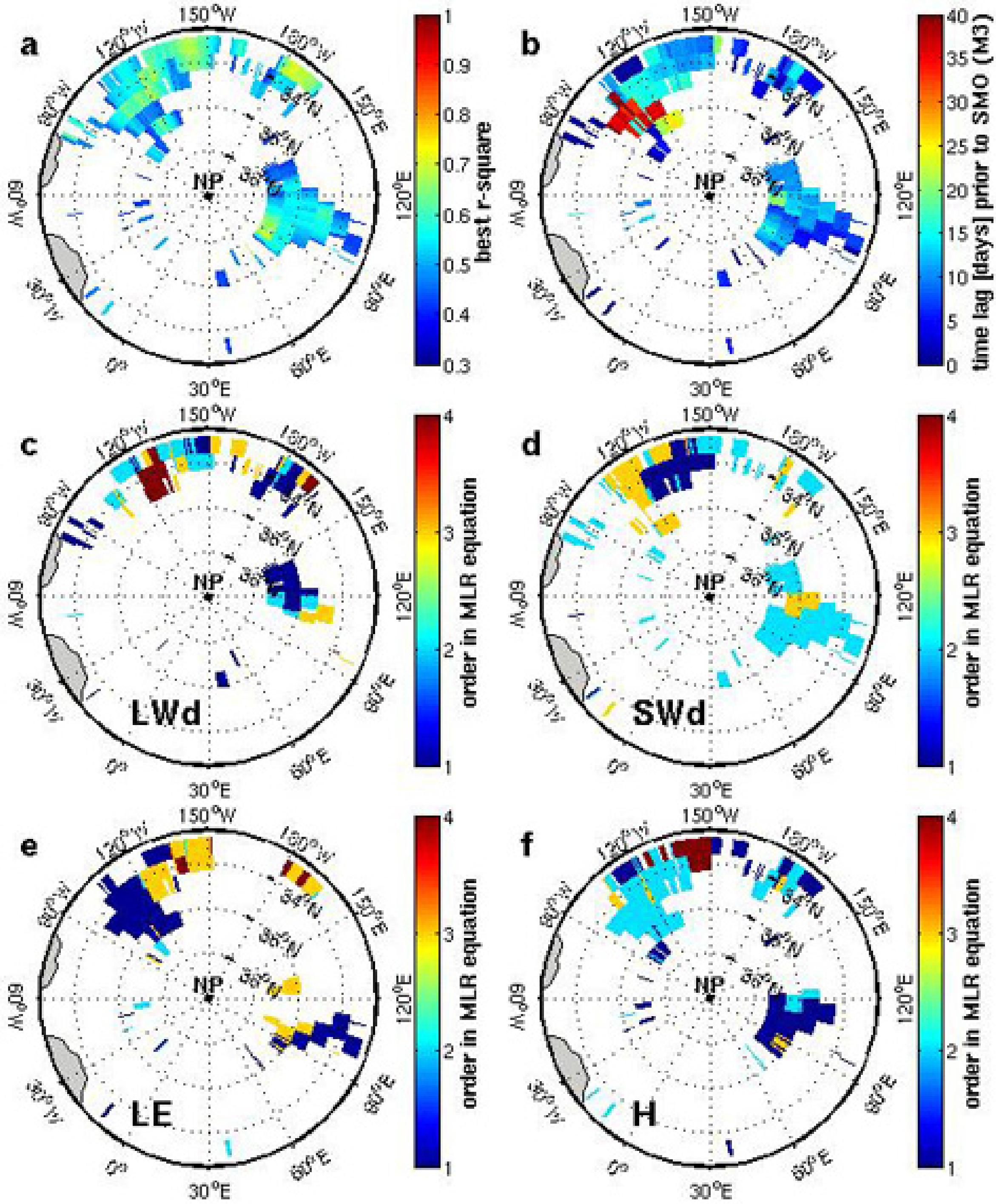

Figure 5.29: Best results for the stepwise multi-linear regression (MLR) analysis at each individual grid location (**method M3**).

(a) Fraction of the local interannual SMO variance (r^2) explained by the best combination of four fluxes: LWd, SWd, LE and H. At each particular location r^2 value is the highest among all combinations of these four fluxes and 40 different flux-averaging periods.

(b) Flux-averaging period suggesting the best r^2 that results from any combination of individual fluxes at each grid location.

(c-f) Rank of the flux components in the best multi-linear regression equation (at each individual grid location). For example, in (c) at those locations where the color code refers to 1, LWd is the most significant flux component (with the smallest p-value) and the first included in the multi-linear regression equation.

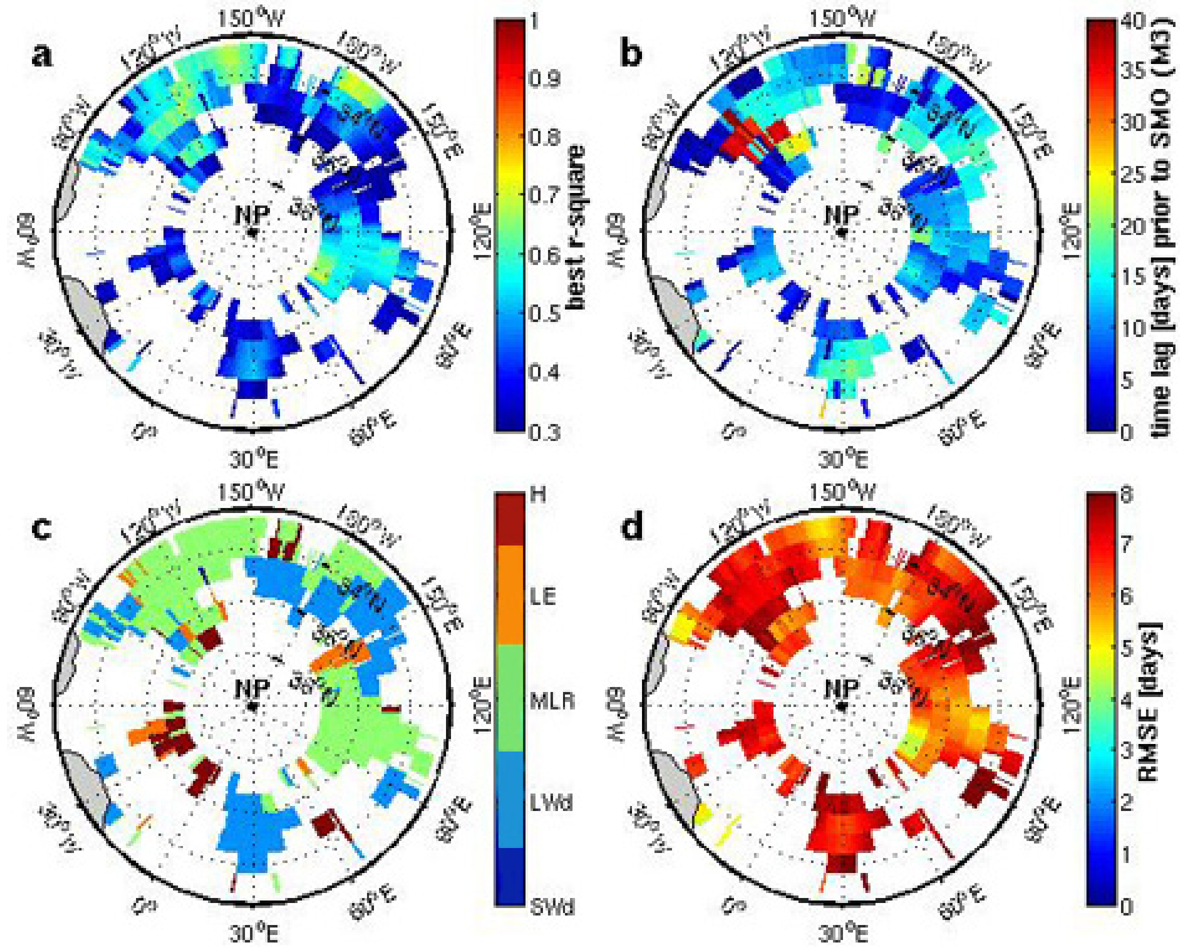

Figure 5.30: Comparison of the bilateral versus multi-linear regression results (**method M3**).

(a) Fraction of the local interannual SMO variance explained by the surface fluxes (r^2): LWd, SWd, LE, H and/or any combination of these 4 fluxes. At each particular location, this r^2 value is the highest among four individual fluxes, all combinations of these four fluxes and all flux-averaging periods.
(b) Flux-averaging period suggesting the best r^2 that results from any individual flux or combination of individual fluxes at each grid location.
(c) The factor best explaining SMO variance: individual fluxes or some combination of them, ranked by r^2. Multi-linear regression (MLR) refers to some combination of LWd, SWd, LE and H flux anomalies, suggesting the best r^2.
(d) RMSE corresponding to the best explaining factor shown in (c).

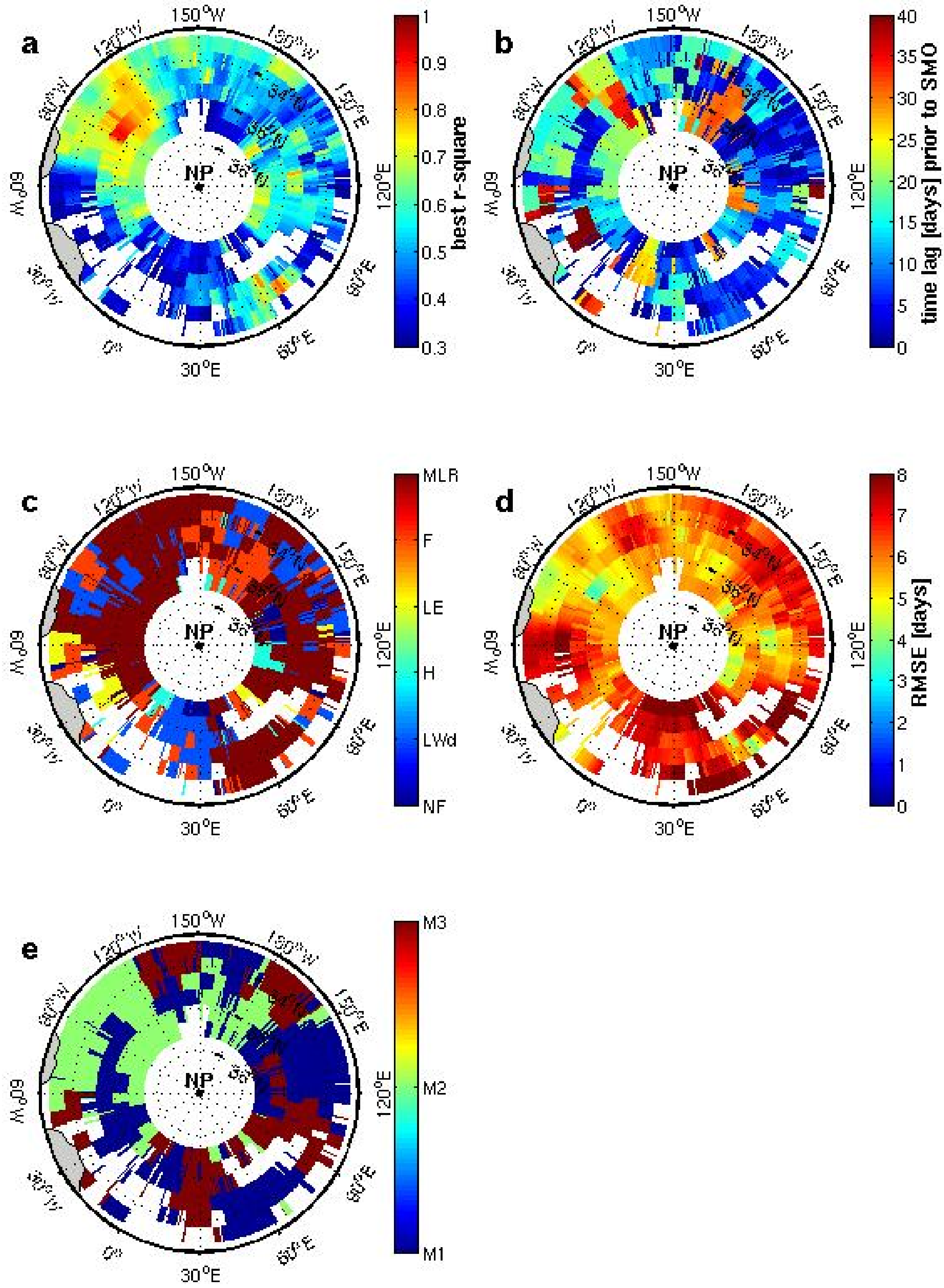

Figure 5.31: Comparison of the bilateral versus multi-linear regression results with **all three methods M1, M2 and M3**. Subpolts a-d are analogous to those in previous Figure, except that NF, SWnet, LWnet, DF and DR are also included into comparison. Map (c) shows the factor best explaining interannual SMO variance, with F representing any of the following fluxes: NF, SWnet, LWnet, DF or DR. (e) Method (M1, M2 or M3) suggesting the best r^2 that results from any individual flux or combination of individual fluxes at each grid location and with any time averaging period.

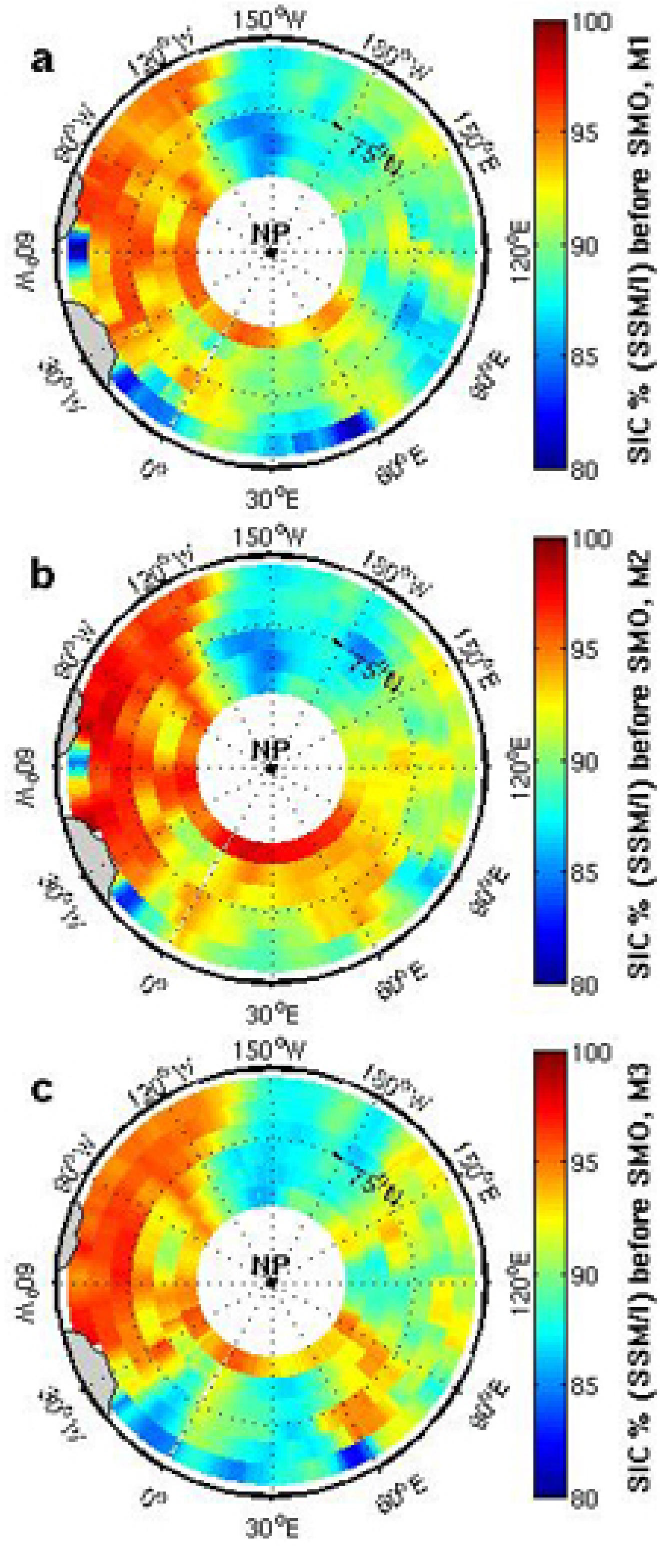

Figure 5.32: The smallest annual-mean spatially-average SIC (SSM/I) in the vicinity of each ERAI grid location (within 50 km radius) during a 40-day pre-melt period and on the SMO day itself (41-day average SIC). Such SIC conditions occurred in any year (1989-2008), in different years at different locations. Three methods M1 (a), M2 (b) and M3 (c) were applied to define the timing of the 40-day pre-melt period. SMO day is included in the examination in order to capture/localise as much as possible of potential errors in ERAI SIC and surface heat fluxes.

5.2 Meteorological conditions affecting Surface Heat Fluxes and Snow Melt Onset timing

Earlier in Section 5.1 we discussed that Snow Melt Onset on top of compact sea ice (SMO) is controlled by the surface heat fluxes. In turn the surface heat fluxes are themselves modified by weather (cloud cover, heat advection, wind speed), snow and sea ice thickness. In this Section we considered a longer chain of interactions: meteorological conditions - surface heat fluxes - SMO timing on top of the sea ice. Similar to Section 5.1, bilateral and stepwise multi-linear regression analysis were applied to evaluate how well the meteorological conditions (individual meteorological variables and various combinations of these variables) explain the interannual and spatial variability in surface fluxes and SMO timing. Among individual meteorological variables we chose: the near-surface (2m) air temperature, skin temperature, total (vertically integrated) column water vapour, liquid water and ice water contents, near-surface (2m) specific humidity, total and low-level cloud fractions, near-surface (10m) wind speed, as well as the horizontal thermal and moisture advection. Two heat flux components were considered, those best explaining the variability in SMO: the net flux (NF) and the downward longwave radiation (LWd).

To evaluate the relationship between surface heat fluxes, meteorological variables and SMO, again we face the question on how to define the timing and duration of the reference study period. When changes in surface heat fluxes and meteorological conditions trigger a better/weaker heat accumulation within a dry snowpack and in turn an early/late SMO timing? It is of evidence: if evaluating the relationship between the surface heat flux (for ex., LWd) and the corresponding meteorological state variable (for ex, total cloud fraction), one should pre-define the reference period of the year (same each year!) to avoid the comparison of the cloud LW radiative forcing during early spring in one year, and during late spring - in another year. The possible solution for the reference study period could be, for example:

(a) a 20-year mean regional average SMO within 83.25-87^{o}N, is the Julian day 174 or 24-25 June (both in 25 km resolution and ERAI grid).
(b) the earliest local SMO (25 km resolution) within the circumpolar central Arctic is the Julian day 76 (16-17 of March).
(c) the earliest local SMO (ERAI grid resolution) within the circumpolar central Arctic is the Julian day 141 (20-21 of May).

In our example here we chose option "c" and further demonstrate the results based on the daily time series of the surface heat fluxes and meteorological variables during a 40-day pre-melt period between 11 April - 20 May. This approach roughly interferes with our method M3, where the earliest SMO is considered as a reference day of the year (the end of the pre-melt period).

As before, three methods M1, M2 and M3 were applied when comparing (1) the time-average anomaly in individual meteorological variable and (2) the corresponding (same year, same location) SMO anomaly.

5.2.1 Snow Melt Onset - Heat Fluxes - Atmospheric Moisture

Although polar air is relatively dry, in reality [*Zhang et al.*, 1997] and in ERAI the day-to-day LWd anomalies are strongly affected by the atmospheric water vapour. During February-April the vertically integrated water vapour content (TCWV) in the central Arctic is about 2-5 kg/m^2, and about 5-12 kg/m^2 in May-June (**Fig 5.33a**). Vertically integrated liquid water content (TCLW) and ice water content (TCIW) are of the order of 0.01-0.05 kg/m^2 [*Francis and Hunter*, 2007] during the pre-melt April-May months (**Fig 5.33 b-c**). The near-surface (2m) specific humidity (q) is typically below 4 g/kg within the sea ice covered Arctic [*Serreze et al.*, 1995b], **Fig 5.33d**.

With a focus on the pre-melt period (11 April-20 May) diurnal anomalies in specific humidity explained 60% of the total variance in LWd, and locally up to 71% of the temporal variations in LWd (**Table 2**, page 129). TCWV accounted for 50% of the overall (temporal and spatial) variance in LWd, locally explaining up to 63% of the temporal LWd variability (**Fig 5.34a**), with the standard error (RMSE) between 18 and 23 W/m^2 (**Fig 5.34b**), and **Table 2** (page 129).

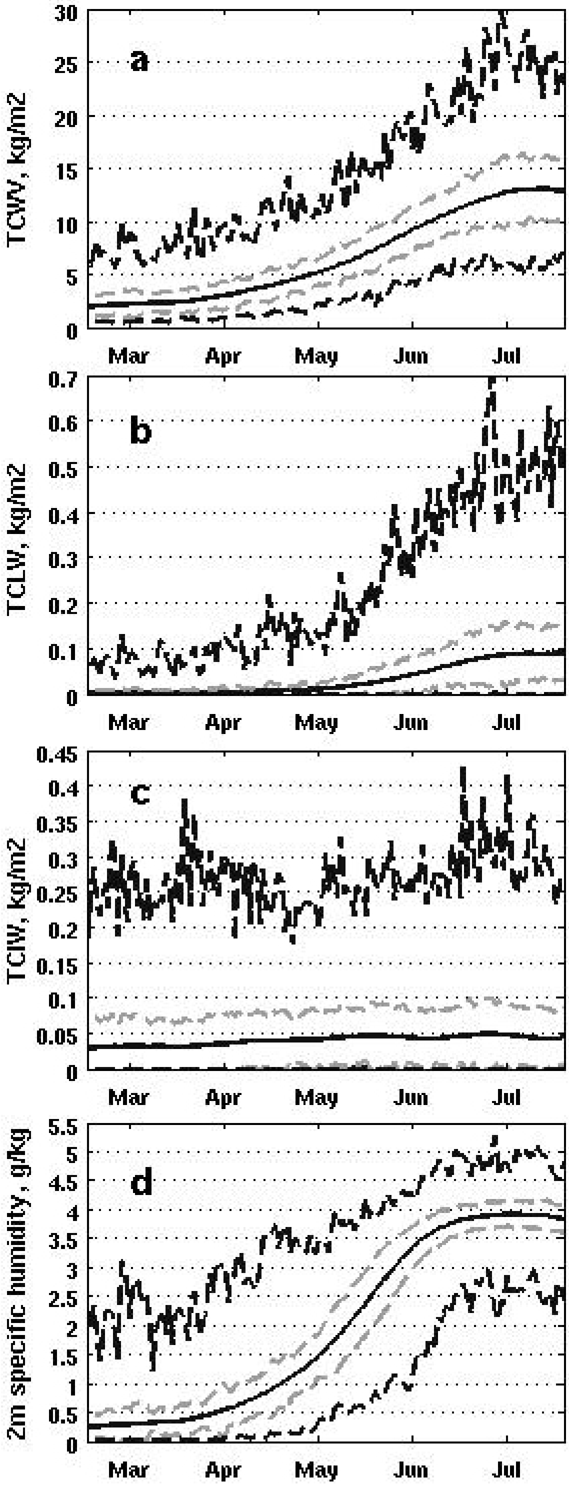

Figure 5.33: Seasonal cycle in (a) total column water vapour; (b) total column liquid water, (c) total column ice water, (d) near-surface specific humidity. The black solid curve is a 20-year average within the circumpolar central Arctic, two grey dashed curves delimit one standard deviation of all daily values, and two black dashed curves delimit the maximum and minimum daily values.

Figure 5.33:

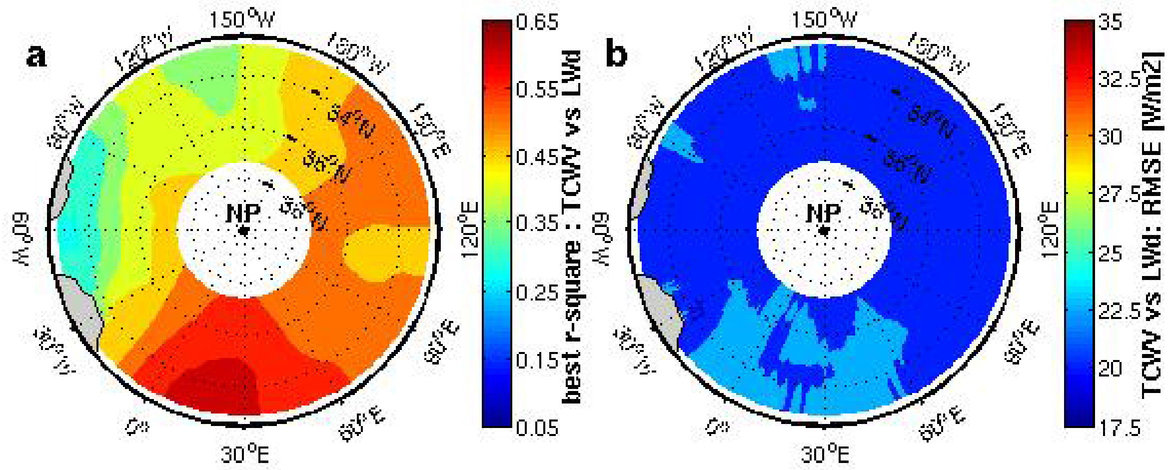

Figure 5.34: Relationship between TCWV and LWd diurnal anomalies.

The local diurnal anomalies are calculated relative to the regional 20-year climatology for the same day of the year within 83.25-87^{o}N (solid black curve in Fig 5.33a). Bilateral regression is calculated for 800 values of TCWV and LWd at each ERAI grid location (40 days x 20 years). Same 40-day pre-melt period from 11 April to 20 May is considered everywhere.
(a) fraction of the local day-to-day variability in LWd explained by diurnal (same day, same location) TCWV anomalies (r^2).
(b) root mean square error of the linear regression model.

Thus on average the anomaly in TCWV of -2 - (-4) kg/m^2 (+4 - +10 kg/m^2) was found in those days when LWd anomaly was negative (positive) by 100 - 0 W/m^2 (+10 - +120 W/m^2), **Fig 5.35**.

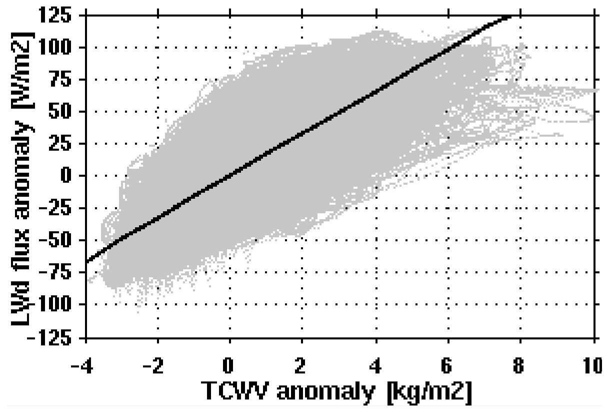

Figure 5.35: Relationship between the diurnal LWd anomaly versus corresponding TCWV anomaly. Each grey dot represents some grid location within 83.25-87^{o}N, some year (1989-2008) and any day of the 40-day pre-melt period (11 Apr-20 May). Black line reflects the linear regression equation in Table 4 (page 130).

Similar comparison for NF evokes that the diurnal anomalies in TCWV (and q) explained 40% of the total (temporal and spatial) NF variance (**Table 3**, page 129), and locally accounting for up to 49% (52%) of the temporal (day-to-day and interannual) variability in NF (**Fig 5.36**).

It is logic: if near-surface specific humidity and TCWV explain a significant portion of the total (spatial and temporal) variance in LWd and NF, and both LWd and NF affect SMO timing, then both near-surface specific humidity and TCWV should somehow affect SMO timing as well. **Fig 5.37** demonstrates the effect of TCWV anomaly averaged over a 1, 2 .. 40-day pre-melt period (and any method M1, M2 and/or M3) on SMO timing. Accordingly TCWV anomalies explained up to 83% of the local interannual variance in SMO (**Fig 5.37a**), where significant relationship (r^2) was detected within about 66% of the circumpolar central Arctic area (shaded grid boxes in **Fig 5.37**). Thus the average 1-7 day anomaly in TCWV of +2 - +6 kg/m^2 (-2- -6 kg/m^2) occurred in those years and at those locations where/when SMO was 10-25 days early (late) compared to the local 20-year average, not shown.

Similar result was found for the near-surface specific humidity (not shown). Year-to-year anomalies in q explained locally up to 73% of the interannual variations in SMO (best with 1-10 day averaging period and M1), revealing significant r^2 within 50% of the circumpolar central Arctic, with RMSE of 5-8 days (not shown).

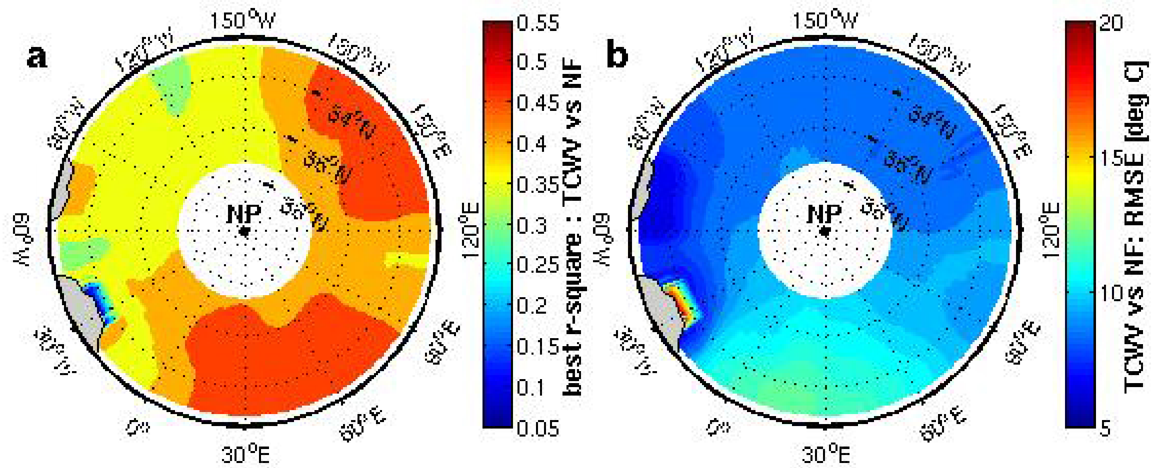

Figure 5.36: Same as in Fig 5.34 but for NF. (a) fraction of the local day-to-day variability in NF explained by diurnal (same day, same location) TCWV anomalies (r^2). (b) root mean square error of the linear regression model.

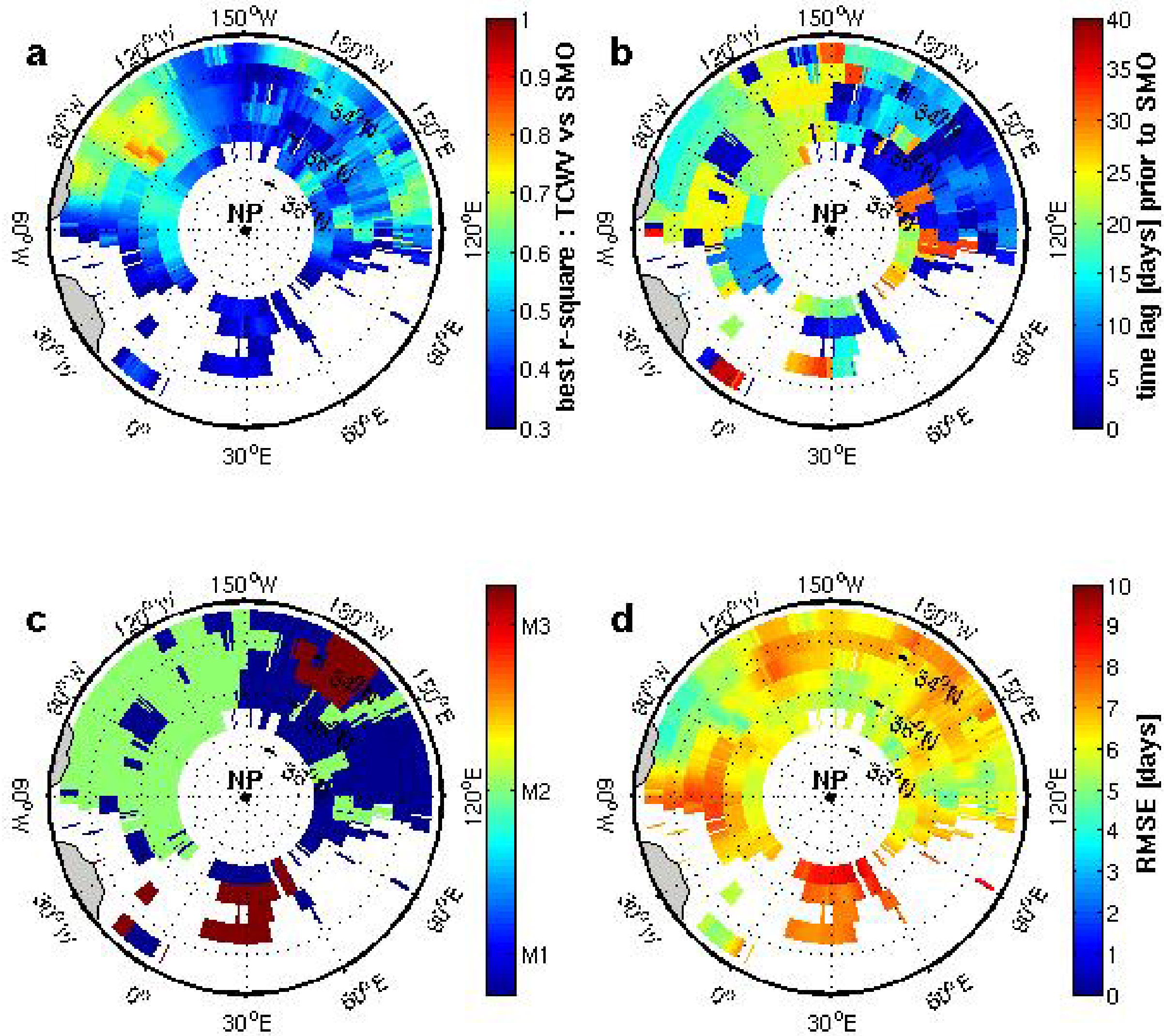

Figure 5.37: Best bilateral regression results on the local relationship between TCWV anomaly and the corresponding SMO anomaly (same location, same year).

(a) fraction of the local interannual SMO variance (r^2) explained by the time average TCWV. At each particular location r^2 value is the highest among three methods (M1, M2 or M3) and 40 different time-averaging periods.
(b) time-averaging period suggesting the best r^2.
(c) method suggesting the highest r^2.
(d) root mean square error of the linear regression model.

5.2.2 Snow Melt Onset - Heat Fluxes - Clouds

Total (TCC) and the low-level (LCC) cloud cover are abundant in the Arctic, smaller in winter and increasing in sprig-summer-fall season. Apparently ERAI captures well this general tendency, showing the increase in both TCC and LCC during February-July period (**Fig 5.38**). Diurnal variations in TCC (LCC) explained 19% (12%) of the total variance in diurnal LWd anomalies, and locally up to 47% (35%) of the temporal changes in LWd anomalies, see **Fig 5.39a** (**Fig 5.40a**) and **Table 2** (page 129).

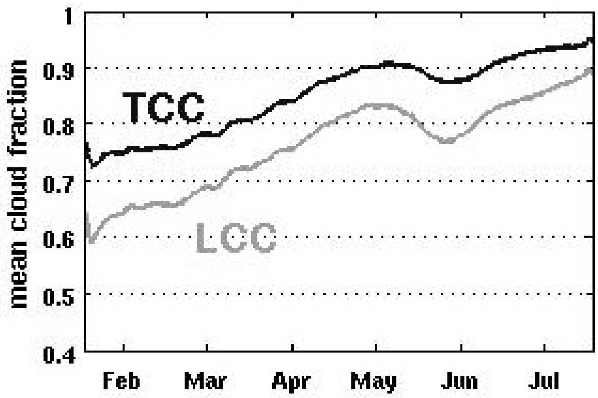

Figure 5.38: Seasonal cycle in ERAI total cloud fraction (TCC, black) and low-level cloud fraction (LCC, grey). Climatology for each day of the year is calculated as a 20-year mean regional average (grid-box area weighted) within 83.25-87^{o}N.

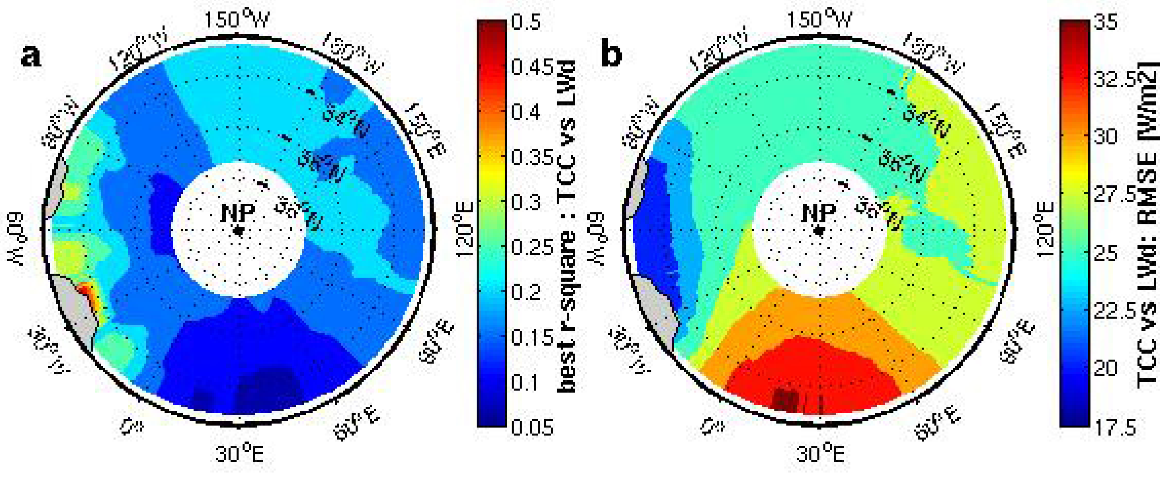

Figure 5.39: Relationship between TCC and LWd diurnal anomalies.
The local diurnal anomalies are calculated relative to the regional 20-year climatology for the same day of the year within 83.25-87^{o}N. Bilateral regression is calculated for 800 values of TCC and LWd at each ERAI grid location (40 days x 20 years). Same 40-day pre-melt period from 11 April to 20 May is considered everywhere.
(a) fraction of the local day-to-day variability in LWd explained by diurnal (same day, same location) TCC anomalies.
(b) root mean square error of the linear regression model.

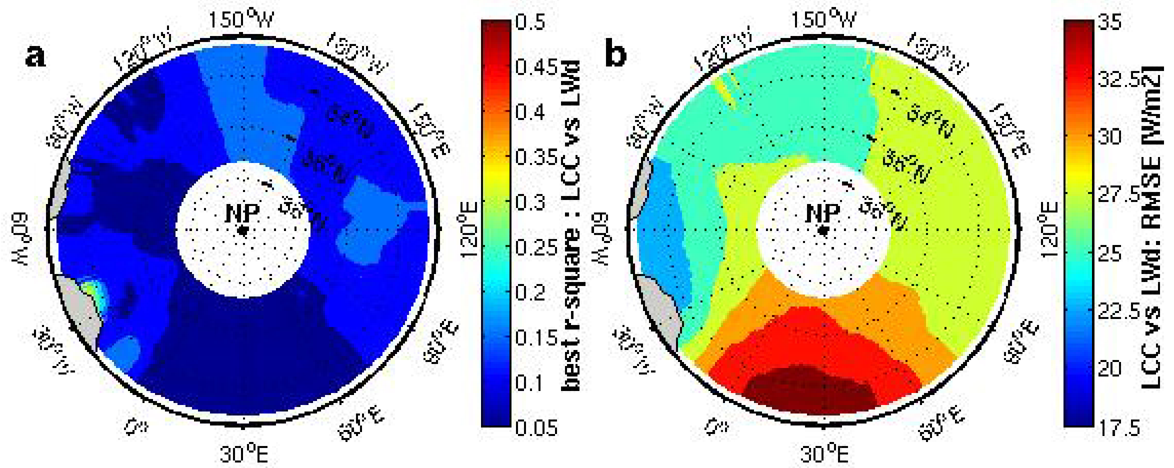

Figure 5.40: Same as in Fig 5.39 but for LCC.
(a) fraction of the local day-to-day variability in LWd explained by diurnal (same day, same location) LCC anomalies.
(b) root mean square error of the linear regression model.

Comparison of the local diurnal anomalies in TCC, LCC and NF established a very weak and positive effect of the cloud fraction on NF anomaly, with r^2 locally not exceeding 14% (**Table 3**, page 129). This result is consistent with the reality, where during most of the year the surface NF in snow covered regions tends to be grater in cloudy periods, compared to clear sky days [*Key et al.*, 1997].

If TCC and LCC tend to affect surface heat fluxes in the pre-melt period (increasing LWd and reducing NF deficit), naturally there should be some contribution of TCC and LCC anomalies in SMO timing. Application and comparison of three methods (M1, M2 abd M3) with TCC (LCC) anomalies averaged over 40 different time lags established significant correlations between local ERAI TCC (LCC) anomalies and SMO timing. Correlations between TCC (LCC) were strongly negative: where the additional cloud fraction (positive anomaly) in the pre-melt period contributed to the earlier SMO timing (negative anomaly). This is consistent with earlier results by *Curry* [1995] and *Zhang et al.* [1996]. Locally TCC and LCC explained up to 69% of the interannual variance in SMO (**Fig 5.41a, 5.42a**) with the best time averaging period for the cloud anomalies within 10-20 days (**Fig 5.41b, 5.42b**), and the most appropriate method M2 (**Fig 5.41c, 5.42c**), and the standard error in SMO *prediction* around 6-9 days (**Fig 5.41d, 5.42d**).

Total (vertically integrated) liquid water (TCLW) and ice water (TCIW) contents are the moisture quantities related to cloud properties. Results for TCLW and TCIW are summarized in **Tables 2-3** (page 129). These explained 31-32% of the total variance

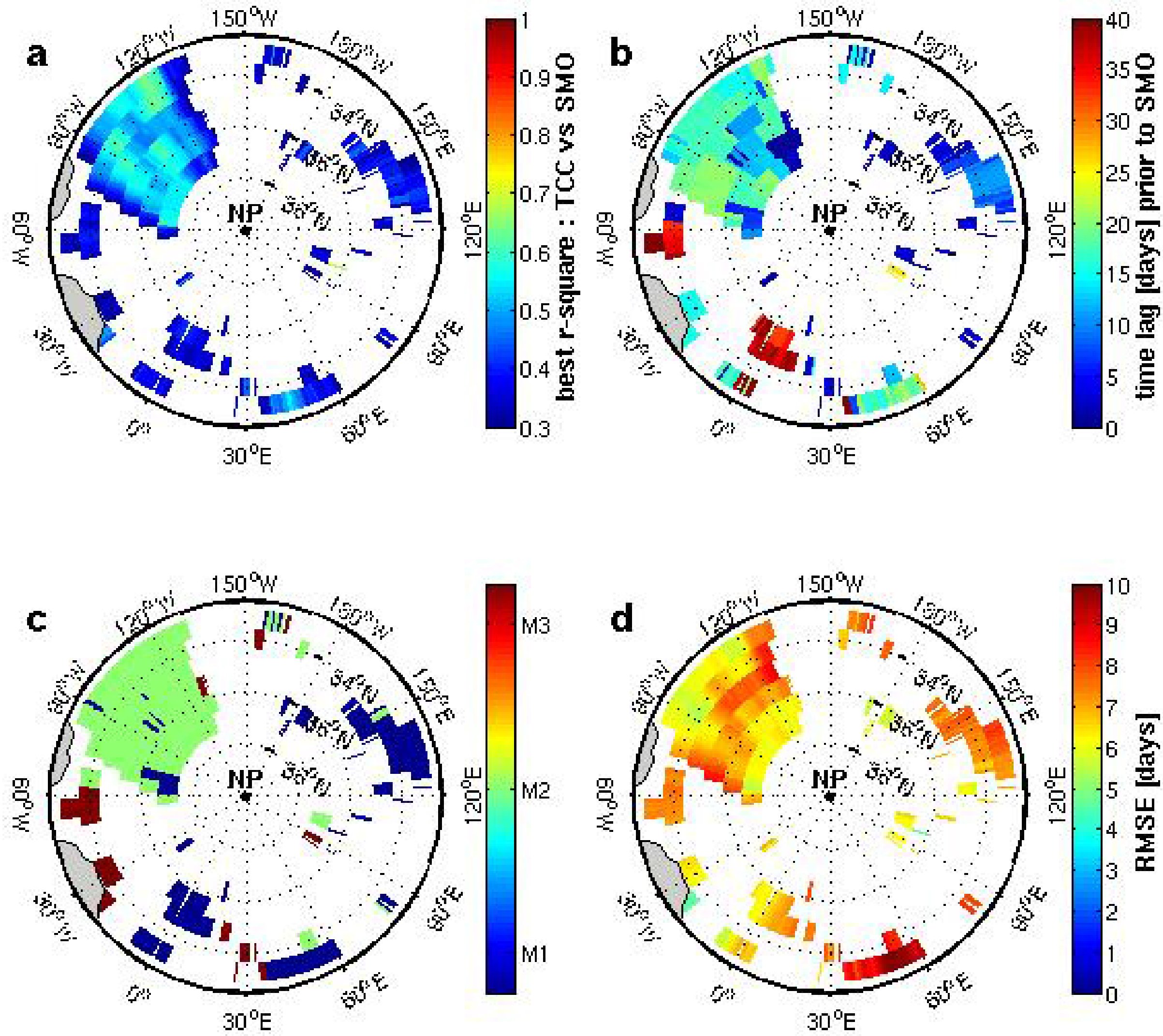

Figure 5.41: Best bilateral regression results on the local relationship between TCC anomaly and the corresponding SMO anomaly (same location, same year).
(a) fraction of the local interannual SMO variance (r^2) explained by TCC. At each particular location r^2 value is the highest among three methods and 40 different time-averaging periods.
(b) time-averaging period suggesting the best r^2.
(c) method suggesting the highest r^2.
(d) room mean square error of the linear regression model.

in LWd and 22-24% of the total variance in NF, locally accounting for up to 47% and 34% of the local temporal changes in LWd and NF, respectively. To note, in reality LWd is particularly sensitive to the variations in TCLW within 0-0.03 kg/m^2, which is exactly the case for the Polar regions, even during summer months [*Curry*, 1995 and *Zhang et al.*, 1996]. Thus the significant relationship between LWd and TCLW diurnal anomalies, as performed in ERAI, seems reasonable. However the relationship between

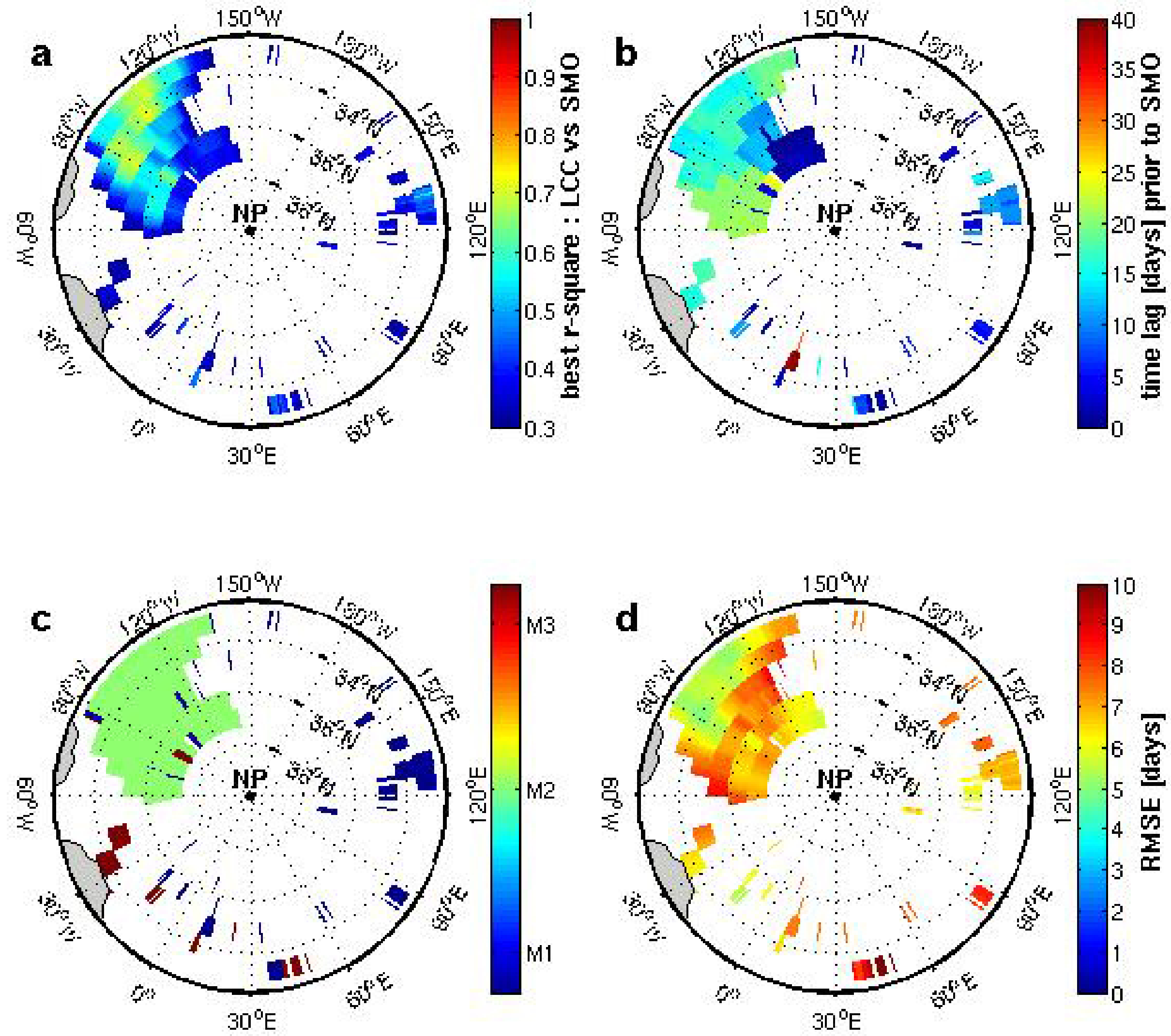

Figure 5.42: Same as in Fig 5.41 but for LCC.
(a) fraction of the local interannual SMO variance (r^2) explained by LCC. At each particular location r^2 value is the highest among three methods and 40 different time-averaging periods.
(b) time-averaging period suggesting the best r^2.
(c) method suggesting the highest r^2.
(d) room mean square error of the linear regression model.

TCIW and surface fluxes, for ex. LWd, is less evident. Based on SHEBA observations *Intrieri and Shupe* [2004] have quantified the radiative properties of the atmospheric ice crystals. They found that TCIW contributed a negligible radiative effect on sea ice surface during November - mid-May period. If following ERAI the result is somehow different, at least during April - mid-May period. As we just said: in ERAI 32% of the total (day-to-day, interannual and spatial) LWd variations are explained by TCIW variations in time and space during April - mid-May period.

When applying the forward stepwise multi-linear regression TCIW improved the explained variance of LWd, but interestingly - not TCLW (**Table 2**, page 129). However, both TCLW and TCIW significantly (negatively) correlated with SMO (not shown): with larger moisture content in those years/areas where SMO occurred earlier than average.

The relationship between cloud fraction and SMO had been addressed earlier by *Serreze et al.* [1993] within the East-Siberian Beaufort Sea region of the Arctic Ocean. A 5-year sample (in the period between 1979 and 1986) was utilized for that study. Both, cloud amounts and SMO were determined with the remote sensing: microwave data from SMMR (Nimbus-7 Scanning Multichannel Microwave Radiometer) and the visible-band observations by DMSP (Defence Meteorological Satellite Program). In spite the apparent evidence, no significant relationship between the regionally averaged cloud cover, northward wind component, the near-surface air temperatures and regionally averaged SMO timing could be established at that moment. Our results evidenced that TCC and LCC significantly contribute to SMO timing. The fact that we have better results is likely related to several factors. First, the data quality was likely worse, compared to our cloud, wind, temperature and SMO products. Second, a 5-year data sample is probably too small to catch a significant relationship between these complex variables.

Credibility of the cloud fractions in ERAI had been recently questioned by *Marta Zigmuntowska* (in press). She compared ERAI TCC and LCC values with the remote sensed estimates. Her preliminary results indicate that ERAI TCC are much larger (year through) compared to those from CALIPSO/CloudSat. According to our knowledge this is the only study addressing the question on the cloud properties in ERAI in the Arctic region. Interestingly to note that: if there exist some constant bias in ERAI meteorological variables and surface heat fluxes, it likely does not perturb the correlation strength. Thus the amplitude of the anomalies does not affect the correlation strength, however errors in daily values and in day-to-day anomalies - do largely affect the correlation strength between heat fluxes, meteorological variables and SMO.

Earlier *Bromwich et al.* [2007] had investigated the cloud radiative properties in the predecessor of ERAI - ERA-40 reanalysis. This study showed a very good representation of LWd (observations vs ERA-40) at Point Barrow in June 2001 "on those days when the total cloud fraction was properly resolved by ERA-40". However, the error in LWd of 20-50 W/m^2 was found in ERA-40 in this period with both: under- and overestimation of the actual TCC and LWd values. We speculate that these errors in TCC and LWd likely hold for ERAI as well.

5.2.3 Snow Melt Onset - Heat Fluxes - Thermal Advection

Horizontal thermal advection (TAD) was calculated at each grid location and each day of the year as explained in **Appendix 1**. Six geopotential heights were considered: 500, 600, 700, 800, 900 and 1000 hPa. The day-to-day statistics of TAD during the pre-melt and the first part of the melt season (March-July) are reflected in **Fig 5.43**. Thus the regional average 20-year climatology within 83-78^{o}N (solid black curve) indicates positive TAD values of 1-2 ^{o}C/day without any seasonal change. To note, this is the weighted mean of all local (grid box) TAD values for each day of the year, and this is not a convergence that we discussed in Chapter I. Examination of the local diurnal values evokes very high TAD values, indicating that locally there can be a very large horizontal heat transport. Naturally, the largest TAD occurs in winter, rather than in summer - when thermal gradients and the intensity (depth) of cyclones are the most pronounced. Results illustrated in **Fig 5.43** indicate that the horizontal thermal gradients and thermal advection are the strongest within the lower troposphere in ERAI, here roughly around 800-900 hPa, which is in agreement with the general expectation [*Nakamura and Oort*, 1988; *Serreze and Barry*, 2005]

Comparison of TAD and LWD diurnal anomalies at each ERAI grid location during the pre-melt period (11 April-20 May) detected that locally TAD anomalies explain up to 16% in temporal variations in LWd (not shown), better in the lower troposphere (800-1000 hPa levels). However, TAD anomalies accounted for less than 1% of the total variability in LWd (not shown). Interestingly, TAD explained better NF variations, than LWd, accounting for 5% of the total NF variance at the lowermost 1000 hPa level (not shown). This partly results from the importance of thermal advection on H and indirectly - on LE.

Since the effect of TAD variations on LWd and NF changes appeared to be minor, the relationship between TAD and SMO was not investigated. We expect that another methodology for calculation thermal advection, and likely, instead of our methodology - the horizontal thermal convergence/divergence should be calculated in further studies.

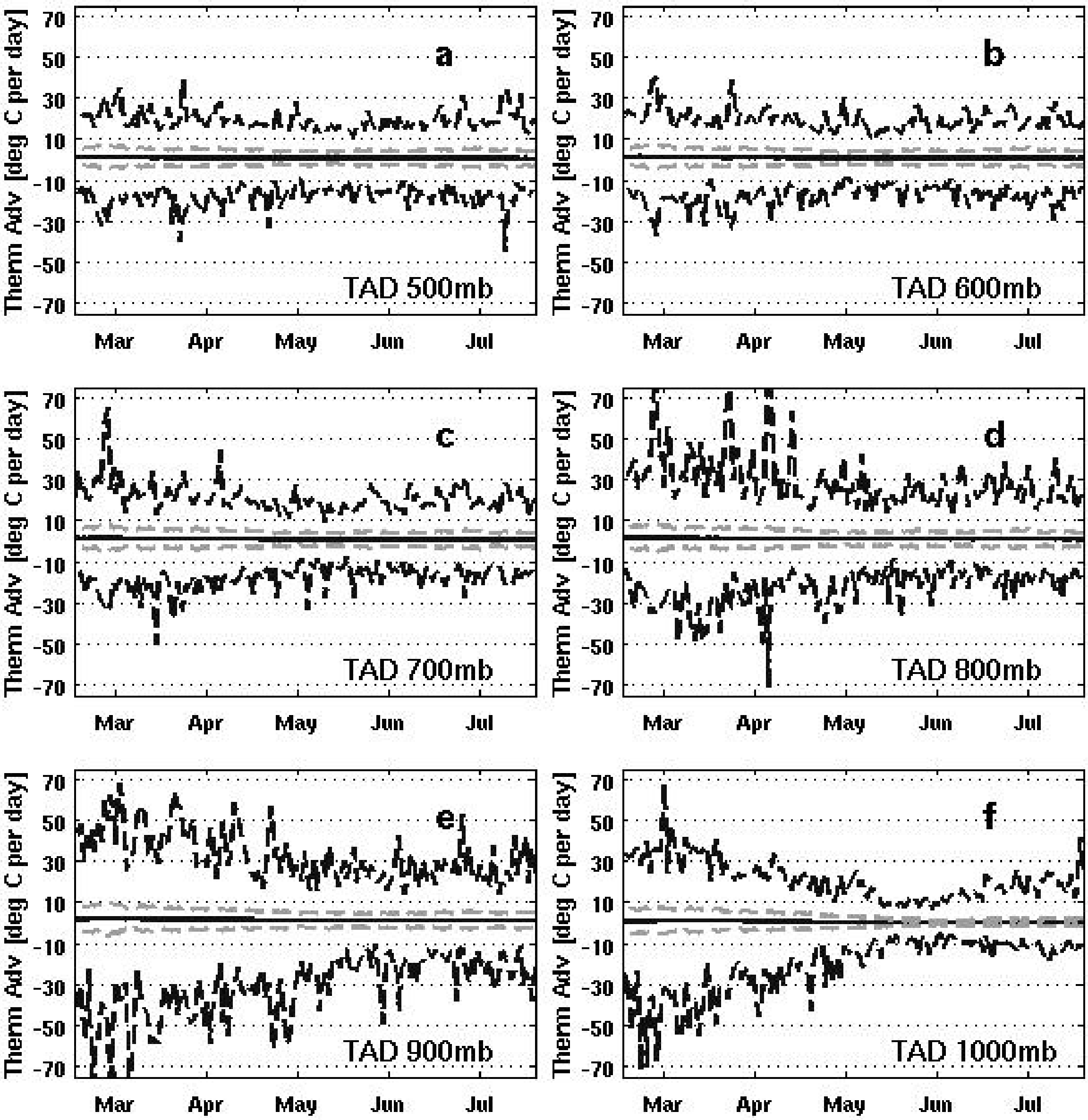

Figure 5.43: Thermal advection (TAD) statistics within 83.25-87^{o}N in the period 1989-2008.

TAD is a relative measure of the diurnal local horizontal gradients in potential temperature and the corresponding wind speed. The black solid curve is a 20-year average regional mean TAD (grid-box area weighted). Two grey dashed curves delimit one standard deviation of all daily values (in a given month) at all grid locations (within 83.25-87^{o}N). Two black dashed curves delimit the maximum and minimum daily values that occurred at any location within 83.25-87^{o}N. Time period: 1 March - 31 July. Six geopotential levels are considered: 500, 600, 700, 800, 900 and 1000 hPa.

5.2.4 Snow Melt Onset - Heat Fluxes - Moisture Advection

Moisture advection was calculated at each grid location and each day of the year as explained in **Appendix 2**. As for thermal advection six geopotential heights were considered: 500, 600, 700, 800, 900 and 1000 hPa. The day-to-day statistics of the moisture (specific heat) advection (MAD) during the pre-melt and the first part of the melt season (March-July) are reflected in **Fig 5.44**

Moisture advection explained less than 1% of the total (temporal and spatial) variance in LWd anomalies, locally accounting for up to 4% of the temporal (day-to-day and interannual) variability in LWd (not shown).

Earlier we have demonstrated that all the moisture content variables strongly affect the day-to-day and spatial differences in LWd (in ERAI). And here we got a surprisingly small effect of the moisture advection on the surface LWd and NF anomalies. This inconsistency indicates that either (a) horizontal advection should be calculated differently, and/or (b) that the relationship between the advected moisture and the local moisture-cloud variables and LWd is not linear, which is a well known fact. In reality moisture advection affects the local specific humidity and the cloud cover, and LWd anomaly occurs if there is a simultaneous increase in both. Relatively poor effect of LCC and TCC day-to-day anomalies on day-to-day LWd anomalies indicates that there are likely some errors in these quantities. And the horizontal moisture advection alone is likely not an appropriate indicator of LWd changes.

Further it could be of interest to compare the horizontal moisture transport divergence as calculated by *Graversen et al.* [2011] - with the seasonal LWd and annual SMO anomalies. Yet, this analysis is still to be done.

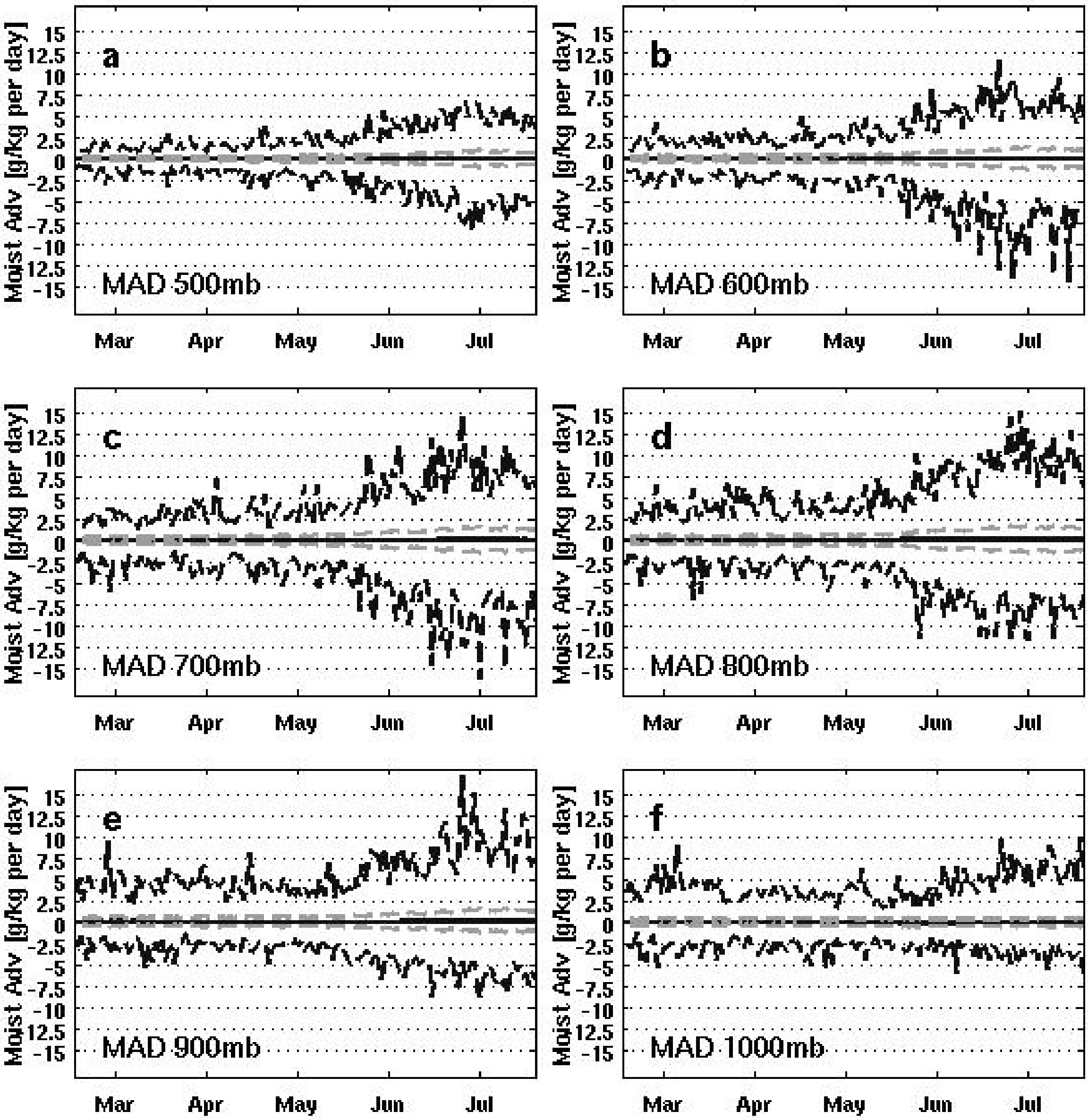

Figure 5.44: Moisture advection (MAD) statistics within 83.25-87^{o}N in the period 1989-2008.

MAD is a relative measure of the diurnal local horizontal gradients in specific humidity and the corresponding wind speed. The black solid curve is a 20-year average regional mean MAD (grid-box area weighted). Two grey dashed curves delimit one standard deviation of all daily values (in a given month) at all grid locations (within 83.25-87^{o}N). Two black dashed curves delimit the maximum and minimum daily values that ever occurred at any location (within 83.25-87^{o}N). Time period: 1 March - 31 July. Six geopotential levels are considered: 500, 600, 700, 800, 900 and 1000 hPa.

5.2.5 Snow Melt Onset - Heat Fluxes - Skin Temperature and Near-Surface Air Temperature

Fig 5.45 demonstrates the seasonal cycle in the ice surface or skin temperature (SKT), and the near-surface air temperature at about 2 meter heigh (SAT) during March-July period. The 20-year climatology within 83-87^{o}N (solid black curve) is about -25-35^{o}C in March, -10-30^{o}C in April, -5-15^{o}C in May and -5-0^{o}C in June-July.

Prior to SMO the snow is dry, surface albedo is high and as a result SKT and the upward LW are mainly driven by the downward longwave radiation [*Serreze and Barry*, 2005]. **Table 4** (page 130) outlines several and only meteorological factors affecting SKT variations on top of the compact sea ice: surface heat fluxes and the individual meteorological variables. The variations in time and in space in ERAI SKT were very well explained by the variations in ERAI LWd (**Table 4**, page 130). Both SKT and LWd anomalies were initially scaled by the regional 20-year climatology. Accordingly, the local diurnal anomalies in LWd explained up to 81% of the temporal variability in SKT (**Fig 5.46a**), with the standard error within 2^{o}C (**Fig 5.46b**). Thus a positive (negative) LWd anomaly of 50-100 W/m^2 produced a positive (negative) SKT anomaly by 0 - +20^{o}C (-40 - 0^{o}C), not shown.

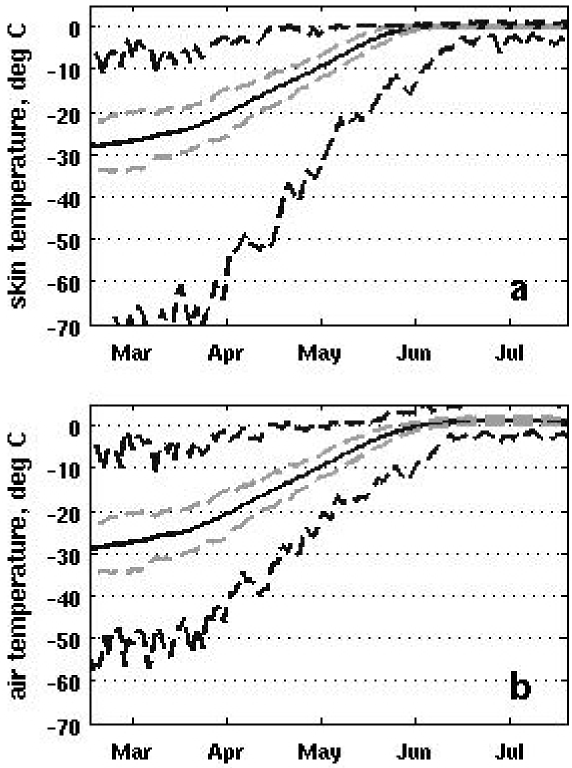

Figure 5.45: Seasonal cycle in ERAI (a) skin and (b) near-surface air temperature. Black solid curve is a 20-year average within 83.25-87^{o}N, two grey dashed curves delimit ± one standard deviation of all daily values, and two black dashed curves delimit the maximum and minimum daily values. Time period 1 March - 31 July, 1989-2008.

We remind that these results refer to the daily mean values of surface heat fluxes and SKT in ERAI grid coordinates.

The effect of LWnet and NF on SKT variations (in time and in space) manifested by the positive correlation coefficients, but not as strong as for LWd flux component (**Table 4**, page 130). Thus warmer SKT coincided with the positive anomalies in NF

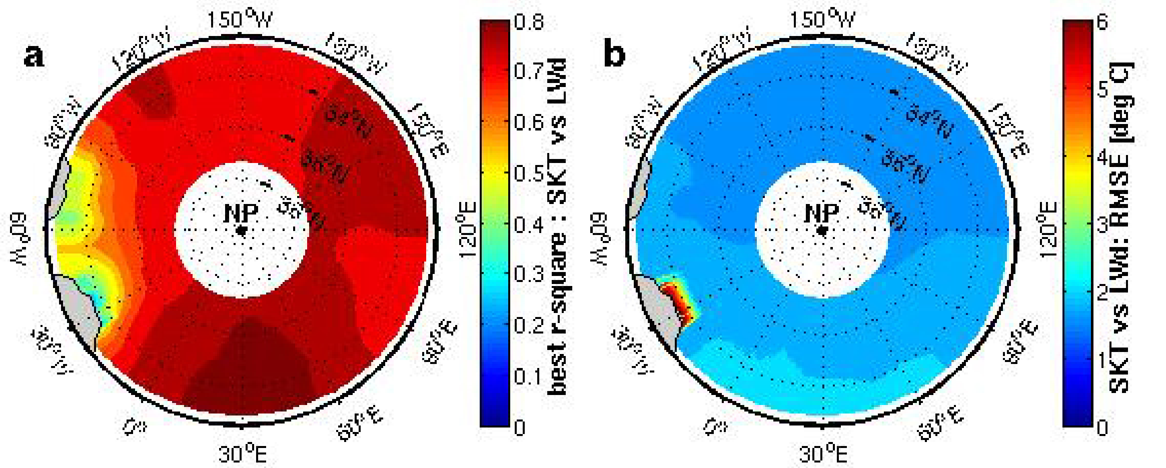

Figure 5.46: Relationship between the skin temperature (SKT) and downward longwave (LWd) diurnal anomalies. The local diurnal anomalies are calculated relative to the regional 20-year climatology for the same day of the year within 83.25-87^{o}N. Bilateral regression is calculated for 800 values of SKT and LWd at each ERAI grid location (40 days x 20 years). Same 40-day pre-melt period from 11 April to 20 May is considered everywhere.

(a) fraction of the local day-to-day variability in SKT explained by diurnal LWd anomalies (same day, same location).

(b) root mean square error of the linear regression model.

and LWnet, *e.i.* a smaller heat deficit. Diurnal anomalies in SWd and SWnet were negatively correlated with SKT during the pre-melt period between 11 April and 20 May (**Table 4**, page 130), indicating that LWd was the major source of heat for the dry ice covered surface, to note - as performed by ERAI. And this is a physically realistic result. One may specify that already in April, SWd may start to overlap LWd, and so far - dominate SKT and the internal snow temperatures, at least at noon on clear-sky days. Such conditions have been observed in reality. Yet this important feature of the diurnal cycle cannot be seen with the daily mean time series of surface heat fluxes and SKT. Comparison of SKT with H and LE values established that only a minor portion (8%) of the total (temporal and spatial) SKT variance was explained by the variations (in time and in space) in LE and H heat fluxes (**Table 4**, page 130).

In spring, when the snow is still cold and dry, a larger LWd and positive NF increase the surface (snow) temperature. When sufficient amount of heat is accumulated at the surface (within the snowpack), the melt temperature is reached (SKT warms-up to 0^{o}C) and the snow melt starts. This reasoning serves to demonstrate that the surface (snow) temperature is not a factor controlling SMO timing. Instead SKT (and its anomalies) is another (and alternative to SMO) estimate of the same thing - of the surface (snow)

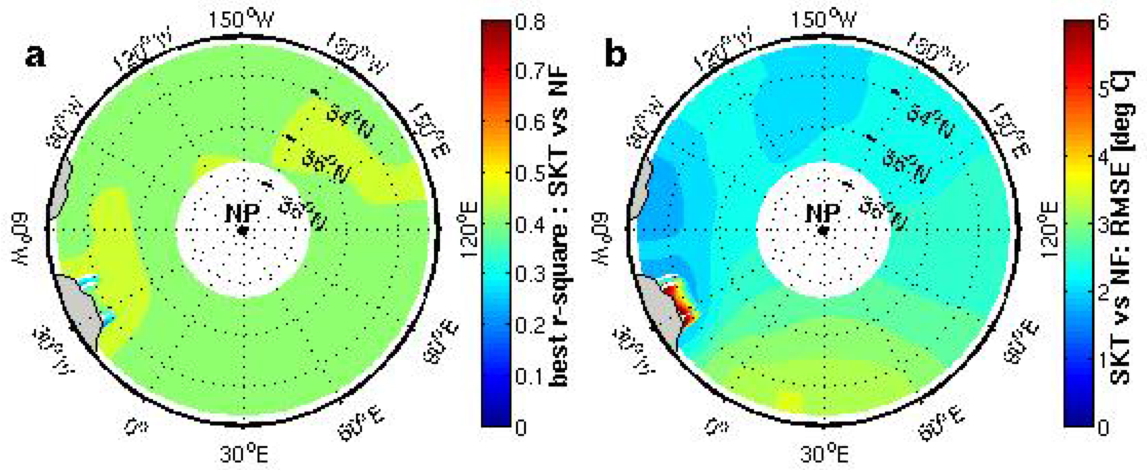

Figure 5.47: Same as in Fig 5.46 but for the net flux (NF). (a) fraction of the local day-to-day variability in SKT explained by diurnal NF anomalies (same day, same location). (b) root mean square error of the linear regression model.

thermal state.

Naturally the surface/internal snow temperatures are / should be warmer, *e.i.* near 0^{o}C, early (late) - in those years when SMO occurs early (late). Bilateral regression analysis with three methods (M1, M2 and M3) established that ERAI SKT anomalies accounted for up to 91% of the local interannual variance in SSM/I-based SMO timing (**Fig 5.48a**), with the standard error of the linear regression ranging between 3 and 9 days depending on the location (**Fig 5.48d**). Best time averaging period for SKT anomaly appeared to be within 1-10 days (**Fig 5.48b**), and the highest r^2 were found with method M1 (**Fig 5.48c**). To note, this result interferes with our conclusions for LWd and NF, where synoptic time averaging period and M1 were also the most relevant to the SSM/I-based SMO time series.

Correlations between SKT and SMO were strongly negative: with a warmer ERAI SKT (positive anomaly) found in those years/grid locations when/where earlier SMO (negative anomaly) was detected with SSM/I **Fig 5.49**. This is reasonable and physically consistent with the reality.

Considering the relationship between LWd and SAT. In spring prior to SMO the surface-based inversions prevail, and 2m SAT is typically slightly warmer than SKT. To note, episodically SAT can be cooler than SKT when horizontal heat advection with the simultaneous thick cloud cover with weak winds produce huge (70-100 W/m^2) LWd anomalies, reduce LWnet deficit and foster intense surface (SKT and near-surface (SAT) heating. In presence of surface-based inversions the day-to-day (daily mean) SAT anomalies are controlled by the turbulent sensible (H) heat flux, being roughly a function of SKT, the overlying air temperature and the wind speed. SWd may produce

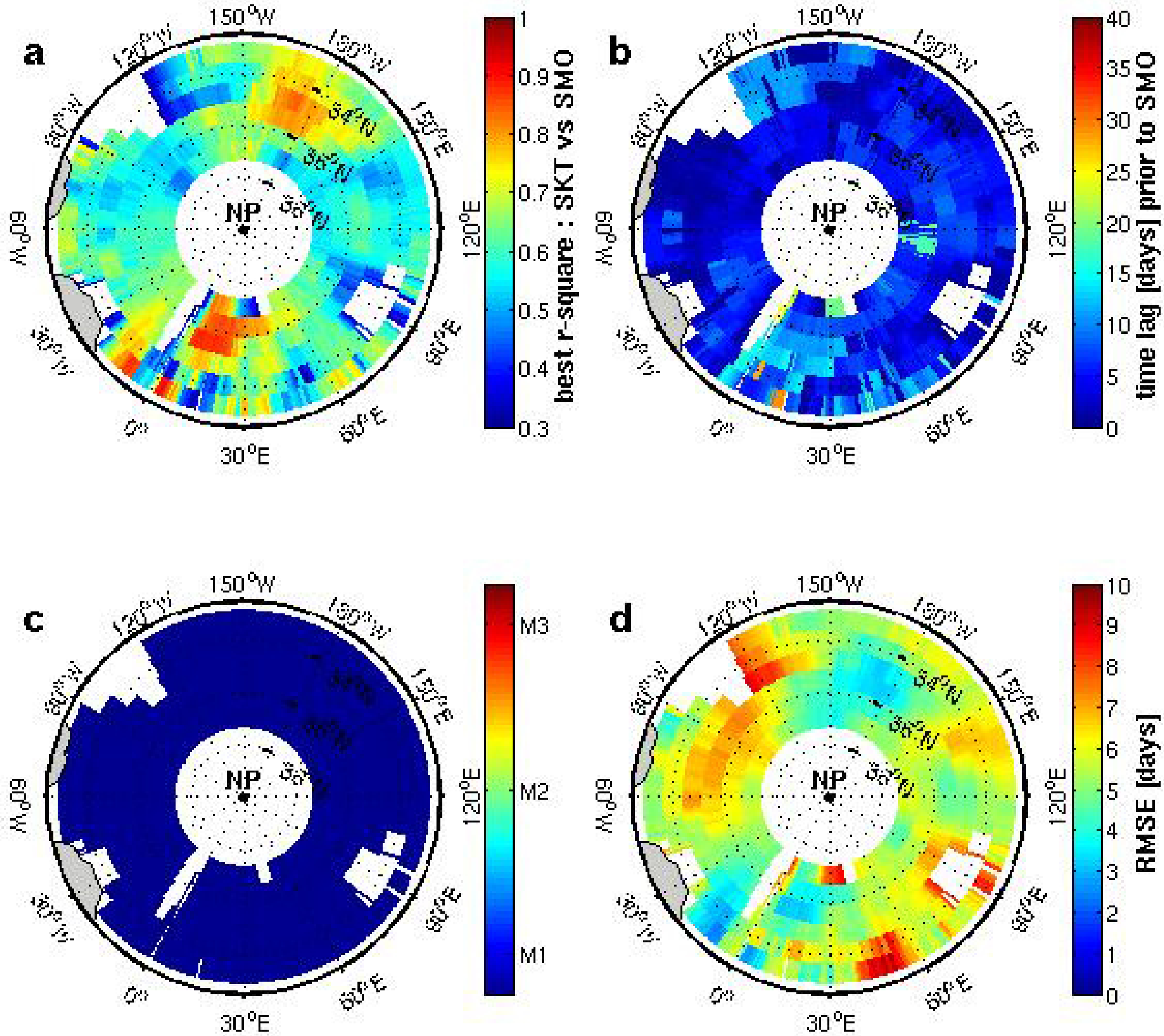

Figure 5.48: Best bilateral regression results on the local relationship between the SKT anomaly and the corresponding SMO anomaly (same location, same year).
(a) fraction of the local interannual SMO variance (r^2) explained by SKT. At each particular location r^2 value is the highest among three methods and 40 different time-averaging periods.
(b) time-averaging period suggesting the best r^2.
(c) method suggesting the highest r^2.
(d) room mean square error of the linear regression model.

the diurnal variations in SKT and SAT, but this is difficult to detect from the daily average record: heating at noon plus cooling at midnight = zero daily mean anomaly.

Correlation of the diurnal anomalies in SAT and anomalies in surface heat fluxes revealed very high and statistically significant relationship between LWd and SAT in ERAI. Thus the additional LWd contributed to warmer SAT in ERAI. Diurnal anoma-

Figure 5.49: Relationship between the diurnal local SKT anomalies and corresponding SMO anomalies. Each grey dot represents some grid location within 83.25-87°N and any year. SKT anomaly is 1-10 day average prior to reference SMO date determined with M1.

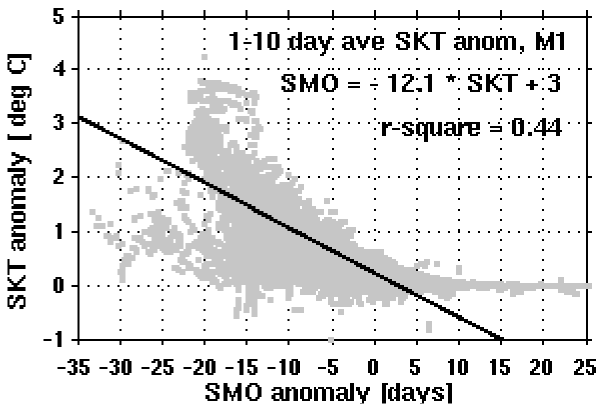

lies in LWd explained 70% of the total (temporal and spatial) variance in SAT, and up to 80% of the temporal changes in local (daily mean) SAT anomalies. This relationship is highly non-linear and schematically could be described as followed. When LWd flux is anomalously large (due to horizontal heat/moisture convergence and clouds), typically the turbulent sensible heat flux (downward heat supply) is larger as well. These two warm-up the near-surface air and the surface (snowpack). This warming of SKT in combination with the weak winds may cancel the turbulent heat exchange. However the thermal (LWd and LWup) radiation can be also trapped by the near-surface moisture. In turn, warming of the lowermost boundary layer can be associated with different combinations of processes, initially and primarily controlled by LWd heat supply.

Table 2. Meteorological variables best explaining the temporal and spatial variability in the **downward longwave radiation** (**LWd**) during the 40-day pre-melt period (11 April - 20 May). Bilateral regression analysis was applied to the combination of all ERAI grid locations within 83.25-87°N and 20 years. Local anomalies in LWd and meteorological variables are scaled by to the 20-year regional climatology. The stepwise forward multi-linear regression equation was calculated with all these meteorological variables and also TCLW as the potential predictors. TCLW was not accepted by the multi-linear regression procedure. All results are significant at 99 % confidence level ($p < 0.01$).

Linear regression equation	**overall r^2**	**overall RMSE [W/m2]**	**best local r^2**
LWd = 59.9 × q + 1.15	0.6	19.7	0.71
LWd = 16.2 × TCWV + 0.18	0.5	22.2	0.63
LWd = 459.3 × TCIW – 0.46	0.32	25.8	0.47
LWd = 1381 × TCLW – 0.01	0.31	26.1	0.41
LWd = 58.9 × TCC – 0.52	0.19	28.2	0.47
LWd = 38.1 × LCC – 0.6	0.12	29.4	0.35
LWd = 46.6 × q + 1.8 × TCWV + 174.1 × TCIW + 10.8 × LCC + 22.4 × TCC + 0.8	0.75	15.9	0.79

Table 3. Meteorological factors best explaining the temporal and spatial variability in the **net flux** (**NF**) flux during the 40-day pre-melt period (11 April - 20 May). Bilateral regression analysis was applied to the combination of all ERAI grid locations within 83.25-87°N and 20 years. Local anomalies in NF and meteorological variables are scaled by to the 20-year regional climatology. The stepwise forward multi-linear regression equation was calculated with all these meteorological variables and also TCLW as the potential predictors. TCLW was not accepted by the multi-linear regression procedure. All results are significant at 99 % confidence level ($p < 0.01$).

Linear regression equation	**overall r-square**	**RMSE [W/m2]**	**best local r-square**
NF = 20.1 × q + 0.74	0.4	9.7	0.52
NF = 5.96 × TCWV + 0.46	0.39	9.8	0.49
NF = 509.2 × TCLW + 0.39	0.24	10.9	0.34
NF = 157.5 × TCIW + 0.22	0.22	11	0.29
NF = 11.43 × TCC + 0.18	0.04	12.2	0.14
NF = 5.15 × LCC + 0.17	0.01	12.4	0.06
NF = 2.22 × SAT + 0.33	0.42	9.48	0.53
NF = 12.4 × q + 2 × TCWV + 69 × TCIW + 1.6 × TCC + 0.63	0.48	9.4	0.57

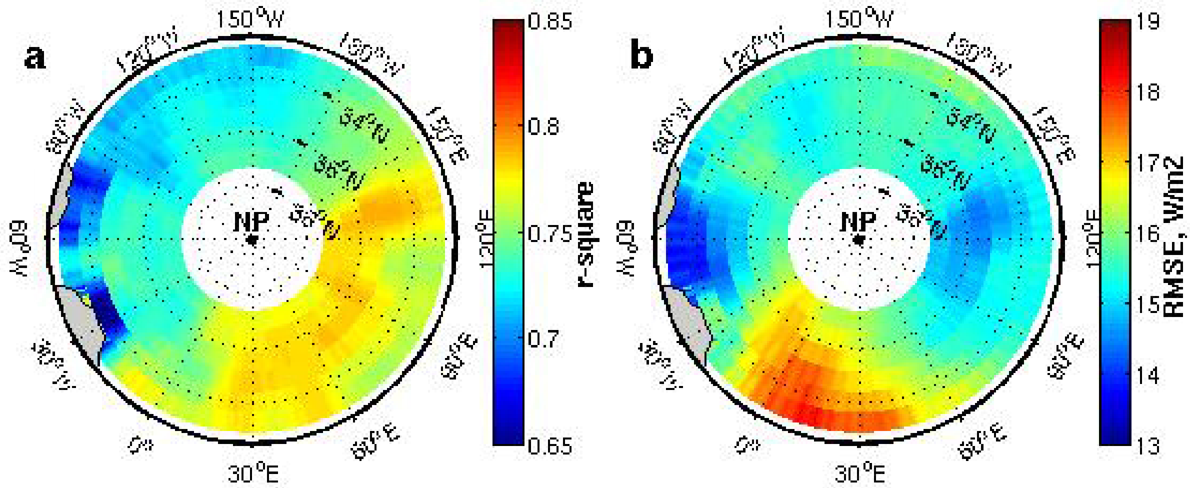

Figure 5.50: Best results from the stepwise multi-linear regression analysis. LWd is an explainable variable and 5 predictors: TCWV, near-surface specific humidity, TCIW, TCC and LCC. (a) fraction (r^2) of the temporal variance in daily LWd explained by any combination of these individual meteorological variables. (b) RMSE corresponding to the best combination of several individual meteorological variables [W/m^2].

Table 4. Factors best explaining the temporal and spatial variability (anomalies) in **skin temperature** (**SKT**) on top of compact sea ice during the 40-day pre-melt period (11 April - 20 May). Bilateral regression analysis was applied to the combination of all ERAI grid locations within 83.25-87°N and 20 years. Local anomalies in heat fluxes and meteorological variables were initially scaled by to the 20-year regional climatology.

Linear regression equation	overall r-square	RMSE [°C]	best local r-square
SKT = 0.1 × LWd - 0.08	0.72	2.0	0.81
SKT = 0.16 × NF – 0.16	0.32	3.0	0.5
SKT = 0.11 × LWnet – 0.14	0.35	3.0	0.47
SKT = - 0.04 × SWd – 0.1	0.28	3.2	0.39
SKT = - 0.18 × SWnet – 0.17	0.29	3.1	0.38
SKT = - 0.36 × LE – 0.004	0.08	3.5	0.14
SKT = 0.17 × H – 0.13	0.08	3.6	0.34
SKT = 1.97 × TCWV – 0.05	0.51	2.6	0.66
SKT = 3.6 × TCC – 0.13	0.05	3.7	0.08
SKT = 2.21 × LCC – 0.13	0.03	3.7	0.07

Discussion

In previous Section we have demonstrated that LWd and NF anomalies explained well the interannual and spatial variations in SMO timing. The aim of this Section was to reconstruct a longer chain of processes affecting/controlling SMO timing on top of compact Arctic sea ice.

The main conclusion of this Section is that 70-80% of the temporal variations in LWd are explained by the temporal variations in vertically integrated water vapour (TCWV) and ice water (TCIW) content, near-surface (2m) specific humidity, total and low-level cloud fractions (**Fig 5.50**). This result reflects the relationships as prescribed in ERAI and refers to a 40-day pre-melt period (mid April - mid May), and the central circumpolar Arctic (83-87^{o}N). The same individual meteorological variables (their anomalies) significantly correlated with SMO timing, when applying methods M1, M2 and/or M3. Thus the additional (less) moisture content, larger (smaller) cloud fractions and warmer (cooler) surface temperatures were suggested by ERAI in those years/areas when SSM/I-based SMO occurred early (late). This is a physically relevant interaction.

The choice of the pre-melt period (from 11 April to 20 May) was quite subjective. Our main arguments for this choice are the following. (1) Defined in this manner the pre-melt period most likely does not overlap with the melt season. (b) We expect that shifting, lagging, reducing, stretching of the "reference pre-melt period" would not dramatically change the correlation between the daily anomalies in meteorological variables and the daily anomalies in surface heat fluxes.

To note that the correlation between the individual meteorological variables and SMO was not affected by this choice, but rather could have been affected, *e.i.*, reduced (1) by errors/biases in rough MO retrievals, (2) by the errors in meteorological state variables in ERAI, (3) by our definition of the "reference SMO" date with M1, M2 and M1 in ERAI grid coordinates, and (4) by our assumption of a "fixed length" pre-melt period in each year.

We recognize that our methodology and conclusions were quite schematic. It is evident that there exist much more meteorological factors and more complex relationships than what we have addressed in our study. The initial objective was to explain the interannual and spatial variations in SMO within the vast Arctic Ocean. However and naturally - many limitations arose along the way. To allow the interpretation and strict reasoning we chose this schematic solution to demonstrate our ideas and several existing possibilities. Certainly more complex methodologies (with a more advanced SIC filter, and allowing variable duration of the pre-melt period) - may/will quantify the addressed relationships much better.

5.3 Trends in MO, SMO and surface heat fluxes

Over the past few decades a tendency towards earlier melt onset has been revealed with the remote sensed "blended" Melt Onset (MO) retrievals. *Anderson and Drobot* [2001] detected significant trends (1979-1998) towards earlier MO in the western central Arctic (8.9 days per decade), Lincoln Sea (4.4 days per decade) and Beaufort Sea (5.1 days per decade). *Belchansky et al.* [2004] calculated the difference between two decadal averages (1979-1988 and 1989-2001) and found earlier MO by 5 days in the Kara - northern Barents and Chukchi Seas, by 9 days in the East Siberian Sea, and by 4 days in the central Arctic with the perennial ice (**Fig 5.51**). A tendency towards later MO (positive trend) was found within the eastern central Arctic and in the central Beaufort Sea (**Fig 5.51**). More recently, also based on SMMR-SSM/I passive microwave record, *Stroeve et al.* [2006] and *Markus et al.* [2009] demonstrated statistically significant ($p < 0.01$) 30-year trends (1979-2007) by 2.5 days per decade in the central Arctic, and 3-4.5 days per decade in Kara, Laptev, East-Siberian, Chukchi and Beaufort Seas. According to our knowledge, reasons for the trends in MO have not been explained yet.

Our study focused on the circumpolar central Arctic (83-87^{o}N) in the period 1989-2008. 20-year linear fit (trend) at each pixel in rough 25 km resolution suggested a *20-year tendency* towards earlier MO ranging **locally between -8 and -18 days per decade** ($p < 0.01$), see **Fig 5.52a**. The regional average trend for those MO pixels with a complete 20-year time series was **13 days per decade**. Negative tendency in MO (towards earlier MO) was found within 83.4 x 10^3 km^2, that is only 5% of the circumpolar central Arctic area (83.25-87^{o}N).

There are three major differences in our results compared to *Markus et al.* [2009]:

(1) central Arctic domain is defined somehow differently,
(2) our study period is 20-year long (1989-2008) against a 29-year period in their study,
(3) this trend estimate is for each individual 25 km MO pixel with a complete 20-year record, whereas in their study the linear regression was applied to the "annual mean regional average MO" within the central Arctic.

When evaluating a *29-year trend* (1979-2007, $p < 0.01$) in the annual mean regional average MO we found a tendency of **-2.6 days per decade** within 80-87^{o}N. This compares well with the result reported by *Markus et al.* [2009] for the same period 1979-2007: with a 99% significant trend of 2.5 days per decade.

20-year tendency of SMO sample in ERAI grid coordinates was computed as well. To remind, SMO is the average of all rough MO pixels within a 130 km radius around each ERAI grid location. Only those rough MO pixels were considered which had minor (small/short) changes in sea ice concentrations (SIC) in a 40-day pre-melt period. Within the circumpolar central Arctic SMO trend was towards earlier seasonal transition as well: about **-8.8 days per decade** (**Fig 5.52b**). This is an area weighted regional average SMO trend. Negative SMO trends were found within 162 x 10^3 km^2, that is about 10% of the circumpolar central Arctic area (83.25-87^{o}N), **Fig 5.52b**.

To discuss a possible relationship between the trends in surface heat fluxes and trends in MO and SMO, again the reference period of the year should be determined first. When do we search for trends in surface fluxes: in February, in May or in June? In the other words: when changes in fluxes might trigger a better/weaker heat accumulation within the dry snowpack on top of sea ice? Moreover, if evaluating trends one should chose a "fixed" season to avoid the comparison of the heat fluxes in early spring in one year, and in late spring - in another years. In our example here we average the surface fluxes during a 30-day "pre-melt period" (21 April - 20 May) prior to the 20-year earliest SMO. Thus the 21st of May was the earliest local SMO in ERAI grid coordinates during 1989-2008. 20-year linear trend of the monthly mean heat fluxes at each ERAI grid location in illustrated in (**Fig 5.53**), all demonstrated results are significant at 99% confidence level.

Accordingly, in the period from 21 April to 20 May SWd, SWnet, H, DR and DF revealed significant 20-year trends within a portion of the study area (83-87^{o}N) not everywhere in the circumpolar central Arctic (**Fig 5.53**). The largest trends were found for SWd, DF and DR: reaching +15-20 W/m^2 per decade north of Greenland and in the Lincoln Sea (**Fig 5.53 c,e,f**). Interestingly, DR and DF trends are large and 99% significant and moreover - appear within the most of the study area (**Fig 5.53 e-f**). To note, over most of the study domain SWd trends were significant only at 95%, and these SWd trends are the primary cause of DR and DF trends! Trends in H and LWnet were negative (**Fig 5.53 a-b**), which is likely a result of increasing SWd and SWnet. Naturally a larger surface warming (by means of SWnet) enhances thermal emission (LWup), increases LWnet deficit (heat loss), reduces the near-surface inversion strength, and weakens the turbulent sensible downward heat sink. NF, LWd and LE trends (during 21 April - 20 May) were insignificant (neither at 99%, nor at 90% significance level), not shown.

In reality NF controls the interannual variability in SMO on top of compact sea ice, the regional (spatial) differences in SMO and any tendency in SMO. Our results showed that, although ERAI NF explained well the interannual and spatial variance in SMO (locally up to 65%, **Section 5.1**), NF (and neither LWd) does not explain the observed (significant) trends in SMO. And since other fluxes performed worse in terms

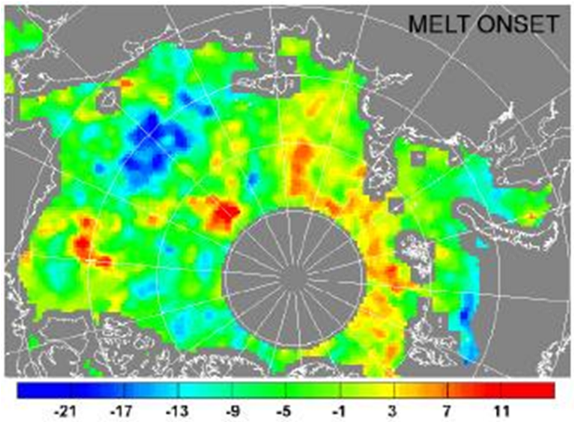

Figure 5.51: SSMR-SSM/I MO tendency in 1979-2001. Reprint from Belchansky et al. (2004). [Mean MO 1989-2001] minus [mean MO 1979-1988]. Blue-green colours reflect the tendency towards earlier MO and yellow-red colours represent the tendency towards later MO. Units [days]. MO is the apparent melt onset, including both, the divergent sea ice drift and the snow melt initiation on top of the compact sea ice cover.

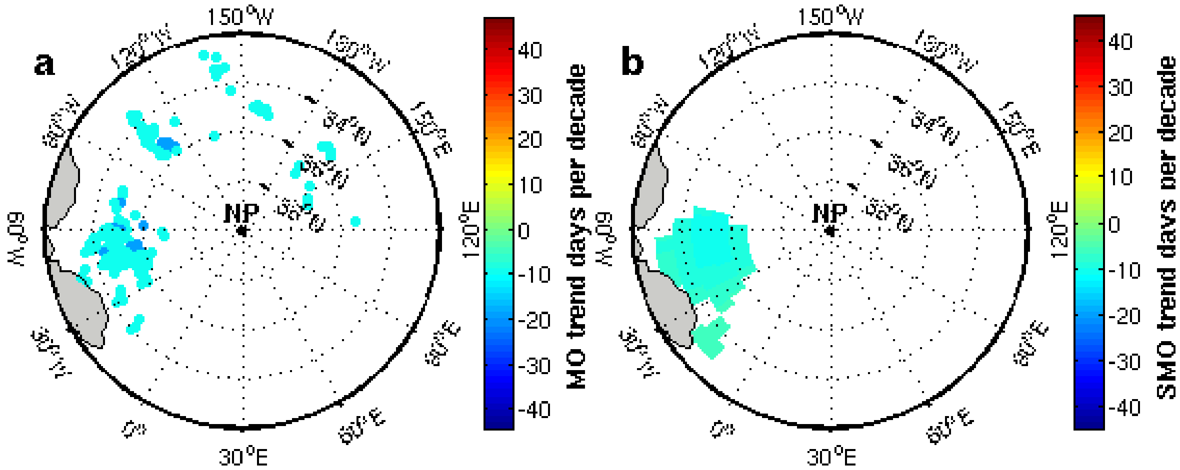

Figure 5.52: **(a)** 20-year linear trend in **rough MO** time series, calculated only for those MO pixels with a complete 20-year record. **(b)** 20-year linear trend in **SMO** (r130km, 40-day SICfilter of 85%), calculated only for all ERAI grid since there was a complete 20-year SMO sample everywhere. **Trends are significant at 99% confidence level**. Units: days per decade.

of the interannual and spatial SMO variance, we attribute this lack of the "expected" relationship to larger errors in those fluxes. In this situation, even if SWd, DR and DF have large and significant trends relevant in sign (strengthening of fluxes) and apparently in line with the negative SSM/I-based SMO tendency (towards earlier melt), we can not accept the hypothesis on the effect of SWd, DF and DR trends on SMO trends. Moreover, here we made an arbitrary choice for pre-melt period of 1 month (21 April 20 May). Certainly, that was a "first-guess", but not necessarily the optimum and best pre-melt period for the surface fluxes. We state that other methods with larger amount of data should be applied to study MO and SMO trends.

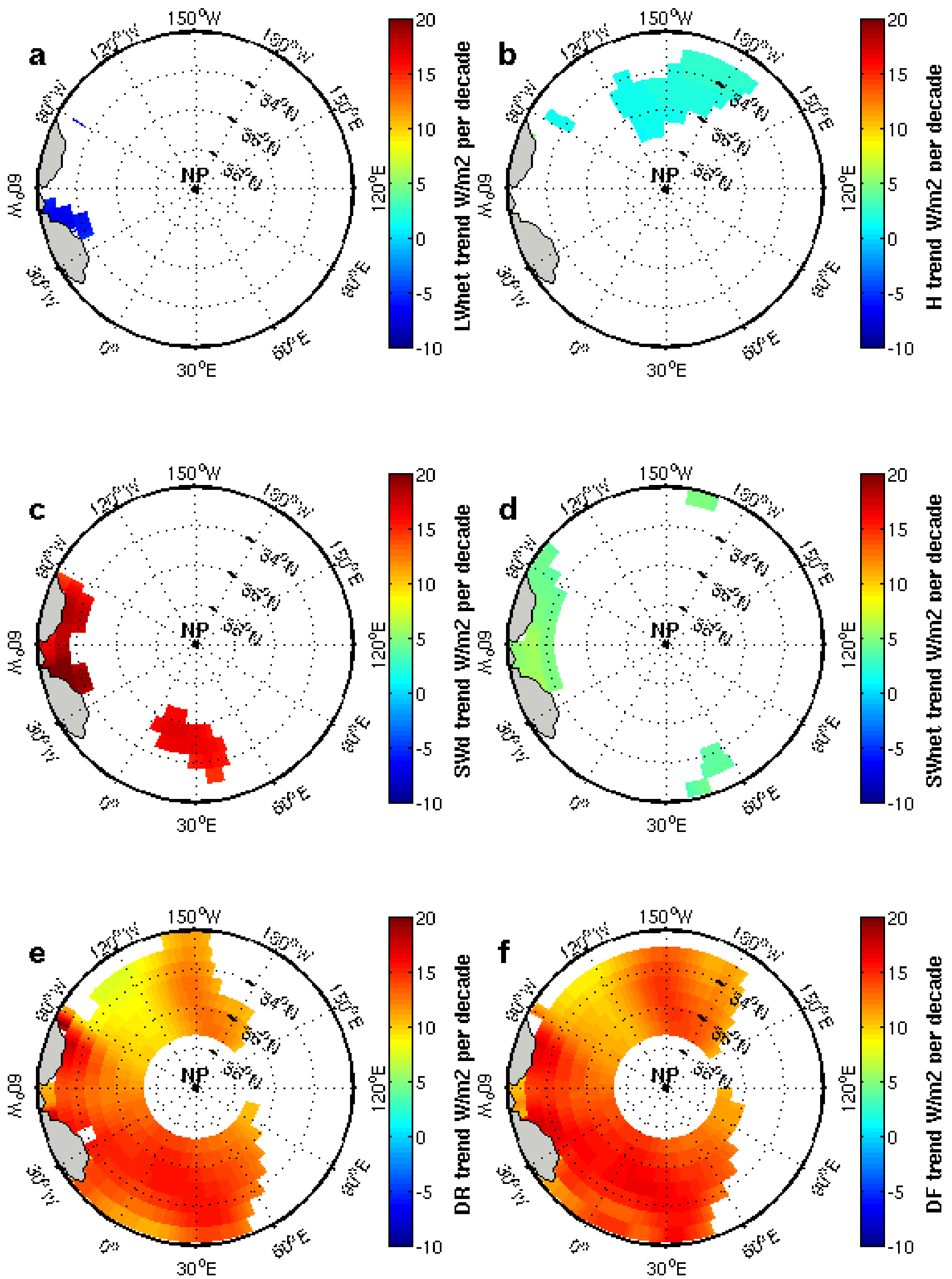

Figure 5.53: 20-year trends in surface heat fluxes, averaged over a 30-day pre-melt period (21 April-20 May), **significant at 99% confidence level**. **(a)** net longwave radiation, LWnet, **(b)** sensible heat flux, H, **(c)** downward solar radiation, SWd, **(d)** absorbed solar radiation, SWnet, **(e)** downward radiation, DR, and **(f)** downward flux, DF. ERAI reanalysis, 1989-2008, 83.25-87°N.

Interestingly, among the factors controlling SMO trends on top of compact sea ice are not only the surface heat fluxes, but also the snow and sea ice thickness. Naturally on top of thin (warm) ice slab the Snow Melt Onset requires smaller downward heat supply compared to the thick (cold) ice slab. So with a zero or even negative NF trend during the pre-melt period, there can be a tendency towards earlier SMO if the sea ice becomes thinner and thinner every year.

To note, the illustrated trends in fluxes report how ERAI represents surface fluxes, which does not imply that the same trends occur in a real world. There was a strong debate on the validity and reliability of trends in reanalysis (*e.g.* ERA-40) within the areas where almost no observational data were assimilated, such as the central Arctic northward from 82^{o}N [*e.g.* Serreze et al., 2007; Graversen et al., 2006, 2008a and 2008b; Bitz and Fu, 2008, Grant et al., 2008; Thorne, 2008; Screen and Simmonds, 2010a, 2010b, 2011b]. Although all these cited studies agree that there were warming trends in the central Arctic, in particular in spring and fall period, the reported magnitudes of trends differ and the altitudes with the strongest warming in the atmosphere depend on the vertical resolution of applied data sets. According to our knowledge, ERAI improved the meteorological component, but has not adopted a better sea ice scheme and likely, does not perform surface fluxes much better compared to ERA-40 in the central Arctic.

Conclusions

In this study we explored the contribution of the surface radiative and turbulent heat fluxes to the observed (SSM/I) spatial (50-130 km) and year-to-year variability in snow melt onset (SMO) on top of the sea ice within the circumpolar central Arctic and over a 20-year period (1989-2008). Many of the analyses and results presented here were not included in our paper on SMO (in press, *Journal of Geophys. Research*).

1. ERAI surface fluxes appeared to be useful in explaining the variability in SMO. High and causally relevant correlations were found between the heat flux anomalies (during the pre-melt period) and SMO timing. A larger NF and LWd and weaker turbulent (LE and H) heat loss from the surface occurred in those springs when earlier SMO was observed. Loceal anomaly in NF explained up to 65% of the interannual variance in SMO. LWd turned out to be the main term of NF, and explained alone up to 90% of the local interannual variance in SMO although within a limited area within the western central Arctic. This result is a strong indication of a good accuracy in both: LWd flux anomalies in ERAI, and our SMO sample deduced from the original MO data set by *Markus et al.* [2009].

2. The effect of turbulent heat fluxes on SMO was not to bring heat to the snow surface, but an anomalously small (large) heat loss favored earlier (later) SMO. 30-40 days average anomalies in H and LE explained, respectively, up to 72% and 56% of the local interannual SMO variance. In combination with radiative fluxes, LE and H increased the explained variance of SMO, still primary controlled by LWd. With a few exceptions, in general, in those areas where LE and/or H *best* explained local interannual SMO variance, the relevant time averaging (with the highest explained variance) was around 30-40 days. we say *best explained* if compared to the other individual fluxes and various combinations of individual fluxes.

3. When considered alone, the incident solar radiation (SWd) and the absorbed solar radiation (SWnet) were nowhere important factors for SMO variability in the central Arctic (83-87^{o}N). This result is reasonable because there is no snow melt and no ice melt in ERAI. So far the representation of diurnal and day-to-day variations in surface albedo, SWd and SWnet on top of the compact sea ice cannot be captured in ERAI, both before, during and after SMO. However, in reality already before the continuous snow melt establishes, the surface albedo and SWnet largely contribute to the net flux (NF) accumulation within the snow, thus affecting the SMO timing. Nevertheless, with the introduction of SWd in the multi-linear regression analysis, the year-to-year SMO variance was better

explained within most of the circumpolar Arctic. This implies that at least the sign of the year-to-year SWd anomalies is reasonably represented in ERAI.

4. We also examined the importance (effect, role) of the duration (length) and timing of the pre-melt period. The goal was to identify the most relevant time scales for each individual heat flux component and the combination of fluxes when the flux anomaly gives the best indication for SMO timing: early or late. Regarding NF, LWnet and LWd the most relevant time scale was about 1-7 days, whereas for H and LE it was around 30-40 days. Heat flux anomalies averaged over other time averaging periods (between 1 and 40 days) also explained a significant portion of SMO variance, but a smaller portion compared to demonstrated results. Duration of the pre-melt period longer than 40 days (prior to SMO) did not improve the capability of surface fluxes to explain SMO timing. None of the methods for determining the reference SMO date (M1, M2 and M3) appeared to be considerably better than the others.

5. The fact that 1-7 days average anomalies in NF, LWnet and LWd were best explaining SMO variance suggests that: (a) these fluxes and their anomalies are quite well represented in ERAI, *i.e.* with reasonable day-to-day variations, amplitudes and signs; and (b) that the longwave radiation (both LWd and LWup) in ERAI is, likely, more accurate than the other components of NF. We speculate that the effect of brief (1-7 days) flux anomalies on surface melt can be distinguished only if the fluxes and MO were well captured in both data sets (ERAI and SSM/I). In fact, if all fluxes were equally accurate in ERAI, NF would correlate with SMO better than any of its components or any combination of some of its components. Yet, this is not the case: individual fluxes and different combinations of them explained the interannual variance in SMO better than NF.

6. Relationships between the meteorological state variables and the main terms of the surface heat fluxes (affecting/controlling SMO timing) NF and LWd were considered. All meteorological variables were taken from ERAI reanalysis as well. Atmospheric moisture content (as presented in ERAI) appeared to be the major factor controlling the temporal and spatial diurnal LWd and NF anomalies. TCWV (2m specific humidity) accounted for 50% (60%) of the overall variance in LWd, locally explaining up to 63% (71%) of the temporal LWd variability. The cloud fraction accounted for 12-19% of the total variance in diurnal LWd anomalies, but had a very weak (negligible) effect on the day-to-day NF anomalies and surface temperatures. Thermal and moisture advection (as calculated here!) could not explain the temporal and spatial anomalies in LWd and NF. Surface (skin) temperature is tightly related to LWd over the compact sea ice in

ERAI with r^2 up to 0.82).

7. Interestingly the vertically integrated water vapour (TCWV) and the near-surface specific humidity were practically as important for SMO timing - as the anomaly in LWd, and much more important than the cloud variables (TCC and LCC). One would expect highest importance of LWd for SMO timing (the direct factor bringing heat to the surface), second highest - for the cloud variables, and relatively smaller effect of the moisture content on SMO. The moisture has to be condensed to clouds to have a notable (70-100 W/m^2) radiative forcing on LWd. However, vertically integrated and near-surface water vapour quantities are probably much more reliable in ERAI than cloud variables. In ERAI the water vapour results directly from model prognostic variables, and is constrained by data assimilation over the ocean areas, whereas cloud water/ice contents and especially cloud fractions heavily depend on the parametrization schemes, and are therefore much more liable to errors.

8. High and statistically significant relationships between SMO, surface fluxes and meteorological state variables were also found south of 83^{o}N and within the seasonal ice zone: Kara, Laptev, East-Siberian, Chukchi and eastern Beaufort Seas and the Baffin Bay. In these areas the NF and SWnet fluxes correlated with the "apparent" MO the best. In contrast to the central circumpolar Arctic (83-87^{o}N), where ERAI surface fluxes were least affected by SIC changes, in the southern areas ERAI SIC has ever dropped below 80% (and even down to 0%) at least once during the pre-melt period. As a result, when the ice concentration reduced, a stronger SW absorption by the open water contributed to the additional NF accumulation. In other words, southward from 83^{o}N the positive NF and SWnet flux anomalies during the pre-melt period were in some years (some individual days) due to sea ice opening. Hence, in some years the positive NF and SWnet flux anomalies at the open sea surface could not be a reason for the early Snow Melt Onset on top sea ice. Thus the statistically significant relationships were only partly due to the causal effect of fluxes on SMO. This result also indicates on the relevant estimation of surface heat fluxes in ERAI, at least the sign of the flux anomaly, both in totally and partially ice-covered areas. This result motivated the introduction/development of a "SIC filter" to distinguish between the "pure" Snow Melt Onset on top of compact sea ice and the divergent ice drift.

9. Examination of the large 30-90 day spatial differences in the MO timing within 50-100 km distance suggested that they are primarily, but not entirely due to opening of leads or polynyas. Comparison of some large MO spatial gradients with the surface fluxes on the Pacific side of the Arctic Ocean (70-85^{o}N) revealed

a few large flux gradients across the areas of abrupt MO gradients, associated with atmospheric fronts and not related to any SIC changes (ERAI). Yet, these short-lived and very localized spatial gradients in NF and H (by up to 25 W/m^2 within 50 km distance) do not convincingly explain the SMO gradients of one month within a 50 km distance. Instead, spatial differences in the ice type could have been a reasonable explanation for these pronounced MO gradients within a totally ice-covered region. Naturally, with the same meteorological forcing SMO starts earlier on top of thinner (warmer) ice, compared to thick multi-year ice.

10. Local MO and SMO trends up to -13 and -9 days per decade respectively were found within a limited area where complete 20-year MO and SMO time series were available. Long term SMO trends should, in principle, be explainable by NF trends: with a larger surface heat gain (positive NF anomaly) producing earlier snow melt (negative SMO anomaly), and vice versa. However SMO trends could not be reasonably explained by ERAI surface heat fluxes. Certainly our simplified methodology could have imposed some crucial limitations for this kind of analysis. Moreover, we stress that the trend estimates strongly depend on the method applied and should be considered with caution. Another important and interesting aspect regarding trends, is that SMO trends may have occurred (at least partly) due to to sea ice thinning, even simultaneously with the negative NF trends.

11. Our results were based on two independent data sets (ERAI and MO), both of quite high spatial (25-100 km) and temporal resolution. Errors detected in ERAI near-surface air temperature and moisture during summer [*Lupkes et al.*, 2010] and simplified SIC representation north of 83^oN indicate that neither surface fluxes are free of errors. However, a good aspect in reanalysis is that the same model and data assimilation system were applied throughout the period, resulting in a spatially and temporally consistent data set. It is unlikely that errors in the surface fluxes could generate artificially improved correlations between the fluxes and SMO. Instead, errors in surface fluxes, in MO detection, ice type classification in the MO algorithm, and our SMO sampling should have increased the scatter in the relationship between SMO and the heat fluxes, thus, reducing correlations.

Study of the divergent ice drift was beyond the scope of present study.

Perspectives

Three reanalysis data sets were used during this work: NCEP/NCAR, ERA-40 and ERAI. Comparison of surface heat fluxes between these three reanalysis was demonstrated in Chapter 1. However, due to time limitations we could not conduct the same exercise as we did for SMO and ERA Interim, but with NCEP/NCAR and ERA-40. In fact, this could be interesting to do. However, to remind, the comparison of SMO and surface heat flux anomalies is not a conclusive validation of either data sets. Our exercise suggested an alternative and justified point of view on the data sets of SSM/I-based Melt Onset and ERAI surface heat fluxes, however without any quantitative evaluation of their errors. Years 1979-1988 and since 2008 could be added in this analysis with ERAI, as well as the other meteorological reanalysis time series, for example JRA-25, NCEP-DOE, NASA's MERRA and NCEP-CSFR.

If considering the effect of meteorological conditions on LWd, NF and SMO, it is of evidence that there exist much more meteorological factors and more complex relationships, rather we have addressed in our study. Thus LWd varies non-linearly with the cloud fraction, the cloud droplet size, liquid water path and the cloud-base height, *i.e.* cloud bottom temperature [*Zhang et al.*, 1996; *Curry*, 1995; *Francis and Hunter*, 2007; *Garrett et al.*, 2009]. It could be of interest to apply/introduce some of these variables in further studies addressing the meteorological effect on SMO timing. Moreover, it is questionable: why we could not detect the effect of the horizontal thermal and moisture advection on LWd, NF and SMO? We suggest that another calculation method should be used for thermal and moisture advection.

Our study highlighted that SMMR-SSM/I-based Melt Onset data by *Markus et al.* [2009] is a blend of two totally different processes: Snow Melt Onset on top of the compact sea ice (radiative origin), and Divergent Ice Drift (dynamic origin). We used the daily data on sea ice concentrations to distinguish between these two processes. However it is of evidence that a more precise distinction between SMO and divergent ice drift is needed. To provide this distinction we suggest to take into account the ice drift data in combination with the sea ice concentrations, and likely including in the "SIC filter" the MO day itself as well.

Successful distinction between SMO on top of sea ice and the divergent ice opening will allow a further study of the *factors controlling these events*.

Ice thickness (type/age) versus SMO. Regarding the SMO, the following step could be the evaluation of the effect of surface heat fluxes on SMO variance on top of different sea ice types (thickness, age). The data on ice type, thickness and ice age data should be, first of all, based on SMMR-SSM/I observations, so it could be easily compared with SMMR-SSM/I based SMO retrievals. Yet, other ice type, ice thickness and ice age products may support such a study as well.

Better distinction between SMO and divergent ice drift may also allow a further study of their long-term tendencies. According to our knowledge, at the moment there is no solid explanation for the observed MO/SMO trends in any part of the Arctic Ocean. An interesting and open question is: whether there is a tendency towards earlier spring ice break-up? And if it is the case: whether and how the earlier spring ice break-up is related to (a) a changing dynamic stress, *e.i.* faster sea ice drift, (b) earlier SMO on top of sea ice, and/or (c) general sea ice thinning?

It is possible that any/this algorithm for MO detection [here by *Markus et al.*, 2009] developed for two ice types can be biased due to this sea ice type detection. The question arises: whether this ice type detection could have affected the long-term trends and the interannual variance in SMO on top of the ice? In the other words: in those areas where MYI type was replaced by the FYI type can we have an "artificial" SMO trend generated by the algorithm itself?

Active MW detection (SAR) of SMO timing has a great potential, suggesting a much better spatial resolution (hundreds of meters). However these rough backscatter time series exist only since 1991 (compared to 1979 with SMMR), and according to our knowledge there is no ready-to-use MO time series native from active MW observations.

Throughout this manuscript we highlight that the spring SMO timing (early or late) has a strong effect on the total ice ablation during the melt season and also contributes to September ice minimum. It could be of interest to evaluate the effect/consequences of SMO timing on further surface (skin and near-surface) temperatures, timing of first ice break-up and summertime sea ice concentrations. Likely this kind of analysis will require some satellite retrievals of these quantities, rather than meteorological reanalysis data sets. How far the effect of SMO timing propagates along the season?

List of variables

DF : surface downward radiation, is a sum of SWd, LWd, LE and H
DR : surface downward radiation, is a sum of SWd and LWd
ERAI : ERA Interim reanalysis
FYI first-year ice
H : surface turbulent sensible heat flux
LCC : low-level cloud cover [fraction]. In ERAI it is the analysis quantity, each value is an instantaneous value valid at the time of analysis. The average of four analysis values (0h , 6h , 12 and 18h) is the daily average.
LE : surface turbulent latent heat flux
LWd : surface downward longwave radiation (also called thermal or infrared), in the electromagnetic spectrum it is between 4 and 50 m wave length
MAD : horizontal moisture (specific humidity) advection
MO : apparent Melt Onset detected with the remote sensing, units [Julian day]
MYI : multi-year ice
NF : surface net flux
RMSE : root mean square error, which is the standard (typical) error of the linear regression model with one or several predictors (explaining variables)
SAT : near-surface air temperature at about 2 m height
SIC : sea ice concentration [percentage within the pixel] or [percentage within of the grid cell covered by sea ice].
SMO : Snow Melt Onset on top of sea ice, units [Julian day]. One value at each location each year.
SWd : surface downward shortwave radiation, within 0.2 4.0 m wave length
SSM/I : Special Sensor Microwave Imager
TAD : horizontal thermal advection
TCC : total cloud cover [fraction]. In ERAI it is the analysis quantity, each value is an instantaneous value valid at the time of analysis. The average of four analysis values (0h , 6h , 12 and 18h) is the daily average.
TCIW : total column ice water content [kg/m2]. It is a vertically integrated value, and is produced as a forecast quantity valid at the instantaneous end time of the forecast. For our study we took the values twice daily: 0+6h and 12+6h. Daily mean is the average of these two values.
TCLW : total column liquid water content [kg/m2] is a vertically integrated value, produced as a forecast quantity valid at the instantaneous end time of the forecast (+12h). For our study we took the values twice daily: 0+12h (valid at 12 UTC) and 12h+12h (valid at 00 UTC).
TCWV : total column water vapor [kg/m^2]. Is the analysis quantity with 6h intervals, four times daily : 0h, 6h, 12 and 18h. Daily average is the average of four values.
q : near-surface (2m) specific humidity, units [g/kg]

Appendix 1

Thermal advection at the central grid location: formulation

Entering data are the daily air temperatures at pressure levels [K], u wind (eastward wind component) and v wind (northward wind component) vectors [m/sec]. +u wind component is from West to East, and +v component is directed from South to North. Potential temperature (Θ) at 6 pressure levels is calculated first (at 500mb - 1000mb with a 100 mb step).
Daily potential temperature (Θ) at each location, each pressure level (for example at the 500mb level) and each day of the year is calculated as:

$$\Theta 500 = T500 * \left(\frac{1000}{500}\right)^{0{,}286} \tag{5.1}$$

here T500 is the air temperature at 500 mb given geopotential height.

Heat advection in the central grid point is calculated as:

$$-V \times \bigtriangledown\Theta = -u\frac{\partial\Theta}{\partial x} - v\frac{\partial\Theta}{\partial y} \tag{5.2}$$

∂x is the length [km] between the neighboring grid locations at 1.5 distance along given latitude circle (2 times 0.75lat) and ∂y is the length [km] between the neighbouring grid locations to the north and south of our central grid location (always 160 km).
$\partial\Theta$ is the difference in Θ between the east and west (E minus W), or north and south (N minus S).
u and v are the wind components at the central grid point.
Thermal advection is in [C per day].
The effect of the altitude on the distance between the neighboring locations along the same latitude circle is neglected. Thus the additional 1-5 km altitude changes the resulting horizontal distance by only about 0.01 km.
We suppose that if horizontal advection below 500 mb does not affect surface fluxes and SMO, neither the advection at the upper levels does.

Appendix 2

Moisture advection at the central grid location: formulation

Specific humidity (q) advection is calculated in the same way as the thermal advection with ∂q instead of $\partial \Theta$.
Initial data are the relative humidity f and air temperature T at 6 pressure levels.

$$q = \left(\frac{0.6224 * e}{P - 0.3776 * e} \right) * 1000 \tag{5.3}$$

q in [g/kg]
e is the is the partial water vapour pressure in [hPa]
P is the geopotential heigh in [hPa]

$$e = \frac{f * e_w}{100} \tag{5.4}$$

f is relative humidity [%]
e_w is the saturation vapour pressure in [hPa]

$$e_w = 6.112 * \exp^{\frac{17.62*T}{243.12+T}} \tag{5.5}$$

T is the air temperature at given geopotential height in [C]
Moisture advection is in [g/kg per day]

Appendix 3: Wintertime near-surface freezing conditions

This section reflects the major results obtained during the early phase of this PhD work. Relationship between the warming trends in air temperatures and retreating and thinning Arctic sea ice was questioned. *How the warming could be translated into sea ice extent and/or ice thickness change?*

At this stage we considered the entire maritime Arctic (60 - 90^{o}N) and the near-surface air temperatures from NCEP/NCAR reanalysis. Daily air temperatures at the lowest model (0.995 sigma) level were chosen, with the spatial resolution of 2.5^{o}lat by 2.5^{o}longit in the period 1979-2008. To note, the vertical sigma coordinate is a terrain-following and convenient for a study of the near-surface processes over a flat surface, for ex., ocean. The 0.995 sigma surface is a level of about 5 hPa above the ground, but it is not a geopotential surface. Representation of the sea ice fraction is very schematic in NCEP/NCAR (either 0%, or 100% ice coverage) and this should strongly affect the near-surface air temperature at 2m height. By choosing a higher level we expected to reduce the effect of the sea ice fraction on the air temperature.

Naturally the sea ice formation is a complex processes. Our objective was to try to find/define some simplified meteorological *index* that could explain some portion of the observed variations and/or changes in sea ice extent and/or ice thickness. Without inventing something new, we applied the method of freezing degree days described by *Maykut* [1986]. Cumulative number of Freezing Degree Days was calculated here for 30 freezing seasons (1979/80 - 2007/08) at each NCEP/NCAR grid location. Where freezing degrees for each day is just the temperature below the freezing point (set to -1.7^{o}C everywhere). Sum of daily freezing temperatures during one freezing season resulted in one FDD value each year at each grid location. The freezing season was schematically defined as the period between the 1st of September and the 31st of May the following year. The units of FDD are in [^{o}C per season].

Thus as the beginning of the freezing season, if there is no ice, the initial ice growth maybe described by the air temperatures alone [*Maykut*, 1986]. Depending on the intensity (temporal evolution) of FDD accumulation, when FDD reaches 500^o the ice thickness by this time attains about 30-75 cm. So far 1000 FDD corresponds to accumulated ice thickness of 60-110 cm (if there is no snow on top).

Cumulative number of FDD in 6 freezing seasons out of thirty are reflected in **Fig 5.54**. These maps nicely demonstrate the climatology of the near-surface thermal conditions: with the cold core within the western Arctic (FDD values are about 6000-8000) and rather mild freezing conditions within the eastern Arctic (with FDD values of 4000-6000). The striking fact is that FDD values seem to reduce (non-linearly) from one year-to-another along the 30-year period. 30-year linear trend in FDD is towards FDD reduction by 30 [^{o}C per season] per year within the central Arctic (north of 85^{o}N), reaching 45-60 FDD per year within the East-Siberian - Chukchi - western Beaufort Seas (**Fig 5.55**). This is in line with the results by *Lindsay and Zhang* [2005] who have found near-surface warming trends of 3^{o}C per decade during fall in the period 1988-2003, also with NCEP/NCAR reanalysis.

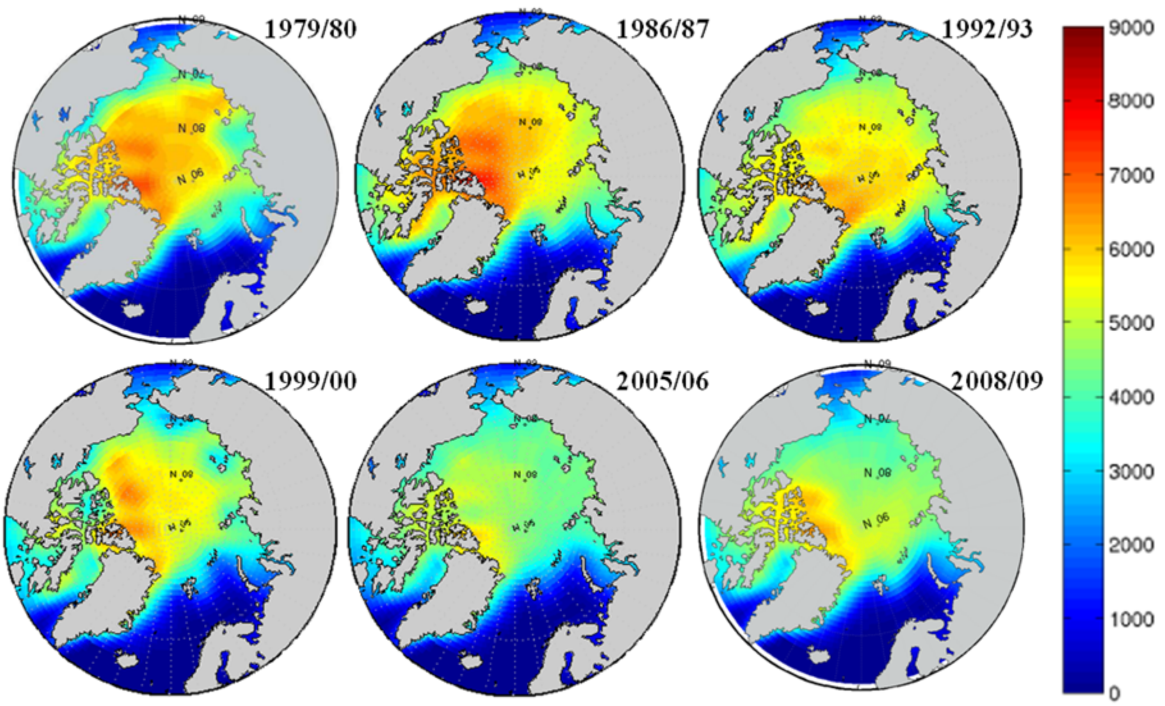

Figure 5.54: Cumulative number of Freezing Degree Days (FDD) during 1 Sept - 31 May period. Computed from NCEP/NCAR 0.995 sigma level air temperatures.

Naturally if FDD reduces it is either due to the warming in some period of the freezing season, or due to shortening of the freezing season, or (likely) due to both warming and shortening. So it was of interest to establish: *in what part of the freezing season these changes in FDD take place*? In fact, springtime near-surface warming (in March-May) likely does not have much effect on sea ice formation, because all the region if well ice covered with the snowpack on top. However if changes (warming) occur during the early freezing season (Sept-November), for example due to retarded fall freeze-up, then the consequences of the delayed freeze-up (and smaller FDD) may have an impact on total sea ice accumulation by the end of the freezing season.

The spatial occurrence of each FDD value can be represented with a spatial distribution curve. Thus we computed the sum of all grid box areas in [km^2] with FDD values falling within one of the pre-determined intervals. The example for three years

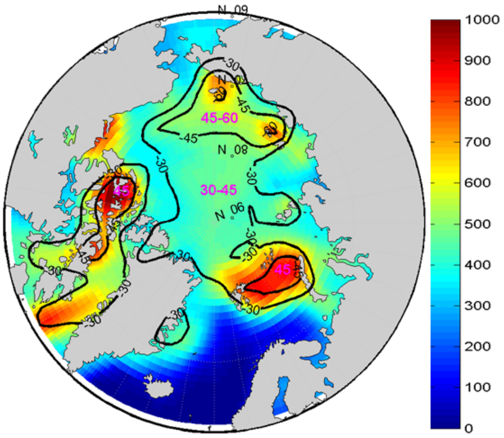

Figure 5.55: Cumulative number of Freezing Degree Days (FDD) during 1 Sept - 31 May period. Standard deviation (in color) and linear trend (contours) of 30 FDD values (30 years) at each grid location in the period 1979/1980-2007/2008. Linear fit is in [FDD per year], significant at 95% confidence level.

is given in **Fig 5.56**.

This technique with the spatial distribution curves was applied to compare three periods of the year (fall, winter and spring) and different decades (**Fig 5.57**). Each curve reflects the typical FDD conditions within the entire region (60-90^{o}N) in one decade. The most spatially popular FDD values within the region are marked by peaks in curves. Very small values (below 300 FDD) naturally are very popular since we have included much of the ice free areas (Greenland and Barents Seas) in our analysis. We found that in all three periods (fall, winter and spring) the entire curve and their peaks shifted to the left, towards smaller FDD values. This means that the large (cold) FDD became less spatially popular, whereas smaller (warmer) FDD became more spatially popular than it was before. To summarize this result: changes (reduction/warming) in FDD are similarly redistributed between fall, winter and spring periods. We found no strong indication that warming occurs in some specific period of the freezing season (fall, winter or spring).

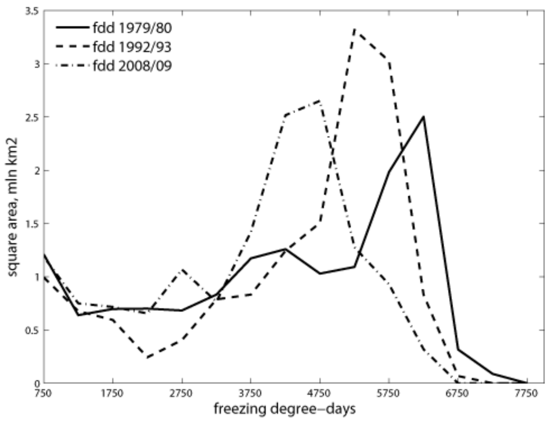

Figure 5.56: Annual accumulation of FDD over the maritime Arctic in three freezing seasons. Each curve means some particular year and each point on the curve is the area (Y axis) occupied by the given value of FDD (X axis) at the end of the freezing season (in May).

As we said, changes in FDD accumulated by the end of the freezing season is either due to overall warming, either due to shortening of the freezing season. Relevant issue (lengthenning of the melt season) has been investigated by *Smith* [1998] with the remote-sensing (SSMR-SSM/I data). Accordingly *Smith* [1998] there was a significant tendency towards delayed fall freeze-up during the 1980s - 90s. So at the next step we examined the length of the freezing season in relation to FDD.

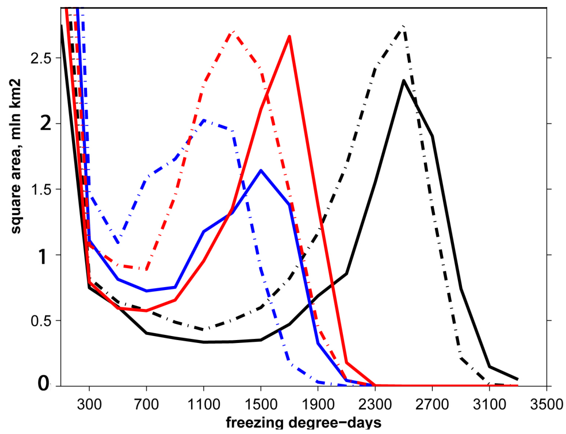

Figure 5.57: Spatial distribution of local FDD values around the region (60-90N). Local FDD values are compared here. The peak in curves indicates the "most popular/frequent" FDD values within the region. Sept-Oct-Nov (blue), Dec-Jan-Feb (black) and Mar-Apr-May (red). Plain curve represents the the decadal average 1979-1988. Dashed-dotted curve reflect the decadal average in 1999-2009.

The question arose: *how to define the beginning and the end of the freezing season*? Do we take the near-surface air temperatures below freezing point as the starting/last day of the freezing season? Do we refer to sea ice concentrations in NCEP/NCAR? Knowing the limitations of the near-surface air temperature and sea ice issues in NCEP/NCAR - probably these are not the best ideas. Can we use then some remote sensed sea ice concentrations to determine the day when sea ice starts to form? At this stage SSM/I-based freeze-up and melt onset became of interest. **Fig 5.58a** illustrates the correlation strength between the annual FDD values and the corresponding timing of first (early) fall freeze-up. Fall freeze-up is SMMR-SSM/I-based data set developed by the group of Stroeve, Markus and Meier, in principle similar to their apparent Melt Onset data set. To note, at that moment this Freeze-up data set was the only available for our study period. Accordingly the fall freeze-up is a definite instance (Julian day) of the year when sea ice appears within given 25 km SSM/I pixel. All pixels within 50,100,150,200,250 and 300 km were averaged to define the average freeze-up date at each NCEP/NCAR grid location. 250 km scale suggested the best correlation strength (between freeze-up and FDD). Accordingly negative correlations were found in the marginal seas (northern Barents, northern Kara, Laptev, Chukchi, southern Beaufort Seas). Thus FDD values were smaller (negative anomaly) in those years (winters) when fall freeze-up occurred later (positive anomaly). This is a logic result. Locally the correlations were up to 0.6.

Similar exercise was done with the fall FDD (accumulated during September-November period). The correlation between fall FDD and freeze-up timing is even more pronounced, with the correlations reaching -0.8 within the marginal seas, and significant correlations found within the most of the Arctic Ocean (**Fig 5.58b**).

To summarise: we established that fall freeze-up affects the interannual variability in

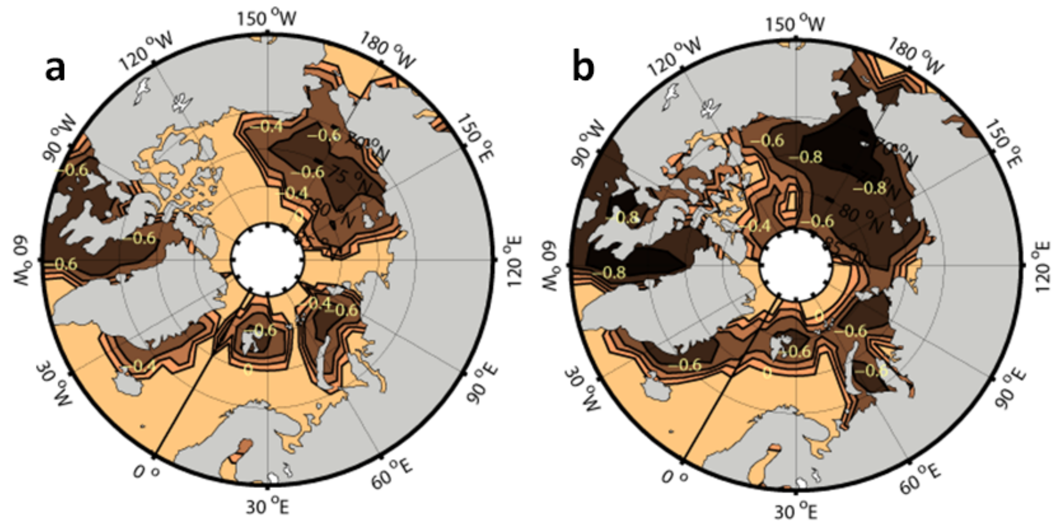

Figure 5.58: Correlation between NCEP/NCAR FDD and SSM/I-based fall Freeze-up. Freeze-up is the average of all 25 km pixels within 250 km radius around each NCEP/NCAR grid location. Period 1979/80-2007/08. Naturally, the fall freeze-up corresponds to the early part of the corresponding freezing season. The hole around the North Pole is where there were no SSMR-SSM/I observations.
(a) FDD is accumulated by the end of the freezing season (September-May).
(b) FDD is accumulated during September-November months only.

total FDD (accumulated by the end of the freezing season) within the marginal Arctic seas. Warming trends in FDD are in line with the tendency towards later ice formation in fall. However to note, both shortening of the freezing season and the overall warming (smaller FDD) were responsible for the reduction in FDD.

To continue - fall freeze-up appeared to dominate the interannual variability in fall FDD. And in fact - it is in fall when the fastest ice formation takes place! To specify: the strongest reduction in FDD during fall is located in the same region where the correlation between fall FDD and freeze-up is the largest.

No relationship was found between the total FDD (accumulated by the end of the freezing season) and the following spring Melt Onset timing. Rough MO data in 25 km resolution was applied to this analysis produced by *Markus et al.* [2009]. This indicates that FDD likely does no affect the timing of the following spring melt onset.

This FDD study suffered from several non-negligible aspects that complicated the reasoning about the importance of FDD trends in sea ice formation or any other changes in sea ice. First: the reduction of FDD from 5000 to 4000 in 30 years is difficult to translate in terms of sea ice thickness. Starting from about 60-100 cm thickness, the ice floe is insensitive to the atmospheric cooling, especially if it is snow covered. Second, the largest FDD trends occurred in those areas where the standard deviation (typical interannual variations) in FDD values is very large as well, of ±1000 FDD around the average (**Fig 5.55**). So, even if the trend is significant, it is too small compared to the typical interannual variations, and can not be "seen"/translated/compared in/to the changes in the sea ice condition in those areas with large 45 FDD trends. Third, we should note that these -30-45 FDD/year trends refer to the period of about 270 days (from September to May), which is only a little daily warming. Reduction by 30 FDD per year is about 0.1^{o}C of daily mean (or monthly mean) warming per year^{-1} (if uniformly distributed warming along the season). This is likely not comparable to reanalysis biases and errors in air temperature.

One may argue that warming of the lower troposphere could be important for the ice formation within leads and polynyas during winter. This is true, however the reduction in total FDD is only 0.1^{o}C in terms of the monthly mean warming. This value is likely not large enough to play a notable role in the wintertime sea ice production.

In turn, we faced the following question. *If the fall freeze-up is so important, what controls its timing*? *What may affect the earlier-later sea ice formation*? Anyway, in the conditions of polar night and intense surface (ocean) cooling ice formation starts at some moment. Timing of the polar night is the same each year. However, the amount of ocean heat can be different, and this is possibly/likely a cause of the interannual and temporal variability in fall freeze-up timing?

These results and reasoning briefly demonstrated the ideas that brought us to the Melt Onset study. We do not show here, but the spring Melt Onset appeared to correlate with the following fall freeze-up in the Arctic Ocean. Thus earlier MO (SSM/I) occurred in those years/areas where following fall freeze-up (SSM/I) was delayed. Also quite reasonable relationship.

Our FDD study was further developed/continued by CLIMPACT group who investigated the temporal changes in FDD (also called freezing index) within a dozen of global climate models and with several climate change scenarios. Non-linear statistical relationships between the summer minimum sea ice extent, summer (June) near-surface air temperature and FDD were applied in their study. However it should be noted, the study by CLIMPACT group showed that the summer minimum sea ice extent does not correlate with FDD accumulated during preceding winter. Neither we found no correlation between the total and/or fall FDD and the following fall freeze-up. Thus FDD alone did not appear to be an appropriate indicator/predictor of/for the summer minimum sea ice extent. However, this FDD index may serve as a good indicator of the general wintertime freezing conditions within vast regions (best without much pretension on the effect on sea ice cover). This idea was implemented in the study by CLIMPACT group, and finalized by Malaak Kallache. This paper by Malaak Kallache is attached here, where I contributed with the meteorological (FDD) Section.

Bibliography

1. Adams, J. M., N. A. Bond, and J. E. Overland (2000), Regional Variability of the Arctic Heat Budget in Fall and Winter J. Climate, 13 (19), 3500-3510, doi: 10.1175/1520-0442(2000)013<3500:RVOTAH>2.0.CO;2.
2. AIDJEX Bulletin, 32, First Data Report (1976): Oceanic Mixed Layer Characteristics.
3. Alam, A., and J.A. Curry (1998), Evolution of new ice and turbulent fluxes over freezing winter leads. J. Geophys. Res., 103 (C8), 15.783-15.802, doi:10.1029/98JC01188.
4. Alam, A., and J.A. Curry (1997), Determination of surface turbulent fluxes over leads in Arctic sea ice. J. Geophys. Res., 102 (C2), pp 3331-3344, doi:10.1029/96JC03606.
5. Ambach, W., (1974), The influence of cloudiness on the net radiation balance of a snow surface with high albedo. J. Glaciol., 13(67)
6. Anderson, M.R., J.L. Busse, and S.D. Drobot (2010), A comparison between SSM/I passive microwave melt onset dates and satellite-derived albedo melt onset dates in the Arctic. Int. J. Rem. Sens., 10.1080/01431161.2010.542198
7. Anderson, M.R. and S.D. Drobot (2001), Spatial and temporal variability in snowmelt onset over Arctic sea ice. Ann. Glaciol., 33, 74-78, doi: 10.3189/172756401781818284.
8. Anderson, M.R. (1987), The onset of spring melt in first year ice regions of the Arctic as determined from Scanning Multichannel Microwave Radiometer data for 1979 and 1980. J. Geophys. Res, 92 (C12), 13,153-13,163, doi: 10.1029/JC092iC12p13153.
9. Andreas, E.L., P.S. Guest, P.O.G. Persson, C.W. Fairall, T.W. Horst, R.E. Moritz and S.R. Semmer (2002), Near-surface water vapor over polar sea ice is always near saturation, J. Geophys. Res., 107 (C10), 8033, doi:10.1029/2000JC000411.
10. Andreas, E. L, and S. F. Ackley (1982), On the differences in ablation seasons of Arctic and Antarctic sea ice. J. Atmos. Sci., 39, 440-447.
11. Arkin, P., and E. Kalnay (2008), Re-analysis of historical climate data for key atmospheric features. Climate Change Science Program, Synthesis and Assessment Product 1.3, Ch. 2.
12. Armour, K.C., I. Eisenman, E. Blanchard-Wrigglesworth, K.E. McCusker, and C.M. Bitz (2011), The reversibility of sea ice loss in a state-of-the-art climate model. Geophys. Res. Lett., 38, L16705, doi:10.1029/2011GL048739.
13. Armstrong, A.E., L.B. Tremblay and L.A. Mysak (2003), A data-model intercomparison study of Arctic sea-ice variability. Clim. Dyn., 20, 465-476, doi: 10.1007/s00382-002-0284-2.

14. Barber, D.G., Iacozza J., and A.E. Walker (2003), Estimation of snow water equivalent using microwave radiometry over Arctic first-year sea ice. Hydrological processes, vol. 17, n17, pp. 3503-3517, doi: 10.1109/IGARSS.2002.1026866.

15. Barber, D. G., A. K. Fung, T. C. Grenfell, S. V. Nghiem, R. G. Onstott, V. I. Lytle, D. K. Perovich, and A. J. Gow (1998a), The role of snow on microwave emission and scattering over first-year sea ice, IEEE Trans. Geosci. Remote Sens., 36(5), 1750-1763.

16. Barber, D.G. and A. Thomas (1998b), The influence of cloud cover on the radiation budget, physicalproperties, and microwave scattering coefficient of first-year and multiyear sea ice. Geosci. and Rem. Sens., IEEE Transactions, 36 (1), pp. 38-50, doi: 10.1109/36.655316.

17. Barber, D.G., S.P. Reddan and E.F. LeDrew (1995), Statistical caracterization of the geophysical and electrical properties of snow on landfast first-year sea ice. J. Geophys. Res., 100 (C2), doi:10.1029/94JC02200.

18. Barber, D.G., T.N. Papakyriakou, and E.F. LeDrew (1994), On the relationship between energy fluxes, dielectric properties, and microwave scattering over snow covered first-year sea ice during the spring transition period. J. Geophys. Res., 99 (C11), 22,401-22,412, doi:10.1029/94JC02201.

19. Barrie, L.A. (1986), Arctic air pollution: an overview of current knowledge. Atmos. Environ., 20 (4), pp 643-663, doi:10.1016/0004-6981(86)90180-0.

20. Barry, G. R. (1986), The meteorlogy of the seasonal sea ice zone. In Geophysics of Sea Ice, edited by N. Untersteiner, pp. 993-1020, NATO ASI Series, New York.

21. Beesley, J.A., (2000a), Estimating the effect of clouds on the Arctic surface energy budget. J. Geophys. Res., 105 (D8), p. 10,103-10,118, doi:10.1029/2000JD900043.

22. Beesley, J.A., C.S. Bretherton, C. Jakob, E.L Andreas, J.M. Intrieri, and T.A. Uttal (2000b), A comparison of the ECMWF forecast model with observations at SHEBA. J. Geophys. Res., 105 (D10), 12,337-12,349, doi: 10.1029/2000JD900079.

23. Beesley, J. A., and R. E. Moritz (1999): Towards an explanation of the annual cycle of cloudiness over the Arctic Ocean. J. Climate, 12 (2), pp. 395-415, doi: 10.1175/1520-0442(1999)012<0395:TAEOTA>2.0.CO;2.

24. Belchansky, G. I., D. C. Douglas, and N. G. Platonov (2004), Duration of the Arctic Sea Ice Melt Season: Regional and Interannual Variability, 1979-2001. J. Climate, 17, 67-80, doi: 10.1175/1520-0442(2004)017

25. Bitz, C. M., and Q. Fu (2008), Arctic warming aloft is data set dependent. Nature 455, E3-E4, doi:10.1038/nature07258.

26. Bitz, C. M., and G. H. Roe (2004), A Mechanism for the High Rate of Sea-Ice Thinning in the Arctic Ocean, J. Climate, 17, 3622-3631.

27. Bitz, C. M., D.S. Battisti, R.E. Moritz, and J.A. Beesley (1996), Low frequency variability in the Arctic atmosphere, sea ice and upper ocean climate system. J. Climate, 9(2), 394-408, doi: 10.1175/1520-0442(1996)009.

28. Bjrk, G., and J. Sderkvist (2002), Dependence of the Arctic Ocean ice thickness distribution on the poleward energy flux in the atmosphere. J. Geophys. Res., 107 (C10), 3173, doi: 10.1029/2000JC000723.

29. Boucher, O., and U. Lohmann (1995), The sulfate-CCN-cloud albedo effect, A sensitivity study with two general circulation models. Tellus, 47B, 281-300.

30. Bourke, R. H., and R.P. Garrett (1987), Sea ice thickness distribution in the Arctic Ocean. Cold Reg. Sci. Technol., 13 (3), 259-280, doi:10.1016/0165-232X(87)90007-3.

31. Bromwich, D.H., R.L. Fogt, K.I. Hodges and J.E. Walsh (2007), A tropospheric assessment of the ERA-40, NCEP, and JRA-25 global reanalyses in the polar regions. J. Geophys. Res., 112 (D10), doi: 10.1029/2006JD007859.

32. Bromwich, D.H., and S.H. Wang (2005), Evaluation of the NCEP/NCAR and ECMWF 15- and 40-yr reanalyses using rawinsonde data from two independent Arctic field experiments. Mon. Weather Rev., 133, 3562-3578.

33. Cavalieri, D., C. Parkinson, P. Gloersen, and H.J. Zwally (1996, updated 2008): Sea ice concentration from Nimbus-7 SMMR and DMSP SSM/I passive microwave data. Boulder, Colorado, NSIDC digital media.

34. Cheng, B., Z. Zhang, T. Vihma, M. Johansson, L. Bian, Z. Li, and H. Wu (2008), Model experiments on snow and ice thermodynamics in the Arctic Ocean with CHINARE 2003 data, J. Geophys. Res., 113, C09020, doi:10.1029/2007JC004654.

35. Cheng, B., T. Vihma, R. Pirazzini, and M. Granskog (2006), Modeling of superimposed ice formation during spring snow-melt period in the Baltic Sea. Ann. Glaciol., 44, 139-146, 2006, doi: 10.3189/172756406781811277.

36. Chiacchio, M., J. Francis and P. Stackhouse (2002), Evaluation of methods to estimate the surface downwelling longwave flux during Arctic winter. J. Appl. Meteorol., 41 (3), 306-318, doi: 10.1175/1520-0450(2002)041<0306:EOMTET >2.0.CO;2.

37. Clarke A.D. and K.J. Noone (1985), Soot in the Arctic snowpack: A cause for perturbations in radiative transfer, Atmospheric Environment 19, pp. 2045-2053, doi: 10.1016/0004-6981(85)90113-1.

38. Colbeck, S. C. (1982), An overview of seasonal snow metamorphism, Rev. Geophys., 20(1), 45-61, doi:10.1029/RG020i001p00045.

39. Comiso, J. C., C. L. Parkinson, R. Gersten, L. Stock (2008), Accelerated decline in the Arctic sea ice cover, Geophys. Res. Lett., 35, L01703, doi: 10.1029/2007GL031972.

40. Comiso, J. C., and F. Nishio (2008), Trends in the sea ice cover using enhanced and compatible AMSR-E, SSM/I, and SMMR data. J. Geophys. Res. 113, doi: 10.1029/2007JC004257.

41. Comiso, J. C., (2006), Abrupt decline in the Arctic winter sea ice cover, Geophys. Res., Lett., 33, L18504, doi:10.1029/2006GL027341.

42. Comiso, J. C., D. J. Cavalieri, and T. Markus, (2003), Sea ice concentration, ice temperature, and snow depth, using AMSR-E data. IEEE Transactions on Geoscience and Remote Sensing 41(2):243-252, 10.1109/TGRS.2002.808317.

43. Crane, R.G., and M.R. Anderson (1989), Spring melt patterns in the Kara/Barents Sea: 1984. GeoJournal-Springer, 18 (1), 25-33, doi: 10.1007/BF00722383.

44. Crochet, P., (2007), A Study of Regional Precipitation Trends in Iceland Using a High-Quality Gauge Network and ERA-40. J. Climate, 20, 4659-4677, doi: 10.1175/JCLI4255.1.

45. Cullather, R. I., and M.G. Bosilovich (2011), The moisture budget of the polar atmosphere in MERRA. J. Climate, 24, 2861-2879, doi: 10.1175/2010JCLI4090.1.

46. Cullather, R. I., D. H. Bromwich, and M.C. Serreze (2000), The Atmospheric Hydrologic Cycle over the Arctic Basin from Reanalyses. Part I: Comparison with Observations and Previous Studies. J. Climate 13, 923-937, doi: 10.1175/1520-0442(2000)013<0923:TAHCOT>2.0.CO;2.

47. Curry, J. A., J. L. Schramm, R. Reeder, T. Arbetter, and P. S. Guest (2002), Evaluation of data sets used to force sea ice models in the Arctic Ocean. J. Geophys. Res., 107 (C10), 8027, doi:10.1029/2000JC000466.

48. Curry, J. A., (1995), Interactions among aerosols, clouds and climate of the Arctic Ocean. Elsevier. The Science of the Total Environment, 160/161, pp 777-791, doi: 10.1016/0048-9697(95)04411-S.

49. Curry, J. A., and E.E. Ebert (1992), Annual Cycle of Radiation Fluxes over the Arctic Ocean: Sensitivity to Cloud Optical Properties, J. Climate, 5 (11), pp. 1267-1280, doi: 10.1175/1520-0442(1992)005<1267:ACORFO>2.0.CO;2

50. Cuxart, J., and coauthors (2006), Single-column model intercomparison for a stably stratified atmospheric boundary layer. Bound.-Layer Meteor., 118, 273-303, doi: 10.1007/s10546-005-3780-1.

51. Cuzzone, J., and S. Vavrus (2011), The relationships between Arctic sea ice and cloud-related variables in the ERA-Interim reanalysis and CCSM3. Environ. Res. Lett. 6, 014016, doi:10.1088/1748-9326/6/1/014016.

52. Dee, D. P., Uppala, S. M., Simmons, A. J., Berrisford, P., Poli, P., Kobayashi, S., Andrae, U., Balmaseda, M. A., Balsamo, G., Bauer, P., Bechtold, P., Beljaars, A. C. M., van de Berg, L., Bidlot, J., Bormann, N., Delsol, C., Dragani, R., Fuentes, M., Geer, A. J., Haimberger, L., Healy, S. B., Hersbach, H., Hólm, E. V., Isaksen, L., Kallberg, P., Kohler, M., Matricardi, M., McNally, A. P., Monge-Sanz, B. M., Morcrette, J.-J., Park, B.-K., Peubey, C., de Rosnay, P., Tavolato, C., Thépaut, J.-N. and Vitart, F. (2011), The ERA-Interim reanalysis: configuration and performance of the data assimilation system. Q. J. R. Met. Soci., 137: 553-597. doi: 10.1002/qj.828

53. Dee, D. P., and S. Uppala, (2009), Variational bias correction of satellite radiance data in the ERA-Interim reanalysis. Q. J. R. Meteorol. Soc., 135(644), 1830-1841, doi: 10.1002/qj.493.

54. Deser, C., and H. Teng (2008), Evolution of Arctic sea ice concentration trends and the role of atmospheric circulation forcing, 1979-2007. Geophys. Res. Lett., 35 (L02), doi: 10.1029/2007GL032023.

55. Deser, C., J.E. Walsh, and M.S. Timlin (2000), Arctic sea ice variability in the context of recent atmospheric circulation trends. J. Clim., 13 (3), 617-633, doi: 10.1175/1520-0442(2000)013<0617:ASIVIT>2.0.CO;2.

56. Dong X., and G.G. Mace (2003), Arctic Stratus Cloud Properties and Radiative Forcing Derived From Ground-Based Data Collected Near Point Barrow, Alaska. J. Clim., 16. 445-461, doi: 10.1175/1520-0442(2003)016<0445: ASCPAR>2.0.CO;2.

57. Draper, N. R., and H. Smith (1998), Applied Regression Analysis. Wiley-Interscience, Hoboken, New Jersey, pp. 307-312.

58. Drinkwater, M. R., and X. Liu, 2000: Seasonal and interannual variability in Antarctic sea ice surface melt. IEEE Transactions on Geoscience and Remote Sensing, Vol. 38 (4), doi: 10.1109/36.851767.

59. Drobot, S.D., (2007), Using remote sensing data to develop seasonal outlooks for Arctic regional sea-ice minimum extent. Rem. Sens. Envi., 111, 136-147, doi:10.1016/j.rse.2007.03.024.

60. Drobot, S. D., J. A. Maslanik, and C. Fowler, 2006. A long-range forecast of Arctic summer sea-ice minimum extent. Geophys. Res. Lett., 33, L10501, doi:10.1029/2006GL026216.

61. Drobot, S.D., and M.R. Anderson (2001), Comparison of interannual snowmelt-onset dates with atmospheric conditions. Ann. Glaciol., 33, 79-84, doi: 10.3189/172756401781818851.

62. Ebert, E.E., J.L. Schramm, and J.A. Curry, 1995: Disposition of solar radiation in sea ice and the upper ocean. J. Geophys. Res., 100 (C8), 15,965-15,976, doi:10.1029/95JC01672.

63. Ebert, E. E., and J. A. Curry (1993), An intermediate one-dimensional thermodynamic sea-ice model for investigating ice-atmosphere interactions. J. Geophys. Res., 98 (C6), 10,08510,109, doi:10.1029/93JC00656.
64. ECMWFs Integrated Forecast System (IFS) Documentation Cy29r1. Part IV: Physical processes, 2005. European Centre for Medium-Range Weather Forecasts, Shinfield Park, Reading, RG2 9AX, England.
65. ECMWFs Integrated Forecast System (IFS) Documentation Cy31r1. Part II: Data Assimilation. European Centre for Medium-Range Weather Forecasts, Shinfield Park, Reading, RG2 9AX, England.
66. ECMWFs Integrated Forecast System (IFS) Documentation Cy31r1. Part IV: Physical Processes. European Centre for Medium-Range Weather Forecasts, Shinfield Park, Reading, RG2 9AX, England.
67. Ehn, J.K., M.A. Granskog, T. Papakyriakou, R. Galley, and D.G. Barber (2006), Surface albedo observations of Hudson Bay (Canada) land-fast sea ice during melt onset. Ann. Glaciol., 44, 23-29, doi: 10.3189/172756406781811376.
68. Eicken, H., Tucker, W.B., and D.K. Perovich (2001a), Indirect measurements of the mass balance of summer Arctic sea ice with an electromagnetic induction technique. Ann.Glaciol., 33, 194-200.
69. Eicken, H. and P. Lemke (2001), The response of polar sea ice to climate variability and change. In: Climate of the 21st century: Changes and risks, edited by Lozan, J. L. et al., pp. 206-211, Wissenschaftliche Auswertungen/GEO, Hamburg.
70. Eisenman, I., and J.S. Wettlaufer (2009), Nonlinear threshold behavior during the loss of Arctic sea ice. Proc National Acad Sci USA 106, 28-32.
71. Fetterer, F., and N. Untersteiner (1998), Observations of melt ponds on Arctic sea ice. J. Geophys. Res., 103(C11), 24,82124,835, doi:10.1029/98JC02034.
72. Forster, R.R., D.G. Long, K.C. Jezek, S.D. Drobot, and M.R. Anderson (2001), The onset of Arctic sea-ice snowmelt as detected with passive- and active-microwave remote sensing. Ann. Glaciol., 33, 85-93, doi 10.3189/172756401781818428.
73. Fouquart, Y., and B. Bonnel (1980), Computations of solar heating of the Earth s atmosphere: A new parameterization, Beitr. Phys. Atmos., 53, 3562.
74. Francis, J.A. and E. Hunter (2007), Changes in the fabric of the Arctics greenhouse blanket. Envir. Res. Lett., 2, 045011, doi: 10.1088/1748-9326/2/4/045011.
75. Francis, J.A. and E. Hunter, 2006: New insight into the disappearing Arctic sea ice. Eos Trans. of AGU, 87, 509-524, doi: 10.1029/2006EO460001.
76. Francis, J., A. Schweiger and J. Key (2003), A 20-year data set of downwelling longwave flux at the Arctic surface from TOVS satellite data. 13th ARM Science team meeting proceedings, Broomfield, Colorado.

77. Frey, K.E., L.C. Smith and D.E. Alsdorf (2003), Controls on the Eurasian coastal sea ice formation, melt onset and decay from ERS scatterometry: regional contrasts and effects of river influx. Int. J. Rem. Sens., 24 (24), pp. 5283-5315(33), doi: 10.1080/0143116031000101684.
78. Frolov I., Z. Gudkovich, V. Radionov, A. Shirochkov, L. Timokhov (2005), The Arctic Basin: Results from the Russian Drifting Stations. Springer-Praxis books in Geophysical Sciences.
79. Garrett, T. J., M. M. Maestas, S. K. Krueger, and C. T. Schmidt (2009), Acceleration by aerosol of a radiative-thermodynamic cloud feedback influencing Arctic surface warming, Geophys. Res. Lett., 36, L19804, doi:10.1029/2009GL040195.
80. Garrett, T.J., L.F. Radke, and P.V. Hobbs (2002), Aerosol effects on cloud emissivity and surface longwave heating in the Arctic, J. Atmos. Sci., 59, 769-778.
81. Gerland, S. and C. Haas (2011), Snow-depth observations by adventurers traveling on Arctic sea ice, Annals of Glaciology, 52(57), 369-376.
82. Gerdes, R. (2006), Atmospheric response to changes in Arctic sea ice thickness, Geophys. Res. Lett., 33, L18709, doi: 10.1029/2006GL027146.
83. Gerding, M., C. Ritter, M. Muller, and R. Neuber (2004), Tropospheric water vapour soundings by lidar at high Arctic latitudes. Atmospheric Res., 71 (4), pp 289-302, doi: 10.1016/j.atmosres.2004.07.002.
84. Gibson, J.K., P. Kallberg, S. Uppala, A. Hernandez, A. Nomura, and E. Serrano (1997), ECMWF Re-Analysis Project report series 1. ECMWF technical report. ECMWF Shinfield Park, Reading GR2 9AX, UK.
85. Giles, K.A., S.W. Laxon, and A.L. Ridout (2008), Circumpolar thinning of Arctic sea ice following the 2007 record ice extent minimum. Geophys. Res. Lett., 35, doi: 10.1029/2008GL035710.
86. Goddard, W.B., (1973), Description of a surface temperature equilibrium energy balance model with application to Arctic pack ice in early spring. In Climate of the Arctic, edd. G. Weller and S.A. Bowling, Univ. Alaska, Fairbanks.
87. Gogineni, S. P., R. K. Moore, T. C. Grenfell, D. G. Barber, S. Digby, and M. Drinkwater (1992), The effects of freeze-up and melt processes on microwave signatures, Chapter 17 in Microwave Remote Sensing of Sea Ice, F. Carsey, ed., AGU, 329-340.
88. Gorodetskaya, I.V., L-B Tremblay, B. Liepert, M.A. Cane, and R.I. Cullather (2008), The influence of cloud and surface properties on the Arctic ocean SW radiation budget in coupled models. J. Clim., 21, p 866, doi: 10.1175/2007JCLI1614.1.
89. Granskog, M., T. Vihma, R. Pirazzini, and B. Cheng (2006), Superimposed ice formation and surface energy fluxes on sea ice during the spring melt-freeze

period in the Baltic Sea. J. Glaciol., 52 (176), 119-127, doi: 10.3189/172756506781828971.

90. Grant, A.N., S. Bronnimann and L. Haimberger (2008), Recent Arctic warming vertical structure contested. Nature, 455, E2-E3, doi: 10.1038/nature07257.
91. Graversen, R.G., Th. Mauritsen, S. Drijfhout, M. Tjernstrom, and S. Martensson (2011), Warm winds from the Pacific caused extensive Arctic sea-ice melt in summer 2007. Clim. Dyn., 36, 11-12, 2103-2112, doi: 10.1007/s00382-010-0809-z.
92. Graversen, R. G., T. Mauritsen, M. Tjernstrom, E. Kallen, and G. Svensson (2008a), Vertical structure of recent Arctic warming. Nature 451, 5356, doi: 10.1038/nature06502.
93. Graversen, R.G., T. Mauritsen, M. Tjernstrom, E. Kallen, and G. Svensson (2008b), On-line supplement to vertical structure of recent Arctic warming. Nature 541, pp 53-56, doi: 10.1038/nature06502.
94. Graversen, R.G., T. Mauritsen, M. Tjernstrom, E. Kallen, and G. Svensson (2008c), Reply. Nature, 455, doi:10.1038/nature07259.
95. Grenfell, T.C. and D.K. Perovich (2004), Seasonal and spatial evolution of albedo in a snow-ice-land-ocean environment, J. Geophys. Res., 109(C1), doi:10.1029/2003JC001866.
96. Grenfell, T. C., B. Light, and M. Sturm (2002), Spatial distribution and radiative effects of soot in the snow and sea ice during the SHEBA experiment, J. Geophys. Res., 107(C10), 8032, doi: 10.1029/2000JC000414.
97. Grenfell, T. C., and D. K. Perovich (1984), Spectral albedos of sea ice and incident solar irradiance in the southern Beaufort Sea, J. Geophys. Res., 89(C7), 3573-3580, doi: 10.1029/JC089iC03p03573.
98. Groves, D. G., and J. A. Francis (2002), Variability of the Arctic atmospheric moisture budget from TOVS satellite data. J. Geophys. Res., 107 (D24), 4785, doi:10.1029/2002JD002285.
99. Haas, C., Lobach, J., Hendricks, S., Rabenstein, L., Pfaffling, A. (2009). 'Helicopter-borne measurements of sea ice thickness, using a small and light-weight digital EM system', J. Appl. Geophysics, 67(3), 234-241.
100. Haggerty, J. A., J. A. Maslanik, and J. A. Curry (2003), Heterogeneity of sea ice surface temperature at SHEBA from aircraft measurements, J. Geophys. Res., 108, 8052, doi: 10.1029/2000JC000560.
101. Hakkinen, S., A. Proshutinsky, and I. Ashik (2008), Sea ice drift in the Arctic since the 1950s, Geophys. Res. Lett., 35, L19704, doi:10.1029/2008GL034791.
102. Hanesiak, J., Barber, D.G. and Flato, G.M. (1999), Role of diurnal processes in the seasonal evolution of sea ice and its snow cover. J. Geophys. Res. 104, 13,593603, doi:10.1029/1999JC900054.

103. Hansen, J. and L. Nazarenko (2004), Soot climate forcing via snow and ice albedos. Proc. Natl. Acad. Sci. U.S.A. 101, 423428, doi:10.1073/pnas.2237157100.

104. Holland, D., L. Mysak, D. Manak, and J. Oberhuber (1993), Sensitivity Study of a Dynamic Thermodynamic Sea Ice Model. J. Geophys. Res., 98, C2, doi:10.1029/92JC02015.

105. Inoue, J., and T. Kikuchi (2007), Outflow of summertime Arctic sea ice observed by ice drifting buoys and its linkage with ice reduction and atmospheric circulation patterns. J. Meteorol. Society of Japan, 85 (6), pp.881-887, doi:10.2151/jmsj.85.881.

106. Inoue, J., T. Kikuchi, D. K. Perovich, and J. H. Morison (2005), A drop in mid-summer shortwave radiation induced by changes in the ice-surface condition in the central Arctic. Geophys. Res. Lett., 32 (L13), doi: 10.1029/2005GL023170.

107. Intrieri J., C.W Fairall., M.D. Shupe, P.O. Persson, E.L. Andreas, P.S. Guest, and R.E. Moritz (2001), An annual cycle of Arctic surface cloud forcing at SHEBA. J. Geophys. Res., 107 (C10), 8039, doi:10.1029/2000JC000439.

108. Jakobson, E. and T. Vihma (2010), Atmospheric moisture budget over the Arctic on the basis of the ERA-40 reanalysis. Int. J. Climatol. 30: 21752194, doi : 10.1002/joc.20392009.

109. Jeffries, M.O., K. Schwartz and S. Li (1997), Arctic summer sea-ice SAR signatures, melt-season characteristics, and melt-pond fractions. Polar Record, 33, pp 101-112 doi: 10.1017/S003224740001442X.

110. Jordan, R.E., E.L. Andreas, and A.P. Makshtas (1999), Heat budget of snow-covered sea ice at North Pole 4. J. Geophys. Res., 104(C4), 7785-7806, doi: 10.1029/1999JC900011.

111. Kalnay, E., M. Kanamitsu, R. Kistler, W. Collins, D. Deaven, L. Gandin, M. Iredell, S. Saha, G. White, J. Woollen, Y. Zhu, A. Leetmaa, R. Reynolds, M. Chelliah, W. Ebisuzaki, W. Higgins, J. Janowiak, K. C. Mo, C. Ropelewski, J. Wang, R. Jenne, D. Joseph (1996), The NCEP/NCAR 40-year reanalysis project. Bull. Amer. Meteol. Soc., 77, 437-471. Doi: 10.1175/1520-0477(1996)077<0437:TNYRP>2.0.C0;2.

112. Kanamitsu, M., et al., 2002: NCEP/DOE AMIP II Reanalysis (R2). Bull. Amer. Meteorol. Soc., 83, 1631-1643.

113. Kanamitsu, M., J.C. Alpert, K.A. Campana, P.M. Caplan, D.G. Deaven, M. Iredell, B. Katz, H.L. Pan, J. Sela and G.H. White, 1991: Recent changes implemented into the global forecast system at NCEP. Weather and Forecasting, 6, 0001-0012.

114. Kato, S., N.G. Loeb, P. Minnis, J.A. Francis, T.P. Charlock, D.A. Rutan, E.E. Clothiaux, and S. Sun-Mack (2006), Seasonal and interannual variations of

TOA irradiance and cloud cover over polar regions derived from the CERES data set. Geophys. Res. Lett., 33(19), doi: 10.1029/2006GL026685.

115. Kellogg, W.W., (1973), Climate feedback mechanisms involving the Polar regions. In Climate of the Arctic, edd. G. Weller and S.A. Bowling, Univ. Alaska, Fairbanks.

116. Key, J., D. Slayback, C. Xu, and A. Schweiger (1999), New climatologies of polar clouds and radiation based on the ISCCP D products. Proceedings of the Fifth Conference on Polar Meteorology and Oceanography, American Meteorological Society, Dallas, TX, January 10-15, 227-232.

117. Key, J.R., Schweiger, A.J., and Stone R.S, (1997), Expected uncertainty in satellite-derived estimates of the surface radiation budget at high latitudes. J. Geophys. Res., 102, 15,837-15,847.

118. Kistler, R., E. Kalnay, W. Collins, S. Saha, G. White, J. Woollen, M. Chelliah, W. Ebisuzaki, M. Kanamitsu, V. Kousky, H. van den Dool, R. Jenne, M. Fiosino (2001), The NCEP-NCAR 50-Year Reanalysis: Monthly Means CD-ROM and Documentation. Bulletin of the American Meteorological Society, Vol. 82, No. 2, pp. 247-268.

119. Krishfield, R.A., and D.K. Perovich (2005), Spatial and temporal variability of oceanic heat flux to the Arctic pack ice. J. Geophys. Res., 110 (C07).

120. Kwok, R., and D.A. Rothrock (2009), Decline in Arctic sea ice thickness from submarine and ACESat records: 1958-2008. Geophys. Res. Lett., 36, doi: 10.1029/2009GL039035.

121. Kwok, R., G.F. Cunningham, M. Wensnahan, I. Rigor, H.J. Zwally and D. Yi, (2009), Thinning and volume loss of the Arctic ocean sea ice cover: 2003-2008. J. Geophys. Res, Vol 114 (C07), doi: 10.1029/2009JC005312.

122. Kwok, R., and G. F. Cunningham (2008), ICESat over Arctic sea ice: Estimation of snow depth and ice thickness, J. Geophys. Res., 113 (C08), doi: 10.1029/2008JC004753.

123. Langleben, M.P., (1972), The decay of an annual cover of sea ice. J.Glaciol., Vol. 11, N 63.

124. Langleben, M.P., (1966), On the factors affecting the rate of ablation of sea ice. Can. J. Earth Sci., 3, 431-439. doi: 10.1139/e66-032.

125. Langlois, A., and D.G. Barber (2007), Passive microwave remote sensing of seasonal snow-covered sea ice. Progress in Physical Geography, Vol 31(6), pp. 539-573, doi: 10.1177/0309133307087082.

126. Laxon, S.W., N. Peacock, and D. Smith (2003), High interannual variability of sea ice thickness in the Arctic region. Nature 425, 947-950, doi: 10.1038/nature02050.

127. Lindsay, R. W., J. Zhang. A. J Schweiger, M. Steele and H. Stern (2009), Arctic sea ice retreat in 2007 follows thinning trend. J. Clim., 22, pp. 165-176, doi: 10.1175/2008JCLI2521.1.

128. Lindsay, R.W., and J. Zhang (2005), The thinning of Arctic sea ice, 1988-2003: Have we reached a tipping point? J. Clim., 18 (22), doi: 10.1175/ JCLI3587.1.

129. Lindsay, R. W. (1998), Temporal variability of the energy balance of thick Arctic pack ice. J. Climate, 11 (3), 313-333, doi: 10.1175/1520-0442(1998)011<0313: TVOTEB>2.0.CO;2.

130. Lindsay, R.W., and D.A. Rothrock (1994), Arctic Sea Ice Surface Temperature from AVHRR. J. Climate, 7 (1), p 174-183, doi: 10.1175/1520-0442(1994)007< 0174:ASISTF>2.0.CO;2.

131. Liu, Y., S. Ackerman, B. Maddux, J. Key, and R. Frey (2010), Errors in cloud detection over the Arctic using a satellite imagery and implications for observing feedback mechanisms, J. Climate, 23 (7), 1894-1907, doi: 10.1175/2009JCLI3386.1.

132. Liu, Y., J. Key, and X. Wang, (2009), Influence of changes in sea ice concentration and cloud cover on recent Arctic surface temperature trends. Geophys. Res. Lett., 36 (L20), doi:10.1029/2009GL040708.

133. Liu, Y., J. Key, J. A. Francis, and X. Wang, 2007: Possible causes of decreasing cloud cover in the Arctic winter, 1982-2000. Geophys. Res. Lett., 34 (L14), doi:10.1029/2007GL030042.

134. Liu, J., J.A. Curry, W.B. Rossow, J.R. Key and X. Wang (2005), Comparison of surface radiative flux data sets over the Arctic Ocean. J. Geophys. Res., 110 (C2), doi:10.1029/2004JC002381.

135. Livingstone, C.E., K.P. Singh and A.L. Gray, 1987. Seasonal and regional variations of active/passive microwave signatures of sea ice. IEEE Transactions on Geosciences and Remote Sensing GE-25 (2): 159-172.

136. Lubin, D., and R. Massom, 2006: Polar Remote Sensing. Volume I. Atmosphere and Oceans. Springer-Praxis, Chichester, UK, 756 pp, ISBN 978-3-540-43097-1.

137. Lupkes, C., T. Vihma, E. Jakobson, G. Konig-Langlo, and A. Tetzlaff (2010), Meteorological observations from ship cruises during summer to the central Arctic: A comparison with reanalysis data. Geophys. Res. Lett., 37, doi:10.1029/2010GL042724.

138. Luthje, M., D.L. Feltham, and P.D. Taylor (2006), Modeling of summertime evolution of sea ice melt ponds. J. Geophys. Res., 111 (C02), doi: 10.1029/2004JC002818.

139. Makshtas, A. P., S. V. Shoutilin, and E. L. Andreas (2003), Possible dynamic and thermal causes for the recent decrease in sea ice in the Arctic Basin, J. Geophys. Res., 108(C7), 3232, doi: 10.1029/2001JC000878

140. Markus T., J.C. Stroeve, and J. Miller (2009), Recent changes in Arctic sea ice melt onset, freeze up and melt season length. J. Geophys. Res., 114 (C12), doi:10.1029/2009JC005436.

141. Martin, S., and E. A. Munoz (1997), Properties of the Arctic 2-meter air temperature field for 1979 to the present derived from a new gridded dataset. J. Clim., 10 (6), 1428-1440, doi: 10.1175/1520-0442(1997)010<1428:POTAMA> 2.0.CO;2.

142. Maslanik, J. A., C. Fowler, J. Stroeve, S. Drobot, J. Zwally, D. Yi, and W. Emery, (2007), A younger, thinner Arctic ice cover: Increased potential for rapid, extensive sea-ice loss. Geophys. Res. Lett., 34 (L24), doi: 10.1029/2007GL032043.

143. Matson, M., C.F. Ropelewski and M.S. Varnadore (1986), An Atlas of satellite-derived Northern Hemisphere snow cover frequency. NOAA/NESDIS, Washington, D.C., 75 pp.

144. Maykut, G.A., and M.G. McPhee (1995), Solar heating of the Arctic mixed layer. J. Geophys. Res., 100, 24,691-24,703.

145. Maykut, G. A. (1986), The surface heat and mass balance, in Geophysics of Sea Ice, edited by N. Untersteiner, pp. 395-463, NATO ASI Series, New York.

146. Maykut, G.A. and P.E. Church (1973), Radiation Climate of Barrow Alaska. J. Appl. Meteor., 12, 620-628; doi: 10.1175/1520-0450(1973)012<0620: RCOBA>2.0.CO;2.

147. McLaren, A.S., J.E. Walsh, R.H. Bourke, R.L. Weaver and W. Wrttmann (1992), Variability in sea-ice thickness over the North Pole from 1977 to 1990. Nature 358, pp 224 - 226, doi:10.1038/358224a0.

148. Meier, W., and D. Notz (2010), A note on the accuracy and reliability of satellite-derived passive microwave estimates of sea-ice extent. CliC Arctic Sea Ice Working Group Consensus Document. Available in web http://www.climate-cryosphere.org/export/sites/clic/documents/CliC_seaice_reliability_oct28.pdf

149. Mlawer, E., Taubman, S., Brown, P., Iacono, M. and Clough, S. (1997). Radiative transfer for inhomogeneous atmospheres: RRTM, a validated correlated-k model for the longwave. J. Geophys. Res., 102(D14), doi: 10.1029/97JD00237. issn: 0148-0227.

150. Molotch, N. P., T. H. Painter, R. C. Bales, and J. Dozier (2004), Incorporating remotely-sensed snow albedo into a spatially-distributed snowmelt model, Geophys. Res. Lett., 31, L03501, doi:10.1029/2003GL019063.

151. Morcrette, J.-J. (1991), Radiation and Cloud Radiative Properties in the European Centre for Medium Range Weather Forecasts Forecasting System, J. Geophys. Res., 96 (D5), 9121-9132, doi:10.1029/89JD01597.

152. Mote, Th. L., (2008), On the Role of Snow Cover in Depressing Air Temperature. J. Appl. Meteor. Climatol., 47, 2008-2022. doi: 10.1175/2007JAMC1823.1

153. Nakamura, N., and A.H. Oort (1988), Atmospheric heat budgets of the polar regions. J. Geophys. Res., 93.

154. NCEP/NCAR problem list, online source at http://www.esrl.noaa.gov/psd/data/reanalysis/problems.shtml

155. Nghiem, S. V., I. G. Rigor, D. K. Perovich, P. Clemente-Colón, J. W. Weatherly, and G. Neumann (2007), Rapid reduction of Arctic perennial sea ice, Geophys. Res. Lett., 34, L19504, doi:10.1029/2007GL031138.

156. Nghiem, S., R. Kwok, D. Perovich, and D. Barber (2003), Impact of cloud cover on sea ice surface melt. Presented at 7th Conf. Polar Meteorology and Oceanography and Joint Symp. High-Latitude Climate Variations. Boston, MA.

157. Nicolaus, M. , Haas, C. and Willmes, S. (2009), Evolution of first- and second-year snow properties on sea ice in the Weddell Sea during spring-summer transition. J. Geophys. Res., 114, D17109, doi:10.1029/2008JD011227.

158. Nicolaus M., C. Haas, J. Bareiss and S. Willmes, (2006), A model study of differences of snow thinning on Arctic and Antarctic first-year sea ice during spring and summer. Ann. Glaciol., 44, pp 147-153.

159. Nicolaus, M., Haas, C., Bareiss, J. (2003), Observations of superimposed ice formation at melt-onset on fast ice on Kongsfjorden, Svalbard. Physics and Chemistry of the Earth, 28, 1241-1248, doi:10.1016/j.pce.2003.08.048.

160. Nilsson, E.D., U Rannik, and M. Hakansson (2001), Surface energy budget over the central Arctic Ocean during late summer and early freeze-up. J. Geophys. Res., 106 (D23), 32,187-32,205, doi: 10.1029/2000JD900083.

161. Notz, D., (2009), The future of ice sheets and sea ice: between reversible retreat and unstoppable loss, Proc. Nat. Ac. Sci., 106 (49), 20,590-20,595. doi: 10.1073/pnas.0902356106.

162. Oort, A.H., (1973), Year-to-year variations in the energy balance of the Arctic Atmosphere. In Climate of the Arctic, edd. G. Weller and S.A. Bowling, Univ. Alaska, Fairbanks.

163. Overland, J. E. (2006), Arctic change: multiple observations and recent understanding. R. Met. Society, Weather, Vol. 61, No. 3, p. 78-83, doi: 10.1256/wea.206.05.

164. Overland, J.E., and M. Wang (2005), The Arctic climate paradox: The recent decrease of the Arctic Oscillation. Geophys. Res. Lett., 32 (6), doi: 10.1029/2004GL021752.

165. Overland, J.E. and P.S. Guest (1991), The Arctic Snow and Air Temperature Budget Over Sea Ice During Winter. J. Geophys. Res., Vol. 96, No. C3, pp. 4651-4662, doi: 10.1029/90JC02264.

166. Parkinson, C. L., and D. J. Cavalieri (2008), Arctic sea ice variability and trends, 1979-2006, J. Geophys. Res., 113 (C07), doi: 10.1029/2007JC004558.

167. Pavelsky, T.M., J. Boe, A. Hall and E.J. Fetzer (2011), Atmospheric inversion strength over polar oceans in winter regulated by sea ice. Clim Dyn, 36, 945-955, doi: 10.1007/s00382-010-0756-8.

168. Perovich, D.K., J. A. Richter-Menge, K. F. Jones, and B. Light (2008), Sunlight, water, and ice: Extreme Arctic sea ice melt during the summer of 2007, Geophys. Res. Lett., 35, L11501, doi:10.1029/2008GL034007.

169. Perovich, D. K., B. Light, H. Eicken, K. F. Jones, K. Runciman, and S. V. Nghiem (2007a), Increasing solar heating of the Arctic Ocean and adjacent seas, 1979-2005: Attribution and role in the ice-albedo feedback. Geophys. Res. Lett., 34, doi: 10.1029/2007GL031480.

170. Perovich, D. K., S. V. Nghiem, T. Markus, and A. Schweiger (2007b), Seasonal evolution and interannual variability of the local solar energy absorbed by the Arctic sea iceocean system, J. Geophys. Res., 112 (C03), doi:10.1029/2006JC003558.

171. Perovich D. and J.A. Richter-Menge (2006), From points to Poles: extrapolating point measurements of sea ice mass balance. Ann. Glaciol. 44.

172. Perovich, D. K., T. C. Grenfell, B. Light and P.V. Hobbs (2002) Seasonal evolution of the albedo of multiyear Arctic sea ice, J. Geophys. Res., 107 (C10), 8044, doi: 10.1029/2000JC000438.

173. Perovich, D. K., and B. Elder (2002), Estimates of ocean heat flux at SHEBA. Geophys. Res. Lett., 29 (9), 1344, doi:10.1029/2001GL014171.

174. Perovich, D.K. and B. Elder (2001), Temporal evolution and spatial variability of the temperature of Arctic sea ice, Ann. Glaciol., 33, 207-212.

175. Perovich, D. K., T. C. Grenfell, B. Light. J. A. Richter-Menge, M. Sturm, W. B. Tucker III, H. Eicken, G. A. Maykut, and B. Elder (1999), SHEBA: Snow and Ice Studies, Version 1.0 [CD-ROM], Cold Regions Res. and Eng. Lab., Hanover, N. H.

176. Persson, P.O.G., C.W. Fairall, E.L. Andreas, P.S. Guest and D.K. Perovich (2002), Measurements near the Atmospheric Surface Flux Group Tower at SHEBA: Near-surface conditions and surface energy budget. J. Geophys. Res., 107, 8045, doi:10.1029/2000JC000705.

177. Pfirman, S., W. F. Haxby, R. Colony, and I. Rigor (2004), Variability in Arctic sea ice drift, Geophys. Res. Lett., 31, L16402, doi:10.1029/2004GL020063.

178. Pinto, J.O., J.A. Curry, and C.W. Fairall (1997), Radiative characteristics of the Arctic atmosphere during spring as inferred from ground-based measurements. J. Geophys. Res., 102, 6941-6952, doi:10.1029/96JD03348.

179. Polyakov, I.V. and M.A. Johnson (2000), Arctic decadal and interdecadal variability. Geophys. Res. Lett., 27 (24), 4097-4100, doi : 10.1029/2000GL011909.

180. Proshutinsky, A., R. Krishfield, E. Carmack, F. McLaughlin, S. Zimmerman, K. Shimada, and M. Itoh (2004), Annual Freshwater and Heat Content From 2003-2004: First Results from the Beaufort Gyre Observing System. EOS Trans. AGU, 85(47), Fall Meet. Suppl., Abstract C41A-0182.

181. Rabenstein, L., S. Hendricks, T. Martin, A. Pfaffhuber and C. Haas (2010), Thickness and surface-properties of different sea-ice regimes within the Arctic Trans Polar Drift: Data from summers 2001, 2004 and 2007, J. Geophys. Res., 115, C12059, doi:10.1029/2009JC005846.

182. Richter-Menge, J.A., D.K. Perovich, B.C. Elder, K. Claffey, I. Rigor and M. Ortmeyer (2006), Ice mass-balance buoys: a tool for measuring and attributing changes in the ice thickness of the Arctic sea ice cover. Ann. Glaciol., 44, doi: 10.3189/172756406781811727.

183. Rigor, I. G., R. L. Colony, and S. Martin (2000), Variations in surface air temperature observations in the Arctic, 1979-97, J. Clim., 13 (5), 896-914, doi: 10.1175/1520-0442(2000)013<0896:VISATO>2.0.CO;2

184. Robinson, D.A., M.C. Serreze, R.G. Barry, G. Scharfen, and G. Kukla (1992), Large-scale patterns and variability of snowmelt and parameterized surface albedo in the Arctic basin. J. Climate, 5 (10), 1109-1119, doi: 10.1175/1520-0442(1992)005<1109:LSPAVO>2.0.CO;2.

185. Robinson, D.A., G. Scharfen, M.C. Serreze, G. Kukla, and R.G. Barry (1986), Snow melt and surface albedo in the Arctic basin. Geophys. Res. Lett., 13 (9), pp. 945-948, doi:10.1029/GL013i009p00945.

186. Rogers A. N., D. H. Bromwich, E. N. Sinclair, and R. I. Cullather (2001), The Atmospheric Hydrologic Cycle over the Arctic Basin from Reanalyses. Part II: Interannual Variability, J. Climate, 14, 2414.

187. Rossow, W. B., and R. A. Schiffer (1991), ISCCP cloud data products, Bull. Am. Meteorol. Soc., 72, 220.

188. Rothrock, D.A., and J. Zhang (2005), Arctic Ocean sea ice volume: what explains its recent depletion? J. Geophys. Res., 110, C01002, doi:10.1029/2004JC002282.

189. Rudels, B., M. Marnela, and P. Eriksson (2008), Constraints on estimating mass, heat and freshwater transports in the Arctic Ocean: an exercise. Chapter 13 in Arctic-Subarctic Ocean Fluxes, editor Dickson R.R. et al. Springer.

190. Sandven, S., O. M. Johannessen, and K. Kloster (2006), Sea Ice Monitoring by Remote Sensing (Chapter 8) Manual of Remote Sensing, vol. 6, 3rd edition: Remote Sensing of the Marine Environment.

191. Sankelo, P., Haapala, J., Heiler, I. and E. Rinne (2010), Melt pond formation and temporal evolution at the drifting station Tara during summer 2007. Polar Research, 29: 311-321. doi: 10.1111/j.1751-8369.2010.00161.x

192. Schweiger, A.J., R.W. Lindsay, S. Vavrus, and J.A. Francis (2008), Relationships between Arctic sea ice and clouds during autumn. J. Climate, 21, 4799-4810, doi : 10.1175/2008JCLI2156.1.

193. Schweiger, A. J. (2004), Changes in seasonal cloud cover over the Arctic seas from satellite and surface observations. Geophys. Res. Lett., 31 (L12), doi:10.1029/2004GL020067.

194. Schweiger, A.J. and J.R. Key (1994), Arctic Ocean radiative fluxes and cloud forcing estimated from the ISCCP C2 cloud dataset, 1983-1990. J. Appl. Meteorol., 33 (8), pp.948-963, doi: 10.1175/1520-0450(1994)033<0948:AORFAC>2.0.CO;2.

195. Screen, J.A., and I. Simmonds (2011a), Declining summer snowfall in the Arctic: causes, impacts and feedbacks. Clim Dyn, (published online, June 2011), doi: 10.1007/s00382-011-1105-2.

196. Screen, J.A., and I. Simmonds (2011b), Erroneous Arctic temperature trends in the ERA-40 reanalysis: A Closer Look. J. Climate, 24, 10, 2620-2627, doi: 10.1175/2010JCLI4054.1

197. Screen, J.A., and I. Simmonds (2010), The central role of diminishing sea ice in recent Arctic temperature amplification. Nature, 464, 1334-1337, doi:10.1038/nature09051.

198. Screen, J.A. and I. Simmonds (2010b), Increasing fall-winter energy loss from the Arctic Ocean and its role in Arctic temperature amplification. Geophys Res Lett., 37 (L16), doi:10.1029/2010GL044136.

199. Sedlar, J., M. Tjernstrom, T. Marutsen, M. Shupe, I. Brooks, O. Persson, C. Birch, C. Leck, A. Sirevaag, and M. Nicolaus (2010), A transitioning Arctic surface energy budget: the impact of solar zenith angle, surface albedo and cloud radiative forcing. Clim. Dyn., 11, doi: 10.1007/s00382-010-0937-5.

200. Sellers, W.D. (1965), Physical Climatology. Univ. of Chicago Press. Chicago, 272 pp.

201. Semmler, T., D. Jacob, K.H. Schlunzen, R. Podzun (2005), The Water and Energy Budget of the Arctic Atmosphere. J. Climate, 18 (13), pp. 2515-2530, doi: 10.1175/JCLI3414.1.

202. Sepp, M., and J. Jaagus (2010), Changes in the activity and tracks of Arctic cyclones. Climatic Change, 105 (3-4), 577-595, doi: 10.1007/s10584-010-9893-7.

203. Serreze, M.C., and A.P. Barrett (2008), The summer cyclone maximum over the central Arctic Ocean. J. Climate, 21, 1048-1065, doi : 10.1175/2007JCLI1810.1.

204. Serreze, M.C., A.P. Barrett, A.G. Slater, M. Steele, J. Zhang, and K.E. Trenberth (2007), The large-scale energy budget of the Arctic. J. Geophys. Res., 112 (D11), doi: 10.1029/2006JD008230.

205. Serreze, M.C., and J.A Francis (2006), The Arctic amplification debate. Springer - Climatic change, 76 (3-4), p. 241-264, doi: 10.1007/s10584-005-9017-y.

206. Serreze, M.C., and R.G. Barry (2005), The Arctic Climate System. Cambridge. University Press: Cambridge.

207. Serreze, M.C., and C.M. Hurst (2002), Representation of mean Arctic precipitation from NCEP/NCAR and ERA reanalyses. J. Climate, 13 (1), pp 182-201, doi: 10.1175/1520-0442(2000)013<0182:ROMAPF>2.0.CO;2.

208. Serreze, M.C., J. R. Key, J. E. Box, J. A. Maslanik, and K. Steffen (1998), A new monthly climatology of global radiation for the Arctic and comparisons with NCEPNCAR reanalyses and ISCCP-C2 fields. J. Climate, 11(2), 121-136, doi: 10.1175/1520-0442(1998)011<0121:ANMCOG>2.0.CO;2.

209. Serreze, M.C., Roger G. Barry, Mark C. Rehder, John E. Walsh and D. Drewry (1995a), Variability in Atmospheric Circulation and Moisture Flux over the Arctic. Philosophical Transactions: Physical Sciences and Engineering, 352 (1699), pp. 215-225.

210. Serreze M.C., R.G. Barry, and J.E. Walsh (1995b), Atmospheric Water Vapor Characteristics at 70N. J. Climate, 8, pp 719.

211. Serreze, M.C., Maslanik J.A., Sharfen G.R. and R.G. Barry (1993), Interannual variations in snow melt over Arctic sea and relationships to atmospheric forcings. Ann. Glaciol., 17, pp. 327-331.

212. Shine, K., and R. Crane (1984), The Sensitivity of a One-Dimensional Thermodynamic Sea Ice Model to Changes in Cloudiness, J. Geophys. Res., 89(C6), 10,615-10,622, doi: 10.1029/JC089iC06p10615.

213. Shupe, M.D., and J.M. Intrieri (2004), Cloud radiative forcing of the Arctic surface: the influence of cloud properties, surface albedo and solar zenith angle: J. of Climate, 17 (3), p 616, doi: 10.1175/1520-0442(2004)017<0616:CRFOTA >2.0.CO;2.

214. Simon, C., L. Arris, and B. Heal (2005), Arctic Climate Impact Assesment. Cambridge Univ. Press, London.

215. Simmonds, I., C. Burke, and K. Keay (2008), Arctic climate change as manifest in cyclone behavior. J. Clim., 21 (22), 5777-5796.

216. Simmons A.J., P.D. Jones, V. da Costa Bechtold, A.C.M. Beljaars, P.W. Kallberg, S. Saarinen, S.M. Uppala, P. Vitebro, and N. Wedi (2004), Comparison of trends and low frequency variability in CRU, ERA-40,

NCEP/NCAR reanalyses of surface air temperature. J. Geophys. Res., 109, D24115, doi: 10.1029/2004JD005306.

217. Sirois, A., and L.A. Barrie (1999), Arctic lower tropospheric aerosol trends and composition at Alert, Canada: 1980-1995. J. Geophys. Res., 104 (D09), 11,599-11,618, doi: 10.1029/1999JD900077.

218. Smedsrud, L. H., A. Sirevaag, K. Kloster, A. Sorteberg, and S. Sandven (2011), Recent wind driven high sea ice export in the Fram Strait contributes to Arctic sea ice decline, The Cryosphere Discuss., doi:10.5194/tcd-5-1311-2011.

219. Smith, D.M. (1998a), Recent increase in the length of the melt season of perennial Arctic sea ice, Geophys. Res. Lett., 25(5), 655-658, doi:10.1029/98GL00251.

220. Smith, D.M. (1998b), Observations of Arctic sea ice melt and freeze-up using passive microwave data. J. Geophys. Res., 103 (C12), doi:10.1029/98JC02416.

221. Sorteberg, A., and J. E. Walsh (2008), Seasonal cyclone variability at 70N and its impact on moisture transport into the Arctic. Tellus A, 60 (3), 570-586, doi : 10.1111/j.1600-0870.2008.00314.x

222. Sorteberg, A. (2007a), Uncertainties in observationally based estimates of the Arctic Surface Radiation Budget. In Arctic Ocean Variability - advection and external forcing encounter local processes and constraints. p. 13-30. Compiled by B. Rudels. Workshop held at DAMOCLES General Assembly.

223. Sorteberg, A., V. Kattsov, J.E. Walsh, T. Pavlova (2007b), The Arctic surface energy budget as simulated with the IPCC AR4 AOGCMs. Clim. Dyn., 29 (2-3), doi: 10.1007/s00382-006-0222-9.

224. Spreen, G., L. Kaleschke, and G. Heygster (2008), Sea ice remote sensing using AMSR-E 89-GHz channels. J. Geophys. Res., 113, C02S03, doi:10.1029/2005JC003384.

225. Stark, J.D, Donlon CJ, Martin MJ, McCulloch ME. 2007. OSTIA: An operational, high resolution, real time, global sea surface temperature analysis system. Proceedings of Oceans 07 IEEE Conference, Marine Challenges: Coastline to Deep Sea, 1821, June 2007, Aberdeen, UK.

226. Steele, M., J. Zhang, and W. Ermold (2010), Mechanisms of summertime upper Arctic Ocean warming and the effect on sea ice melt, J. Geophys. Res., 115 (C11), doi:10.1029/2009JC005849.

227. Stone, R.S., D.C. Douglas, G.I. Belchansky, S.D. Drobot, and J. Harris (2005), Cause and effect of variations in western Arctic snow and sea ice cover. Paper No. 8.3, presented at Proceedings of the American Meteorological Society Eighth Conference on Polar Oceanography and Meteorology, San Diego, California.

228. Stroeve, J., Th. Markus, W.N. Meier, and J. Miller (2006), Recent changes in the Arctic melt season. Ann. Glaciol., 44(1), 367-374, doi: 10.3189/172756406781811583.

229. Sturm, M., J.A. Maslanik, D.K. Perovich, J.C. Stroeve, J. Richter-Menge, T. Markus, J. Holmgren, J.F. Heinrichs and K. Tape (2006), Snow depth and ice thickness measurements from the Beaufort and Chukchi Seas collected during the AMSR-Ice03 Campaign. IEEE Trans. Geosci. and Rem. Sens., 44 (11), doi: 10.1109/TGRS.2006.878236.

230. Sturm, M., J. Holmgren, and D. Perovich (2002a), Thermal conductivity and heat transfer through the snow on the ice of the Beaufort Sea. J. Geophys. Res, 107 (C10), 8043, doi:10.1029/2000JC000409.

231. Sturm, M., J. Holmgren, and D. Perovich (2002b), Thermal conductivity and heat transfer through the snow on the ice of the Beaufort Sea. J. Geophys. Res, 107 (C10), 8043, doi:10.1029/2000JC000409.

232. Tegen, I., P. Hollrig, M. Chin, I. Fung, D. Jacob, and J. Penner (1997), Contribution of different aerosol species to the global aerosol extinction optical thickness: Estimates from model results. J. Geophys. Res., 102, 23,895-23,915, doi:10.1029/97JD01864.

233. Thiébaux, J., E. Rogers, W. Wang, and B. Katz (2003), A New High-Resolution Blended Real-Time Global Sea Surface Temperature Analysis. Bull. Am. Met. Soc., 84, 645-656 doi: 10.1175/BAMS-84-5-645.

234. Thomas, A., and D.G. Barber (1998), On the use of multi-year ice ERS-1sigma as a proxy indicator of melt period sea ice albedo. Int. J. Rem. Sens., 19 (14), pp. 2807-2821, doi: 10.1080/014311698214523.

235. Thorndike, A.S., and R. Colony (1982), Sea ice motion in response to geostrophic winds, J. Geophys. Res., 87(C8), 5845-5852, doi:10.1029/JC087iC08p05845.

236. Thorndike, A.S. (1986), Kinematics of Sea Ice, in Geophysics of sea ice, edited by N. Untersteiner, pp. 395-463, NATO ASI Series, New York.

237. Thorne, P.W. (2008), Arctic tropospheric warming amplification? Nature 455, E1-E2, doi:10.1038/nature07256.

238. Tiedtke, M., (1993), Representation of clouds in large-scale models. Mon. Wea. Rev., 121, 3040-3061.

239. Tietsche, S., D. Notz, J.H. Jungclaus, and J. Marotzke (2011): Recovery mechanisms of Arctic summer sea ice, Geophys. Res. Lett. 38, L02707, doi:10.1029/2010GL045698

240. Tjernstrom, M., and R.G. Graversen (2009), The vertical structure of the lower Arctic troposphere analysed from observations and the ERA-40 reanalysis. The Quarterly Journal of the Royal Meteorological Society, 135 (639), pp. 431-443.

241. Tjernstrom, M., J. Sedlar, and M. D. Shupe (2008), How well do regional climate models reproduce radiation and clouds in the Arctic? An evaluation of ARCMIP simulations. J. Appl. Meteorol. and Climatol., 47, 2405-2422.

242. Tjernstrom, M. (2005), The Summer Arctic Boundary Layer during the Arctic Ocean Experiment 2001 (AOE-2001). Boundary-Layer Meteorol. 117, p. 5-36, doi: 10.1007/s10546-004-5641-8.

243. Tsukernik, M., D. N. Kindig, and M. C. Serreze (2007), Characteristics of winter cyclone activity in the northern North Atlantic: Insights from observations and regional modeling. J. Geophys. Res., 112, D03101, doi:10.1029/2006JD007184.

244. Tucker, W.B.I., J.W. Weatherly, D.T. Eppler, D. Farmer., D.L. Bentley, 2001: Evidence of the Rapid thinning of sea ice in the western Arctic ocean at the end of 1980s. Geophys. Res. Lett., 28 (14), 2851-2854, doi:10.1029/2001GL012967.

245. Uppala S., D. Dee, S. Kobayashi, P. Berrisford and A. Simmons (2008), Towards a climate data assimilation system: status update of ERA Interim. ECMWF Newsletter No. 115, 12-18.

246. Vihma, T., M. Johansson, and J. Launiainen (2009), Radiative and turbulent surface heat fluxes over sea ice in the western Weddell Sea in early summer. J. Geophys. Res.,114 (C04), doi:10.1029/2008JC004995.

247. Vihma, T., J. Jaagus, E. Jakobson, and T. Palo (2008), Meteorological conditions in the Arctic Ocean in spring and summer 2007 as recorded on the drifting ice station Tara. Geophys. Res. Lett., 35 (L18), doi:10.1029/2008GL034681.

248. Vihma, T., J. Uotila, B. Cheng, and J. Launiainen (2002), Surface heat budjet over the Weddel sea: buoy results and model comparisons. J. Geophys. Res., 107, doi : 10.1029/2000JC000372.

249. Wadhams, P., and N. R. Davis (2000), Further evidence of ice thinning in the Arctic Ocean, Geophys. Res. Lett., 27(24), 3973-3975, doi:10.1029/2000GL011802

250. Wadhams, P., (2000), Ice in the Ocean. Published by Taylor and Francis, 1st edition.

251. Walsh, J.E., and W.L. Chapman (1998), Arctic cloud-radiation-temperature associations in observational data and atmospheric reanalyses. J. Clim., 11, 3030-3045.

252. Wang, J., H. Eicken, Y. Yu, X. Bai, J. Zhang, H. Hu, M. Ikeda, K. Mizobata, and J. Overland (2010), Model-Data Fusion Studies of Pacific Arctic Climate and Ice-Ocean Processes. Springer PAR Synthesis Book Chapter 6.

253. Wang, X., J.R. Key, C. Fowler, and J. Maslanik (2007), Diurnal cycles in Arctic surface radiative fluxes in a blended satellite-climate reanalysis data set. J. Appl. Rem. Sens., 1.

254. Wang, X., V.R. Swail, and F.W. Zwiers (2006), Climatology and changes of extratropical cyclone activity: comparison of ERA-40 with NCEP-NCAR Reanalysis for 1958-2001, J. Climate, 19 (13), pp. 3145-3166, doi: 10.1175/JCLI3781.1.

255. Wang, X., and J. R. Key (2005a), Arctic surface, cloud, and radiation properties based on the AVHRR Polar 36 Pathfinder dataset. part I: spatial and temporal characteristics, J. Climate., 18 (14), 2558-2574, doi: 10.1175/JCLI3438.1.

256. Wang, X., and J. R. Key (2005b), Arctic surface, cloud, and radiation properties based on the AVHRR Polar 36 Pathfinder dataset. Part II: Recent trends. J. Climate, 18 (14), 2575-2593, doi: 10.1175/JCLI3439.1.

257. Wang, X., and J. R. Key (2003), Recent Trends in Arctic Surface, Cloud, and Radiation Properties from Space. Science, 299 (5613), 1725-1728, doi: 10.1126/science.1078065.

258. Warren, S.G., I.G. Rigor, N. Untersteiner, V.F. Radionov, N.N. Bryazgin, Y.I Aleksandrov and R. Colony (1999), Snow depth on Arctic sea ice. J. Climate, 12 (6), 1814-1829, doi : 10.1175/1520-0442(1999)012.

259. Warren, S.G., C.J. Hahn, J. London, R.M. Chervin, and R.L. Jenne (1988), Global distribution of total cloud cover and cloud type amounts over the ocean. NCAR Tech. Note, NCAR/TN-317+STR, 41 pp.

260. Weatherly, J. W., D. K. Perovich, and S. V. Nghiem (2005), Variability in the Arctic sea ice melt season, J6.7, paper presented at 85th American Meteorological Society Meeting, San Diego, Calif.

261. Wendler, G., B. Moore, B. Hartmann, M. Stuefer, and R. Flint (2004), Effects of multiple reflection and albedo on the net radiation in the pack ice zones of Antarctica. J. Geophys. Res. 109 (DO6), doi:10.1029/2003JD003927.

262. Wendler, G., (1986), The "radiation paradox" on the slopes of the Antarctic continent. Polarforschung, 56 (1/2), 33-41.

263. Willmes, S., Bareiss, J., Haas, C., and M. Nicolaus (2009a), Observing snowmelt dynamics on fast ice in Kongsfjorden, Svalbard, with NOAA/AVHRR data and field measurements. Polar Research 28(2): 203-213, doi:10.1111/j.1751-8369.2009.00095.x.

264. Willmes, S., Haas, C., Nicolaus, M. and J. Bareiss (2009b), Satellite microwave observations of the interannual variability of snowmelt on sea ice in the Southern Ocean, J. Geophys. Res., 114, C03006.

265. Wilson, A. B., D. H. Bromwich, and K. M. Hines (2011), Evaluation of Polar WRF forecasts on the Arctic System Reanalysis domain: Surface and upper air analysis, J. Geophys. Res., 116, D11112, doi:10.1029/2010JD015013.

266. Winebrenner, D.P., E.D. Nelson, R. Colony, and R.D. West (1994), Observation of melt onset on multiyear Arctic sea ice using the ERS-1 synthetic aperture

radar, J. Geophys. Res., 99 (C11), pp. 22,425-22,441, doi:10.1029/94JC01268.

267. Winton, M. (2006), Does the Arctic sea ice have a tipping point? Geophys. Res. Lett., 33, L23504, doi:10.1029/2006GL028017.

268. Xin Lin (2008). PhD thesis: . University of Manitoba, Winnipeg, Canada.

269. Yackel, J.J., D.G. Barber, T.N. Papakyriakou, and C. Breneman (2007), First-year sea ice spring melt transitions in the Canadian Arctic Archipelago from time-series synthetic aperture radar data, 1992-2002. Hydrol. Process., 21, 253-265, doi: 10.1002/hyp.6240.

270. Yackel, J.J. (1999). PhD thesis: On the Use of Synthetic Aperture Radar (SAR) for Estimating the Thermodynamic Evolution of Snow Covered First Year Sea Ice. Centre for Earth Observation Science, Department of Geography, University of Manitoba, Winnipeg, Canada.

271. Yu, Y., G.A. Maykut, and D.A. Rothrock (2004), Changes in the thickness distribution of Arctic sea ice between 1958-70 and 1993-79, J. Geophys. Res., 109 (C08), doi:10.1029/2003JC001982.

272. Yueh, S.H., and R. Kwok (1998), Arctic sea ice extent and melt onset from NSCAT observations. Geophys. Res. Lett., 25 (23), pp. 4369-4372, doi: 10.1029/1998GL900080.

273. Zhang, X., J.E. Walsh, J. Zhang, U.S. Bhatt, and M Ikeda (2004), Climatology and interannual variability of Arctic cyclone activity: 1948-2002. J. Climate, 17 (12), 2300-2317, doi: 10.1175/1520-0442(2004)017. (read in my lib! ref in Chap 1, Sec 1.1)

274. Zhang, T., S. A. Bowling, and K. Stamnes (1997), Impact of the atmosphere on surface radiative fluxes and snowmelt in the Arctic and Subarctic. J. Geophys. Res., 102 (D4), 4287-4302, doi: 10.1029/96JD02548.

275. Zhang, J., K. Stamnes, and S.A. Bowling (1996), Impact of clouds on surface radiative fluxes and snow melt in the Arctic and sub Arctic. J. Climate, 9(9), 2110-2123, doi: 10.1175/1520-0442(1996)009.

276. Zhao, Y., and A.K. Liu (2007), Arctic Sea-Ice Motion and Its Relation to Pressure Field. J. Oceanography, 63 (3), pp. 505-515, doi: 10.1007/s10872-007-0045-2.

277. Zubov, N.N. (1943), Arctic ice. U.S. Naval Oceanographic Office. In English Translation (1963).

278. Zuidema, P., B. Baker, Y. Han, J. Intrieri, J. Key, P. Lawson, S. Matrosov, M. Shupe, R. Stone, and T. Uttal (2005), An Arctic springtime mixed-phase cloudy boundary layer observed during SHEBA. J. Atmos. Sci., 62 (1), 160-176, doi: doi: 10.1175/JAS-3368.1.

JOURNAL OF GEOPHYSICAL RESEARCH, VOL. 117, C07012, doi:10.1029/2011JC007220, 2012

The effect of surface heat fluxes on interannual variability in the spring onset of snow melt in the central Arctic Ocean

Elena Maksimovich[1] and Timo Vihma[2]

Received 21 April 2011; revised 25 May 2012; accepted 25 May 2012; published 14 July 2012.

[1] The timing of spring snow melt onset (SMO) on Arctic sea ice strongly affects the heat accumulation in snow and ice during the melt season. SMO itself is controlled by surface heat fluxes. Satellite passive microwave (SSM/I) observations show that the apparent melt onset (MO) varies a lot interannually and even over 50–100 km distances. The MO record appeared to be a complex blend of SMO on top of sea ice and opening of leads and polynyas due to divergent sea ice drift. We extracted SMO out of the original MO record using sea ice concentration data. Applying ERA Interim reanalysis, we evaluated the portion of SMO variance explained by radiative and turbulent surface heat fluxes in the period of 1989–2008. The anomaly of the surface net heat flux 1–7 days prior to SMO explained up to 65% of the interannual variance in SMO in the central Arctic. The main term of the net flux was the downward longwave radiation, which explained up to 90% of SMO variance within the western central Arctic. The role of the latent and sensible heat fluxes in earlier/later SMO was not to bring more/less heat to the surface but to reduce/enhance the surface heat loss. Solar radiation was not an important factor alone, but together with other fluxes improved the explained variance of SMO. Local 20-year SMO trends averaged over the central Arctic Ocean are toward earlier melt by 9 days per decade.

Citation: Maksimovich, E., and T. Vihma (2012), The effect of surface heat fluxes on interannual variability in the spring onset of snow melt in the central Arctic Ocean, *J. Geophys. Res.*, *117*, C07012, doi:10.1029/2011JC007220.

1. Introduction

[2] The melt season on Arctic sea ice is short, typically about 2–4 months (May–August), with the most intense incident solar shortwave (SW) radiation during May–July of 150–300 W/m^2 (daily means) at the surface [*Ebert and Curry*, 1993]. Prior to the melt onset (MO) on top of compact sea ice, the snowpack is dry and reflects 80–90% of the incident SW radiation. With MO, free water appears within the snowpack and snow crystals coarsen. As a result, SW scattering within the snowpack weakens and SW absorption increases [*Grenfell and Perovich*, 1984, 2004]. Therefore, an earlier snow melt by a few days increases the accumulation of SW radiation within the snowpack, which makes an important contribution to the total surface heat storage during the melt season [*Bitz et al.*, 1996]. Radiation measurements in the central Arctic have quantified that one day earlier MO on top of the sea ice increases the melt season cumulative absorbed SW energy at the sea ice - ocean surface by approximately 8.7 MJ/m^2, corresponding to the additional 3 cm of summer ice melt [*Perovich et al.*, 2007b]. In comparison, 1-day delay in fall freeze-up results in an increase by only 1.5 MJ/m^2, or less than 0.5 cm of additional ice melt. An early MO on sea ice and the associated early generation of open water areas favor heat accumulation in the upper ocean [*Drobot*, 2007; *Eicken and Lemke*, 2001; *Perovich et al.*, 2007a]. Further, it takes more time in autumn to cool warmer water masses down to the freezing point. As a result, the freeze-up starts later, which contributes to sea ice thinning in the following year [*Laxon et al.*, 2003].

[3] Over the past few decades a tendency toward earlier MO in the Arctic has been revealed based on satellite observations. Already *Anderson and Drobot* [2001] have detected significant trends (1979–1998) toward earlier MO in the western central Arctic (8.9 days per decade), Lincoln Sea (4.4 days per decade) and Beaufort Sea (5.1 days per decade). *Belchansky et al.* [2004] evaluated the difference between two decadal averages (1979–1988 and 1989–2001): by 5 days in the Kara - northern Barents and Chukchi Seas, by 9 days in the East Siberian Sea, and by 4 days in the central Arctic. More recently, also based on a satellite passive microwave record, *Stroeve et al.* [2006] and *Markus et al.* [2009] demonstrated statistically significant 29-year (1979–2007) MO trends by 2–4 days per decade in the central Arctic, Laptev, East-Siberian, Chukchi and Beaufort Seas and the Baffin Bay. The tendency toward earlier MO and sea ice thinning [*Giles et al.*, 2008; *Kwok and Rothrock*, 2009] are essential elements in the recent Arctic warming,

[1]Laboratoire d'Océanographie et du Climat: Expérimentation et Approches Numériques, Paris, France.
[2]Finnish Meteorological Institute, Helsinki, Finland.

Corresponding author: E. Maksimovich, Laboratoire d'Océanographie et du Climat: Expérimentation et Approches Numériques, 4, place Jussieu, Tour 45-55, Paris CEDEX 05, France. (maksimovich.elena@gmail.com)

0148-0227/12/2011JC007220

but, according to our knowledge, reasons for the statistically significant 20–30-year trends in MO have not been explained yet.

[4] Trends as well as the interannual and regional variations in snow MO on top of sea ice are controlled by the surface heat fluxes. The surface fluxes, in turn, are affected by the air temperature and humidity, wind speed, clouds, snow and ice thickness, and the heat conductivity of snow and ice. By *surface* fluxes we mean the fluxes in the uppermost ~0.2 m of the snowpack. SW radiation penetrates into the snowpack, so that melt often starts a few cm below the surface [*Cheng et al.*, 2006, 2008]. An early (late) snow MO on top of sea ice is only due to an early and fast (late and retarded) net heat flux accumulation.

[5] Previous studies on the factors controlling the spring snow MO on sea ice have mostly addressed the role of a large-scale atmospheric circulation on the regional average MO, or the local effect of radiative and turbulent surface heat fluxes observed during field campaigns. Field observations by *Barber et al.* [1994], *Granskog et al.* [2006] and *Vihma et al.* [2009] demonstrated the importance of synoptic-scale variations and the diurnal cycle in the surface heat fluxes. *Cheng et al.* [2008] showed that success in modeling of snow MO strongly depends on the vertical resolution applied: with a 15–20 layer snow model resolving the snow MO better than a 3 layer model. The study by *Yackel et al.* [2007] indicated on a poor agreement (no significant relationship) between the near-surface air temperatures (daily means reaching 0°C) and the remote sensed MO on sea ice.

[6] *Drobot and Anderson* [2001] and *Belchansky et al.* [2004] both developed algorithms for MO detection by remote sensing and found that interannual variations in the regional mean MO within the Arctic are affected by the large-scale atmospheric circulation (the Arctic Oscillation index) and the near-surface air temperatures (SAT) during preceding months. The role of clouds and atmospheric moisture content in snow MO timing on sea ice has been addressed by *Zuidema et al.* [2005], *Stone et al.* [2005], and *Nghiem et al.* [2003], but only a few direct investigations of the cloud radiative forcing on snow MO have been made [*Zhang et al.*, 1996, 1997], based on a radiative transfer model only. Little attention has been paid to small-scale spatial differences and interannual variations in the observed snow MO and surface fluxes.

[7] Our approach is totally different. We examine whether radiative and turbulent surface heat fluxes on top of Arctic sea ice (based on meteorological reanalysis) can explain the interannual and spatial (50–130 km scale) variations in snow MO (based on remote sensing retrievals) within a vast domain (83–87°N) and over a 20-year period (1989–2008). This kind of analysis requires (1) a distinct definition of what is regarded as snow MO, (2) an estimation of the relative importance of the individual surface fluxes (shortwave and longwave radiation as well as the turbulent fluxes of sensible and latent heat) and various combinations of fluxes in the further timing of snow MO, and (3) an evaluation of the length of a relevant pre-melt period when surface flux anomalies are crucial for further timing of snow MO.

[8] The three data sets utilized in this study are described in section 2: ERA Interim reanalysis of surface fluxes and two remote sensing records of (a) sea ice concentrations and (b) MO. As we will highlight, the satellite retrievals of MO do not only represent the snow melt onset (SMO) on top of the compact sea ice, but also include cases of divergent sea ice drift. Hence, our first task was to extract the SMO signature from the original MO record. The methodology applied is outlined in section 3.1. To compare the SMO timing and the heat flux anomaly prior to SMO we introduce three alternative and complementary methods. At this stage we make assumptions on the relevant temporal and spatial scales of the processes (sections 3.2 and 3.3). 20-year climatologies of the original MO record and the extracted SMO sample are illustrated in section 4.1, and statistics of the surface heat flux components are presented in section 4.2. The main result of this study: the role of the surface fluxes in SMO variability is outlined in sections 4.3 and 4.4. 20-year tendencies in MO, SMO and surface fluxes are considered in section 4.5. The results and perspectives for future work are discussed in section 5, and the concise conclusions are drawn in section 6.

2. Data

2.1. Melt Onset Data

[9] The appearance of water in snow causes the grains to cluster, resulting in larger grains with a more rounded shape. As a result, the snow emissivity increases in the near-infrared and microwave wavelengths, and the reflectivity decreases in the visible spectrum. Field observations show that the initial surface melt is often followed by episodic re-freezing and melting, each time affecting the emissivity and reflectivity of the surface [*Barber et al.*, 1994; *Ehn et al.*, 2006]. First attempts to detect MO with the help of satellite visible, near-infrared and microwave measurements date to 1980s [*Anderson*, 1987; *Grenfell and Perovich*, 1984; *Robinson et al.*, 1986]. It was soon found that cloud cover and precipitation have the strongest effect on the visual and near-infrared spectrum [*Forster et al.*, 2001; *Yackel et al.*, 2007], thus making the microwave observations the most compatible for MO detection. For this reason, the recently updated Arctic-wide MO record derived from the Scanning Multichannel Microwave radiometer and Special Sensor Microwave Imager (SMMR-SSM/I) passive microwave measurements of brightness temperature [*Markus et al.*, 2009] was chosen for our study. MO data set is available on http://neptune.gsfc.nasa.gov/csb/index.php?section=50.

[10] The MO spatial resolution (pixel size) is approximately 25 km with the northward limit at 87°N. Compared to the other time series, the major advantage of this MO record is that until recently it was the only one to cover the complete 30-year period of 1979–2008 and both multiyear and first-year ice areas.

[11] *Markus et al.* [2009] defined the MO as the first day of the continuous melt. Thus, at each individual 25 km pixel, the snow MO is the day of the year when water in liquid phase stays continuously present on top of sea ice (first-year or multiyear), either within the snowpack or on top of the bare ice. Otherwise, if no clear snow MO signal is detected, the day when the sea ice concentration drops below 80% for the last time before the area (pixel) becomes ice-free, is considered as MO. It means that formation of open water areas (leads and polynyas) is also included in the MO record, although leads and polynyas may open without any melt, but only due to divergent sea ice drift.

[12] This MO retrieval has been compared by *Markus et al.* [2009] with buoy observations of surface air temperature (SAT) and reanalysis data from the National Center for Environmental Prediction and the National Center for Atmospheric Research (NCEP/NCAR). At two locations (one multiyear and the other with first-year sea ice) SSM/I-based and SAT-based snow MO agree within less than 8 days (better over first-year ice). Over the entire Arctic Ocean these three MO estimates (SSM/I, buoy SAT and reanalysis SAT) were compared during one particular year in terms of their spatial distribution statistics. While spatial distribution curves do not perfectly mirror one another, they are in a very good agreement. This comparison, however, does not provide the conclusive quantitative validation for the SSM/I-based snow MO retrievals. First, because SAT data (both buoy observations and reanalysis) themselves have errors. Second, because melt within the snowpack does not necessarily coincide with 0°C or −1°C air temperatures at 2 m height [*Yackel et al.*, 2007]. Third, because when varying the threshold applied to SAT data by ±2°C, the resulting SAT-based MO ranges by as much as ±50 days [*Markus et al.*, 2009].

2.2. Sea Ice Concentration

[13] We utilized a daily Arctic sea ice concentration (SIC) record by *Cavalieri et al.* [1996], which is based on the same SMMR-SSM/I brightness temperature measurements with the same spatial resolution as the MO data. These SIC data were produced with the NASA Team Algorithm and obtained from the National Snow Ice Data Center website http://nsidc.org/data/nsidc-0051.html. Note that in the algorithm for the MO detection developed by *Markus et al.* [2009] the same NASA Team Algorithm was applied for SIC estimation.

2.3. ERA Interim Reanalysis Data

[14] ERA Interim reanalysis (ERAI) of the surface heat fluxes with 12 h intervals [*Dee et al.*, 2011] were chosen for the comparison with the MO record. ERAI is the newest of the three reanalyses produced by the European Centre for Medium-Range Weather Forecasts (ECMWF). ERAI has a global coverage with a spatial resolution of 0.72° latitude by 0.72° longitude, spanning the period from 1989 onwards. ERAI benefits from the experience of previous reanalyses, with several major improvements: higher resolution, assimilation of more extensive and diverse observational data with a more sophisticated technique (four-dimensional variational data assimilation), an improved hydrological cycle and a variational bias correction of satellite radiance data [*Dee and Uppala*, 2009]. Compared to the earlier ERA-40 reanalysis, ERAI also has a better vertical consistence of the air temperature in the Arctic region [*Uppala et al.*, 2008; *Dee and Uppala*, 2009]. This comparison was done against 2000 radiosonde reports inland north of 70°N. With the introduction of the variational bias correction in ERAI, the vertical structure is now more efficiently constrained by radiosonde observations [*Uppala et al.*, 2008; *Dee and Uppala*, 2009].

[15] Over Arctic sea ice ERAI vertical profiles of air temperature, humidity and wind have been validated against observations from three ship campaigns [*Lüpkes et al.*, 2010]. It was found that ERAI overestimates the near-surface humidity and air temperature during summer, whereas the near-surface winds in ERAI are represented more accurately, with the differences increasing at higher altitudes but remaining less than 1 m s^{-1}. According to our knowledge, the accuracy of ERAI surface fluxes on top of Arctic sea ice is yet to be validated.

[16] In ERAI the SIC is prescribed in the same way as for ERA-40 prior to January 2002 [*Fiorino*, 2004]. From 1 January 2002 to 31 January 2009 ERAI follows the ECMWF operational forecasting system [*Thiébaux et al.*, 2003]. Sea ice concentrations below 20% are set to 0%. South of 82.5°N, SIC in ERAI is based on SSM/I passive microwave measurements, and northward from 83°N SIC is set to 100% [*European Centre for Medium-Range Weather Forecasts* (*ECMWF*), 2008a], although this is not realistic. Sea ice in ERAI has a uniform thickness of 1.5 m and no snow cover on top [*ECMWF*, 2008b]. No data on snow or ice surface temperature are assimilated to ERAI. In this formulation, the variability of the conductive heat flux through the ice and snow is limited and depends primarily on the atmospheric fluxes. Radiative and turbulent surface fluxes from ERAI include downward longwave radiation (LWd), net longwave radiation (LWnet), downward shortwave radiation (SWd), net (absorbed) shortwave radiation (SWnet) and turbulent fluxes of latent (LE) and sensible (H) heat. Positive values represent heat flux to the surface.

3. Methodology

3.1. Determination of Snow MO

[17] Considering the definition of the continuous MO by *Markus et al.* [2009], the ice conditions may evolve as follows. During some period in spring, the ice field diverges and SIC reduces to less than 80% (even down to 0%) in a SSM/I pixel. Then the wind changes and due to sea ice drift, SIC temporarily increases back to values exceeding 80% in the given pixel. A few days/weeks later, the snow melt onsets on top of sea ice or divergent ice drift exposes open water within the same area. In this situation the MO algorithm by *Markus et al.* [2009] determines the continuous MO as the last drop in SIC (below the 80% threshold) before the area becomes ice free or as the last snow MO event on top of the compact sea ice.

[18] In nature when SIC stays high (100%) throughout the pre-melt period, surface fluxes (and meteorological conditions) affect SMO and not vice versa. To ensure that SIC was high throughout the pre-melt period, we first distinguish the MO cases (pixels and years) least affected by the SIC changes in the pre-melt period. For that we tested several SIC filters, where the MO pixel was considered to be a *snow MO pixel*, if the daily (or time averaged) SIC prior to the MO did not fall below some threshold (80, 85 or 95%; see below).

3.2. Evaluation of the Relevant Temporal and Spatial Scales

[19] Besides removing those MO pixels that have already experienced the drop in SIC prior to MO, the two data sets (MO and surface fluxes) also need to be converted to a comparable spatial resolution. A question arises: what is the sea ice area that is affected by the surface fluxes at a fixed grid location? A drifting sea ice floe is under the effect of the flux at a fixed grid cell only during some limited period of

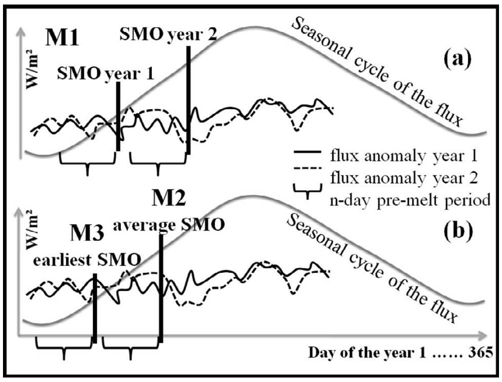

Figure 1. Schema of three methods (M1, M2 and M3) used to determine the pre-melt period and for calculation of the flux anomaly prior to SMO. In method M1 the pre-melt period is defined to start n days (n = 1–40) prior to the exact local SMO date, which varies both interannually and spatially. In methods M2 and M3 the pre-melt period varies spatially but not interannually. In M2 the pre-melt period starts n days before the local 20-year average SMO date, whereas in M3 the pre-melt period starts n days before the earliest local SMO during the 20-year period. The SMO date itself is not included in the n-day pre-melt period.

time. Before and after that, the ice slab is affected by surface fluxes at the neighboring grid cells.

[20] A comparison of different solutions led to the formulation of the following assumptions. Those MO pixels with a 40-day average SSM/I-based SIC ≥ 85% during a 40-day pre-melt period were considered to be *snow MO pixels.* This 85% SIC filter allows for SIC changes in time, removing those pixels with a pronounced SIC reduction, and, at the same time, keeping those MO events least affected by SIC reduction already in the pre-melt period. Stronger SIC filters tend to reject most of the MO data set, which drastically reduces the study material. Snow MO timing in ERAI grid coordinates was determined as the average MO date of all *snow MO pixels* within a 130-km radius around each ERAI grid location. The radius is based on the following assumptions. With a typical wind speed of 5 m/s in spring, assuming that sea ice drift speed is 2% of the wind speed [*Thorndike and Colony*, 1982] and that the monthly displacement is half a trajectory length, the monthly ice displacement is approximately 130 km. This rough estimate agrees well with the satellite data on sea ice displacements (F. Girard-Ardhuin, IFREMER/LOS, personal communication, 2011). The monthly displacement naturally varies in space and time, but we only need an order of magnitude estimate to provide SMO spatial averaging.

[21] For clarity, we use the abbreviation SMO for the snow MO on sea ice and reserve the abbreviation MO for the melt onset as defined by *Markus et al.* [2009].

3.3. Comparison of SMO and Surface Fluxes

[22] We compared SMO data against ERAI daily surface heat flux anomalies (relative to the 20-year climatology) in the common 20-year period of 1989–2008. The very recent extension of ERAI for the period 1979–1988 became available too late for this study. The flux anomalies were averaged over 1–40 days before a reference SMO date, and then compared to the SMO anomaly at the same location and year. Time averaging up to 40 days is demonstrated here, because it appeared that longer periods prior to SMO did not improve the capability of surface fluxes to explain the SMO timing. The definition of the reference SMO date and the further flux averaging were done using three alternative methods, schematically illustrated in Figure 1.

[23] With method M1 the flux anomalies were calculated right before the exact SMO date. As the SMO date is different each year and varies from one location to another, the variations in the reference date slightly hamper the interannual comparison of the flux anomalies. To fix the reference SMO date, we chose the 20-year average SMO date (method M2) and the 20-year earliest SMO date (method M3) at each location. This allows for a more suitable comparison of flux anomalies between different years, but the drawback is that the period just a few days before SMO is usually (M3) or in approximately half of the cases (M2) not included in the calculations.

[24] First order (bilateral) linear regression analysis was used to compare (correlate) two 20-year time series: the n-day average (n = 1 to 40) flux anomaly and the SMO anomaly, both in the same ERAI grid (Figure 2, example for the net flux). A statistically significant relationship with a 99% confidence level ($p < 0.01$) is established when the correlation coefficient (r) exceeds 0.56 ($r^2 > 0.31$). Over a compact sea ice cover, a causal effect of the surface flux anomaly on SMO requires a negative r: a positive flux anomaly precedes an early SMO and vice versa (Figure 2, example for the net flux). Considering the physical interpretation, r^2 represents the percentage of the interannual

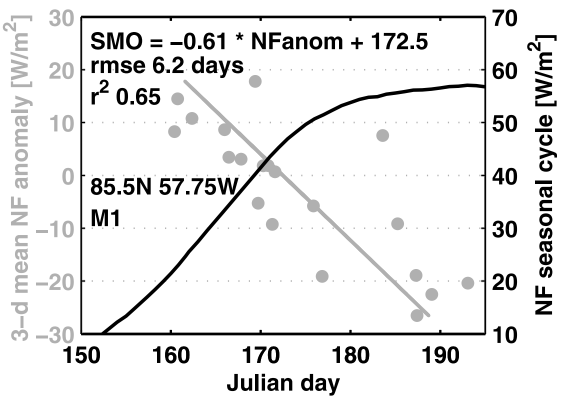

Figure 2. Causal relationship between a 3-day average NF anomaly and the corresponding SMO timing [Julian day] at one location 85.5°N 57.75°W. Black curve (right *y* axis) shows the 20-year mean seasonal cycle of NF at this location. Gray circles and their linear fit show the relationship between SMO (*x* axis) and the preceding NF anomaly (left *y* axis) averaged during 3-day pre-melt period prior to SMO (method M1). The linear regression equation suggests that a 3-day average local NF anomaly prior to exact SMO date explains 65% of the interannual local variance in SMO, with RMSE of 6.2 days.

variance in SMO timing explained by the interannual changes in the flux anomaly.

[25] Stepwise forward multiple linear regression analysis [*Draper and Smith*, 1998] was applied to find out how well various combinations of flux anomalies (LWd, SWd, LE and H) explain the interannual variance of SMO, and which combinations of ERAI fluxes best reflect SMO variability. Among 4 potential predictors (individual fluxes) the first term included in the multilinear regression equation correlates the best with SMO. At this stage we get a first-order linear regression equation. At the next step the predictor best explaining the residuals from the existing linear regression equation is accepted. This procedure is repeated further, as long as the correlation coefficient between the potential predictors and the residuals is significant. The overall multilinear regression equations (with 2, 3 or 4 terms) for each of 40 time averaging periods are examined for significance with an *F* test. The critical F-value depends only on a number of predictors included in the multilinear regression equation. Length of the time series is constant of 20 years, and $p < 0.01$. To note, the anomalies of all flux components included in the multilinear regression equation are averaged over the same time averaging period.

[26] In sections 2 and 3 we briefly described the MO algorithm developed and applied by *Markus et al.* [2009] to the daily brightness temperature measurements to evaluate the apparent MO at each 25 km pixel and each year (1979–2008). *Continuous* MO is considered here. However, usually some transition period characterized by alternating melting and re-freezing events occurs. During this period the daily amplitude in brightness temperature increases until it reaches a maximum in the beginning of the continuous melt [*Markus et al.*, 2009]. Time-space resolution of both data sets (SSM/I-based MO and ERAI fluxes) is limited. So it is evident that many of the localized (tens to hundreds of meters scales) episodic (of a few hours) snow melt events are not captured in either data set. From this point of view, it seems that the onset of *continuous* snow melt is a more distinct event than any *episodic* melt, and it should be better represented in both remote sensing records and meteorological reanalysis.

4. Results

4.1. MO and SMO Climatology

[27] According to the MO record produced by *Markus et al.* [2009], on average (in 1989–2008), the melt starts around late May at the southernmost ice margin: in the Greenland Sea, northern Barents Sea, southern Kara Sea, as well as Bering and Davis Straits (Figures 3a and 3b). The northward advance of melt from the Alaskan and Siberian coast and the northern Greenland Sea up to 87°N takes approximately 40 days (Figures 3a and 3b). The area farther north is unfortunately not covered by SSM/I observations.

[28] The analysis is complicated by the fact that MO timing is very variable in space (Figure 3e) and interannually (Figures 3c and 3d). In the central Arctic the MO differences over a 50 km distance are mostly less than 25 days (0.5 days km^{-1}), but there are some areas where the MO difference over a 50 km distance has even reached 3 months (2 days km^{-1}, Figure 3e). The majority of cases (pixel years) with the large horizontal MO gradients are due to early ice opening: lead and polynya formation already in March. Accordingly, vast leads have occurred as far as 80–85°N. In the presence of compact (100%) sea ice cover, the regional differences in snow melt timing are controlled by the surface fluxes. Visual comparison of the MO maps with the surface fluxes on the Pacific side of the Arctic Ocean (70–85°N, 170–220°E) revealed a few large spatial gradients in heat fluxes across the areas of abrupt MO differences. Some of these differences in heat fluxes and MO seem to be associated to the atmospheric fronts, and not related to SIC changes (according to SSM/I-based SIC data). These MO events were, most likely, the true SMO cases. Yet, the episodic, short-lived (1–5 days) and highly localized spatial gradients in NF, SWd and H by up to 25 W/m^2 within a 50 km distance (between neighboring ERAI grid locations) do not convincingly explain SMO spatial gradients exceeding 1 month within a 50 km distance. Instead, the spatial differences in the ice type may provide an explanation for these pronounced MO gradients within totally ice-covered region. Field observations in April–May demonstrated that thinner sea ice is 5–10°C warmer at the snow-ice interface compared to thick ice [*Perovich and Elder*, 2001]. This is due to a larger conductive heat flux through thinner ice. Thus, with the same meteorological conditions and a uniform snow depth, on top of thin ice it takes less time to heat the snow to the melting point. In consequence, SMO starts earlier on top of thinner (initially warmer) ice floe, compared to thick multiyear ice.

[29] The typical local (same pixel) interannual fluctuations in MO are about ±2 weeks around the average MO date in the central Arctic, increasing in the marginal seas, locally up to ±4 weeks (Figure 3c). Application of the SIC filter to the original MO data, yielding the SMO sample (see section 3.2), reduced the local interannual variations and smoothed the spatial differences in the timing of surface melt initiation (Figures 3b and 3d).

[30] Figure 3f demonstrates the smallest one day SIC (SSM/I-based data of 25 km resolution) in a 40-day pre-melt period prior to MO (M1). Smallest SIC observed during 1989–2008 is shown for each 25 km pixel. As discussed already in section 3.1, our analysis reveals vast areas where SIC values have episodically fallen below 80% and sometimes even below 50% already before MO (Figure 3f). This means that already prior to continuous MO (divergent ice drift or snow MO) the reduced SIC has in some springs affected the surface heat fluxes, although not necessarily in ERAI.

4.2. ERAI Climatology of Surface Fluxes in April–June Within 83–87°N

[31] The ERAI fluxes least affected by SIC changes are those within the circumpolar Arctic between 83.25°N and 87°N, where the SIC in ERAI (but not in reality) is 100% every year during the entire pre-melt period. Hereafter we focus on this circumpolar central Arctic region which occupies an area of approximately 1.7×10^6 km^2.

[32] SWd increases rapidly as the polar day progresses on average from 90 ± 40 W/m^2 in April up to 250 ± 70 W/m^2 in June (Figure 4a). Absorption of SW radiation (SWnet) enhances in spring (Figure 4b) due to increasing downwelling SWd radiation: from 20 ± 10 W/m^2 in April to 75 ± 25 W/m^2 in June, becoming the most efficient in July. In ERAI the monthly albedo of sea ice and open water are prescribed according to the seasonal means as determined by

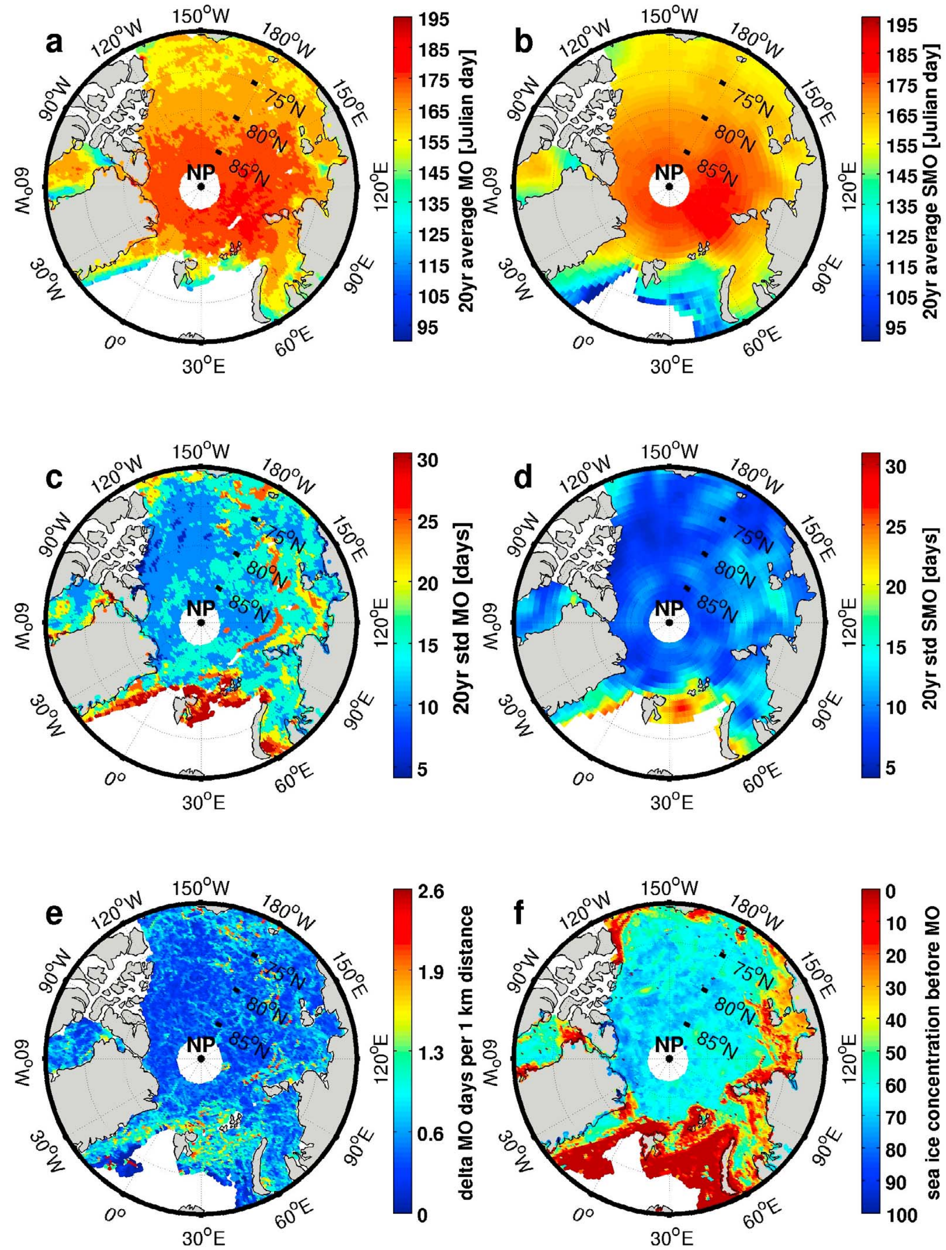

Figure 3. Maps of statistics of MO (SSM/I resolution of 25 km, based on *Markus et al.* [2009]), SMO (ERAI grid resolution), and SIC (SSM/I) in the period 1989–2008: (a) 20-year average MO, (b) 20-year average SMO, (c) standard deviation of MO, (d) standard deviation of SMO, and (e) the largest differences in MO timing ever observed between two pairs of neighboring pixels (in the same year). These most extreme MO gradients were found in different years in different areas. (f) The smallest ever observed one day SIC in a 40-day pre-melt period prior to MO (method M1).

Ebert and Curry [1993]. The bare sea ice albedo value of 0.51 is taken as a representative value for summer, the dry snow albedo value of 0.77 is used for the winter months, and the open water albedo is approximately 0.06 [*Screen and Simmonds*, 2012].

[33] LWd is a major source of energy for the Arctic snow/ice surface all year-round. From April to June the air moisture content increases, which promotes a larger LWd: of about 190 ± 40 W/m^2 in April, reaching 290 ± 30 W/m^2 in June (Figure 4c). Throughout the year, on average, there is a persistent surface radiative cooling in the central Arctic, with the negative net longwave radiation LWnet values (Figure 4d). Heat loss by means of LWnet reduces in spring from 40 ± 25 W/m^2 in April to 25 ± 20 W/m^2 in June (Figure 4d).

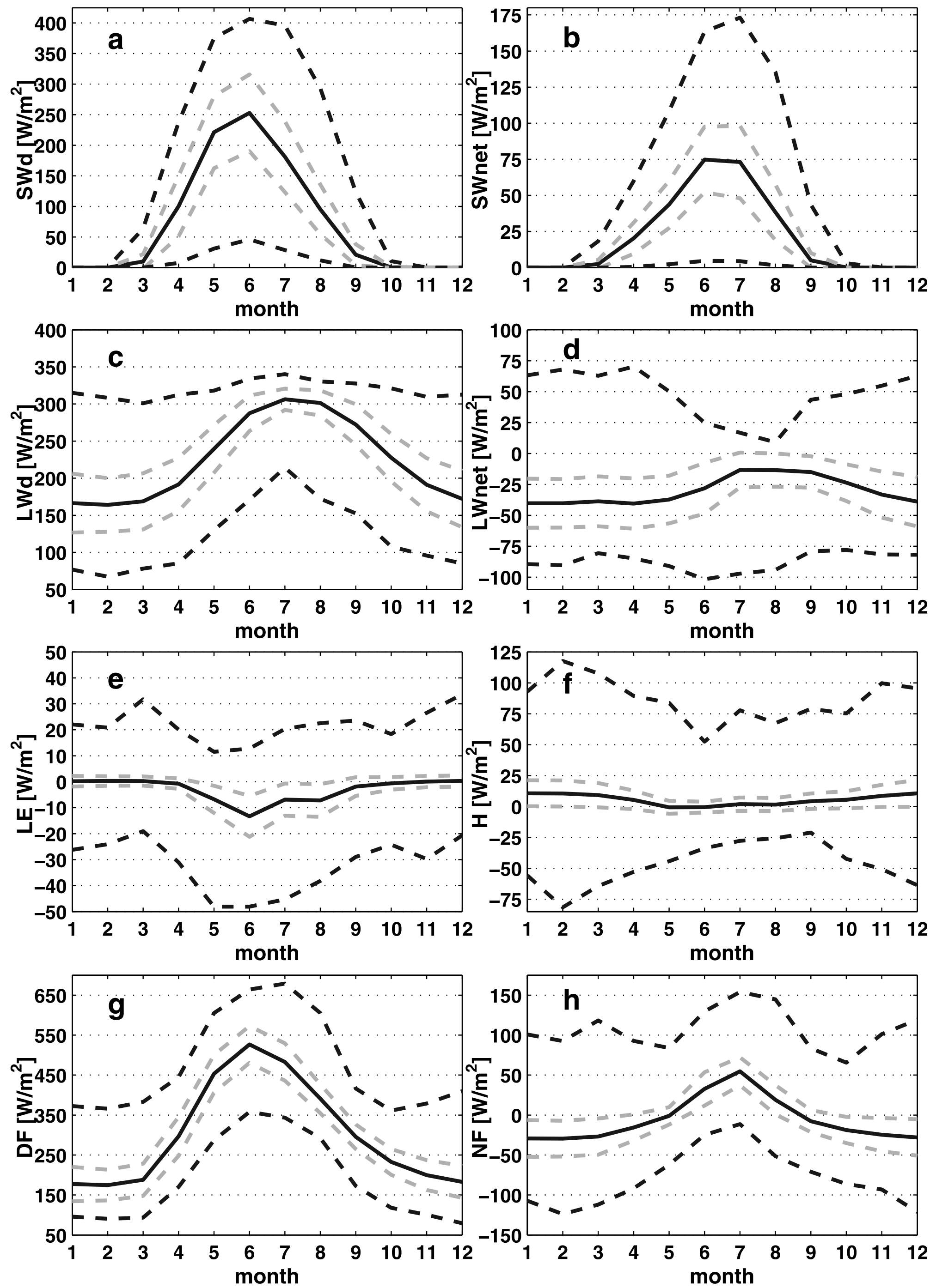

Figure 4. Seasonal cycle of ERAI surface fluxes within 83.25–87°N in the period 1989–2008: (a) downward solar radiation SWd, (b) absorbed solar radiation SWnet, (c) downward longwave radiation LWd, (d) net longwave radiation LWnet, (e) latent heat flux LE, (f) sensible heat flux H, (g) downward flux DF, and (h) the net heat flux NF. The black solid curve is a 20-year average flux (grid-box area weighted). Two gray dashed curves delimit ± one standard deviation of all daily values (in a given month) at all grid locations (within 83.25–87°N). Two black dashed curves delimit the maximum and minimum daily flux values ever occurred at any location (within 83.25–87°N) on any day of each month. Following ERAI convention, negative values correspond to surface heat loss (upward fluxes).

[34] The turbulent surface fluxes are on average relatively weak in spring, of the order of ± 20 W/m^2 [*Ebert and Curry*, 1993]. According to ERAI, sublimation of snow usually takes place during the pre-melt period, roughly April–May months (latent heat flux is upwards). In line with ERAI convention, the monthly and daily mean LE is represented by negative values in Figure 4e. Surface warming during May and early June results in a slightly unstable stratification near the surface, in both nature [*Persson et al.*, 2002] and ERAI. As a result, in May–June the monthly mean sensible heat flux is slightly negative (upwards), of the order of 2 ± 2 W/m^2 (Figure 4f). The day-to-day variability in H and LE is about 5 W/m^2 and quite uniform regionally (not shown here).

[35] Downward radiation (DR) is the sum of LWd and SWd. Both LWd and SWd affect the local surface heat balance, but are not directly influenced by local feedbacks, such as changes in albedo and surface temperature. Although DR increases rapidly as the summer progresses (from 300 to 370 W/m^2 in April to 500 W/m^2 in June), the day-to-day variations are only 40–50 W/m^2 and rather uniform in space (not shown here). The downward flux (DF) is the sum of DR, H and LE (Figure 4g). Compared to DR, DF is more sensitive to surface properties (SIC and albedo) and small-scale processes (wind and near-surface thermal stratification). Nevertheless, over the sea ice the climatology of DR and DF is very similar. In spring DF increases rapidly: from 300 ± 50 W/m^2 in April to 520 ± 50 W/m^2 in June (Figure 4g).

[36] The net flux (NF) is the sum of LWnet, SWnet, H and LE. From August to May NF is negative on average, in the circum-polar central Arctic (Figure 4h). In spring the net surface heat loss switches to surface net heat gain, reaching 30 ± 20 W/m^2 by June (Figure 4h). The local 40-day average NF prior to SMO (M1) is positive (10–15 W/m^2) in the circum-polar central Arctic (not shown).

4.3. Effect of the Surface Fluxes on the Interannual Variations in SMO

[37] After removing the MO pixels largely affected by the sea ice opening in the pre-melt period, methods M1, M2 and M3 were applied to calculate the time-average flux anomalies prior to the SMO date. Bilateral linear regressions were then calculated (at each grid cell) for the 20-year time series of SMO anomalies and corresponding surface flux anomalies. Results obtained with M1, M2 and M3 are qualitatively similar. Depending on the flux, one of the methods appears slightly better than the others. In this context, the best method (M1, M2 or M3) reveals the highest explained variance (r^2). Moreover the best method evokes the relationship (significant r^2) between SMO anomaly and the corresponding heat flux anomaly over a larger area than the other two methods. Comparison of r^2 at various locations suggests that M3 was slightly better for NF (Figure 5g) and M2 for LWd (Figure 5h). To illustrate the main results of this study, we made a compromise by selecting method M1, which reveals a stronger relationship between SMO and both NF and LWd (Figures 5g and 5h).

[38] The local interannual SMO variance is well explained by the interannual changes in NF. The highest r^2 is found with a synoptic time averaging period of about 1–7 days (Figure 5a), explaining locally up to 55–65% (maximum $r^2 = 0.65$) of the interannual SMO variance (Figures 5a and 5e). Considering the entire area where significant r^2 is detected (shaded area in Figure 5e), the 4-day average NF anomaly explains 28% of the total (spatial and interannual) variance in SMO (Table 1). These results indicate that a large portion of our data sample contains a stronger surface NF accumulation (positive NF anomaly relative to the climatology) before the anomalously early snow melt (negative SMO anomaly). And correspondingly, the anomalously weak NF accumulation and even NF loss (negative NF anomaly) are suggested by ERAI in those years and locations where SMO is retarded (positive SMO anomaly).

[39] Next we consider the flux intensity: how large are ERAI NF anomalies (during this optimum 1–7 day pre-melt period) in those locations and years where and when SMO occurred particularly early or late? More precisely: what are the magnitudes of SMO and NF anomalies within the domain where the relationship between SMO and NF is established (shaded area in Figure 5e)? Figure 5c illustrates a group of 20-year time series at different grid locations: (1) SMO anomalies and (2) corresponding 1–7 day average NF anomalies. All ERAI grid locations with a significant r^2 at any (1–7 day) time averaging period are regrouped in Figure 5c. On average, when SSM/I-based SMO occurs anomalously early, for example by 15–20 days, the 1–7 day mean NF anomaly (ERAI) just before SMO is positive of about 17–18 W/m^2 (Figure 5c). An equally large negative NF anomaly is related to SMO delayed by 15–20 days.

[40] Results obtained with three fairly similar methods (M1, M2 and M3) show that the magnitude of the time average flux anomaly and its impact on SMO timing strongly depend on the definition of the pre-melt period. Whereas M1 suggests a high correlation between SMO and brief NF anomalies, M2 and M3 fail to detect the synoptic-scale effect of NF on SMO. Thus with M1 the effect of 1–7 days NF anomalies is detected over the area of 372×10^3 km^2, which represents 22% of the circumpolar central Arctic. Instead, M2 and M3 are better in detecting the areas where SMO correlates with the NF anomaly over the preceding 20–40 days: 340×10^3 km^2 for M2, 216×10^3 km^2 for M3, and only 109×10^3 km^2 for M1 (not shown).

[41] Considering the individual flux components, LWd alone explains up to 90% of the local interannual SMO variance, although only over a small area (Figures 5b and 5f). Among different time averaging periods, the 1–7 day LWd anomaly (M1) seems to best reflect the local interannual SMO variance compared to longer LWd history (Figure 5b). Thus for a time averaging period of 8 days or more, the highest r^2 drops lower than that for a 1 day time scale (Figure 5b). Similar results emerge when considering the entire shaded area in Figure 5f (as a group of locations and years, without regional averaging). Within this area the anomalous local (ERAI resolution) 6-day average LWd before the SMO accounts for 27% of spatial and interannual variance in SMO (Table 1). Within the same area, on average, the 1–7 day mean LWd anomaly of +25 (-14) W/m^2 is followed by 15–20 days earlier (later) SMO (Figure 5d). Below we summarize the size of area with significant correlations between LWd flux and SMO anomalies (not shown in figures). The effect of 1–7 day average LWd anomaly (just before SMO) on SMO appears within 589×10^3 km^2 with M1 (35% of the circumpolar Arctic), compared to the area of 277×10^3 and 192 km^2 $\times 10^3$ km^2 with M2 and M3 respectively. Similar to NF, calculations with M2 reveal vast

areas where LWd flux anomalies averaged over a longer (20–40 days) pre-melt period reflect the interannual behavior of the SMO. Thus the effect of LWd anomalies during a 20–40 day pre-melt period on SMO is present over an area of 733×10^3 (with M2) and 339×10^3 km^2 (with M1). That is about 43% and 20% of the circumpolar central Arctic respectively. As for NF, the magnitude of the time-average LWd anomalies (which correlate with the SMO timing) depends on the definition of the pre-melt period. Using M1, LWd anomalies of about 20–40 W/m^2 during a 20-40-day

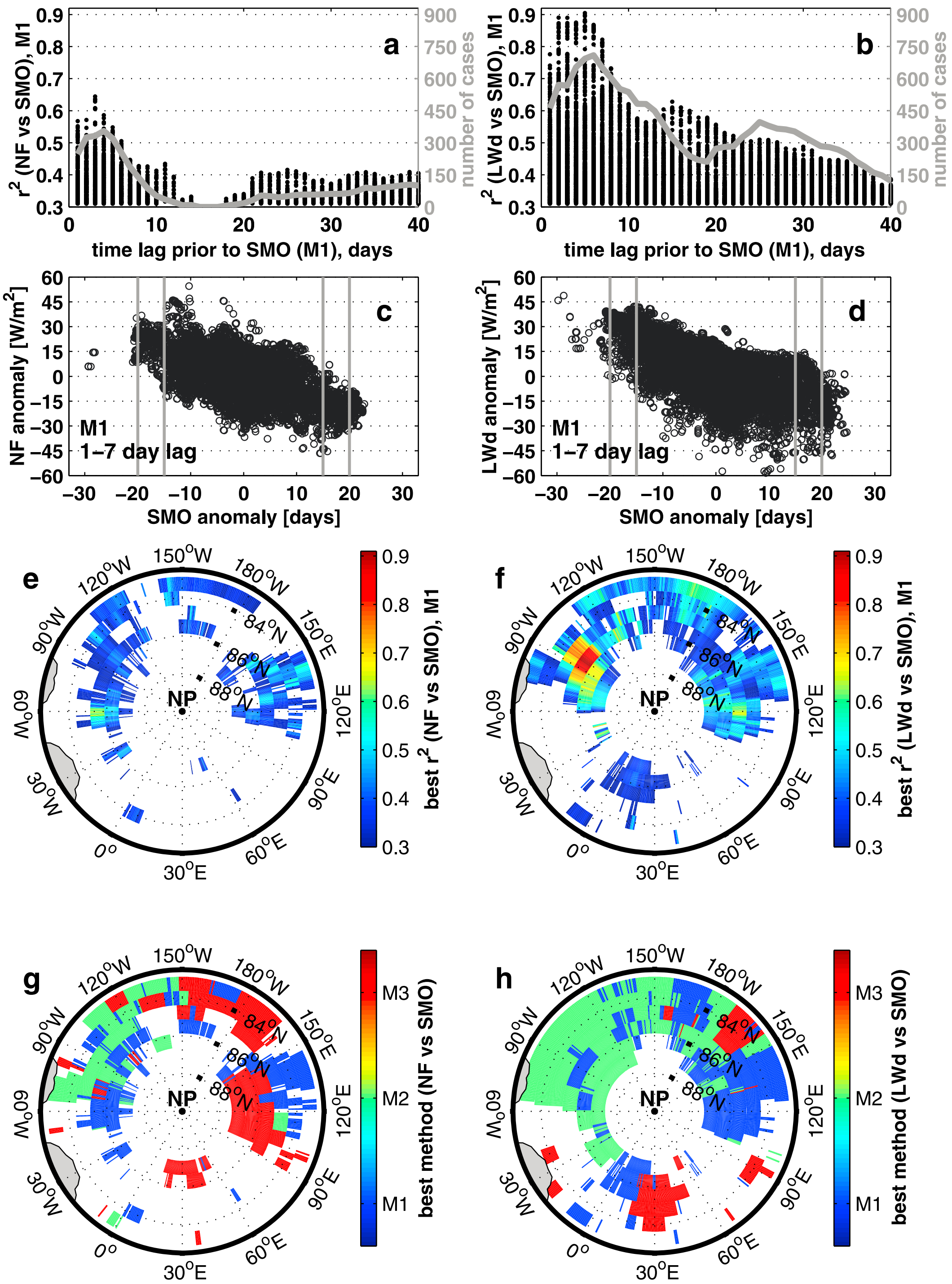

Figure 5

Table 1. Linear Relationships Between the Surface Heat Flux Anomaly (Prior to SMO) and SMO Anomaly Within the Circumpolar Arctic[a]

Linear Regression Equation	Flux Averaging Period Prior to SMO (days)	r-Square	RMSE (days)	Area Where the Equation is Valid
SMO = −0.38 × NF + 0.03	4	0.28	7.5	Shaded area in Figure 5e
SMO = −0.35 × LWd + 0.96	6	0.27	7.3	Shaded area in Figure 5f
SMO = −2.58 × LE − 1.38	40	0.31	7.3	Shaded area in Figure 6e
SMO = −4 × H − 0.68	37	0.25	7.5	Shaded area in Figure 6f
SMO = −0.31 × LWd − 0.08 × SWd − 0.67 × H − 0.03 × LE + 0.45	5	0.18	7.7	Entire circumpolar area within 83.25–87°N

[a]The results presented are significant with $p < 0.01$. Bilateral regression analysis was applied to the combination of all those grid locations where at least one flux-averaging period suggests a significant relationship ($p < 0.01$) between a given flux and SMO (M1). The stepwise multi-linear regression equation (combination of LWd, SWd, LE and H) is valid for the entire circumpolar area within 83.25–87°N (M1). Depending on the flux (column 1), a certain n-day averaging period (column 2) yields the strongest relationship (column 3) between the corresponding n-day average flux anomaly and SMO. The strongest linear relationship has the highest r^2 compared to other flux-averaging periods (1–40 days prior to SMO). For example, the first line means that the 4-day average NF anomaly before the SMO date (M1) explains 28% of the total SMO variance (from year-to-year and between neighboring grid locations) with RMSE of 7.6 days. The stepwise multiple linear regression equation for the entire circumpolar central Arctic (83.25–87°N) ranks the contribution of individual heat fluxes in the equation.

pre-melt period affect SMO timing by as much as 18 days (not shown).

[42] The best results obtained with the three methods (M1, M2 and M3) are compared in Figures 5g and 5h. Within the colored domain at least one method and at least one time-averaging period evoke a statistically significant r^2. All three methods detect the relationship between ERAI fluxes and SMO timing, complementing one another. None of the methods is much better than the other two.

[43] Very similar results are obtained for the LWnet flux (not shown): 1–7 day time scales are the most illustrative for the seasonal transition (r^2 up to 0.9), with a secondary peak at about 30-day lag (r^2 up to 0.6). We speculate that the effect of brief (1–7 day) flux anomalies on surface melt can only be distinguished if the heat fluxes and SMO are well captured in both data sets.

[44] Anomalies in LE and H are positive (negative) in the early (late) SMO years (Figures 6c and 6d). Seasonal 30–40 day flux anomalies in H and LE (M1) explain up to 72% and 56% of the local interannual SMO variance respectively (Figures 6a and 6b). Local LE and H flux anomalies within the shaded areas in Figures 6e and 6f respectively account for 31% and 25% of the spatial and interannual variance in SMO (Table 1). On average 1–2 W/m^2 weaker (stronger) loss of sensible heat and 2–3 W/m^2 weaker (stronger) loss of latent heat (sublimation) during May–June (30–40 day pre-melt period) contribute to the advance (delay) in SMO by 15–20 days (Figures 6c and 6d). A statistically significant effect of 30–40 day mean flux anomalies (M1) to SMO variance is found over the areas of 254×10^3 km^2 for LE and 300×10^3 km^2 for H (15% and 18% of the circumpolar Arctic). To note, these areas are only a part of the shaded domain in Figures 6e and 6f (where all time averaging periods are considered together). The performance of three methods (M1, M2 and M3) in terms of r^2 is compared in Figures 6g and 6h. Accordingly, LE and H flux anomalies computed with either M1 or M2 capture the interannual local variability in SMO better (with larger r^2) than M3.

[45] Our results show that SWd and SWnet (on their own) do not play any role in the interannual and/or spatial variability in SMO within the central Arctic (83–87°N). This is reasonable, as until mid-May the sea ice albedo in ERAI is rather high (0.77), and since there is no snow melt (and no ice melt) in ERAI, the representation of SWnet variations in time is unrealistic.

[46] The effect of DF and DR anomalies on SMO is weak: although the anomalies locally explain up to 50% of the interannual variance in SMO, a significant r^2 is found only for less than 2% of the circumpolar Arctic.

4.4. Effect of the Combination of Surface Fluxes on Interannual Variations in SMO

[47] Stepwise forward multiple linear regression analysis was applied to find those combinations of surface fluxes that best explain the SMO variance. Four predictors were taken into account: LWd, SWd, LE and H. These individual fluxes and various combinations of them are considered here as the direct factors controlling SMO.

[48] A combination of 2–4 fluxes explains locally from 30 to 92% of local interannual SMO variance within roughly

Figure 5. Bilateral regression results on the relationship between the flux anomaly and the corresponding SMO anomaly (same location, same year). The study domain is within 83.25–87°N. The flux anomaly is averaged over various pre-melt periods (1–40 days, method M1). Left-hand plots illustrate the results for NF and right-hand plots for LWd. (a, b) Dependence of the squared correlation (r^2) on the length of the pre-melt period. The black dots show all significant r^2 values ($p < 0.01$) for each flux-averaging period. The gray curve shows the number of ERAI grid locations where a significant r^2 was found with the given flux-averaging period. It indicates which time averaging period is the most successful in explaining interannual SMO variance. (c, d) Scatter of 1–7-day flux anomalies against corresponding SMO anomaly. All locations evoking a significant r^2 at any flux-averaging period between 1 and 7 days are regrouped. Each location is represented with 20 black open circles (20 years). Four vertical gray lines delimit ±15–20 day SMO anomalies. The average of 1–7 day flux anomalies corresponding to these ±15–20 day SMO anomalies is cited in the text. (e, f) The highest r^2 found with some of the flux-averaging periods (1–40 days), method M1. All grid locations where at least one significant r^2 was detected with M1 are shown. (g, h) Comparison of the highest r^2 ($p < 0.01$) obtained with the three methods (M1, M2 and M3) and all flux-averaging periods (1–40 days).

a half (46%) of the circumpolar central Arctic area (Figure 7a), with a root mean square error (RMSE) about 6–7 days (not shown). In the western central Arctic, within the area where 3–7 day average flux anomalies (Figure 7b) explain 80–90% of SMO variance (Figure 7a) at least 3 fluxes (Figures 7c–7f) appear in the multilinear regression equation, with LWd the dominating term (Figure 7c). Within another sector in the western Arctic, a 40-day time average (Figure 7b) LE and H are either the only or most important terms included in the best multilinear regression equation

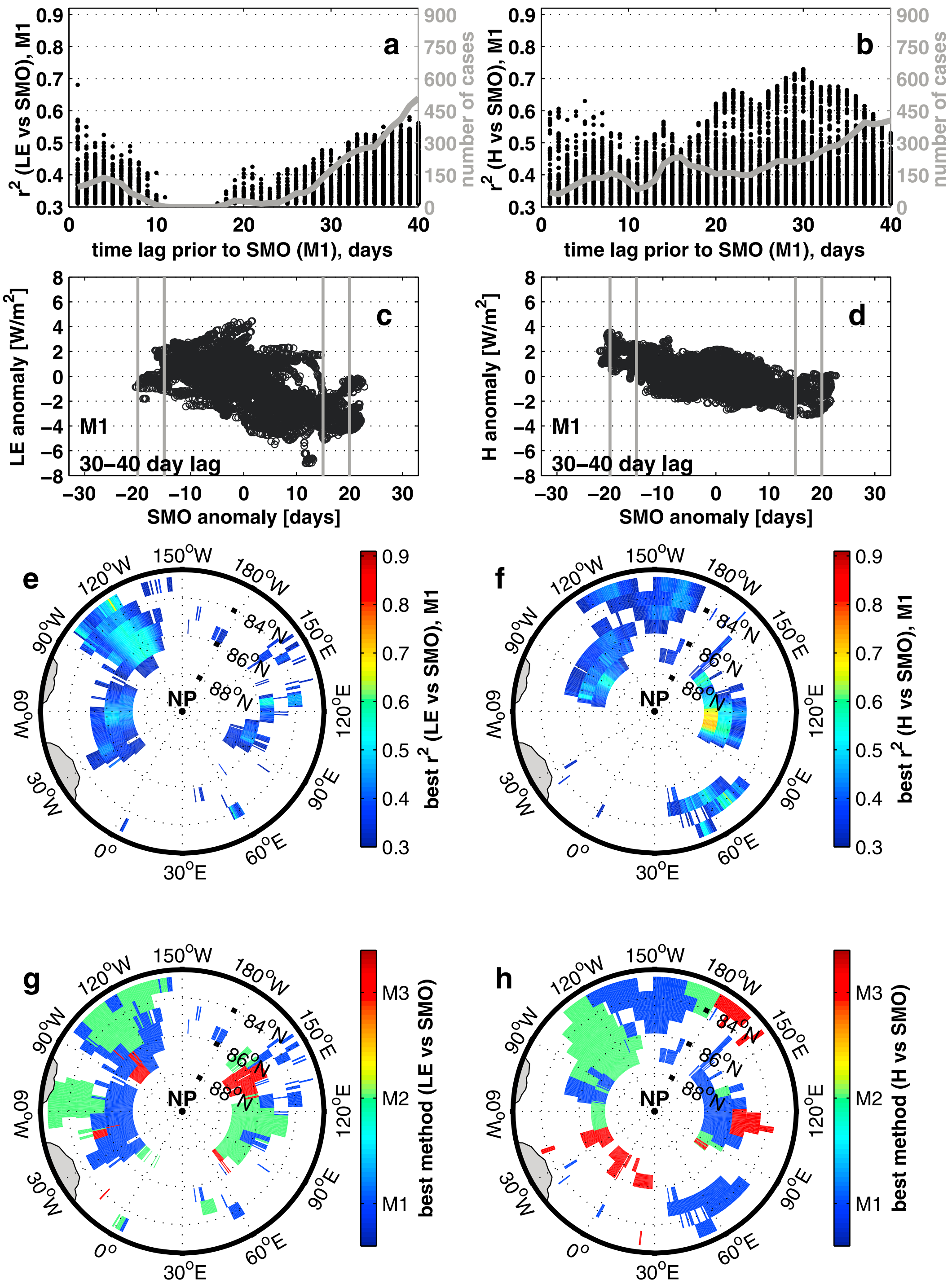

Figure 6

(Figures 7e and 7f). Interestingly, although SWd by itself does not correlate with SMO, the inclusion of SWd into the multilinear regression equation improves the explained variance of SMO over most of the central Arctic (Figure 7d).

[49] Figure 8 compares the best results obtained with the bilateral and multiple regression analysis. Over most of the central circumpolar Arctic (68% of the study domain, shaded area) a combination of fluxes explains SMO better than any of the individual fluxes (Figure 8c) or their sum. LWd largely dominates over the other fluxes within the Pacific and Atlantic sectors of the central Arctic (Figure 8c). The best time averaging period within the Atlantic sector is 25 days on average (Figure 8b). On the Pacific side the best time averaging period has two peaks at 4–7 and 20–27 days.

[50] Stepwise multilinear regression analysis was also applied to the composite of all maritime grid locations (2862 in total) within the circumpolar central Arctic. Calculated in this manner, the combination of 5-day average LWd, SWd, LE and H anomalies explains 18% of the total SMO variance, with a standard error of the linear regression model of about one week (Table 1). To note, the total variance includes both interannual and spatial variance. Figure 9 demonstrates how well the best multilinear regression equation (in Table 1) reconstructs the local SMO features in three years: 1990, 2003 and 2007. Year 2003 is illustrated as a typical year with the SMO close to the 20-year average (Figures 9c and 9d). Year 2007 is taken for comparison as the most famous for its unique sea ice conditions (Figures 9e and 9f). SMO in 1990 is shown in contrast to SMO pattern observed in 2007: with essentially opposite SMO anomalies (Figures 9a and 9b). Accordingly, the best combination of four fluxes well captures the spatial features of SMO (Figure 9), but cannot explain SMO anomalies larger than 15 days.

4.5. Trends

[51] We first focused on the local MO trend at those SSM/I MO pixels with a complete 20-year time series. Statistically significant ($p < 0.01$) trend is found within 83.400 km^2 (shaded locations in Figure 10a), that is only 5% of the circumpolar central Arctic area (83.25–87°N). Depending on the location, the MO tendency is toward earlier MO, ranging locally between −8 and −18 days per decade (Figure 10a). The average of these significant local (in 25 km resolution) MO trends is −13 days per decade.

[52] There are three major differences in our experimental setup compared to *Markus et al.* [2009]. (1) Central Arctic domain is defined differently. (2) Our study period is only 20 years long (1989–2008) against a 29-year period in the study by *Markus et al.* [2009]. (3) Our trend estimate is for each individual 25 km MO pixel, whereas *Markus et al.* [2009] calculated the trend for the "annual areal average MO" within the central Arctic region. According to *Markus et al.* [2009] in the central Arctic the MO trend was about −2.5 days per decade (1979–2007) and our calculations for the same 29-year period confirm this result ($p < 0.01$).

[53] Area average 20-year trend in SMO sample within the circumpolar central Arctic is −8.8 days per decade (Figure 10b). These results nicely illustrate how different approaches produce very different trends in MO/SMO: by −2.5, −8.8 and −13 days per decade.

[54] Both the interannual variability and trends in SMO should, in principle, be explainable by interannual variability and trends in NF. In contrast, the interannual variability and trends in the apparent MO can be also related to the sea ice dynamics. To discuss a possible relationship between the trends in surface fluxes and trends in SMO, again we first need to define the reference period of the year when changes in fluxes might trigger a larger/smaller heat accumulation within a dry snowpack. In our example here we averaged the surface fluxes during a 30-day pre-melt period (21 April–20 May) every year and calculated the linear trend at each ERAI grid location (Figures 10c and 10f). Where the 21 May is the earliest local SMO found within the circumpolar central Arctic (83–87°N) in the period 1989–2008.

[55] In the period of 21 April–20 May ERAI SWd, SWnet, LWnet, H, DR and DF follow significant 20-year trends within a portion of the study area (83–87°N), but not everywhere in the circumpolar central Arctic (Figure 10). The largest trends are found for SWd, DF and DR: reaching +15–20 W/m^2 per decade north of Greenland and in the Lincoln Sea. Since DR and DF trends are very similar in magnitude and have the same spatial features, only DF is illustrated here (Figure 10e). H and LWnet trends are negative (Figure 10f), which seems to be a consequence of a larger SWd and SWnet in ERAI: where H, LWup and LWnet strengthen (heat loss) with an increased surface heating by means of SWd. NF, LWd and LE trends in the period 21 April–20 May are insignificant. DR and DF trends are large and appear within the most of the study area.

[56] In reality the trends in SMO and surface fluxes (NF) could partly be due to changes in sea ice and snow cover and partly due to evolution of meteorological conditions. Recent studies manifested a significant thinning of sea ice in the Arctic Ocean [*Kwok and Rothrock*, 2009]. We speculate that younger (saltier, thinner and warmer) ice should have impacted the true NF at the snow surface, and likely contributed to the observed advance of snow melt in the spring (SSM/I). An interesting aspect to be highlighted: in the areas

Figure 6. Bilateral regression results revealing the relationship between the flux anomaly and the corresponding SMO anomaly (same location, same year). The study domain is within 83.25–87°N. The averaging period for the flux anomaly ranges from 1 to 40 days prior to SMO (method M1). Left-hand plots illustrate the results for LE and right-hand plots for H. (a, b) Dependence of the squared correlation (r^2) on the flux-averaging period. The black dots show all significant r^2 values for each flux-averaging period. The gray curve shows the number of ERAI grid locations where a significant r^2 was found with the given flux-averaging period. (c, d) Scatter of 30–40 day flux anomalies against corresponding SMO anomaly. Each location is represented with 20 black open circles (20 years). All locations evoking a significant r^2 at any flux-averaging period between 30 and 40 days are regrouped. Four vertical gray lines delimit ±15–20 day SMO anomalies. The average of 30–40 day flux anomalies corresponding to these ±15–20 day SMO anomalies is cited in the text. (e, f) The highest r^2 found with some of the flux-averaging periods (1–40 days), method M1. All grid locations where at least one significant r^2 was detected with M1 are shown. (g, h) Comparison of the highest r^2 ($p < 0.01$) obtained with the three methods (M1, M2 and M3) and all flux-averaging periods (1–40 days).

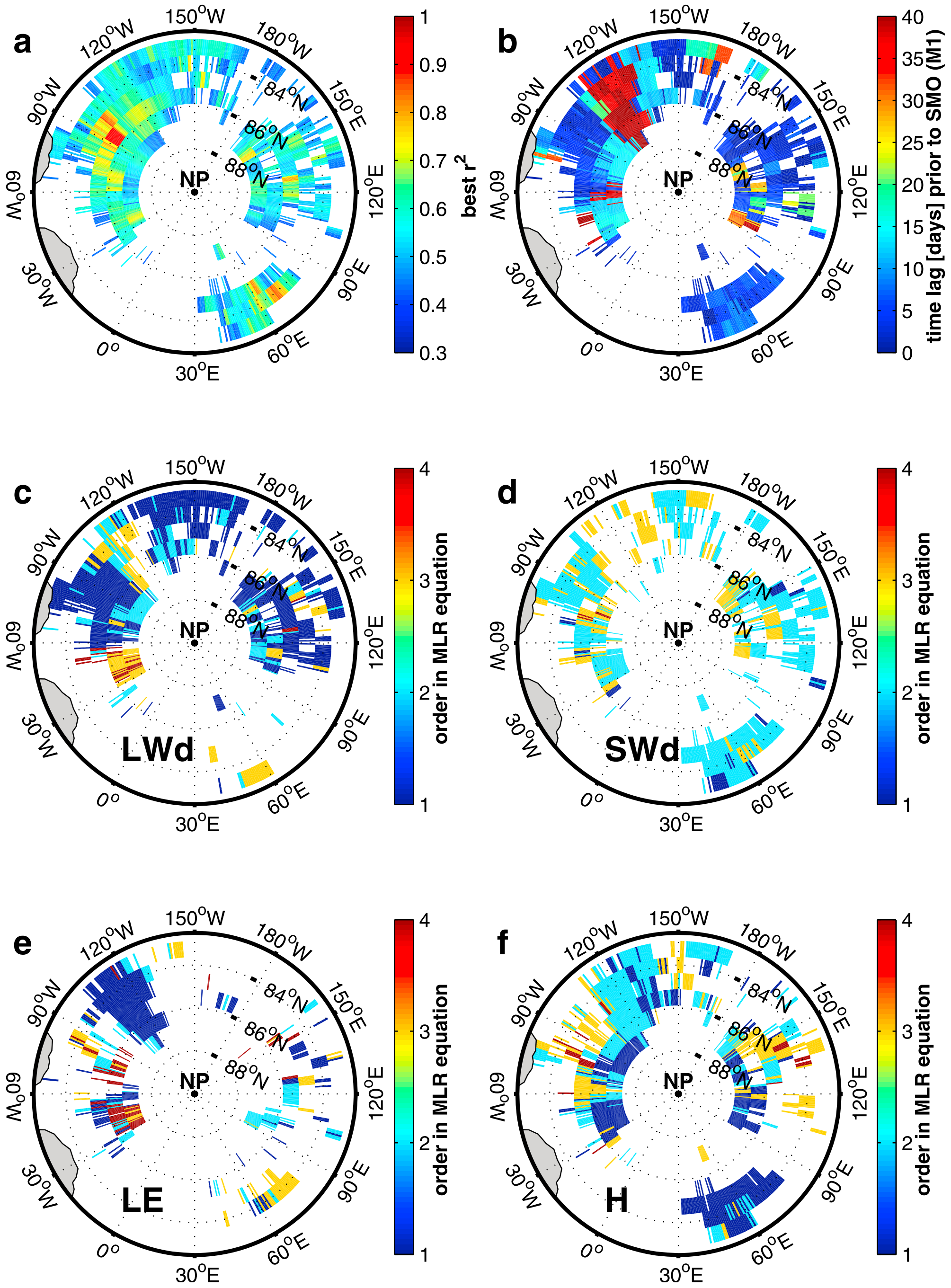

Figure 7. Best results for the stepwise multilinear regression (MLR) analysis at each individual grid location ($p < 0.01$), method M1. (a) Fraction of the local interannual SMO variance (r^2) explained by the best combination of four fluxes: LWd, SWd, LE and H. At each particular location r^2 value is the highest among all combinations of these four fluxes and 40 different flux averaging periods. (b) Flux averaging period suggesting the highest r^2 that results from the best combination of four individual fluxes. (c–f) Rank of the flux components in the best multilinear regression equation (at each individual grid location). For example, in Figure 7c at those locations where the color code refers to 1, LWd is the most significant flux component (with the smallest p-value) and the first included in the forward multilinear regression analysis.

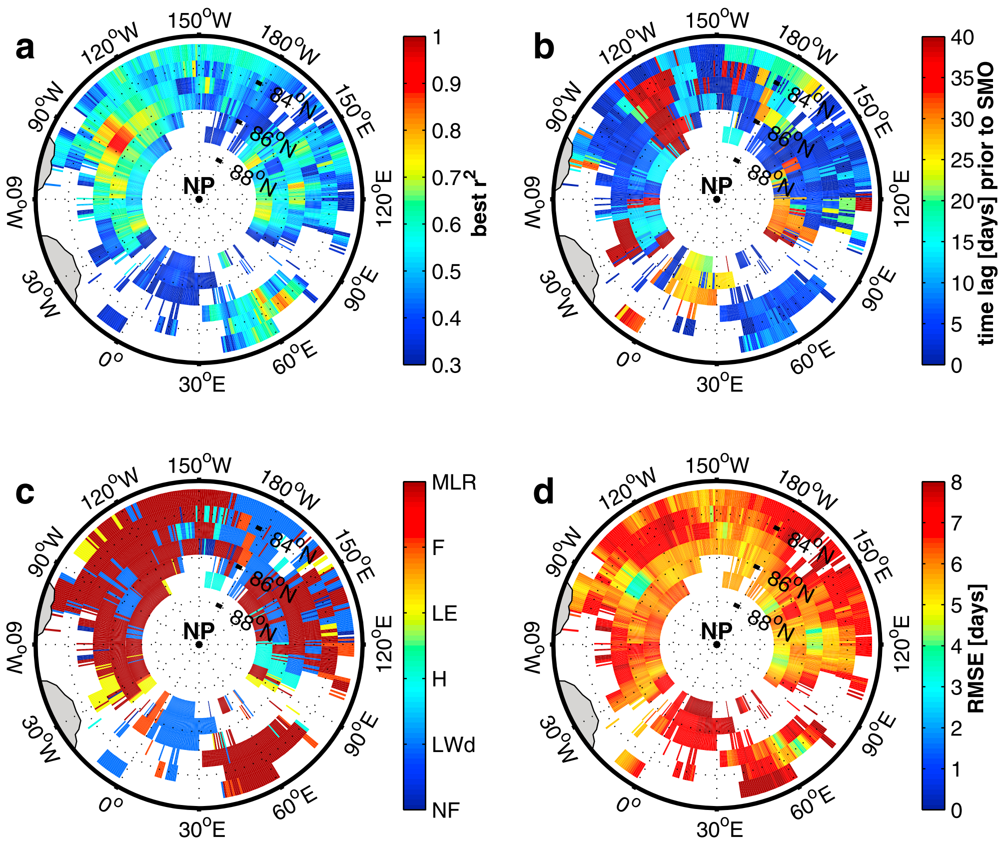

Figure 8. Comparison of the bilateral versus multilinear regression results, method M1. (a) Fraction of the local interannual SMO variance explained by the surface fluxes (r^2): NF, LWd, LWnet, SWd, SWnet, LE, H, DF, DR or any combination of 4 major fluxes (multilinear regression with LWd, SWd, LE and H flux components). At each particular location, this r^2 value is the highest among the individual heat fluxes, all combinations of four major fluxes and all flux averaging periods. (b) Flux averaging period suggesting the best r^2 that results from any individual flux or combination of individual fluxes at each grid location. (c) The factor best explaining SMO variance (individual fluxes or some combination of them, ranked by r^2) at each grid location. Multilinear regression (MLR) refers to some combination of LWd, SWd, LE and H flux anomalies, suggesting the best r^2. Notation "F" corresponds to any of the following fluxes: NF, LWnet, SWd, SWnet, DF or DR. (d) RMSE corresponding to the best explaining factor shown in Figure 8c.

where the ice and/or snow have become thinner, a trend toward an earlier SMO might occur even with a negative trend in NF, LWd and SWd.

[57] The illustrated trends in surface heat fluxes are only based on ERAI, and not validated against observations. So far, the field spring-time flux measurements only exist for limited periods in a few ice stations. A strong debate has taken place on the reliability of trends in reanalyses (*e.g.* ERA-40) in areas where almost no observational data were assimilated, such as the central Arctic northward of 82°N [e.g., *Graversen et al.*, 2008; *Bitz and Fu*, 2008; *Grant et al.*, 2008; *Thorne*, 2008; *Screen and Simmonds*, 2011]. Although the reported magnitudes of trends differ among various data sets, all these cited studies agree that there have been warming trends in the central Arctic, in particular in spring and fall, with the earlier spring snow melt and later fall freeze-up. According to *Uppala et al.* [2008], *Dee and Uppala* [2009], and *Dee et al.* [2011], ERAI reproduces meteorological processes in the Arctic better than earlier reanalyses, which possibly has also improved the accuracy of radiative and turbulent fluxes on sea ice, but this is still an open question.

5. Discussion

[58] To successfully quantify the effect of surface fluxes on SMO, it was essential to take into account the following. First, instead of analyzing fluxes themselves, we paid attention to the flux anomalies relative to the 20-year climatology. Contrary to the flux anomalies, radiative fluxes themselves have a non-causal positive correlation with SMO: when SMO occurs late, corresponding seasonal values of LWd and SWd are larger. Second, we found that there is no single time scale for the pre-melt period when the contribution of surface fluxes to SMO is the most important. For NF, LWnet and

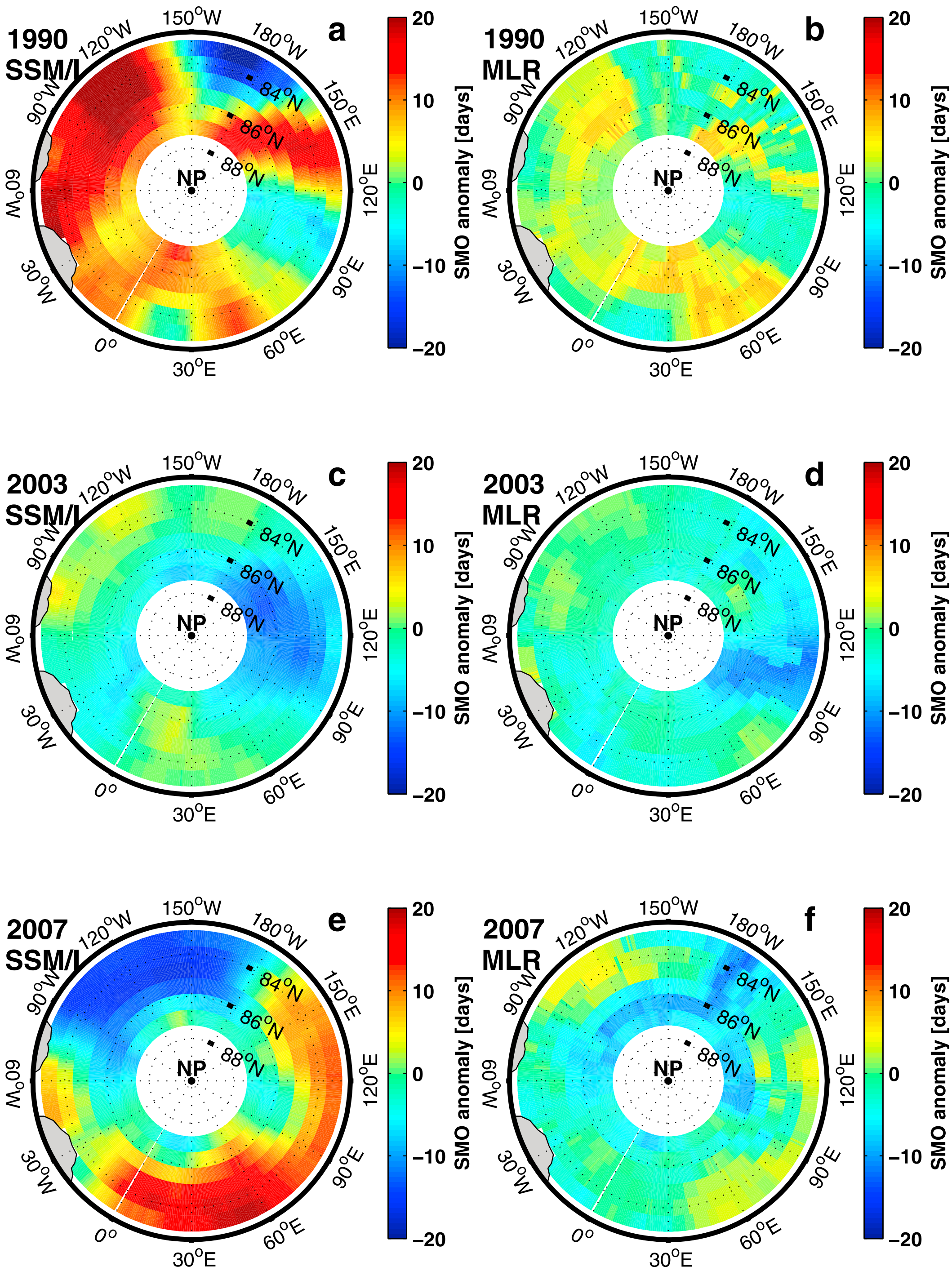

Figure 9. Comparison of the original SSM/I-based SMO time series (left-hand maps) versus the reconstructed SMO time series (right-hand maps) in (a, b) 1990, (c, d) 2003 and (e, f) 2007. SSM/I-based SMO anomalies (left-hand maps) are calculated relative to the 20-year local mean SMO date. The multilinear regression (MLR) equation from Table 1 and the local heat flux anomalies (5-day average, method M1) are applied to reconstruct SMO anomalies at each ERAI grid location.

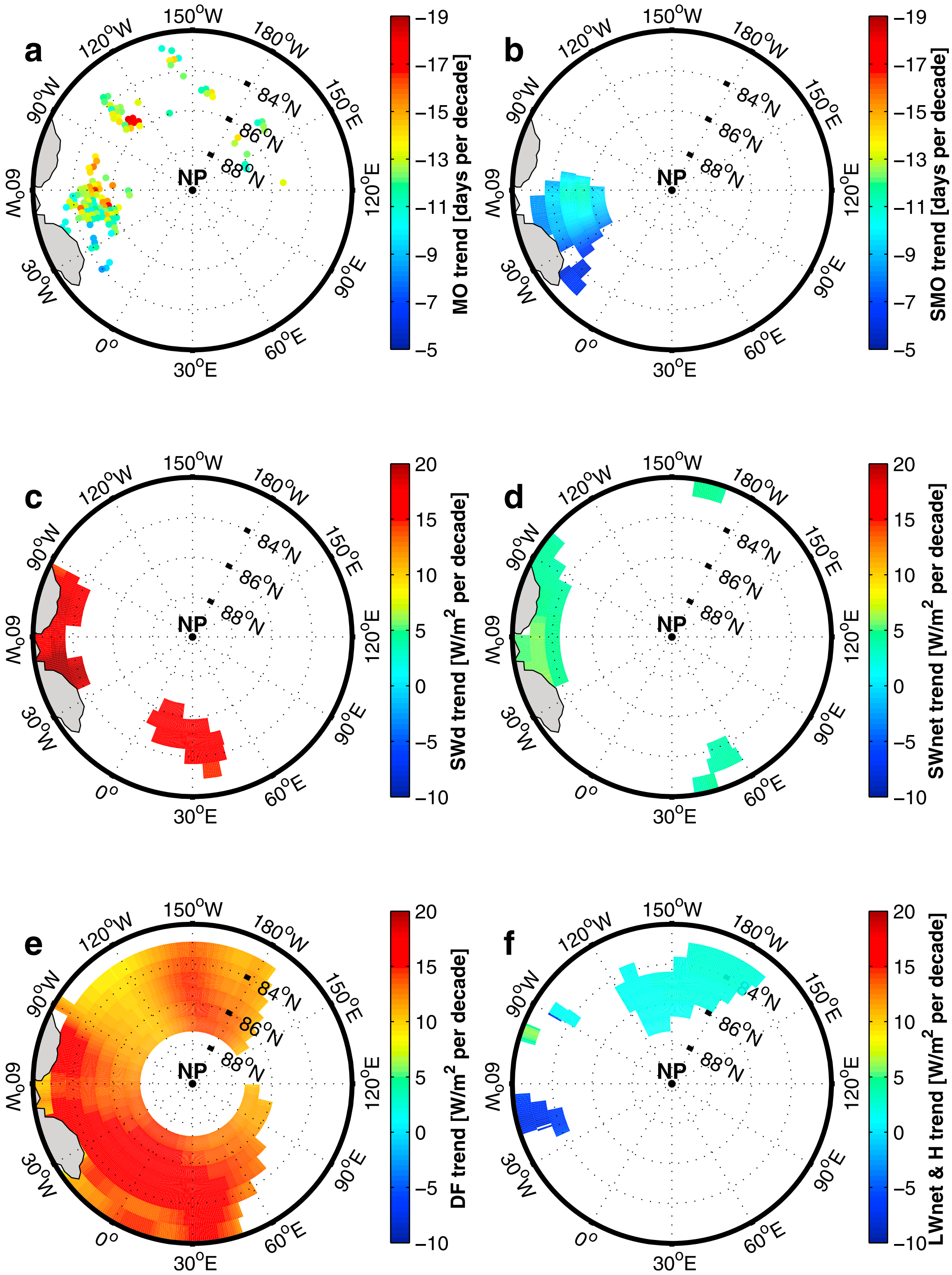

Figure 10. 20-year (1989–2008) local trends in (a) original MO data in 25 km resolution, (b) SMO in ERAI grid resolution, (c) SWd, (d) SWnet, (e) DF and (f) LWnet together with H. In Figure 10f dark blue represents LWnet trend, and light blue - green colors reflect H trend. Trends for ERAI surface fluxes are calculated based on the monthly mean heat fluxes in the same pre-melt period each year (20 April–21 May) and around the region. Trends were calculated only for the complete 20-year records, significant at $p < 0.01$.

LWd the most relevant time scale was 1–7 days, whereas for H and LE it was around 30–40 days. Yet, we note that significant r^2 were also found with other time averaging periods (Figure 5a, 5b, 6a, and 6b). The differences are probably related to the daily magnitudes of flux anomalies: NF and LWd reach larger magnitudes than LE and H and, accordingly, a long-term anomaly in LE and H is needed to cause a statistically significant effect on SMO.

[59] Over most of the central Arctic a combination of 2–4 fluxes explained SMO better than the individual fluxes alone or their sum (DR, DF and NF) (Figure 8c). This must be due to a different accuracy of the individual fluxes. However, if all fluxes were equally accurate in ERAI, NF should correlate with SMO better than any of its components or any combination of some of its components.

[60] The combination of LWd, SWd, LE and H anomalies (multilinear regression) well captures the spatial and interannual differences in SMO (Figures 7 and 9). Large SMO anomalies (of 15–35 days) and huge spatial differences in SMO (by 1–3 months within 50 km distances) are, however, poorly explained by surface fluxes. This is related to errors in fluxes (ERAI) and possibly also to the distinction of two sea ice types in the MO algorithm (SSM/I). The algorithm for MO detection applied by *Markus et al.* [2009] is different for the multiyear and first-year ice. We suspect that differences between ice types, most likely contribute to the interannual variations in SMO. Further studies are needed to find out how well surface fluxes explain SMO variance on top of different ice types.

[61] A detailed statistical investigation of the effect of snow and ice thickness and the conductive heat flux on SMO variance and trends would require data with spatial and temporal resolution comparable to ERAI, but no such data are currently available. We may, however, assume that the variability in the conductive heat flux was one of the main factors that reduced the capability of radiative and turbulent fluxes to explain SMO variance.

[62] The original MO record of *Markus et al.* [2009] is not fully independent of ERAI, because SSM/I data of sea ice concentration were applied in both. However, if focusing on the circumpolar central Arctic with a prescribed SIC of 100% in ERAI, and also extracting the SMO signal from the MO record, we can consider these data sets fully independent. In the future, the SMO data could be utilized to improve reanalyses by means of surface (skin) temperature assimilation. Regarding the hole at the North Pole and the spatial resolution, the active microwave time series of the backscatter [*Kwok et al.*, 2003] could be used to fill in the gap and to improve the spatial coverage of the existing MO records.

[63] Errors detected in ERAI near-surface air temperature and moisture during Arctic summer [*Lüpkes et al.*, 2010] and simplified SIC representation north of 83°N indicate that neither surface fluxes are free of errors. However, a good aspect in reanalysis is that the same model and data assimilation system were applied throughout the period, resulting in a spatially and temporally consistent data set. Errors in surface fluxes may, however, depend on weather and sea ice conditions, which could generate interannual variations in the errors, but such a possible dependence has not been investigated over Arctic sea ice yet. Furthermore it is unlikely that errors in the surface fluxes could generate artificially improved correlations between the fluxes and SMO. Instead errors in surface heat fluxes, in MO detection, and SMO sampling (used as the reference date for the pre-melt period definition) should have increased the scatter in the observed relationship between SMO and the fluxes, thus reducing correlations.

[64] We also highlight that the *continuous* MO detected with the remote sensing by *Markus et al.* [2009] is an instance (Julian day) when either (a) liquid water remains on top of the sea ice (snow melt), or (b) the final sea ice divergence occurs. Although SMO and the ice divergence are closely related, they have a different origin. SMO on top of large and compact ice slab is due to a sufficient accumulation of the net heat flux (NF) within the snowpack, whereas opening of leads and polynyas (before melt ponds appear on top of sea ice) is due to divergent ice drift, typically caused by winds, tides, ocean currents of other origin, or bottom melt of ice. Studies on the latter processes are beyond the scope of this paper, but these aspects are essential for the treatment and interpretation of the original MO data. It seems that in the earlier analyses of satellite-based MO records, SMO and opening of leads and polynyas have not been distinguished.

[65] We presented quantitative SMO versus heat flux relationships only for the central Arctic (83–87°N), where it was possible to reliably detect the causal effect of surface fluxes on SMO. However, strong statistical relationships between SMO and surface fluxes were also found in the seasonal ice zone: Kara, Laptev, East-Siberian, Chukchi and eastern Beaufort Seas and the Baffin Bay. In these areas the most important fluxes were NF and SWnet. In contrast to the central Arctic (83–87°N) where ERAI surface fluxes were the least affected by SIC changes, in areas south of 83°N ERAI SIC dropped below 80% at least once during the pre-melt period (Figure 3f). As a result, when the ice concentration is reduced, the stronger SW absorption by the open water contributed to the additional NF accumulation. In other words, southward from 83°N, the positive NF and SWnet flux anomalies during the pre-melt period were due to the opening of leads or polynyas at least once within the 20-year record. Hence, some positive NF and SWnet flux anomalies were not a reason for the early SMO, and the statistically significant relationships were only partly due to the causal effect of fluxes on SMO. The effect of SIC on LWd was not as straightforward as in the case of NF and SWnet. Interannual LWd anomalies explained up to 70% of the local interannual SMO variance southward from 83°N, significant within vast areas of the northern Kara Sea, Laptev Sea, northward of the East-Siberian-Beaufort Seas (75–83N) and in the western Baffin Bay.

6. Conclusions

[66] Applying ERAI reanalysis of radiative and turbulent surface heat fluxes and satellite passive microwave (SSM/I) data of sea ice concentration and SMO in the period of 1989–2008, we evaluated the portion of the interannual variance in SMO explained by the surface fluxes over the central Arctic Ocean at 83–87°N. High and causally relevant correlations are found between the surface flux anomalies and SMO timing: a larger net heat flux and downward longwave radiation and weaker heat loss from the surface via the turbulent fluxes (LE and H) occur in springs/locations with an earlier SMO.

[67] The anomaly of the net heat flux 1–7 days prior the SMO explains up to 65% of the interannual variance in SMO. The main term of the net flux is the downward longwave radiation, which alone accounts for up to 90% of SMO variance over a limited area in western central Arctic. Solar radiation is not an important factor alone, but in combination with other fluxes improves the explained variance of SMO. Seasonal 30 to 40-day anomalies in the turbulent fluxes of sensible and latent heat explain locally up to 72% and 56% of the interannual SMO variance respectively. Regarding method M1, the individual heat fluxes and various combinations of them account for about 30–90% of the interannual SMO variance within as much as 68% of the study domain (Figure 8). When comparing all three methods (M1, M2 and M3) a significant explained variance in SMO timing is detected within 83.5% of the study domain (not shown).

[68] The downward longwave radiation is the most important flux term, best explaining the timing of SMO. This points out on the importance of clouds and air moisture. The difference in downward longwave radiation between overcast and clear skies is typically 70–100 W/m^2 [*Beesley*, 2000; *Intrieri et al.*, 2002; *Wang and Key*, 2005]. It is, however, not only the cloud fraction and thickness that control longwave radiation, but also the phase of clouds; water clouds have a significantly higher longwave emissivity than ice clouds [*Wang and Key*, 2005; *Pinto et al.*, 1997]. The association of an early SMO with a small heat loss from the surface by the turbulent fluxes of sensible and latent heat suggests that an early SMO is related to the presence of warm and moist air over the sea ice. Warm air advection is an important mechanism for synoptic-scale near-surface warming events over Arctic sea ice, and it is often associated with low-level liquid-phase clouds [*Persson et al.*, 2002; *Vihma and Pirazzini*, 2005]. These are the conditions that favor both large downward longwave radiation and reduced turbulent heat loss from the surface, accordingly also favoring an early SMO.

[69] Local SMO gradients of up to one month per 50 km distance are occasionally related to large surface flux gradients (up to 25 W/m^2 in NF within 50 km distance) associated with the atmospheric fronts, and further should be examined together with the sea ice types. In agreement with the earlier SSM/I-based studies, the 20-year MO and SMO trends in the central circumpolar Arctic Ocean are toward earlier spring melt. Local MO and SMO trends of 13 and 9 days per decade, respectively, are found within a limited area where complete 20-year time series were available. SMO trends cannot be reasonably explained by ERAI surface fluxes. Moreover, we stress that the trend estimates strongly depend on the method applied and should be considered with caution.

[70] To reach these results, it was essential to extract the SMO signal out of the original MO record by *Markus et al.* [2009], which also includes cases of opening of leads and polynyas. The analysis based on three alternative methods (M1, M2, or M3) yields essentially similar results. While differences exist in detailed numerical values (r^2, rmse, length of the best time averaging period), the main conclusions of the work do not depend on the method.

[71] We stress that more studies are needed to better understand and quantify the factors controlling SMO. A high priority should be given to the studies investigating the relationships between the sea ice, surface heat fluxes, local meteorological conditions (clouds, wind, air temperature and humidity), cyclones, and large-scale circulation. In particular, the important role of downward longwave radiation on SMO calls for more studies on the cloud radiative forcing, sources of Arctic clouds (advection from lower latitudes versus evaporation from ice-free areas in the Arctic), and the evolution of cloud properties with changing sea ice cover. The results obtained may increase the potential for seasonal prediction of Arctic sea ice conditions. As the SMO initiates the albedo feedback process, the conditions favorable for early SMO are also favorable for larger ice melt and heat storage in the upper ocean [*Perovich et al.*, 2007a, 2007b; *Notz*, 2009], and hence, for reduced sea ice cover and later freeze-up in the following fall.

[72] **Acknowledgments.** We are grateful to J. Stroeve, T. Markus and W. Meier for providing MO time series and the interaction during the study. We would like to thank our two reviewers, and also M. Tjernström, J. C. Gascard and T. Pleavin for very constructive and valuable suggestions, corrections and comments. This work was supported by the European projects DAMOCLES (Developing Arctic Modeling and Observing Capabilities for Long-term Environmental Studies, contract number 018509) and SEARCH for DAMOCLES (contract number 037111), both financed by the European Commission in the 6th Framework program. Those two projects were also IPY projects.

References

Anderson, M. R. (1987), Snow melt on sea ice surfaces as determined from passive microwave satellite data, in *Large Scale Effects of Seasonal Snow Cover (Proceedings of the Vancouver Symposium, August 1987)*, *IAHS Publ. 166*, 329–342.

Anderson, M. R., and S. D. Drobot (2001), Spatial and temporal variability in snowmelt onset over Arctic sea ice, *Ann. Glaciol.*, *33*, 74–78, doi:10.3189/172756401781818284.

Barber, E., T. N. Papakyriakou, and E. F. LeDrew (1994), On the relationship between energy fluxes, dielectric properties, and microwave scattering over snow covered first-year sea ice during the spring transition period, *J. Geophys. Res.*, *99*(C11), 22,401–22,411, doi:10.1029/94JC02201.

Beesley, J. A. (2000), Estimating the effect of clouds on the arctic surface energy budget, *J. Geophys. Res.*, *105*(D8), 10,103–10,117, doi:10.1029/2000JD900043.

Belchansky, G. I., D. C. Douglas, and N. G. Platonov (2004), Duration of the Arctic Sea ice melt season: Regional and interannual variability, 1979–2001, *J. Clim.*, *17*, 67–80, doi:10.1175/1520-0442(2004)017<0067:DOTASI>2.0.CO;2.

Bitz, C. M., and Q. Fu (2008), Arctic warming aloft is data set dependent, *Nature*, *455*, E3–E4, doi:10.1038/nature07258.

Bitz, C. M., D. S. Battisti, R. E. Moritz, and J. A. Beesley (1996), Low frequency variability in the Arctic atmosphere, sea ice and upper ocean climate system, *J. Clim.*, *9*(2), 394–408, doi:10.1175/1520-0442(1996)009<0394:LFVITA>2.0.CO;2.

Cavalieri, D., C. Parkinson, P. Gloersen, and H. J. Zwally (1996), Sea ice concentration from Nimbus-7 SMMR and DMSP SSM/I passive microwave data, digital media, Natl. Snow and Ice Data Cent., Boulder, Colo. [Updated 2008.]

Cheng, B., T. Vihma, R. Pirazzini, and M. Granskog (2006), Modeling of superimposed ice formation during spring snow-melt period in the Baltic Sea, *Ann. Glaciol.*, *44*, 139–146, doi:10.3189/172756406781811277.

Cheng, B., Z. Zhang, T. Vihma, M. Johansson, L. Bian, Z. Li, and H. Wu (2008), Model experiments on snow and ice thermodynamics in the Arctic Ocean with CHINARE 2003 data, *J. Geophys. Res.*, *113*, C09020, doi:10.1029/2007JC004654.

Dee, D. P., and S. Uppala (2009), Variational bias correction of satellite radiance data in the ERA-Interim reanalysis, *Q. J. R. Meteorol. Soc.*, *135*(644), 1830–1841, doi:10.1002/qj.493.

Dee, D. P., et al. (2011), The ERA-Interim reanalysis: Configuration and performance of the data assimilation system, *Q. J. R. Meteorol. Soc.*, *137*, 553–597, doi:10.1002/qj.828.

Draper, N. R., and H. Smith (1998), *Applied Regression Analysis*, pp. 307–312, Wiley-Interscience, Hoboken, N. J.

Drobot, S. D. (2007), Using remote sensing data to develop seasonal outlooks for Arctic regional sea-ice minimum extent, *Remote Sens. Environ.*, *111*, 136–147, doi:10.1016/j.rse.2007.03.024.

Drobot, S. D., and M. R. Anderson (2001), Comparison of interannual snowmelt-onset dates with atmospheric conditions, *Ann. Glaciol.*, *33*, 79–84, doi:10.3189/172756401781818851.

Ebert, E. E., and J. A. Curry (1993), An intermediate one-dimensional thermodynamic sea-ice model for investigating ice-atmosphere interactions, *J. Geophys. Res.*, *98*(C6), 10,085–10,109, doi:10.1029/93JC00656.

European Centre for Medium-Range Weather Forecasts (ECMWF) (2008a) Integrated Forecast System (IFS) documentation–Cy33r1. Part II: Data assimilation, Reading, U. K.

European Centre for Medium-Range Weather Forecasts (ECMWF) (2008b), Integrated Forecast System (IFS) documentation–Cy33r1. Part IV: Physical processes, operational implementation, Reading, U. K.

Ehn, J. K., M. A. Granskog, T. Papakyriakou, R. Galley, and D. G. Barber (2006), Surface albedo observations of Hudson Bay (Canada) land-fast sea ice during melt onset, *Ann. Glaciol.*, *44*, 23–29, doi:10.3189/172756406781811376.

Eicken, H., and P. Lemke (2001), The response of polar sea ice to climate variability and change, in *Climate of the 21st Century: Changes and Risks*, edited by J. L. Lozan et al., pp. 206–211, Wiss. Auswertungen/GEO, Hamburg, Germany.

Fiorino, M. (2004), A multi-decadal daily sea surface temperature and sea ice concentration data set for the ERA-40 reanalysis, *ERA-40 Proj. Rep. Ser. 12*, Eur. Cent. for Medium-Range Weather Forecasts, Reading, U. K.

Forster, R. R., D. G. Long, K. C. Jezek, S. D. Drobot, and M. R. Anderson (2001), The onset of Arctic sea-ice snowmelt as detected with passive- and active-microwave remote sensing, *Ann. Glaciol.*, *33*, 85–93, doi:10.3189/172756401781818428.

Giles, K. A., S. W. Laxon, and A. L. Ridout (2008), Circumpolar thinning of Arctic sea ice following the 2007 record ice extent minimum, *Geophys. Res. Lett.*, *35*, L22502, doi:10.1029/2008GL035710.

Granskog, M., T. Vihma, R. Pirazzini, and B. Cheng (2006), Superimposed ice formation and surface energy fluxes on sea ice during the spring melt-freeze period in the Baltic Sea, *J. Glaciol.*, *52*(176), 119–127, doi:10.3189/172756506781828971.

Grant, A. N., S. Bronnimann, and L. Haimberger (2008), Recent Arctic warming vertical structure contested, *Nature*, *455*, E2–E3, doi:10.1038/nature07257.

Graversen, R. G., T. Mauritsen, M. Tjernstrom, E. Kallen, and G. Svensson (2008), Vertical structure of recent Arctic warming, *Nature*, *451*, 53–56, doi:10.1038/nature06502.

Grenfell, T. C., and D. K. Perovich (1984), Spectral albedos of sea ice and incident solar irradiance in the southern Beaufort Sea, *J. Geophys. Res.*, *89*(C3), 3573–3580, doi:10.1029/JC089iC03p03573.

Grenfell, T. C., and D. K. Perovich (2004), Seasonal and spatial evolution of albedo in a snow-ice-land-ocean environment, *J. Geophys. Res.*, *109*, C01001, doi:10.1029/2003JC001866.

Intrieri, J., C. W. Fairall, M. D. Shupe, P. O. Persson, E. L. Andreas, P. S. Guest, and R. E. Moritz (2002), An annual cycle of Arctic surface cloud forcing at SHEBA, *J. Geophys. Res.*, *107*(C10), 8039, doi:10.1029/2000JC000439.

Kwok, R., and D. A. Rothrock (2009), Decline in Arctic sea ice thickness from submarine and ACESat records: 1958–2008, *Geophys. Res. Lett.*, *36*, L15501, doi:10.1029/2009GL039035.

Kwok, R., G. F. Cunningham, and S. V. Nghiem (2003), A study of melt over the Arctic Ocean in RADARSAT synthetic aperture radar data, *J. Geophys. Res.*, *108*(C11), 3363, doi:10.1029/2002JC001363.

Laxon, S. W., N. Peacock, and D. Smith (2003), High interannual variability of sea ice thickness in the Arctic region, *Nature*, *425*, 947–950, doi:10.1038/nature02050.

Lüpkes, C., T. Vihma, E. Jakobson, G. König-Langlo, and A. Tetzlaff (2010), Meteorological observations from ship cruises during summer to the central Arctic: A comparison with reanalysis data, *Geophys. Res. Lett.*, *37*, L09810, doi:10.1029/2010GL042724.

Markus, T., J. C. Stroeve, and J. Miller (2009), Recent changes in Arctic sea ice melt onset, freeze up and melt season length, *J. Geophys. Res.*, *114*, C12024, doi:10.1029/2009JC005436.

Nghiem, S., R. Kwok, D. Perovich, and D. Barber (2003), Impact of cloud cover on sea ice surface melt, paper presented at Seventh Conference on Polar Meteorology and Oceanography and Joint Symposium on High-Latitude Climate Variations, Am. Meteorol. Soc., Boston, Mass.

Notz, D. (2009), The future of ice sheets and sea ice: Between reversible retreat and unstoppable loss, *Proc. Natl. Acad. Sci. U. S. A.*, *106*(49), 20,590–20,595, doi:10.1073/pnas.0902356106.

Perovich, D. K., and B. Elder (2001), Temporal evolution and spatial variability of the temperature of Arctic sea ice, *Ann. Glaciol.*, *33*, 207–211, doi:10.3189/172756401781818158.

Perovich, D. K., B. Light, H. Eicken, K. F. Jones, K. Runciman, and S. V. Nghiem (2007a), Increasing solar heating of the Arctic Ocean and adjacent seas, 1979–2005: Attribution and role in the ice-albedo feedback, *Geophys. Res. Lett.*, *34*, L19505, doi:10.1029/2007GL031480.

Perovich, D. K., S. V. Nghiem, T. Markus, and A. Schweiger (2007b), Seasonal evolution and interannual variability of the local solar energy absorbed by the Arctic sea ice–ocean system, *J. Geophys. Res.*, *112*, C03005, doi:10.1029/2006JC003558.

Persson, P. O. G., C. W. Fairall, E. L. Andreas, P. S. Guest, and D. K. Perovich (2002), Measurements near the Atmospheric Surface Flux Group Tower at SHEBA: Near-surface conditions and surface energy budget, *J. Geophys. Res.*, *107*(C10), 8045, doi:10.1029/2000JC000705.

Pinto, J. O., J. A. Curry, and C. W. Fairall (1997), Radiative characteristics of the Arctic atmosphere during spring as inferred from ground-based measurements, *J. Geophys. Res.*, *102*, 6941–6952, doi:10.1029/96JD03348.

Robinson, D. A., G. Scharfen, M. Serreze, G. Kukla, and R. Barry (1986), Snow melt and surface albedo in the Arctic basin, *Geophys. Res. Lett.*, *13*(9), 945–948, doi:10.1029/GL013i009p00945.

Screen, J. A., and I. Simmonds (2011), Erroneous Arctic temperature trends in the ERA-40 reanalysis: A closer look, *J. Clim.*, *24*(10), 2620–2627, doi:10.1175/2010JCLI4054.1.

Screen, J. A., and I. Simmonds (2012), Declining summer snowfall in the Arctic: Causes, impacts and feedbacks, *Clim. Dyn.*, *38*, 2243–2256, doi:10.1007/s00382-011-1105-2.

Stone, R. S., D. C. Douglas, G. I. Belchansky, S. D. Drobot, and J. Harris (2005), Cause and effect of variations in western Arctic snow and sea ice cover, Paper 8.3 presented at Eighth Conference on Polar Oceanography and Meteorology, Am. Meteorol. Soc., San Diego, Calif.

Stroeve, J., T. Markus, W. N. Meier, and J. Miller (2006), Recent changes in the Arctic melt season, *Ann. Glaciol.*, *44*(1), 367–374, doi:10.3189/172756406781811583.

Thiébaux, J., E. Rogers, W. Wang, and B. Katz (2003), A new high-resolution blended real-time global sea surface temperature analysis, *Bull. Am. Meteorol. Soc.*, *84*, 645–656, doi:10.1175/BAMS-84-5-645.

Thorndike, A., and R. Colony (1982), Sea ice motion in response to geostrophic winds, *J. Geophys. Res.*, *87*(C8), 5845–5852, doi:10.1029/JC087iC08p05845.

Thorne, P. W. (2008), Arctic tropospheric warming amplification?, *Nature*, *455*, E1–E2, doi:10.1038/nature07256.

Uppala S., D. Dee, S. Kobayashi, P. Berrisford, and A. Simmons (2008), Towards a climate data assimilation system: Status update of ERA Interim, *ECMWF Newsl. 115*, pp. 12–18, Eur. Cent. for Medium-Range Weather Forecasts, Reading, U. K.

Vihma, T., and R. Pirazzini (2005), On the factors controlling the snow surface and 2-m air temperatures over the Arctic sea ice in winter, *Boundary Layer Meteorol.*, *117*(1), 73–90, doi:10.1007/s10546-004-5938-7.

Vihma, T., M. M. Johansson, and J. Launiainen (2009), Radiative and turbulent surface heat fluxes over sea ice in the western Weddell Sea in early summer, *J. Geophys. Res.*, *114*, C04019, doi:10.1029/2008JC004995.

Wang, X., and J. R. Key (2005), Arctic surface, cloud, and radiation properties based on the AVHRR Polar 36 Pathfinder dataset. Part I: Spatial and temporal characteristics, *J. Clim.*, *18*(14), 2558–2574, doi:10.1175/JCLI3438.1.

Yackel, J. J., D. G. Barber, T. N. Papakyriakou, and C. Breneman (2007), First-year sea ice spring melt transitions in the Canadian Arctic Archipelago from time-series synthetic aperture radar data, 1992–2002, *Hydrol. Processes*, *21*, 253–265, doi:10.1002/hyp.6240.

Zhang, J., K. Stamnes, and S. A. Bowling (1996), Impact of clouds on surface radiative fluxes and snow melt in the Arctic and sub Arctic, *J. Clim.*, *9*(9), 2110–2123, doi:10.1175/1520-0442(1996)009<2110:IOCOSR>2.0.CO;2.

Zhang, T., S. A. Bowling, and K. Stamnes (1997), Impact of the atmosphere on surface radiative fluxes and snowmelt in the Arctic and Subarctic, *J. Geophys. Res.*, *102*(D4), 4287–4302, doi:10.1029/96JD02548.

Zuidema, P., B. Baker, Y. Han, J. Intrieri, J. Key, P. Lawson, S. Matrosov, M. Shupe, R. Stone, and T. Uttal (2005), An Arctic springtime mixed-phase cloudy boundary layer observed during SHEBA, *J. Atmos. Sci.*, *62*(1), 160–176, doi:10.1175/JAS-3368.1.

Multimodel Combination by a Bayesian Hierarchical Model: Assessment of Ice Accumulation over the Oceanic Arctic Region

MALAAK KALLACHE

CLIMPACT and LSCE-IPSL, Paris, France

ELENA MAKSIMOVICH

LOCEAN-IPSL, Paris, France

PAUL-ANTOINE MICHELANGELI

CLIMPACT, Paris, France

PHILIPPE NAVEAU

LSCE-IPSL, Gif-sur-Yvette, France

(Manuscript received 3 March 2009, in final form 20 April 2010)

ABSTRACT

The performance of general circulation models (GCMs) varies across regions and periods. When projecting into the future, it is therefore not obvious whether to reject or to prefer a certain GCM. Combining the outputs of several GCMs may enhance results. This paper presents a method to combine multimodel GCM projections by means of a Bayesian model combination (BMC). Here the influence of each GCM is weighted according to its performance in a training period, with regard to observations, as outcome BMC predictive distributions for yet unobserved observations are obtained. Technically, GCM outputs and observations are assumed to vary randomly around common means, which are interpreted as the actual target values under consideration. Posterior parameter distributions of the authors' Bayesian hierarchical model are obtained by a Markov chain Monte Carlo (MCMC) method. Advantageously, all parameters—such as bias and precision of the GCM models—are estimated together. Potential time dependence is accounted for by integrating a Kalman filter. The significance of trend slopes of the common means is evaluated by analyzing the posterior distribution of the parameters. The method is applied to assess the evolution of ice accumulation over the oceanic Arctic region in cold seasons. The observed ice index is created out of NCEP reanalysis data. Outputs of seven GCMs are combined by using the training period 1962–99 and prediction periods 2046–65 and 2082–99 with Special Report on Emissions Scenarios (SRES) A2 and B1. A continuing decrease of ice accumulation is visible for the A2 scenario, whereas the index stabilizes for the B1 scenario in the second prediction period.

1. Introduction

Today it is well accepted that global climate change has an effect on the polar regions (cf. Parry et al. 2007). The characteristics of the feedback is still under investigation and is related to important questions such as future sea level rise (cf. Charbit et al. 2008) and the influence of the polar regions on midlatitude patterns of atmospheric circulation and precipitation (Stroeve et al. 2007). General circulation model (GCM) projections are instrumental to exploring the effect of climate change in the future (see, e.g., Baettig et al. 2007). These models are run under contemporary conditions and possible future scenarios that reflect assumptions about the evolution of environment and society, especially the potential change in CO_2 emissions and concentrations. In this work two common greenhouse gas and aerosol emission scenarios (Nakicenovic and Swart 2000)—Special Report on Emissions Scenarios (SRES) A2 and B1—are employed for projections. The GCMs are based on complex dynamics and their performance varies across space and time. It is therefore not obvious whether to reject or

Corresponding author address: Malaak Kallache, CLIMPACT, 79 rue du Faubourg Poissonnière, 75009 Paris, France.
E-mail: mk@climpact.com

DOI: 10.1175/2010JCLI3107.1

prefer a certain GCM when projecting into the future. A simple combination of the different GCM outputs, which we denote the multimodel ensemble, might average out extremes. For diverse application fields it has nevertheless been shown that multimodel ensemble averaging (MEA) or Bayesian model averaging can generate better projections than each single model (cf. Raftery et al. 2005; van Loon et al. 2007).

Bayesian inference allows for the incorporation of expert knowledge and the assessment of parameter uncertainties. The approach has been increasingly used in climate change studies (see, e.g., Tol and De Vos 1998; Rougier 2007). For a general discussion of Bayesian statistics, refer to Congdon (2003) or Gelman et al. (2004). Combining multimodel ensembles by using a Bayesian approach has been pursued by a variety of studies. Among them, several are related to climate change and aim at the enhancement of projections. Coelho et al. (2004) regressed the multimodel ensemble mean on observations. This does not allow for a differentiation of bias and variance of the diverse models. Raftery et al. (2005) regressed observations on a weighted linear combination of model projections. Weights, which indicate the importance of each model, and regression parameters were estimated in a training period for which observations were available. Then they were transferred to a prediction period. Regression on the sum of model projections may cause overfitting when too many models are used. Therefore, the number of models and the length of the training period play an important role in this approach. Min and Hense (2006) proceeded likewise, where the weights for the linear combination of model outputs were obtained from Bayes factors. Tebaldi et al. (2005) treated observations and model outputs as random variables. Both data sources varied around common means. These means were interpreted as unobserved values of the assessed variable, the target values. In this way a connection between model outputs and observations is established. Tebaldi et al. (2005) explored the change of mean temperature between the training and prediction periods. Here stationarity of the variable was assumed within each period. Berliner and Kim (2008) followed a similar approach, but they allowed for time-dependent variables under consideration by applying a data assimilation framework. The target values were modeled as autocorrelated hidden states, which are influenced by covariates. They estimated a potential bias of each model as averaged deviation from these target values.

The study presented here is in line with Tebaldi et al. (2005) and Berliner and Kim (2008). We allow for a temporal gap between the training and prediction periods. That is, contrary to Tebaldi et al. (2005), projections are not regressed on model outputs of the training period. Model outputs and observations are assumed to vary around common means, that is, both have an error. In the training period, model outputs and observations are combined to a weighted average, whereas we assume that observations have no bias. In this way a potential bias and the variability of each GCM are estimated in comparison to the observations. This differs from Berliner and Kim (2008), who did not directly involve observations to estimate these parameters. A Kalman filter is integrated in a Markov chain Monte Carlo (MCMC) routine to estimate the parameters of our Bayesian hierarchical model (Chib and Greenberg 1996). This allows for sequential prediction and for updating steps and the assessment of time-dependent variables, which are especially required when analyzing the effect of climate change. The common means of model outputs and observations are modeled as hidden states comprising a stationary autoregressive and a trend component. As application we assess the evolution of an ice index.

We proceed as follows: In section 2 the data are described and the construction of the ice index for the oceanic Arctic region is presented. The Bayesian model combination (BMC) framework is outlined in section 3 and its application to the ice index is illustrated in section 4. Last, a summary of our results and a conclusion are given in section 5.

2. Ice accumulation over the oceanic Arctic region

Sea ice area reductions are related to increases of surface air temperature in the polar regions (Hassol 2004); such reductions have been well documented by observational and modeling studies (cf. Zhang and Walsh 2006; Cavalieri and Parkinson 2008). Temperature-based ice indices represent primarily sea ice thickness and volume: the intensity of sea ice accumulation during the freezing season is a result of heat fluxes between ocean and air reservoirs through snow-covered sea ice. Sea ice accumulation has, for example, been estimated by Anderson (1961) and Maykut (1986), who utilize daily near-surface temperature fields for this purpose. Sea ice thickness and volume are important for sea ice–related feedbacks (Stroeve et al. 2007). They influence, for example, ice forming and drifting processes.

Here atmospheric surface temperatures (SATs), 2 m above the surface, are used to calculate an ice index as a proxy for the ice accumulation over the oceanic Arctic region. This ice index has been developed within the European Union (EU) project Developing Arctic Modeling and Observing Capabilities for Long-term Environmental Studies (DAMOCLES; available online at http://www.damocles-eu.org). We use daily SAT data to calculate the index, either provided by GCMs or by

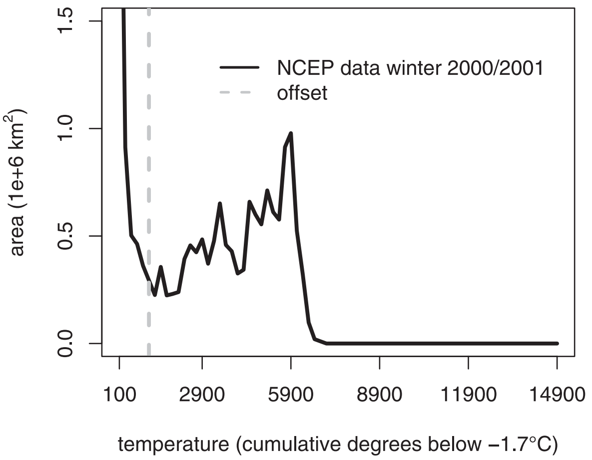

FIG. 1. Accumulated area over oceanic Arctic region, classified by iciness. The level of iciness is measured by the sum of degrees below −1.7°C per freezing season (September–May). The ice index is created as an integral over the black curve, weighted by the classes of iciness (*x* axis). Areas below the offset (gray line) are disregarded.

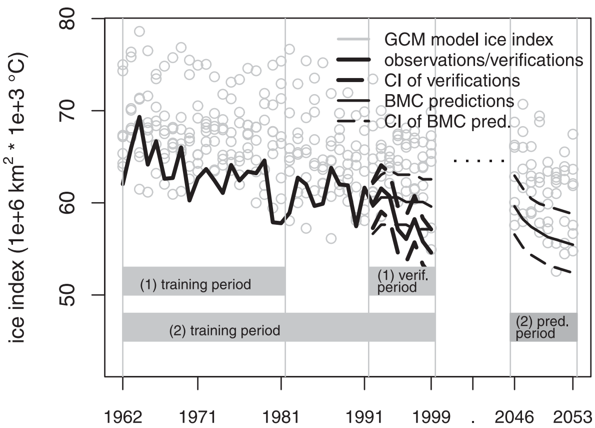

FIG. 2. Outline of the BMC framework: first, the framework is inspected by projecting from a training period to a verification period, where observations are also given (1); then, a training period is chosen to project to a future period (2). The winter ice index generated from NCEP reanalysis data (with 66% confidence intervals in the verification period) is shown as thick black lines, and the BMC projections (with 66% credibility intervals) as thin black lines.

National Centers for Environmental Prediction (NCEP) reanalysis data. The ice index was designed in the following way: The area over the oceanic Arctic region was classified regarding its iciness over the freezing season (September–May). The level of iciness was estimated by taking at each grid point the sum of degrees below −1.7°C over the season. The iciness classes had a width of 200°C. Data at different grid points represent areas of distinct size; in this way, area and classes of iciness are linked. Figure 1 exemplarily shows the levels of iciness of the oceanic Arctic region for the freezing season 2000/01 and NCEP reanalysis data. The winter ice index was obtained by taking the integral of the classified area, that is, the black curve in Fig. 1. Here the summands of the Riemann integral have been weighted with the iciness class levels and the area of the warmest classes, where the sum of degrees below −1.7°C is smaller than 1100°C, were disregarded. In this way the focus is set on the colder levels, and the intensity of freezing conditions during the polar winter is explored. This ice index, therefore, is related to sea ice volume accumulated by the end of winter rather than to sea ice extent. Further details are provided in Maksimovich and Gascard (2010). We analyze the ice index for the historical period 1962–99 and projection periods 2046–65 and 2082–99 and SRES A2 and B1. NCEP reanalysis data are used to calculate the observed ice index. Outputs of 13 Intergovernmental Panel on Climate Change (IPCC) models cover all three periods and are therefore chosen for our analysis (see Fig. 3 for model acronyms). Within the historical period, the models are run with the twentieth-century run (20c3m) scenario, that is, with increasing greenhouse gases and anthropogenic sulfate aerosol forcing as observed through the twentieth century. The model surface temperature data have been obtained from the Program for Climate Model Diagnosis and Intercomparison (available online at www-pcmdi.llnl.gov).

3. Bayesian model combination

Let BMC denote our technique to average over many competing models by setting up a statistical model. The quantities of interest are parameters of this model, which are estimated while evaluating GCM outputs and observations. The effect of each GCM is weighted according to its performance in a training period, where observations are available for comparison. In this way model uncertainty is incorporated in the calculation of the BMC projections. Expert knowledge may be integrated as prior information. The aim of BMC is the improvement of predictive performance. For the analysis we proceed in two steps, as illustrated in Fig. 2. First, the BMC framework is inspected on a verification period. Here the BMC projections are compared to observations not used in the calibration. The BMC results in predictive distributions. We take the mean of these distributions as actual BMC projections. Their uncertainty is deduced by calculating credibility intervals from the predictive distributions. In Fig. 2 BMC projections of the ice index (black line) are depicted together with GCM projections (gray dots) and observations (thick black lines). For the verification period shown, the BMC projections are located much closer to the observations than the projections of each single model. A more detailed evaluation of the performance of the BMC is provided by using scores, see section 4a. In a second step, we choose a training period to project to future periods, where no observations are available. The bias of the GCMs is estimated in the training period and maintained for the projections. Figure 2 shows, for example, that the BMC projections lie below the output of each single model, just like the observations in the training period. Our goal is to project the yet unobserved observations Y_0, which we take as mean of the predictive distribution $[Y_0|\mathbf{D}]$. Here the data vector $\mathbf{D} = (\mathbf{X}_0, \mathbf{X}_1, \ldots, \mathbf{X}_M, \mathbf{Y}_1, \ldots, \mathbf{Y}_M)$ is given by the vectors of observations $\mathbf{X}_0$ and model outputs in the training period $\mathbf{X}_i$ and in the prediction period $\mathbf{Y}_i$. In our example $\mathbf{X}_0$ is a winter ice index created of surface temperature over the oceanic Arctic region and $\mathbf{X}_i$ denotes this ice index computed by model i over the same region and at the same period.

Bayesian inference presumes that parameters are not point estimates but have a distribution. For each model parameter, say, θ_i, a prior distribution is assumed, which comprises our knowledge about the uncertainty of the parameter values. Then we learn from the data $\mathbf{D}$ to obtain the posterior distribution of the parameters, say, $[\mathbf{\Theta}|\mathbf{D}]$. This is formalized with Bayes's theorem (cf. Gelman et al. 2004). Let $[\mathbf{D}|\mathbf{\Theta}]$ denote the conditional distribution of $\mathbf{D}$ given $\mathbf{\Theta}$, that is, the likelihood of the data. We can say that $[\mathbf{\Theta}|\mathbf{D}]$ is proportional to the product of likelihood and prior distribution of the parameters, that is,

$$[\mathbf{\Theta}|\mathbf{D}] \propto [\mathbf{\Theta}][\mathbf{D}|\mathbf{\Theta}]. \tag{1}$$

Integration over all parameters leads to the predictive distribution of Y_0 given $\mathbf{D}$:

$$[Y_0|\mathbf{D}] = \int_{\mathbf{\Theta}} [Y_0|\mathbf{\Theta}][\mathbf{\Theta}|\mathbf{D}]\, d\mathbf{\Theta}. \tag{2}$$

Equation (2) implies the conditional independence of Y_0 and $\mathbf{D}$ given $\mathbf{\Theta}$. For further details see Congdon (2003).

a. State-space model

Climate projections for the Arctic often exhibit trends, which are superimposed by decadal oscillations (Döscher et al. 2009). To be able to distinguish and track characteristics due to potentially different processes, we model the evolution of the ice index in time. To do so a sequential data assimilation procedure is employed within our Bayesian framework (cf. DelSole 2007).

We permit a gap of G' time steps between the training and prediction periods and introduce $G = T + G'$; thus $t = G + 1, \ldots, G + P$ is the time index of the prediction period of length P (see Fig. 2). At each time point t in $1, \ldots, T, G + 1, \ldots, G + P$, there is a prediction and update step of the parameter distributions. Let $\mathbf{D}_t$ denote the vector of data per time step,

$$\mathbf{D}_t = \begin{cases} (X_{0_t}, X_{1_t}, \ldots, X_{M_t}) & \text{for} \quad t = 1, \ldots, T, \\ (Y_{1_t}, \ldots, Y_{M_t}) & \text{for} \quad t = G+1, \ldots, G+P. \end{cases} \tag{3}$$

The relations between model outputs and observations are given by the *data equations*

$$\begin{aligned} X_{i_t} &= c_T + \mu_t + d_t + b_i + \epsilon_{i_t} \quad \text{for} \quad t = 1, \ldots, T, \quad i = 0, \ldots, M \quad \text{and} \\ Y_{i_t} &= c_P + \nu_t + \delta_t + b_i + e_{i_t} \quad \text{for} \quad t = G+1, \ldots, G+P, \quad i = 1, \ldots, M, \end{aligned} \tag{4}$$

with $b_0 = 0$, and Gaussian distributions for the noise, that is, $\epsilon_{i_t} \sim N(0, \lambda_i^{-1}), e_{i_t} \sim N[0, (\gamma\lambda_i)^{-1}]$. Here $N(\mu, \sigma^2)$ denotes normal distribution with mean μ and variance σ^2 as parameters; λ_i is the precision of model i and is equal to the reciprocal value of the variance. The precision of the observations λ_0 reflects the natural variability specific to the season and other physical factors. In our model λ_0 is externally given and estimated from the observations. The parameter γ allows for a different model precision for the training and prediction periods. It is assumed that all models experience the same degree of change, that is, γ is the same for all models. Moreover, it is presumed that each GCM has a constant bias b_i, and this bias is transferred from the training period to the prediction period.

The common means of model outputs and observations are modeled as composition of an intercept, a stationary autoregressive component, and a trend component. This gives the common means for the training period $\mathrm{MT}_t = c_T + \mu_t + d_t$ and for the prediction period $\mathrm{MP}_t = c_P + \nu_t + \delta_t$. Empirical series often exhibit autocorrelated noise. Here the assumption of uncorrelated noise may bias the estimate of the magnitude of the systematic change (cf. Bloomfield 1992). Therefore, we allow for an autocorrelated part, which is a common approach in time series analysis (cf. Cohn and Lins 2005; Harvey et al. 2007). The results for the ice index assessment confirm this choice: we find significant autocorrelation for all settings analyzed (see section 4d). The stationary autoregressive components μ_t and ν_t and the linear trend components d_t and δ_t are modeled separately. By doing so, we differentiate systematic changes and other variations of the common mean (see, e.g., West 1997).

The temporal dependence is modeled by the following *state-space equations:*

$$\begin{aligned}
\mu_t &= \phi\mu_{t-1} + \omega_{\mu_t} \quad \text{for} \quad t = 1, \ldots, T,\\
d_t &= d_{t-1} + k_1 + \omega_{d_t} \quad \text{for} \quad t = 1, \ldots, T,\\
\nu_t &= \phi\nu_{t-1} + \omega_{\nu_t} \quad \text{for} \quad t = G+1, \ldots, P, \quad \text{and}\\
\delta_t &= \delta_{t-1} + k_2 + \omega_{\delta_t} \quad \text{for} \quad t = G+1, \ldots, P,
\end{aligned} \tag{5}$$

with $\omega_{\mu_t} \sim N(0, \lambda_\mu^{-1})$, $\omega_{d_t} \sim N(0, \lambda_d^{-1})$, $\omega_{\nu_t} \sim N(0, \lambda_\nu^{-1})$, and $\omega_{\delta_t} \sim N(0, \lambda_\delta^{-1})$ being independent and identically distributed. The state-space parameters are constructed such that they have the Markov property (Chib and Greenberg 1996). Here μ_t and ν_t are autoregressive (AR) components of order one [AR(1) processes]. We suppose short-term variability to be an intrinsic characteristic of the system assessed; therefore, the autoregressive parameter ϕ is transferred from the training period to the prediction period. On the other hand, there may be a gap of several decades between the training and prediction periods. Consequently, transferring trend slope estimates from the training period to the prediction period is not feasible. Here the unknown potential trend in the prediction period is therefore inferred from the GCM projections. In this way trend slope and intercept may differ in both periods; k_1 and k_2 denote the trend slopes times Δt, which is the time difference between two consecutive observations (see, e.g., Dethlefsen and Lundbye-Christensen 2005).

The parameter vector at time t is given by

$$\mathbf{\Theta}_t = \begin{cases} (c_T, \mu_t, d_t, \lambda_1, \ldots, \lambda_M, \phi, k_1, b_1, \ldots, b_M, \lambda_\mu, \lambda_d) & \text{for} \quad t = 1, \ldots, T,\\ (c_P, \nu_t, \delta_t, \lambda_1, \ldots, \lambda_M, \gamma, \phi, k_2, b_1, \ldots, b_M, \lambda_\nu, \lambda_\delta) & \text{for} \quad t = G+1, \ldots, G+P. \end{cases} \tag{6}$$

Conditional independence from the data of previous time steps given the parameter values is supposed, that is,

$$\begin{aligned}
[\mathbf{\Theta}_t|\mathbf{\Theta}_{t-1}, \mathbf{D}_1, \ldots, \mathbf{D}_{t-1}] &= [\mathbf{\Theta}_t|\mathbf{\Theta}_{t-1}] \quad \text{for} \quad t = 1, \ldots, T, G+1, \ldots, G+P,\\
[\mathbf{D}_t|\mathbf{\Theta}_t, \mathbf{D}_1, \ldots, \mathbf{D}_{t-1}] &= [\mathbf{D}_t|\mathbf{\Theta}_t] \quad \text{for} \quad t = 1, \ldots, T, G+1, \ldots, G+P.
\end{aligned} \tag{7}$$

Thus, the model given by Eqs. (4) and (5) has the form

$$\mathbf{D}_t = \mathbf{H}_t\mathbf{\Theta}_t + \mathbf{K}_t + \mathbf{\Sigma}_t \quad \text{for} \quad t = 1, \ldots, T, G+1, \ldots, G+P \quad \text{and} \tag{8}$$

$$\mathbf{\Theta}_t = \mathbf{F}_t\mathbf{\Theta}_{t-1} + \mathbf{U}_t + \mathbf{W}_t \quad \text{for} \quad t = 1, \ldots, T, G+1, \ldots, G+P, \tag{9}$$

with $\mathbf{\Sigma}_t$ and $\mathbf{W}_t$ being the respective error matrices. The state-space parameters are assumed to be independent; consequently, both matrices have nonzero values only in the diagonal; $\mathbf{H}_t$, $\mathbf{K}_t$, $\mathbf{F}_t$, and $\mathbf{U}_t$ contain either zeros or constants and can be deduced from Eqs. (4) and (5).

To keep the number of parameters low, we chose a simple structure of the state-space variables; however, more complicated structures can be easily integrated (cf. Harvey et al. 2007). The distinction between trend and autoregressive components may be difficult, as outlined in Kallache et al. (2005). A state-space model, as presented in Eq. (5), is a possibility to represent time series, which may consist of those both components. Its appropriateness has been explored by Koop and Van Dijk (2000), for example. Moreover, we verify the adequateness of our model given by Eqs. (4) and (5); the results are provided in section 4a.

b. *Sequential updating*

As common in data assimilation, alternating update and prediction steps of the state-space variables are performed. Here this is also done in the prediction period, and the GCM outputs are treated as biased observations. A projection Y_{0_t} is based on this evolution.

The *update formula* or *filtering formula* is given by

$$\begin{aligned}
[\mathbf{\Theta}_{t-1}|\mathbf{D}_1, \ldots, \mathbf{D}_{t-1}] &= \frac{[\mathbf{D}_{t-1}|\mathbf{\Theta}_{t-1}][\mathbf{\Theta}_{t-1}|\mathbf{D}_1, \ldots, \mathbf{D}_{t-2}]}{[\mathbf{D}_{t-1}|\mathbf{D}_1, \ldots, \mathbf{D}_{t-2}]}\\
&\propto [\mathbf{D}_{t-1}|\mathbf{\Theta}_{t-1}][\mathbf{\Theta}_{t-1}|\mathbf{D}_1, \ldots, \mathbf{D}_{t-2}].
\end{aligned} \tag{10}$$

With respect to $\mathbf{\Theta}_t$, the marginal likelihood of the data $[\mathbf{D}_t|\mathbf{D}_1, \ldots, \mathbf{D}_{t-1}]$ is a constant, so we neglect this term. This update step is equivalent to the calculation of the posterior distribution of the parameters at time step t, with the prior distribution given as $[\mathbf{\Theta}_t|\mathbf{D}_{t-1}]$.

The *prediction formula* is denoted by

$$[\mathbf{\Theta}_t|\mathbf{D}_1, \ldots, \mathbf{D}_{t-1}] = \int_{\mathbf{\Theta}_{t-1}} [\mathbf{\Theta}_t|\mathbf{\Theta}_{t-1}][\mathbf{\Theta}_{t-1}|\mathbf{D}_1, \ldots, \mathbf{D}_{t-1}]\, d\mathbf{\Theta}_{t-1}, \tag{11}$$

and Eqs. (10) and (11) are the Bayesian solution to calculate the state-space model given in Eqs. (8) and (9).

The state-space model consists of linear and Gaussian equations; therefore, we apply the Kalman filter to obtain the posterior distribution of the parameters. In this way the integral in Eq. (11) can be derived by characteristics of the normal distribution. Let $\mathbf{\Theta}_{t-1}|\mathbf{D}_{t-1} \sim N(\hat{\mathbf{\Theta}}_{t-1}, \mathbf{S}_{t-1})$ with $\hat{\mathbf{\Theta}}_{t-1}$ and $\mathbf{S}_{t-1}$ being the expected value and the variance of $\mathbf{\Theta}_{t-1}|\mathbf{D}_{t-1}$, and then $\mathbf{\Theta}_t|\mathbf{D}_{t-1} \sim N(\mathbf{F}_t\hat{\mathbf{\Theta}}_{t-1}\mathbf{F}_t', \mathbf{F}_t\mathbf{S}_{t-1}\mathbf{F}_t' + \mathbf{W}_t)$ (see, e.g., Meinhold and Singpurwalla 1983).[1]

c. Prior distributions

We choose uninformative priors because of the lack of prior knowledge. The precisions λ_i, $i = 1, \ldots, M$ and λ_μ, λ_d, λ_ν, and λ_δ are assumed to have uniform prior densities $U(0, c)$. A uniform prior for the precision λ is proportional to a uniform prior for the standard deviation σ (see, e.g., Gelman 2006). Similarly, we choose $\gamma \sim U(0, c)$ as a prior for γ. The upper bound $c =$ 1 000 000 is chosen to be large to include any plausible prior value and to avoid an impact of this choice on the results. The uniform distribution is conditionally conjugate to the normal distribution. Therefore, this prior results in a posterior gamma distribution, similar to when choosing an informative gamma distribution as prior. However, by using a uniform prior, we avoid distortions of the posterior (cf. Harvey et al. 2007) and do not have to specify hyperparameters for a gamma prior, which may result in an improper posterior density in case these hyperparameters tend to zero.

For μ_t and d_t a nearly flat prior, that is, a normal distribution with variance near to infinity, is selected, and the same applies for ν_t and δ_t, respectively. We model a trend and an autoregressive component. Therefore, the autoregressive component is assumed to be stationary, and for the parameter ϕ a uniform prior on the interval $(-1, 1)$ is chosen. The trend slope parameters k_1 and k_2, the intercepts c_T and c_P, and the model biases $b_1, \ldots, b_M$ have uniform priors on the real line.

d. Calculation of the posterior distribution

The joint posterior distribution of the parameters $[\mathbf{\Theta}|\mathbf{D}]$ is the target density, which we will obtain by means of Eq. (1) and sequential calculation of the time dependent parameters.

The likelihood of the data is given by

$$[\mathbf{D}|\mathbf{\Theta}] = [\mathbf{X}_0, \mathbf{X}_1, \ldots, \mathbf{X}_M, \mathbf{Y}_1, \ldots, \mathbf{Y}_M|\mathbf{\Theta}] \propto \prod_{i=1}^{M}\left(\sqrt{\gamma^P}\sqrt{\lambda_i^{(T+P)}}\exp\left\langle -\frac{\lambda_i}{2}\left\{\sum_{t=1}^{T}[X_{i_t} - (c_T + \mu_t + d_t + b_i)]^2 + \gamma\sum_{t=G+1}^{G+P}[Y_{i_t} - (c_P + \nu_t + \delta_t + b_i)]^2\right\}\right\rangle\right) \times \exp\left\{-\frac{\lambda_0}{2}\sum_{t=1}^{T}[X_{0_t} - (c_T + \mu_t + d_t)]^2\right\}. \quad (12)$$

To consider the dependencies within the parameters, we separately assess the constant components of the parameter vector $\mathbf{\Theta}_{\text{stat}} = (c_T, c_P, \gamma, \phi, k_1, k_2, \lambda_1, \ldots, \lambda_M, b_1, \ldots, b_M, \lambda_\mu, \lambda_\nu, \lambda_d, \lambda_\delta)$ and the state-space components μ_t, d_t, ν_t, and δ_t. The posterior distribution of the constant parameters is given by

$$[\mathbf{\Theta}_{\text{stat}}|\mu, d, \nu, \delta, \mathbf{D}] \propto [\mathbf{D}|\mathbf{\Theta}] \times [\mu, d, \nu, \delta|\mathbf{\Theta}_{\text{stat}}] \times [c_T] \times [c_P] \times [\gamma] \times [\lambda_1] \times \ldots \times [\lambda_M] \times [\lambda_\mu] \times [\lambda_d] \times [\lambda_\nu] \times [\lambda_\delta] \times [\phi] \times [k_1] \times [k_2] \times [b_1] \times \ldots \times [b_M]. \quad (13)$$

Inference of the analytic form of the posterior distribution of the parameters cannot be drawn, but the priors of the stationary parameters are conjugate to the likelihood. Thus, the marginal conditional densities of the parameters are given, and a MCMC simulation through a Gibb's sampler is employed to approximate the marginal posterior distributions of the parameters (cf. Tebaldi et al. 2005). Further details are provided in the appendix. The posterior distribution of the intercepts c_T and c_P is normal with variance $[T(\lambda_0 + \sum_{i=1}^{M}\lambda_i)]^{-1}$ and $(\gamma P\sum_{i=1}^{M}\lambda_i)^{-1}$. The mean of the intercepts is a weighted average of observations and model outputs, whereas the precisions λ_i serve as weights:

[1] The vector $\mathbf{F}_t'$ is the transpose of $\mathbf{F}_t$.

$$\mu_{c_T} = \frac{\sum_{t=1}^{T}\left\langle \sum_{i=1}^{M}\{\lambda_i[X_{i_t} - (\mu_t + d_t + b_i)]\} + \lambda_0[X_{0_t} - (\mu_t + d_t)]\right\rangle}{T\left(\lambda_0 + \sum_{i=1}^{M}\lambda_i\right)} \quad \text{and} \quad \mu_{c_P} = \frac{\sum_{i=1}^{M}\sum_{t=G+1}^{G+P}\lambda_i[Y_{i_t} - (\nu_t + \delta_t + b_i)]}{P\sum_{i=1}^{M}\lambda_i}. \tag{14}$$

The posterior distribution of the state-space parameters $[\mu_t, \nu_t, d_t, \delta_t|\mathbf{\Theta}, \mathbf{D}]$ at each time step $t = 1, \ldots, T, G + 1, \ldots, G + P$ is obtained by applying the update and prediction steps of Eqs. (10) and (11) by means of a Kalman filter–based simulation smoother (Meinhold and Singpurwalla 1983; De Jong and Shephard 1995; Durbin and Koopman 2002; Harvey et al. 2007). The Kalman filter and smoother are run at each Gibb's sampling iteration (i) with the current stationary parameters $\mathbf{\Theta}_{\text{stat}}^{(i)}$.

The predictive distribution Y_{0_t} at time t is derived by using the corresponding parameter vector $\mathbf{\Theta}_t$ for Eq. (2). This parameter vector is actually calculated by utilizing all data information $\mathbf{D}$, because a Kalman smoother is employed for the state-space variables (cf. Dethlefsen and Lundbye-Christensen 2005).

e. Approximation of the predictive distribution

Let the conditional distribution of Y_0 given the parameters be $Y_0|\mathbf{\Theta} \sim N(c_P + \nu_t + \delta_t, \lambda_0^{-1})$. The assumption of a similar variability of the observations in the training and prediction periods is commonly used (cf. Min et al. 2004; Raftery et al. 2005). Other modeling approaches would require detailed physical knowledge of the prediction period. We use Monte Carlo integration to calculate the predictive distribution of Y_{0_t}; that is, equation (2) is interpreted as the calculation of the expectation of $[Y_0|\mathbf{\Theta}]$, which is the predictive distribution (Davison 2003). As an approximation of the posterior predictive distribution, we get

$$[Y_{0_t} = y_{0_s}|\mathbf{D}] = R^{-1}\sum_{r=1}^{R}[Y_0 = y_{0_s}|\mathbf{\Theta}_r], \tag{15}$$

where $\mathbf{\Theta}_1, \ldots, \mathbf{\Theta}_R$ represent draws from the posterior probability of the parameters $[\mathbf{\Theta}|\mathbf{D}]$, which are obtained by Gibb's sampling. Equation (15) is evaluated for each y_{0_s}, $s = 1, \ldots, S$, where the set of y_{0_s} covers the whole domain of the posterior predictive distribution; R denotes the number of Gibb's sampling iterations kept for evaluation (see the appendix for further details).

4. Ice index assessment

The BMC framework is applied to an ice index representing the ice accumulation over the oceanic Arctic region for a freezing season (see section 2). The index is derived from surface temperature, a climatic variable, and is not directly related to sea ice physics.

We combine single runs of several GCMs; thus, the natural variability of the GCMs themselves is not considered. However, Gregory et al. (2002) and Zhang and Walsh (2006) do not find a major influence of internal model variability on the trends of sea ice extent. Given the strong decrease of the ice accumulation index for the prediction periods (see section 4d), we deduce that internal model variability may also be neglected for the quantitative interpretation of the ice index assessment results.

Our results are verified by comparisons with an ice index created from reanalysis data. Bromwich et al. (2007) find NCEP reanalysis data to be a suitable tool to study the Arctic region, despite some deficiencies. Sufficiently accurate observations were not available until now. Sea ice volume or thickness can only be measured with large uncertainty, since the data are derived from submarine sonar measurements, which do not have sufficient coverage (Gregory et al. 2002), or from satellite measurements (Laxon et al. 2003; Kwok and Rothrock 2009).

a. Verification

For verification, training periods of different lengths are used, namely, freezing seasons spanning 5 (1977–81), 10 (1972–81), 15 (1967–81), and 20 (1962–81) yr. The verification period covers from 1992 to 1999 and the derived predictive distributions are compared to observations for this period.

We utilize common measures for verification, such as the mean absolute error (MAE) or the root-mean-square error (RMSE). Furthermore, we employ the continuous ranked probability score (CRPS) and the ignorance score (IS) to evaluate distributions. The CRPS gets better the closer a verification y is to the center of the predictive cumulative distribution function $F(\cdot)$. The CRPS is the integral of the Brier score at all possible threshold values t for the continuous predictand and is defined as

$$\text{CRPS}(F, y) = \int_{-\infty}^{\infty}[F(t) - H(t - y)]^2\, dt, \tag{16}$$

where $H(t - y)$ denotes the Heaviside function with $H(t - y) = 0$ for $t < y$ and $H(t - y) = 1$ otherwise (see Gneiting et al. 2005). To approximate the CRPS, we use the discretized predictive distribution evaluated at 200 quantiles (cf. Hersbach 2000). The IS is the negative logarithm of the predictive density $f(\cdot)$ at the verification y, that is,

$$\mathrm{IS}(f, y) = -\log f(y). \tag{17}$$

Both scores indicate a better performance when having a lower value. All comparisons are done with the average of these scores over the whole verification period.

To further evaluate the Bayesian framework, we carried out simulation studies with artificial data (results not shown). The data were generated from a Gaussian white noise process or from an AR(1) process and a linear trend or no trend was added. Then we calibrated the BMC model in a training period and projected to a verification period. The scores described in this section were used as an evaluation criterion. In all cases the simulation studies showed good performance of the BMC framework and superiority to just taking the multimodel ensemble mean.

b. *Size of the multimodel ensemble*

Thirteen GCMs cover the historical period and the two projection periods (see section 2). In Fig. 3 the precision λ_i of all models is shown. The precision signifies how closely the GCMs vary around the common means. It is an indicator for the quality of the models, and the contribution of each model to the constant part of the common means, c_T and c_P, is weighted by the precision, which is apparent in Eq. (14).

Six of the GCMs include natural forcing in their 20C3M runs, such as variations in solar input and volcanic forcing. Most of those models have a high precision (see Fig. 3). However, anthropogenic forcing is assumed to be the main factor for the increase of northern SAT (Kaufman et al. 2009) and the decrease of Arctic sea ice extent (cf. Gregory et al. 2002; Johannessen et al. 2004) observed for the last third of the twentieth century. It is expected that Arctic sea ice extent will continue to decline through the twenty-first century also because of atmospheric greenhouse gas loading (Stroeve et al. 2007). To evaluate the potential advantage of using solely GCMs, which include natural forcing, we compare BMC ice index projection skills of the sets of GCMs with and without natural forcing (results not shown). The projection period of 1989–95 is taken, because here Stroeve et al. (2007) found a stronger downward trend for sea ice extent, which is not well reproduced by the IPCC Fourth Assessment Report (AR4) models. Stroeve et al. (2007) attributed this effect to an intense positive

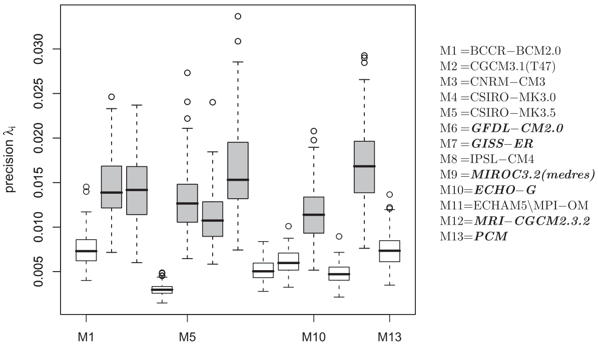

FIG. 3. Box plots of GCM precisions λ_i, which are estimated by using the historical period 1962–99. The models with high precision are accented in gray. Models that include natural forcing in their 20C3M run are listed in bold italic.

state of the winter northern annular mode, which in turn is linked to solar activity (cf. Ruzmaikin and Feynman 2002). Thus, strong differences of the ice index projections for this period are expected. However, the set of GCMs that include natural forcing did not ameliorate the reproduction of the observed decline of the ice index for this period. This indicates that other model characteristics—for example, the implementation of sea ice, ocean and atmospheric physics, and the coupling between those modules—might have a stronger influence on the ice index evolution than the inclusion of natural forcing. Thus, we consider all 13 GCMs as valid candidates for our analysis.

Figure 3 reveals that some models have a very low precision, which points at reducing the number of GCMs. To decide whether to delimit the number of models for the projection, we compare the prediction scores of the set of all models and a selection of seven models with good precision (the precision box plot of the selection is accented gray in Fig. 3). The prediction scores of the smaller set of models are on a par with the set of all models for all verification settings except the one with 15 yr of training length (see Fig. 4). Therefore, we chose to utilize the selection of seven models with the best precision in the further analysis.

c. *Length of the training period*

The influence of the length of the training period is evaluated by comparing prediction scores for different training period lengths and a verification period from 1992 to 1999 (see section 4a). Results are depicted in Fig. 4. In Figs. 4a,b the RMSE and MAE for the BMC projections and the MEA are shown. Apparently, the BMC projections outperform projections made by just taking the multimodel ensemble average. The CRPS and IS scores for different training period lengths are depicted

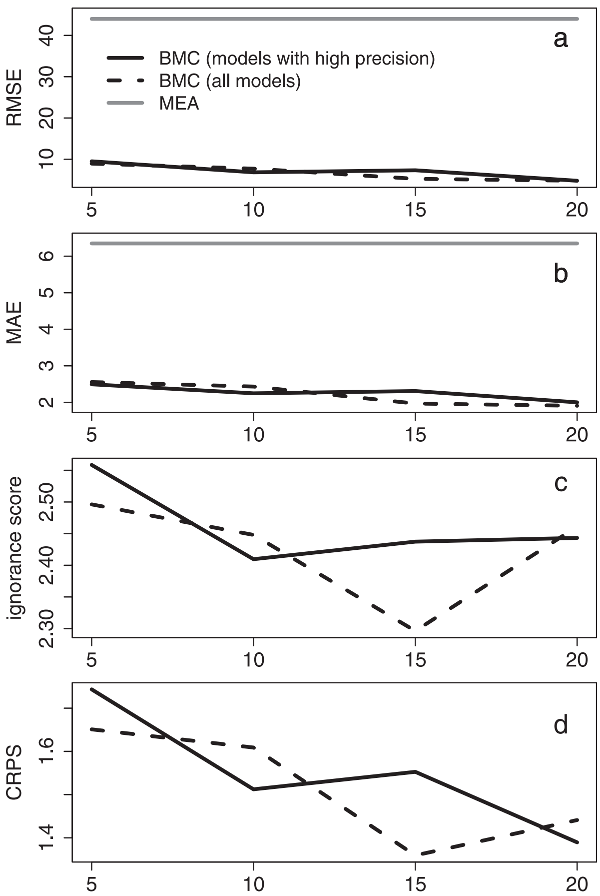

FIG. 4. (a) RMSE, (b) MAE, (c) IS, and (d) CRPS for the BMC projections using the seven models with the highest precision (black solid line), the BMC projections using all the models (black dashed line), and the MEA projections (gray line) for training periods using freezing seasons spanning 5 (1977–81), 10 (1972–81), 15 (1967–81), and 20 (1962–81) yr. The verification period is from 1992 to 1999.

in Figs. 4c,d, respectively. They reveal that a longer training period does not necessarily result in better scores. However, the longest training period leads to comparatively good results. We also could not find any physical reasons to dismiss parts of the historical data, and no signs of overfitting because of too much information were apparent. Therefore, we chose the whole historical period (1962–99) as the training period for the projections. Here also the scores of the set of seven models with high precision, which we choose for the analysis, are on par with the BMC projections of all the models.

d. Results

Projections are carried out for the A2 and B1 scenarios. Scenario A2 is a rather pessimistic scenario; a regionalized, heterogeneous world with high population growth and energy use and slow technological evolution is assumed, which results in high CO_2 concentrations hitting about 840 ppm at the end of the twenty-first century. By contrast B1 expects low population growth and energy use and a medium technical evolution, and is therefore a low-emission scenario. In Fig. 5 exemplarily marginal posterior parameter distributions for the projection to years 2082–99 and the A2 scenario are shown. The posterior parameter distributions are a means to test for significance. The slope of the trend in the training period (Fig. 5a) and prediction period (Fig. 5b) differ in size, but both are significant; that is, zero is not included in the slope distributions. With a length of approximately 20 years, the prediction periods are relatively short. Therefore, the term significance is related to the existence of a trend in presence of noise rather than pointing to an irreversible downward trend. For the B1 scenario, no significant trend could be found for the years 2082–99. The parameter ϕ, shown in Fig. 5c, reflects the autocorrelation present in the data, and in Fig. 5d a model bias is depicted. The BMC projections are the basis for the examination of the future ice accumulation over the oceanic Arctic region. This might give insight into the minimal ice accumulation of the oceanic Arctic ice at the end of the summer, in case the relation to SAT temperature is the same for the end of the twentieth and twenty-first centuries, which is assumed when projecting the ice index. This index allows for a qualitative assessment of the ice accumulation, since quantitatively the ice amount estimated from NCEP reanalysis data differs from the actual amount of ice. Figure 6 shows projections for years 2046–65 and 2082–99 and the A2 (Fig. 6a) and B1 (Fig. 6b) scenarios. Apparently, the variability of the mean of the predictive distributions, which we take as point projection, is very low. This might be a side effect of Kalman filtering. However, the projection is expected to occur within the bandwidth of the whole predictive distribution. Thus, the variability of the observations is more or less preserved for the projections. The first projection period shows a comparable decline of the ice index for both scenarios. Under the A2 scenario, this tendency of reduction of the ice accumulation over the oceanic Arctic region in the freezing season continues in the years 2082–99, whereas for the B1 scenario, interestingly, a stabilization of the ice accumulation is indicated. Correspondingly, Zhang and Walsh (2006) and Gregory et al. (2002) find a decreasing trend for sea ice extent for those scenarios and the twenty-first century. However, they do not analyze the evolution of this trend.

To evaluate the choice of the state-space model, we compare our results in Fig. 7. Here the evolution of the

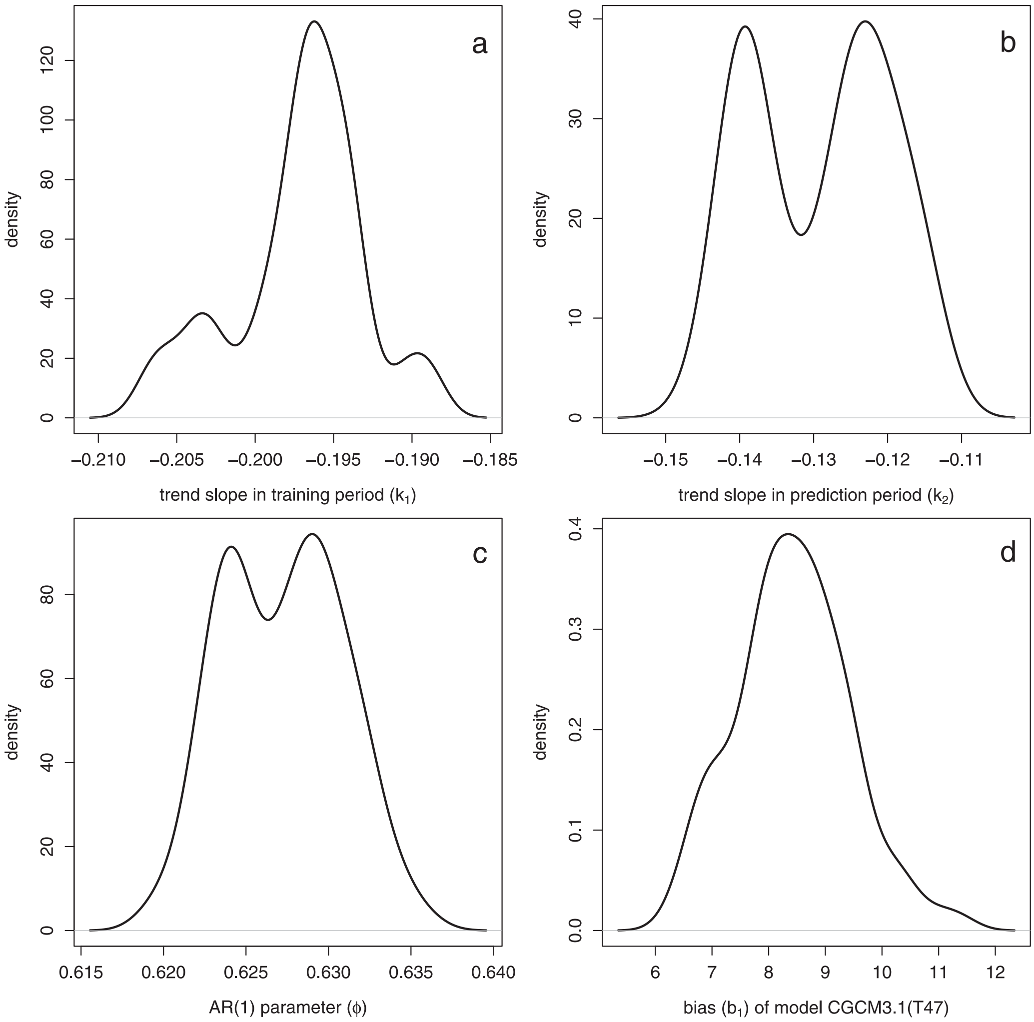

FIG. 5. Posterior distribution of the trend slope in the (a) training period k_1 and (b) prediction period k_2, (c) AR(1) parameter ϕ, and (d) estimated bias b_1 of Canadian Centre for Climate Modelling and Analysis (CCCma) Coupled General Circulation Model, version 3.1 [CGCM3.1(T47)] for the projection to years 2082–99 under the A2 scenario.

distribution of the common means MT_t is shown for the training period (Fig 7a) and MP_t for the prediction period 2082–99 for the B1 scenario (black lines; Fig. 7b). Furthermore, the following state-space models are assessed: The common means being composed of intercept and trend (gray lines), of intercept and AR component (black dashed lines), and of a constant intercept only (gray dashed lines). The width of the densities reflects the uncertainty of the estimate of the common means, not the variability of the projected observations. We find that the projected common means are estimated with approximately the same accuracy as the common means in the training period; all distributions span about 4×10^9 km^2 °C. Furthermore, the less complex state-space models are capable of estimating the projected common means with comparable good accuracy. Similar results are obtained for the other three projection periods (not shown). In Fig. 8 results for the four state-space models are compared for the A2 scenario projection period 2046–65. In Fig. 8a the densities of the difference of the common means in the training and projection periods are shown (the densities of the nonstationary state-space models have been averaged over the training period and the prediction period, respectively). This important figure indicates the expected average change of the ice index. In line with Fig. 7, it is nearly the same for all four state-space models. The mean of the densities is at about -16×10^9 km^2 °C; that is, a decrease of the ice index of 26% is expected. We find for the B1 scenario and this period an expected change of 22.9%, and for the second

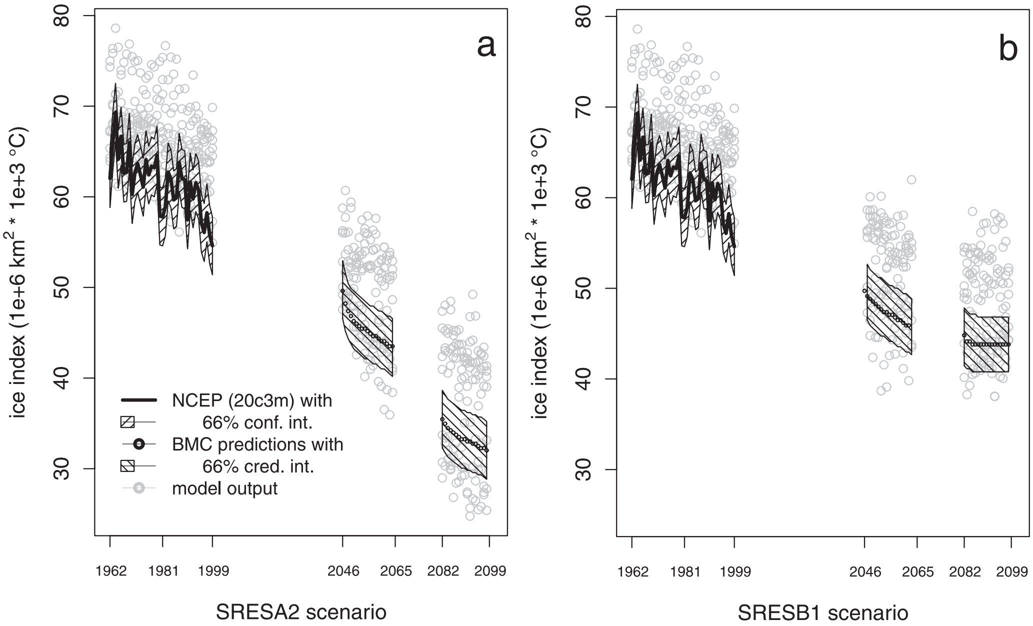

FIG. 6. Ice index generated from NCEP reanalysis data (black line, with 66% confidence interval) and BMC projections of the ice index (black dots, with 66% credibility interval) into future periods 2046–65 and 2082–99 for the (a) A2 and (b) B1 scenarios.

prediction period 2082–99 expected changes of 28.4% for the B1 scenario and 45.7% for the A2 scenario, which indicates nearly a halving of the ice volume. In Fig. 8b the evolution of the projected observations Y_0 are shown. Here the advantage of including a trend component becomes obvious (in case the GCM projections reflect the right trend behavior). The inclusion of an AR component (black dashed line) does not lead to deviations of the projections of a constant common mean (gray dashed line). However, the nonzero estimate

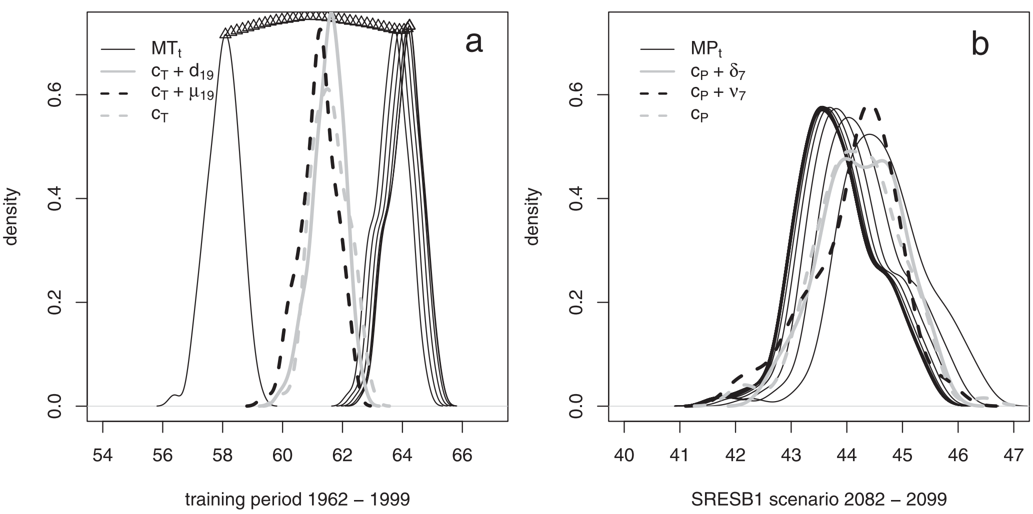

FIG. 7. Evolution of the distribution of the common means: (a) MT_t in the training period and (b) MP_t in the prediction period 2082–99 of the B1 (black lines) scenario. In addition, results for other state-space models are shown, including the common means composed of intercept and trend (gray lines), of intercept and AR component (black dashed lines), and of an intercept (gray dashed lines). For clarity some of the common mean distributions in the training period are indicated by black triangles and exemplarily only one distribution is depicted for the other nonstationary state-space models.

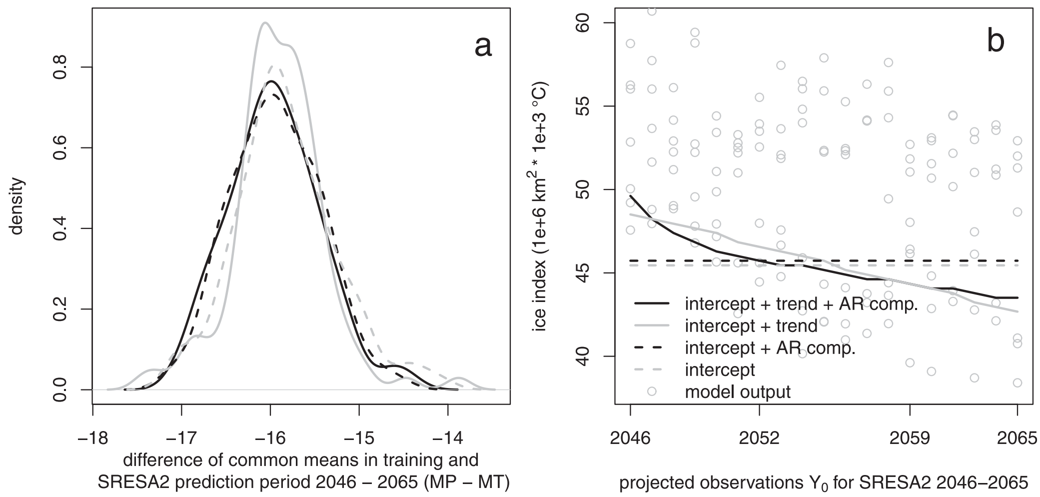

FIG. 8. (a) Expected average change of the ice index and (b) evolution of the projected observations Y_0 for years 2046–65 under the A2 scenario. Results for the different state-space models are depicted, i.e., common means comprising all three components (black lines), intercept and trend (gray lines), intercept and AR component (black dashed lines), and intercept (gray dashed lines).

of the AR parameter ϕ hints at the necessity of including an AR component. This component causes differences in the trend behavior (a comparison of black and gray lines), as discussed earlier.

In case constant common means are assumed, the approach of Tebaldi et al. (2005) is recovered (results are depicted as dashed gray lines in Figs. 7, 8). Thus, the main difference to this approach consists of nonstationary projections. Furthermore, we do not explicitly introduce any dependence between GCM outputs in the training and prediction periods.

To investigate the robustness of our results with respect to the different training periods, we compare the projections of training periods 1962–79 (T1), 1971–89 (T2), and 1981–99 (T3) to the period 1946–65 for the A2 scenario. In Fig. 9a the mean of the GCM biases for the different training periods and their average are shown. The dispersal of the bias among the models is similar for all the training periods evaluated, and the averaged biases are very close together. The training period 1981–99 has the highest averaged model bias, which may be related to the fact that IPCC GCM runs do not reproduce well the decrease of sea ice extent within this period (Stroeve et al. 2007). The average precision of all models is on par for nearly all training periods; it is slightly worse for 1971–89 (results not shown). However, these differences do not strongly influence the projection results: Figure 9b exemplarily shows the distribution of the common mean for year 2054. In our model we assume the same bias for the training and projection periods. The bias correction is largest for the training period 1981–99; therefore, those projections lie below the other projections. The width of the density of the common mean is largest for the training period 1962–79, which hints at a larger spread of the model outputs during that period. The use of a longer training period (gray lines) does not lead to a coarser density of the common mean estimate. Nevertheless, a longer training period allows for a better estimation of the constant parameters such as model biases, which are meant to represent average values. In Fig. 9c the evolution of the common means are depicted. We find comparable trend tendencies within the projection period for all the training periods assessed. All in all the projection results show to be robust. This is due to the little differences in model bias and precision for the training periods chosen.

In Fig. 10 the BMC projections are depicted in comparison to the total global cumulative CO_2 emissions (cf. Nakicenovic and Swart 2000). A direct link between global emission amounts and the ice index, which represents dynamics on the comparatively small oceanic Arctic region, might not exist. However, for the first projection period, the emission paths for both scenarios overlap significantly, whereas for the second prediction period already a clear separation appears visible. This fits well with the evolution of the ice index for both scenarios. Furthermore, the potential stabilization of the ice accumulation decrease for the B1 scenario and the second prediction period is accompanied by a decelerated increase of the cumulative CO_2 emissions: In the B1 scenario an actual reduction of the global annual CO_2 emissions is achieved from 2050 on, whereas this annual contribution never ceases to increase for the A2 scenario. This seems to have an effect on the SAT

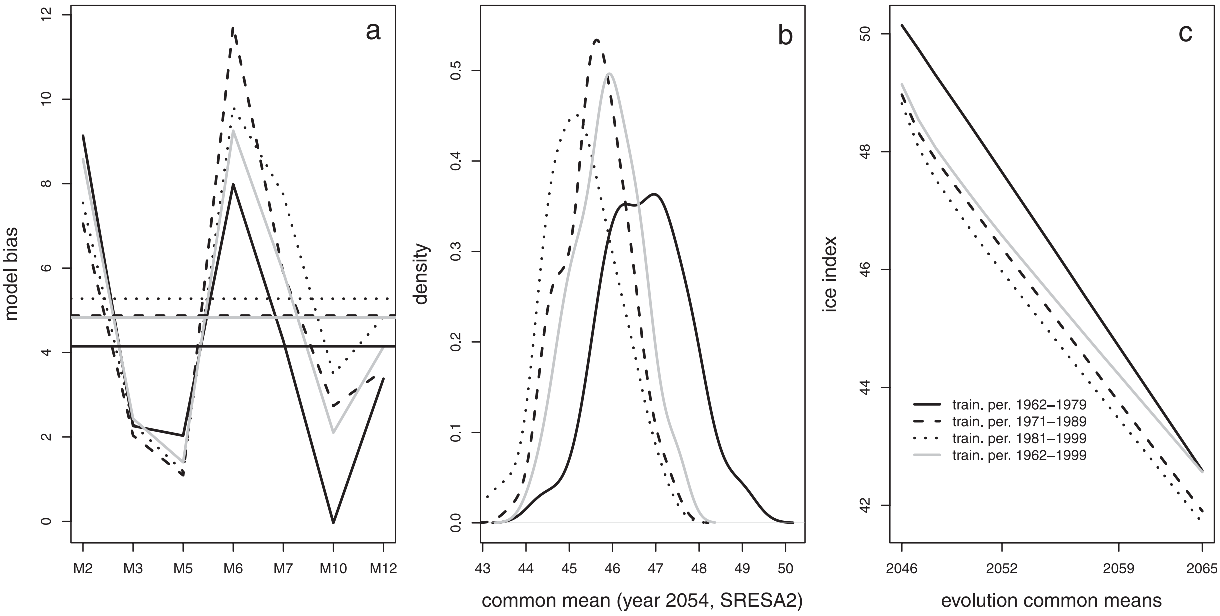

FIG. 9. Comparison of projections to period 2046–65 of the A2 scenario with training periods 1962–79 (black lines), 1971–89 (black dashed lines), 1981–99 (black dotted lines), and with the entire historical training period (gray lines). Shown are (a) model biases and the average model bias, (b) the density of the common mean at year 2054, and (c) the evolution over the common means over time.

and therefore on the ice accumulation over the oceanic Arctic.

5. Conclusions

In this paper we present a Bayesian method to enhance projections. Information from a multimodel ensemble is combined within a statistical framework. The parameters of the statistical model are estimated by regarding observations and multimodel outputs as random variables, which float (with a potential bias) around a common mean. This allows assess to model-specific deficiencies, namely, variability and bias. It is advantageous that all parameters are estimated together, which reduces estimation errors. Although we start from diffuse priors, informative posterior distributions are derived for all parameters. The methodology is applied to an ice index representing the ice accumulation over the oceanic Arctic region during cold seasons. Under the A2 scenario, we find a continuing decrease of the ice index, whereas for the B1 scenario, stabilization appears visible by the end of the twenty-first century. The stabilization hints at the retention of a minimum of ice rebuilding capacity in the freezing season for this scenario, which is important for questions related to adaptation and resilience (cf. Chapin et al. 2006; Laidler 2006).

Information from the entire training and prediction period is utilized for the BMC projections, whereas for simple averaging, only GCM outputs at one time step are relevant. Furthermore, here the models are not combined additively. In this way we do not have to adjust the length of the training period to the amount of information available. The Bayesian combination of multimodel ensembles were shown to potentially ameliorate projection skills in comparison to single-model projections or to the average of ensemble projections. A possible extension is the integration of expert knowledge on the GCM outputs by means of the priors.

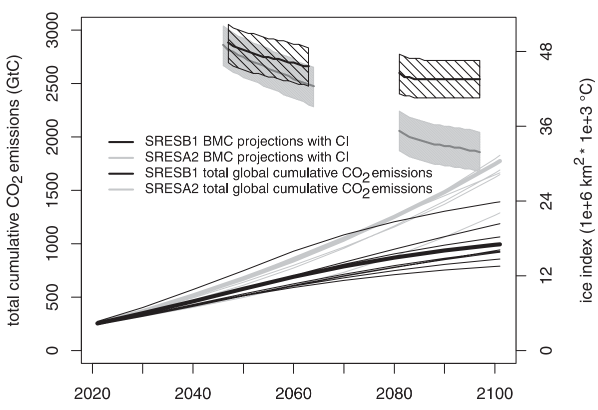

FIG. 10. BMC projections of the ice index into future periods 2046–65 and 2082–99 for the A2 (dark gray line and gray-shaded credibility intervals) and B1 (black line and black-shaded credibility intervals) scenarios with the axis on the right-hand side. For comparison total global cumulative CO_2 emissions for the A2 (gray lines) and B1 (black lines) scenario groups are shown [Source: data tables, appendix VII of Nakicenovic and Swart (2000)].

Acknowledgments. This work has been realized within the EU Marie Curie research network Network for Ice Sheet and Climate Evolution (NICE, available online at nice.ipsl.jussieu.fr; Contract 036127). In addition, Philippe Naveau's work has been supported by the EU-FP7 ACQWA project (www.acqwa.ch; Contract 212250), by the PEPER-GIS project (www.gisclimat.fr/projet/peper), and by the ANR-MOPERA project. We wish to thank both projects for their financial support. Furthermore, we are grateful to Michel Kolasinski for the preprocessing of the data and for helpful comments. The technique to create the ice index, which has been evaluated in this study, has been developed in the context of the EU project DAMOCLES (available online at www.damocles-eu.org), and we especially thank J.-C. Gascard for its provision.

APPENDIX

MCMC Routine for Model with Time-Dependent Parameters

A MCMC routine is used to generate pseudorandom drawings from the posterior distribution of the state-space components $\boldsymbol{\Theta}$ (cf. Harvey et al. 2007). To obtain the joint posterior $[\boldsymbol{\Theta}|\mathbf{D}]$, we divide a Gibb's sampling procedure in several blocks: First, the state-space parameters $\mu_t^{(i)}$, $d_t^{(i)}$, $\nu_t^{(i)}$, and $\delta_t^{(i)}$ are obtained by Kalman filtering and smoothing; then, marginal conditional likelihoods of the stationary parameters are evaluated. Next, for the parameter ϕ, a Metropolis–Hastings step is integrated in the Gibb's procedure. The algorithm converges to the joint posterior distribution of the parameters (cf. Chib and Greenberg 1996).

The vector of initial values for the stationary parameters $\boldsymbol{\Theta}_{\text{stat}}^{(0)} = (c_T^{(0)}, c_P^{(0)}, \gamma^{(0)}, \phi^{(0)}, k_1^{(0)}, k_2^{(0)}, \lambda_1^{(0)}, \ldots, \lambda_M^{(0)}, b_1^{(0)}, \ldots, b_M^{(0)}, \lambda_\mu^{(0)}, \lambda_\nu^{(0)}, \lambda_d^{(0)}, \lambda_\delta^{(0)})$ is provided. Then, the MCMC routine is run to produce a sequence of draws $\boldsymbol{\Theta}^{(i)}$, $i = 1, \ldots, R$. We utilize a burn in the period of 5000 steps, set $R = 100$, and keep the parameter values only every 50th iteration to avoid correlations between the $\boldsymbol{\Theta}^{(i-1)}$ and $\boldsymbol{\Theta}^{(i)}$. In each iteration step, we proceed as follows:

1) To draw $\mu^{(i)}$, $\nu^{(i)}$, $d^{(i)}$, and $\delta^{(i)}$ out of $[\mu^{(i)}, d^{(i)}, \nu^{(i)}, \delta^{(i)}|\boldsymbol{\Theta}_{\text{stat}}, \mathbf{D}]$ given the most recent iterate of $\boldsymbol{\Theta}_{\text{stat}}^{(i-1)}$, a Kalman smoother proposed by Dethlefsen and Lundbye-Christensen (2005) is employed (see also Durbin and Koopman 2002). We restrict the trend components to have mean 0; a potential deviation from this is captured by the intercepts c_T and c_P.
2) We sample $\boldsymbol{\Theta}_{\text{stat}}$ in block from $[\boldsymbol{\Theta}_{\text{stat}}^{(i)}|\mu^{(i)}, d^{(i)}, \nu^{(i)}, \delta^{(i)}, \mathbf{D}]$ by using the Gibb's sampler. The constant parameters have independent priors and their posterior distribution is given by Eq. (13). We only use information of the training period to estimate the precision of the models λ_i and their bias b_i. Therefore, we obtain

$$\lambda_i{:}U(0,c) \Rightarrow G\left\{\frac{T+2}{2}, \frac{\sum_{t-1}^{T}[X_{i_t} - (c_T + \mu_t + d_t + b_i)]^2}{2}\right\}$$

and

$$b_i{:}U(-\infty,\infty) \Rightarrow N\left\{\frac{\sum_{t=1}^{T}[X_{i_t} - (c_T + \mu_t + d_t)]}{T}, (\lambda_i T)^{-1}\right\}. \quad \text{(A1)}$$

The marginal posterior distribution of the change in precision γ is given by

$$\gamma{:}U(0,c) \Rightarrow G\left\{\frac{\mathrm{MP}+2}{2}, \frac{\sum_{i=1}^{M}\sum_{t=G+1}^{G+P}\lambda_i[Y_{i_t} - (c_P + \nu_t + \delta_t + b_i)]^2}{2}\right\}. \quad \text{(A2)}$$

For the precisions of the state-space model,

$$\lambda_\mu{:}U(0,c) \Rightarrow G\left[\frac{T+1}{2}, \frac{\sum_{t=2}^{T}(\mu_t - \phi\mu_{t-1})^2}{2}\right],$$

$$\lambda_d{:}U(0,c) \Rightarrow G\left[\frac{T+1}{2}, \frac{\sum_{t=2}^{T}(d_t - d_{t-1} - k_1)^2}{2}\right],$$

$$\lambda_\nu{:}U(0,c) \Rightarrow G\left[\frac{P+1}{2}, \frac{\sum_{t=G+2}^{G+P}(\nu_t - \phi\nu_{t-1})^2}{2}\right], \quad \text{and}$$

$$\lambda_\delta{:}U(0,c) \Rightarrow G\left[\frac{P+1}{2}, \frac{\sum_{t=G+2}^{G+P}(\delta_t - \delta_{t-1} - k_2)^2}{2}\right] \quad \text{(A3)}$$

holds, and the posterior marginal distributions of k_1 and k_2 are given by

$$k_1{:}U(-\infty,\infty) \Rightarrow N\left\{\frac{\sum_{t=2}^{T}(d_t - d_{t-1})}{T-1}, [(T-1)\lambda_d]^{-1}\right\}$$

and

$$k_2{:}U(-\infty,\infty) \Rightarrow N\left\{\frac{\sum_{t=G+2}^{G+P}(\delta_t - \delta_{t-1})}{P-1}, [(P-1)\lambda_\delta]^{-1}\right\}. \quad \text{(A4)}$$

3) The autoregressive parameter ϕ is drawn from

$$[\phi|k_1, k_2, b_1, \ldots, b_M, c_T, c_P, \gamma, \lambda_1, \ldots, \lambda_M, \lambda_\mu, \lambda_d, \lambda_\nu, \lambda_\delta, \mu, d, \nu, \delta, \mathbf{D}] \propto [\mathbf{D}|\mathbf{\Theta}][\mu, d, \nu, \delta|\mathbf{\Theta}_{\text{stat}}][\phi] \propto [\mu, d, \nu, \delta|\mathbf{\Theta}_{\text{stat}}][\phi]. \quad \text{(A5)}$$

As posterior marginal distribution, we obtain

$$\phi{:}U(-1,1) \Rightarrow N\left(\frac{\lambda_\mu \sum_{t=2}^{T} \mu_t \mu_{t-1} + \lambda_\nu \sum_{t=G+2}^{G+P} \nu_t \nu_{t-1}}{\lambda_\mu \sum_{t=2}^{T} \mu_{t-1}^2 + \lambda_\nu \sum_{t=G+2}^{G+P} \nu_{t-1}^2}, \left(\lambda_\mu \sum_{t=2}^{T} \mu_{t-1}^2 + \lambda_\nu \sum_{t=G+2}^{G+P} \nu_{t-1}^2\right)^{-1}\right), \quad \text{(A6)}$$

whereas ϕ is sampled from a truncated normal. The state-space variables depend on ϕ, and the relation is more complex than for the other parameters. Therefore, we include a Metropolis–Hastings step to sample ϕ: a proposal value ϕ^* is obtained from a symmetric proposal distribution, and Eq. (A6) is evaluated for $\phi^{(i-1)}$ and ϕ^*. If $[\phi^*|\cdot] > [\phi^{(i-1)}|\cdot]$, the proposal ϕ^* is accepted, that is, $\phi^{(i)} = \phi^*$; otherwise, ϕ^* is accepted with probability $[\phi^*|\cdot]/[\phi^{(i-1)}|\cdot]$.

REFERENCES

Anderson, D. L., 1961: Growth rate of sea ice. *J. Glaciol.,* **3,** 1170–1172.

Baettig, M. B., M. Wild, and D. M. Imboden, 2007: A climate change index: Where climate change may be most prominent in the 21st century. *Geophys. Res. Lett.,* **34,** L01705, doi:10.1029/2006GL028159.

Berliner, L. M., and Y. Kim, 2008: Bayesian design and analysis for superensemble-based climate forecasting. *J. Climate,* **21,** 1891–1910.

Bloomfield, P., 1992: Trends in global temperature. *Climatic Change,* **21,** 1–16.

Bromwich, D. H., R. L. Fogt, K. I. Hodges, and J. E. Walsh, 2007: A tropospheric assessment of the ERA-40, NCEP, and JRA-25 global reanalyses in the polar regions. *J. Geophys. Res.,* **112,** D10111, doi:10.1029/2006JD007859.

Cavalieri, D. J., and C. L. Parkinson, 2008: Antarctic sea ice variability and trends, 1979–2006. *J. Geophys. Res.,* **113,** C07004, doi:10.1029/2007JC004564.

Chapin, F. S., III, and Coauthors, 2006: Building resilience and adaptation to manage Arctic change. *Ambio,* **35,** 198–202.

Charbit, S., D. Paillard, and G. Ramstein, 2008: Amount of CO_2 emissions irreversibly leading to the total melting of Greenland. *Geophys. Res. Lett.,* **35,** L12503, doi:10.1029/2008GL033472.

Chib, S., and E. Greenberg, 1996: Markov chain Monte Carlo simulation methods in econometrics. *Econ. Theory,* **12,** 409–431.

Coelho, C. A. S., S. Pezzulli, M. Balmaseda, F. J. Doblas-Reyes, and D. B. Stephenson, 2004: Forecast calibration and combination: A simple Bayesian approach for ENSO. *J. Climate,* **17,** 1504–1516.

Cohn, T. A., and H. F. Lins, 2005: Nature's style: Naturally trendy. *Geophys. Res. Lett.,* **32,** L23402, doi:10.1029/2005GL024476.

Congdon, P., 2003: *Applied Bayesian Modelling*. John Wiley & Sons, 457 pp.

Davison, A. C., 2003: *Statistical Models*. Cambridge University Press, 726 pp.

De Jong, P., and N. Shephard, 1995: The simulation smoother for time series models. *Biometrika,* **82,** 339–350.

DelSole, T., 2007: A Bayesian framework for multimodel regression. *J. Climate,* **20,** 2810–2826.

Dethlefsen, C., and S. Lundbye-Christensen, 2005: Formulating state space models in R with focus on longitudinal regression models. Aalborg University Research Rep. Series R-2005-21, 12 pp.

Döscher, R., K. Wyser, H. E. M. Meier, M. Qian, and R. Redler, 2009: Quantifying Arctic contributions to climate predictability in a regional coupled ocean-ice-atmosphere model. *Climate Dyn.,* 1157–1176, doi:10.1007/s00382-009-0567-y.

Durbin, J., and S. J. Koopman, 2002: A simple and efficient simulation smoother for state space time series analysis. *Biometrika,* **89,** 603–616, doi:10.1093/biomet/89.3.603.

Gelman, A., 2006: Prior distributions for variance parameters in hierarchical models. *Bayesian Anal.,* **1,** 515–534.

——, J. B. Carlin, H. S. Stern, and D. B. Rubin, Eds., 2004: *Bayesian Data Analysis*. 2nd ed. Chapman & Hall/CRC, 668 pp.

Gneiting, T., A. E. Raftery, A. H. Westveld III, and T. Goldman, 2005: Calibrated probabilistic forecasting using ensemble model output statistics and minimum CRPS estimation. *Mon. Wea. Rev.,* **133,** 1098–1118.

Gregory, J. M., P. A. Stott, D. J. Cresswell, N. A. Rayner, C. Gordon, and D. M. H. Sexton, 2002: Recent and future changes in Arctic sea ice simulated by the HadCM3 AOGCM. *Geophys. Res. Lett.,* **29,** 2175, doi:10.1029/2001GL014575.

Harvey, A. C., T. M. Trimbur, and H. K. Van Dijk, 2007: Trends and cycles in economic time series: A Bayesian approach. *J. Econ.,* **140,** 618–649, doi:10.1016/j.jeconom.2006.07.006.

Hassol, S. J., 2004: *Impacts of a Warming Arctic: Arctic Climate Impact Assessment*. Cambridge University Press, 139 pp.

Hersbach, H., 2000: Decomposition of the continuous ranked probability score for ensemble prediction systems. *Wea. Forecasting,* **15,** 559–570.

Johannessen, O. M., and Coauthors, 2004: Arctic climate change: Observed and modelled temperature and sea-ice variability. *Tellus,* **56A,** 328–341.

Kallache, M., H. W. Rust, and J. Kropp, 2005: Trend assessment: Applications for hydrology and climate. *Nonlinear Processes Geophys.,* **12,** 201–210.

Kaufman, D. S., and Coauthors, 2009: Recent warming reverses long-term Arctic cooling. *Science,* **325,** 1236–1239, doi:10.1126/science.1173983.

Koop, G., and H. K. Van Dijk, 2000: Testing for integration using evolving trend and seasonals models: A Bayesian approach. *J. Econ.,* **97,** 261–291.

Kwok, R., and D. A. Rothrock, 2009: Decline in Arctic sea ice thickness from submarine and ICESat records: 1958–2008. *Geophys. Res. Lett.,* **36,** L15501, doi:10.1029/2009GL039035.

Laidler, G. J., 2006: Inuit and scientific perspectives on the relationship between sea ice and climate change: The ideal complement? *Climatic Change,* **78,** 407–444, doi:10.1007/s10584-006-9064-z.

Laxon, S., N. Peacock, and D. Smith, 2003: High interannual variability of sea ice thickness in the Arctic region. *Nature,* **425,** 947–950, doi:10.1038/nature02050.

Maksimovich, E., and J. C. Gascard, cited 2010: Winter near-surface warming in NCEP/NCAR reanalysis I. Reanalysis error or arctic warming? Earlier melt onset and later freeze-up? [Available online at http://www.damocles-eu.org/artman2/uploads/1/poster_Sopot_task_5.2.1.pdf.]

Maykut, G. A., 1986: The surface heat and mass balance. *The Geophysics of Sea Ice,* N. Untersteiner, Ed., NATO ASI Series B, Vol. 146, Plenum Press, 395–463.

Meinhold, R. J., and N. D. Singpurwalla, 1983: Understanding the Kalman filter. *Amer. Stat.,* **37,** 123–127.

Min, S.-K., and A. Hense, 2006: A Bayesian assessment of climate change using multimodel ensembles. Part I: Global mean surface temperature. *J. Climate,* **19,** 3237–3256.

——, ——, H. Paeth, and W.-T. Kwon, 2004: A Bayesian decision method for climate change signal analysis. *Meteor. Z.,* **13,** 421–436.

Nakicenovic, N., and R. Swart, Eds., 2000: *Special Report on Emissions Scenarios*. Cambridge University Press, 599 pp.

Parry, M. L., O. F. Canziani, J. P. Palutikof, P. J. van der Linden, and C. E. Hanson, Eds., 2007: *Climate Change 2007: Impacts, Adaptation and Vulnerability*. Cambridge University Press, 976 pp.

Raftery, A. E., T. Gneiting, F. Balabdaoui, and M. Polakowski, 2005: Using Bayesian model averaging to calibrate forecast ensembles. *Mon. Wea. Rev.,* **133,** 1155–1174.

Rougier, J., 2007: Probabilistic inference for future climate using an ensemble of climate model evaluations. *Climatic Change,* **81,** 247–264, doi:10.1007/s10584-006-9156-9.

Ruzmaikin, A., and J. Feynman, 2002: Solar influence on a major mode of atmospheric variability. *J. Geophys. Res.,* **107,** 4209, doi:10.1029/2001JD001239.

Stroeve, J., M. M. Holland, W. Meier, T. Scambos, and M. Serreze, 2007: Arctic sea ice decline: Faster than forecast. *Geophys. Res. Lett.,* **34,** L09501, doi:10.1029/2007GL029703.

Tebaldi, C., R. L. Smith, D. Nychka, and L. O. Mearns, 2005: Quantifying uncertainty in projections of regional climate change: A Bayesian approach to the analysis of multimodel ensembles. *J. Climate,* **18,** 1524–1540.

Tol, R. S. J., and A. F. De Vos, 1998: A Bayesian statistical analysis of the enhanced greenhouse effect. *Climatic Change,* **38,** 87–112.

van Loon, M., and Coauthors, 2007: Evaluation of long-term ozone simulations from seven regional air quality models and their ensemble. *Atmos. Environ.,* **41,** 2083–2097.

West, M., 1997: Time series decomposition. *Biometrika,* **84,** 489–494.

Zhang, X., and J. E. Walsh, 2006: Toward a seasonally ice-covered Arctic ocean: Scenarios from the IPCC AR4 model simulations. *J. Climate,* **19,** 1730–1747.